# Localisation de la déformation dans les géomatériaux : caractérisation expérimentale et modélisation

Pierre Bésuelle

Pierre Bésuelle. Localisation de la déformation dans les géomatériaux : caractérisation expérimentale et modélisation. Mécanique des solides [physics.class-ph]. Université Joseph Fourier (Grenoble I), 2011. tel-02014040

HAL Id: tel-02014040
https://hal.univ-grenoble-alpes.fr/tel-02014040v1
Submitted on 11 Feb 2019

Mémoire pour obtenir le diplôme

d'**habilitation à diriger des recherches**

de l'Université de Grenoble

présenté par

**Pierre Bésuelle**

Chargé de Recherche au CNRS

Laboratoire Sols, Solides, Structures et Risques

UMR 5521 (CNRS - UJF - Grenoble INP)

---

# Localisation de la déformation dans les géomatériaux : caractérisation expérimentale et modélisation

---

présenté le $1^{er}$ juillet 2011

JURY

| | | |
|---|---|---|
| Gilles Pijaudier-Cabot | Université de Pau et des Pays de l'Adour (Anglet) | Rapporteur |
| James R. Rice | Université de Harvard (USA) | Rapporteur |
| Claudio Tamagnini | Université de Perugia (Italie) | Rapporteur |
| René Chambon | Université Joseph Fourier (Grenoble) | Président |
| Stéphane Roux | Ecole Normale Supérieure de Cachan | Examinateur |
| Jean Sulem | Ecole des Ponts Paritech (Champs-sur-Marne) | examinateur |

Mémoire pour obtenir le diplôme

d'**habilitation à diriger des recherches**

de l'Université Joseph Fourier

présenté par

**Pierre Bésuelle**

Chargé de Recherche au CNRS

Laboratoire Sols, Solides, Structures et Risques

UMR 5521 (CNRS - UJF - Grenoble INP)

# Localisation de la déformation dans les géomatériaux : caractérisation expérimentale et modélisation

# Table des matières

**Annexe 1** : sélection de publications, travaux expérimentaux

**Annexe 2** : sélection de publications, travaux de modélisation

# 1 Introduction

La localisation de la déformation dans les géomatériaux est le phénomène physique qui a motivé la plupart de mes travaux jusqu'à présent. Faut-il rappeler qu'il s'agit d'un aspect important de la géomécanique puisqu'il contrôle nombre de modes de rupture dans diverses applications des sciences de l'ingénieur : génie civil, géotechnique, génie pétrolier, stockage de déchets radioactifs en grande profondeur, pour en citer quelques uns. Il intéresse aussi la géologie structurale puisque la listhosphère présente des structures de localisation. Il est présent à diverses échelles, du kilomètre au micromètre (voire en dessous) pour simplifier. La localisation de la déformation se décrit comme la transition d'un mode de déformation diffus vers un mode où la déformation se concentre dans des structures étroites et élancées (bandes de déformation). Il s'agit de ce fait d'un changement d'échelle au point de vue cinématique. On peut aussi le considérer comme un problème de non unicité du mode de déformation : un mode de déformation alternatif au mode de déformation diffus qui prévalait auparavant devient possible sous certaines conditions. C'est par les conséquences qu'elle induit que la localisation de la déformation justifie qu'on s'y intéresse. Parce qu'il y concentration spatiale de la déformation, il y a aussi accroissement majeur de l'amplitude de la déformation à l'intérieur des bandes. Les géomatériaux ne peuvent subir des déformations importantes sans une altération notable, entrainant assez souvent une perte de résistance, pouvant parfois conduire à une fissuration (discontinuité matérielle). On peut ajouter à l'argument purement mécanique la prise en compte des couplages physiques, par exemple en considérant un matériaux poreux rempli d'un liquide. La localisation peut entrainer des variations de porosité, d'où des variations de la pression interstitielle, ou bien des changements des propriétés de transport, qui fait qu'une bande de déformation joue un rôle de drain ou de barrière pour l'écoulement du fluide (aquifère, réservoir pétrolier, déchets). On l'aura compris, le phénomène de localisation peut avoir dans le pire des cas des effets importants avec des répercussions pour les activités humaines (tenue des fondations d'un ouvrage, glissement de terrain, faille sismique), mais aussi, et heureusement, les effets peuvent rester bénins, ce qui n'empèche pas un ouvrage de continuer à assurer sa fonction.

Les enjeux vis-à-vis des sciences de l'ingénieur sont d'une part d'expliciter les conditions d'apparition de la localisation pour un problème aux limites, et d'autre part, quand celle-ci s'est mise en place, de la modéliser pour un cerner les effets. Pour cela, plusieurs ingrédients doivent être particulièrement soignés. Tout d'abord, la richesse de la loi de comportement[1] détermine les conditions d'ap-

---

[1] On se place ici dans une approche de type milieu continu. La loi de comportement du matériau, à l'échelle macroscopique, décrit de manière simplifiée les phénomènes de déformation à l'échelle microscopique.

parition de la localisation, c'est de la forme mathématique même de la relation constitutive que dépend en partie la naissance des bandes, que l'on peut expliciter par un critère de localisation[2]. Ensuite, dès que l'on s'intéresse au régime de post-localisation (en présence de bandes de déformation), ce sont les outils numériques qui doivent être plus élaborés que ceux utilisés classiquement (qui eux restent pertinents tant qu'il n'y a pas de localisation), cela nécessite d'utiliser des formalismes de milieu continu enrichis, afin de limiter certains artefacts numériques et de contrôler la largeur des bandes de localisation.

Ma contribution à l'étude de la localisation dans les géomatériaux repose sur plusieurs approches que l'on peut décomposer, c'est le canevas proposé pour ce mémoire, en deux parties. L'une est d'ordre expérimental, visant à caractériser le comportement (homogène) de quelques géomatériaux (en l'occurence, grès, roches argileuses, roches calcaires, sables) ; à caractériser le lien entre le comportement et les structures de localisation observées ; à caractériser le lien entre localisation de la déformation et couplages physiques, principalement hydro - mécaniques ; à caractériser les micro-mécanismes de déformation mis en jeu lors la localisation. La seconde partie concerne la modélisation, d'une part pour établir le lien entre loi de comportement et mode de rupture plus ou moins fragile des roches par une analyse en bifurcation ; d'autre part pour modéliser le régime de post-localisation à l'aide de mileux enrichis.

Dans la suite de ce mémoire, après avoir listé mes principales publications scientifiques, je propose une première synthèse sur mon activité expérimentale, puis une seconde synthèse sur mes travaux de modélisation. A chaque fois, j'ai pris le soin d'insérer à la suite de ces résumés quelques publications. Je termine enfin par une conclusion et quelques perspectives de travail. Notons enfin que ce texte ne se veut pas comme une synthèse exhaustive de mes travaux, simplement un condensé de mes principales contributions, celles qui sont le plus abouties à ce stade.

[3, 73, 4, 8, 5, 2, 1, 12, 9, 6, 11, 7, 10], [13, 15, 16, 14], [19, 30, 20, 21, 24, 25, 18, 31, 33, 29, 26, 23, 28], [32, 35, 34, 27, 17, 22], [58, 48, 40, 37, 39, 38, 69, 45, 49, 47, 64, 62, 46, 63, 59, 60, 57, 54, 68, 61, 53, 55, 52, 56, 44, 50, 42, 43, 67, 65, 66, 51, 41, 70, 36], [71],[72, 77, 74, 76, 75]

---

[2] Ce critère de localisation peut lui être déduit par une approche en bifurcation, analysant la naissance de la localisation comme un problème de non unicité

# 3 Liste des publications

## Références

### Revues (WOS) à comité de lecture

[1] P. Bésuelle, *Compacting and dilating shear bands in porous rock : Theoretical and experimental conditions*, J. Geophys. Res. **106** (2001), no. B7, 13435–13442.

[2] P. Bésuelle, *Evolution of strain localisation with stress in a sandstone : brittle and semi-brittle regimes*, Phys. Chem. Earth, Part A **26** (2001), no. 1-2, 101–106.

[3] P. Bésuelle, P. Baud, and T.-f. Wong, *Spatial distribution of damage in Rothbach sandstone in the brittle ductile transition*, Pure Appl. Geophys. **160** (2003), no. 5-6, 851–868.

[4] P. Bésuelle, R. Chambon, and F. Collin, *Switching mode of deformation in post-localization solutions with a quasi brittle material*, J. Mech. Mater. Struct. **1** (2007), no. 7, 1115–1134.

[5] P. Bésuelle and J. Desrues, *An internal instrumentation for axial and radial strain measurements in triaxial tests*, Geotech. Test. J. **24** (2001), no. 2, 193–199.

[6] P. Bésuelle, J. Desrues, and S. Raynaud, *Experimental characterisation of the localisation phenomenon inside a Vosges sandstone in a triaxial cell*, Int. J. Rock Mech. Min. Sci. **37** (2000), no. 8, 1223–1237.

[7] S.A. Hall, M. Bornert, J. Desrues, Pannier Y., N. Lenoir, G. Viggiani, and P. Bésuelle, *Discrete and continuum analysis of localised deformation in sand using X-ray micro CT and volumetric digital image correlation*, Géotechnique **60** (2010), no. 5, 315–322.

[8] P. Kotronis, S. Al Holo, P. Bésuelle, and R. Chambon, *Shear softening and localization, modelling of the evolution of the width of the shear zone*, Acta Geotechnica **3** (2008), no. 2, 85–97.

[9] J. Lanier, D. Caillerie, R. Chambon, G. Viggiani, P. Bésuelle, and J. Desrues, *A general formulation of hypoplasticity*, Int. J. Numer. Anal. Meth. Geomech. **28** (2004), no. 15, 1461–1478.

[10] N. Lenoir, M. Bornert, J. Desrues, P. Bésuelle, and G. Viggiani, *Volumetric digital image correlation applied to X-ray microtomography images from triaxial compression tests on argillaceous rock*, Strain **43** (2007), 193–205.

[11] F. Tagliaferri, J. Waller, E. Andò, S.A. Hall, G. Viggiani, P. Bésuelle, and J.T. DeJong, *Observing strain localisation processes in bio-cemented sand using X-ray imaging (in print)*, Granular Matter (2011).

[12] G. Viggiani, N. Lenoir, P. Bésuelle, M. Di Michiel, S. Marello, J. Desrues, and M. Kretzschmer, *X-ray microtomography for studying localized deformation in fine-grained geomaterials under triaxial compression*, C. R. Acad. Sci. Paris **332** (2004), 819–826.

## Chapitres de livre et livre (avec acte de review)

[13] P. Bésuelle and J.W. Rudnicki, *Localization : Shear bands and compaction bands*, Mechanics of Fluid-Saturated Rocks (Y. Guéguen and M. Boutéca, eds.), Academic Press, Elsevier, 2004, pp. 219–321.

[14] J. Desrues, P. Bésuelle, and H. Lewis, *Strain localization in geomaterials*, The relationship between Damage and Localization (H. Lewis and G.D. Couples, eds.), vol. 289, Geological Society of London Special Publications, 2007, pp. 47–73.

[15] J. Desrues, G. Viggiani, and P. Bésuelle, *Advances in X-ray tomography for geomaterials*, Proceedings 2nd Int. Workshop on X-Ray CT for Geomaterials, GeoX 2006, ISTE Ltd, Grenoble & Aussois, October 4-7, 2006, 452 pages.

[16] Y. Guéguen and P. Bésuelle, *Damage and localisation : 2 key concepts in rock deformation studies*, The relationship between Damage and Localization (H. Lewis and G.D. Couples, eds.), vol. 289, Geological Society of London Special Publications, 2007, pp. 7–17.

## Proceedings de congrès internationaux à comité de lecture

[17] E. Andò, S.A. Hall, G. Viggiani, J. Desrues, and P. Bésuelle, *Analyzing the evolution of grains and contacts in sand under load*, Proc. Inter. Symp. on Geomechanics and Geotechnics : From Micro to Macro, IS-Shanghai 2010 (Shanghai, China, October 10-12) (M.D. Bolton, S. Leroueil, and Z.-Y. Chen, eds.), 2010.

[18] P. Bésuelle, *X-ray ct observations of strain localization and failure in two porous sandstones*, Proc. of the International Workshop on X-ray CT for Geomaterials, Soils, Concrete, Rocks, GeoX 2003 (Kumamoto, Japan, November 6-7) (J. Otani and Y. Obara, eds.), Balkema, Rotterdam, 2004, pp. 287–292.

[19] P. Bésuelle and R. Chambon, *Modelling the post-localization regime with local second gradient models : Non uniqueness of solutions and non persistent*

*shear bands*, Modern Trends in Geomechanics (Proc. Int. Workshop, Vienna, Austria, june 27-29, 2005) (W. Wu and H.-S. Yu, eds.), Springer, Berlin, 2006, pp. 209–221.

[20] P. Bésuelle and J. Desrues, *Homogeneous and localised deformation in sandstone specimens tested in a triaxial cell*, Proc. The Geotechnics of Hard Soils - Soft Rocks (Napoli, Italy) (Evangelista and Picarelli, eds.), Balkema, Rotterdam, 1998, pp. 37–43.

[21] P. Bésuelle and J. Desrues, *Internal instrumentation for strain measurements on soft rocks tested in an axisymmetric triaxial cell*, Proc. Int. Conf. The Geotechnics of Hard Soils - Soft Rocks (Napoli, Italy) (Evangelista and Picarelli, eds.), Balkema, Rotterdam, 1998, pp. 45–48.

[22] P. Bésuelle and S.A. Hall, *Characterization of the strain localization in a porous rock in plane strain condition using a new true-triaxial apparatus*, Proc. 9th International Workshop on Bifurcation and Degradation in Geomaterials, IWBDG 2011 (Porquerolles, France, may 23-26) (S. Bonelli, C. Dascalu, and F. Nicot, eds.), 2011.

[23] P. Bésuelle, G. Viggiani, N. Lenoir, J. Desrues, and M. Bornert, *X-ray micro CT for studying strain localization in clay rocks under triaxial compression (keynote lecture)*, Advances in X-Ray Tomography for Geomaterials, Proc. 2nd International Workshop on X-Ray CT for Geomaterials, GeoX 2006 (Grenoble & Aussois, France, October 4-7) (J. Desrues, G. Viggiani, and P. Bésuelle, eds.), ISTE, 2006.

[24] C. Coll, J. Desrues, P. Bésuelle, and G. Viggiani, *Characterizing in the laboratory permeability changes induced by deviatoric stress in clayey rocks*, Proc. Int. Conf. on Coupled T-H-M-C Processes in Geo-systems : Fundamentals, Modelling, Experiments & Applications (Stockholm, Sweden) (L. Jing, ed.), 2003, pp. 544–549.

[25] C. Coll, J. Desrues, P. Bésuelle, and G. Viggiani, *Permeability changes induced by deviatoric stress in clayey rocks*, Proc. Int. Conf. Impact of the excavation disturbed or damaged zone (EDZ) on the performance of radioactive waste geological repositories (Luxembourg) (European Commission and EIG Euridice, eds.), 2003, pp. 255–260.

[26] J. Desrues, P. Bésuelle, C. Coll, F. Collin, and X.L. Li, *Poro hypo plastic analysis of the progressive excavation of the Mol URL connecting gallery*, Proc of the European Regional ISRM Symp., Multiphysics coupling and long term behaviour in rock mechanics, Eurock 2006 (Liège, Belgium, May 9-12) (A. Van Cotthem, J.-P. Tshibangu, and R. Charlier, eds.), 2006.

[27] S.A. Hall, N. Lenoir, G. Viggiani, P. Bésuelle, and J. Desrues, *Characterisation of the evolving grain-scale structure in a sand deforming under triaxial com-*

*pression*, Proc. 3rd International Workshop on X-Ray CT for Geomaterials, GeoX 2010 (New Orleans, Louisiana, March 1-3) (K.A. Alshibli and A. Reed, eds.), ISTE, 2010.

[28] S.A. Hall, N. Lenoir, G. Viggiani, J. Desrues, and P. Bésuelle, *Strain localisation in sand under triaxial loading : characterisation by X-ray micro tomography and 3D digital image correlation*, Proc. Int. Symp. on computational geomechanics ComGeo I (Juan-les-Pins, France, April 29 - May 1), 2009.

[29] M. Hosseini, C. Rousseau, J. Desrues, P. Bésuelle, and G. Viggiani, *Development of an experimental device to carry out tests on thick-walled hollow cylinders*, Proc of the European Regional ISRM Symp., Multiphysics coupling and long term behaviour in rock mechanics, Eurock 2006 (Liège, Belgium, May 9-12) (A. Van Cotthem, J.-P. Tshibangu, and R. Charlier, eds.), 2006.

[30] P. Kotronis, F. Collin, P. Bésuelle, R. Chambon, and J. Mazars, *Local second gradient models and damage mechanics : 1D post-localisation studies in concrete specimens*, Proc. 7th Int. Workshop on Bifurcation, Instabilities and Degradation in Geomechanics (Chania, Greece, june 13-16, 2005) (G. Exadaktylos and I. Vardoulakis, eds.), 2006.

[31] N. Lenoir, S. Marello, G. Viggiani, P. Bésuelle, J. Desrues, and M. Di Michiel, *X-ray micro tomography characterization of strain localization upon deviatoric loading of saturated fine-grained soils*, Proc. of the International Workshop on X-ray CT for Geomaterials, Soils, Concrete, Rocks, GeoX 2003 (Kumamoto, Japan, November 6-7) (J. Otani and Y. Obara, eds.), Balkema, Rotterdam, 2004, pp. 147–155.

[32] S. Levasseur, P. Bésuelle, F. Collin, R. Chambon, R. Charlier, and G. Viggiani, *EDZ in clayey rocks : which effect on permeability ?*, Proc. Int. Conf. on impact of thermo-hydro-mechanical-chemical (THMC) processes on the safety of underground radioactive waste repositories (Luxembourg, September 29-October 1), 2009.

[33] S. Marello, N. Lenoir, G. Viggiani, P. Bésuelle, J. Desrues, and M. Di Michiel, *Shear banding in plane strain compression of beaucaire marl studied through post-mortem X-ray micro tomography*, Proc. of the International Workshop on X-ray CT for Geomaterials, Soils, Concrete, Rocks, GeoX 2003 (Kumamoto, Japan, November 6-7) (J. Otani and Y. Obara, eds.), Balkema, Rotterdam, 2004, pp. 139–146.

[34] D. Takano, P. Bésuelle, J. Desrues, and S.A. Hall, *Deformation in fractured argillaceous rock under seepage flow using X-ray CT and digital image correlation*, Proc. 3rd International Workshop on X-Ray CT for Geomaterials, GeoX 2010 (New Orleans, Louisiana, March 1-3) (K.A. Alshibli and A. Reed, eds.), ISTE, 2010.

[35] G. Viggiani, P. Bésuelle, S.A. Hall, and J. Desrues, *Sand deformation at the grain scale quantified through X-ray imaging (keynote lecture)*, Proc. 3rd International Workshop on X-Ray CT for Geomaterials, GeoX 2010 (New Orleans, Louisiana, March 1-3) (K.A. Alshibli and A. Reed, eds.), ISTE, 2010.

## Communications à des congrès internationaux à comité de sélection, sans acte

[36] E. Andò, S.A. Hall, G. Viggiani, J. Desrues, and P. Bésuelle, *Experimental characterisation of grain-scale kinematics in sand under triaxial compression*, Proc. 9th International Workshop on Bifurcation and Degradation in Geomaterials, IWBDG 2011 (Porquerolles, France, may 23-26) (S. Bonelli, C. Dascalu, and F. Nicot, eds.), 2011.

[37] P. Bésuelle, *Dilating and compacting shear bands inside a sandstone*, European Geophysical Society, EGS 2000 (Nice, France), 2000.

[38] P. Bésuelle, R. Chambon, D. Caillerie, F. Collin, and R. Charlier, *Implementation of a new finite element for local second gradient models, application to the post localization*, ALERT European Workshop, session Post Failure behaviour (Aussois, France, October 6-8), 2003.

[39] P. Bésuelle and J. Desrues, *Evolution of strain localization in a porous rock in the brittle to ductile transition*, Int. Workshop on Bifurcations and Instabilities in Geomechanics (Minneapolis, USA, June 2-5) (J. Labuz and A. Drescher, eds.), 2002.

[40] P. Bésuelle, J. Desrues, and S. Raynaud, *Localization phenomena inside a Vosges sandstone*, 2nd Euroconference on Rock Physics and Rocks Mechanics (Edinburgh, U.K.), 1999.

[41] P. Bésuelle and G. Viggiani, *A laboratory experimental study of strain localization in Boom clay*, ALERT European Workshop, session Mechanics of clay rocks (Aussois, France, October 4-6), 2010.

[42] P. Bésuelle, S.A. Hall, N. Lenoir, J. Desrues, G. Viggiani, M. Bornert, and Y. Pannier, *Grain scale mechanisms of deformation during strain localization in a granular material (conférence invitee)*, 3rd US-France Symposium ICACM on Damage and failure on heterogeneous materials (Shalimar, Florida, USA, April 22-24), 2009.

[43] P. Bésuelle, S.A. Hall, N. Lenoir, G. Viggiani, J. Desrues, M. Bornert, and Y. Pannier, *Investigation of localized deformation in granular materials by means of X-ray CT and grain scale digital volume correlation*, 7th EUROMECH Solid Mechanics Conference (ESMC2009) (Lisbon, Portugal, September 7-11), 2009.

[44] E.M. Charalampidou, S.A. Hall, P. Bésuelle, L. Restaino, P. Roux, and G. Viggiani, *Ultrasonic tomography to study localised deformation in sandstone*, ALERT European Workshop, session Localisation in geomaterials (Aussois, France, October 6-8), 2008.

[45] C. Coll, J. Desrues, P. Bésuelle, and G. Viggiani, *Characterizing in the laboratory permeability changes induced by deviatoric stress in clayey rocks*, ALERT European Workshop, session Multi-physics coupling (Aussois, France, October 6-8), 2003.

[46] C. Coll, J. Desrues, P. Bésuelle, and G. Viggiani, *Does strain localization affect permeability in argillaceous rocks ?*, 7th Int. Workshop on Bifurcation, Instabilities and Degradation in Geomechanics (Chania, Greece, June 13-16), 2005.

[47] C. Coll, J. Desrues, P. Bésuelle, and G. Viggiani, *Permeability evolution of a plastic clay with deviator stress : an experimental study*, Int. Symp. on Clays in Natural and Engineered barriers for Radioactive Waste Confinement (Tours, France, March 14-18), 2005.

[48] J. Desrues and P. Bésuelle, *Experiments on strain localisation in Vosges sandstone*, ALERT European Workshop (Aussois, France, October), 1998.

[49] J. Desrues, P. Bésuelle, and C. Rousseau, *Long-term behaviour of argiliceous rocks : evaluation of stimulated creep*, Int. Symp. on Clays in Natural and Engineered barriers for Radioactive Waste Confinement (Tours, France, March 14-18), 2005.

[50] J. Desrues, N. Lenoir, G. Viggiani, P. Bésuelle, and M. Bornert, *3D volumetric dic of X-ray microtomographic images to study localized deformation in a stiff clayey rock*, ICTAM XXII (Adelaide, Australia, August 25-29), 2008.

[51] S.A. Hall, E. Andò, P. Bésuelle, G. Viggiani, and J. Desrues, *4D analysis of grain-contact evolution in sand undergoing localized deformation*, 2nd Int. Conf. on 3D imaging of materials and systems (3D-IMS2010) (Carcans- Maubuisson, France, September 6-10) (D. Bernard, ed.), 2010.

[52] S.A. Hall, P. Bésuelle, L. Restaino, E.M. Charalampidou, and G. Viggiani, *Ultrasonic tomography to study localised deformation in rocks*, 1st Int. Conf. on 3D imaging of materials and systems (3D-IMS2008) (Carcans-Maubuisson, France, September 8-12) (D. Bernard, ed.), 2008.

[53] S.A. Hall, N. Lenoir, Y. Pannier, J. Desrues, M. Bornert, G. Viggiani, P. Bésuelle, M. Di Michiel, and J. Otani, *Characterisation of localised deformation in granular geomaterials using X-ray (micro)tomography and 3D-volumetric digital image correlation*, Photomechanics 2008 (Lougborough, UK, July), 2008.

[54] S.A. Hall, N. Lenoir, G. Viggiani, P. Bésuelle, and J. Desrues, *X-ray CT and 3D digital image correlation to study localised deformation in geomaterials under triaxial compression*, European Geophysical Union General Assembly (Vienna, Austria, April 13-18), 2008.

[55] S.A. Hall, N. Lenoir, G. Viggiani, P. Bésuelle, J. Desrues, M. Bornert, and Y. Pannier, *Investigation of localized deformation in granular materials under triaxial compression by means of X-ray microCT and 3D digital image correlation*, 1st Int. Conf. on 3D imaging of materials and systems (3D-IMS2008) (Carcans-Maubuisson, France, September 8-12) (D. Bernard, ed.), 2008.

[56] S.A. Hall, N. Lenoir, G. Viggiani, P. Bésuelle, J. Desrues, M. Bornert, and Y. Pannier, *X-ray micro-CT and 3D DIC to study localised deformation in geomaterials under triaxial compression*, ALERT European Workshop, session Localisation in geomaterials (Aussois, France, October 6-8), 2008.

[57] S.A. Hall, G. Viggiani, and P. Bésuelle, *Analysis of fracture in a soft rock (neapolitan tuff) using digital image correlation with displacement discontinuity quantification*, Euroconference of rock physics and geomechanics on natural hazards : themo-hydro-mechanical processes in rocks (Erice, Italy, September 25-30) (S. Vinciguerra and Y. Bernabé, eds.), 2007.

[58] P. Kotronis, R. Chambon, S. Al Holo, and P. Bésuelle, *Shear softening and localization, modelling of the evolution of the width of the shear zone*, ALERT European 18th Workshop, session 'Multi-scale Approaches to Geomaterials' (Aussois, France, October 9-11, 2006), 2006.

[59] N. Lenoir, M. Bornert, J. Desrues, P. Bésuelle, and G. Viggiani, *3D image correlation applied to X-ray micro tomographic images of in-situ triaxial tests on argiliceous rock performed at ESRF*, Photomechanics 2006 (Clermont-Ferrand, France, July 10-12) (M. Grédiac, ed.), 2006.

[60] N. Lenoir, J. Desrues, G. Viggiani, P. Bésuelle, M. Bornert, and J.D. Barnichon, *Fracturation in callovo-oxfordian argillite under triaxial compression studied by X-ray microtomography*, 3rd international meeting on Clays in natural & engineered barriers for radioactive waste confinement (Lille, France, September 17-20) (J.F. ANDRA Aranyossy, ed.), 2007.

[61] N. Lenoir, Y. Pannier, S.A. Hall, M. Bornert, P. Bésuelle, J. Desrues, and G. Viggiani, *Combining X-ray CT and 3D digital image correlation for studying strain localization in granular materials*, 8th Int. Workshop on Bifurcations and Degradations in Geomaterials (Lake Louise, Alberta, Canada, May 2008), 2008.

[62] N. Lenoir, G. Viggiani, P. Bésuelle, and J. Desrues, *X-ray micro tomography for studying localized deformation in clay rocks under triaxial compression*, 7th Int. Workshop on Bifurcation, Instabilities and Degradation in Geomechanics (Chania, Greece, June 13-16), 2005.

[63] N. Lenoir, G. Viggiani, P. Bésuelle, and J. Desrues, *X-ray micro tomography for studying localized deformation in clay rocks under triaxial compression*, ALERT European Workshop, session Advances in experimental methods (Aussois, France, October 10-12), 2005.

[64] N. Lenoir, G. Viggiani, P. Bésuelle, J. Desrues, and M. Di Michiel, *X-ray micro tomography for studying fracturation in Callovo-Oxfordian argillites under triaxial compression*, Int. Symp. on Clays in Natural and Engineered barriers for Radioactive Waste Confinement (Tours, France, March 14-18), 2005.

[65] S. Levasseur, P. Bésuelle, F. Collin, Y. Sieffert, R. Chambon, R. Charlier, and G. Viggiani, *EDZ and permeability in clayey rocks*, 4th Int. meeting on Clays in Natural & Engineered Barriers for Radioactive Waste Confinement (Nantes, France, March 29 - April 1) (ANDRA, ed.), 2010.

[66] A.R. Moldovan, P. Bésuelle, and S.A. Hall, *Experimental study of localized deformation in a calcarenite using X-ray tomography*, 2nd Int. Conf. on 3D imaging of materials and systems (3D-IMS2010) (Carcans-Maubuisson, France, September 6-10) (D. Bernard, ed.), 2010.

[67] D. Takano, P. Bésuelle, A. Simionovici, L. Charlet, J. Desrues, and S.A. Hall, *Investigation of deformation and deposition of Se nanoparticles in fractured argillaceous rock under seepage flow using X-ray computed tomography*, 4th Int. meeting on Clays in Natural & Engineered Barriers for Radioactive Waste Confinement (Nantes, France, March 29 - April 1) (ANDRA, ed.), 2010.

[68] G. Viggiani, S.A. Hall, N. Lenoir, P. Bésuelle, and J. Desrues, *Combining X-ray CT and 3D digital image correlation for studying localized deformation in stiff clay under triaxial compression*, 8th Int. Workshop on Bifurcations and Degradations in Geomaterials (Lake Louise, Alberta, Canada, May 2008), 2008.

[69] G. Viggiani, N. Lenoir, P. Bésuelle, and J. Desrues, *X-ray tomography characterization of strain localization upon deviatoric loading of saturated fine-grained stiff soils*, ALERT European Workshop, session Post Failure behaviour (Aussois, France, October 6-8), 2003.

[70] A. Wrzesniak, C. Dascalu, and P. Bésuelle, *Development of a multi-scale damage model for frictional micro-cracks*, 1st Int. Conf. Multiscale Modelling (Paris, France, September 1-2) (B. Gatmiri, ed.), 2010.

## Quelques autres

[71] P. Bésuelle, *Déformation et rupture dans les roches tendres et les sols indurés : comportement homogène et localisation*, 1999, Thèse de Doctorat, Université J. Fourier (Grenoble I), 370 pages.

[72] P. Bésuelle, *Localisation des déformations dans les roches granulaires, caractérisations expérimentales et prédictions théoriques*, Mécamat 2001, Multi approches en mécanique des matériaux : changement d'échelle, localisation, endommagement et microstructure (Aussois, France, 28 janvier-1er février), 2001, pp. 51–54.

[73] P. Bésuelle, *Implémentation d'un nouveau type d'élément fini dans le code Lagamine pour une classe de lois à longueur interne*, Rapport Interne, FNRS, Belgique (2003), 17 pages.

[74] P. Bésuelle and R. Chambon, *Etude de la localisation de la déformation à l'aide de modèles second gradient*, Journée CSMA-Mécamat (Clamart EDF R&D, 16 juin) (S. Andrieux, E. Lorentz, D. Halm, and S. Michel-Ponnelle, eds.), 2006.

[75] P. Bésuelle, F. Collin, S.A. Hall, P. Kotronis, and G. Viggiani, *Comportement hydro-mécanique des roches en régime post-rupture*, rapport de fin de projet, ACI jeunes chercheurs 2003-2006 (2006), 44 pages.

[76] P. Bésuelle, S.A. Hall, N. Lenoir, G. Viggiani, J. Desrues, Y. Pannier, and M. Bornert, *Localisation de la déformation dans un milieu granulaire vue jusqu'à l'échelle du grain à l'aide de la tomographie à rayons X*, Mécamat 2010, Nouvelles approches en mécanique expérimentale (Aussois, France, 11-15 janvier) (E. Maire, J.Y. Buffière, and O. Bouaziz, eds.), 2010, 6 pages.

[77] R. Chambon, P. Bésuelle, and J.C. Moullet, *Modélisation numérique des milieux continus de second gradient locaux, application à la localisation dans un matériau de Von Mises quasi fragile*, Mécamat 2004, Mécanismes et Mécanique des Matériaux et Structures à Longueur interne : Comportement et Effets d'Echelles (Aussois, France, 30 janvier), 2004, 8 pages.

Autres actes non listés.

# 4 Travaux expérimentaux

## 4.1 Etude du comportement homogène et de la localisation

### 4.1.1 Localisation dans le grès des Vosges

La rupture dans les géomatériaux est associée dans la plupart des cas au phénomène de localisation, tout du moins dans les conditions de faibles contraintes et faible température. Si l'on considère le comportement d'une roche à l'échelle macroscopique, les zones de ruptures peuvent être considérées comme des bandes de localisation de la déformation. Cette description est classique pour les sols (sables, argiles). Les études de laboratoire sur ces derniers montrent généralement un pic de contrainte dans la réponse des échantillons, tandis que la déformation se concentre dans les bandes de cisaillement. En dehors des bandes, la déformation est très faible (Desrues, 1998 ; Desrues *et al.*, 2007 [14]). Selon ces observations expérimentales, la rupture dans les sols peut être considérée comme généralement associée au développement de bandes de cisaillement, ce qui alors explique le radoucissement dans la réponse de l'échantillon (Wawersik et Fairhurst, 1970). Pour prédire l'apparition de la localisation, une approche en bifurcation a été développée par Rice (1973). Cette approche a été par la suite intensémment étendue pour les sols (*e.g.*, Vardoulakis *et al.*, 1976 ; Kolymbas, 1981 ; Desrues, 1989), et pour les roches tendres (*e.g.*, Vardoulakis, 1984 ; Chambon *et al.*, 1994 ; Sulem *et al.*, 1999). D'un point de vue expérimental, une description macroscopique de la localisation dans les roches poreuses, telles les grès, testées en laboratoire se justifie. Cependant, la description à l'échelle microscopique est également nécessaire. Les bandes de localisation dans les roches poreuses sont caractérisées à l'échelle micro par une forte augmentation de la densité locale de micro-fissuration, comparée au matériau en dehors des bandes (*e.g.*, Dunn *et al.*, 1973 ; Menéndez *et al.*, 1996). Le matériau à l'intérieur s'endommage rapidement, ce qui dégrade rapidement ses caractéristiques mécaniques (radoucissement local dans la bande). En conséquence, le comportement dans la bande influence fortement la réponse de l'échantillon, il est donc important de s'y intéresser. Par ailleurs, il est bien connu qu'une déformation volumique dilatante peut prendre place dans une bande de cisaillement, mais l'existence d'une contractance est toujours en question, voire même de bandes de compaction (pas de glissement relatif des bords de la bande mais simplement un rapprochement). Notons toutefois qu'une telle contractance dans des bandes de cisaillement a déjà été observée dans des sols (Colliat-Dangus, 1986 ; Tillard-Ngan *et al.*, 1993 ; Hicher et Wahyudi, 1994) et dans des structures géologiques naturelles (Antonellini, 1994).

Dans cet esprit, nous avons mené une étude assez exhaustive du comportement du grès des Vosges. L'étude expérimentale a porté en particulier sur le com-

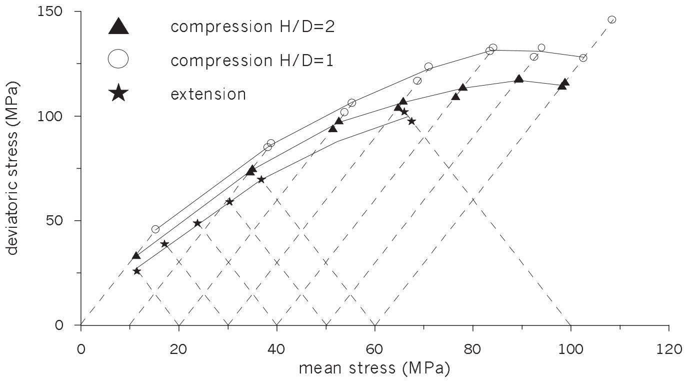

FIGURE 1 – Enveloppe de rupture observée dans le grès des Vosges, pour des compressions axisymétriques en élancement deux et un, et pour des extensions axisymétriques.

portement homogène de la roche et sur la caractérisation de la localisation de la déformation. Les essais ont été conduits dans une cellule triaxiale axisymmétrique jusqu'à des confinements de 60 MPa. En terme de comportement de la roche, j'ai pu mettre en évidence l'influence primordiale du niveau de contrainte moyenne, tant sur la résistance maximum du matériau que son comportement en volume (dilatance à faible confinement et compaction à fort confinement). Une enveloppe de rupture fortement non linéaire dans le plan premier *vs* deuxième invariant a été mise en évidence, montrant l'esquisse d'une surface fermée aux plus forts niveaux de confinement accessibles (Fig. 1). La dépendance des structures de localisation par rapport à la contrainte moyenne a également été mise en évidence, en terme de seuil d'apparation, d'orientation, de nombre de bandes, de microstructure, etc... (Fig. 2).

On a montré, à l'aide de la tomographie à rayons X (LMA Marseille) et de la microscopie quantitative, que la déformation dans les bandes de cisaillement était accompagnée d'une variation de porosité, qui pouvait aller dans le sens d'une augmentation de la porosité aux faibles confinements, ou d'une diminution de la porosité aux forts confinements (Fig. 3). Cette évolution est elle-même accompagnée d'une évolution de l'orientation des bandes, allant des bandes parallèles à la contrainte principale majeure aux faibles confinements, aux bandes fortement inclinées aux forts confinements (angle supérieur à $45^o$ pour 60 MPa de confinement).

Le travail précédent a été étendu, en particulier pour étudier les structures de localisation à des confinements plus élévés, dans le cadre d'une collaboration avec T.-f. Wong et P. Baud. Le grès de Rothbach (un autre grès des Vosges), assez

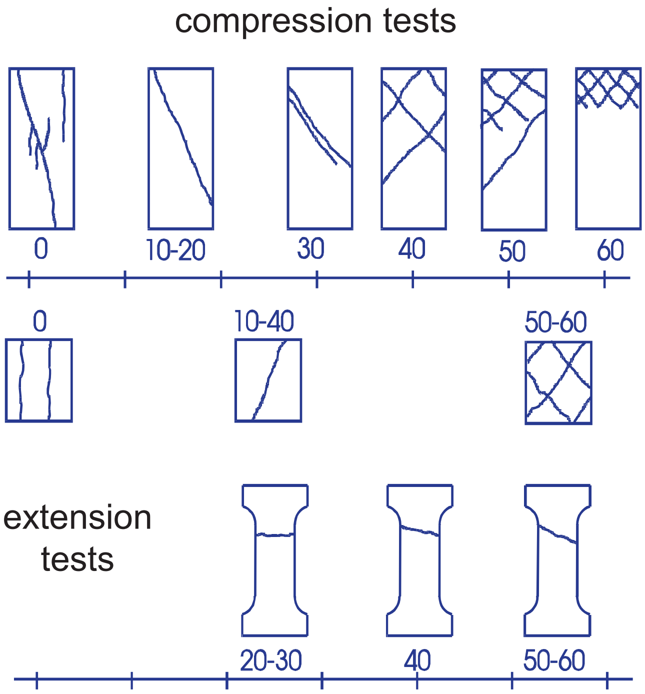

FIGURE 2 – Schématisation des structures de localisation observées visuellement dans le grès des Vosges, en fonction de la pression (MPa) de confinement des échantillons en condition axisymmétrique. En haut, compression sur des échantillons d'élancement 2 ; au milieu, compression sur des échantillons d'élancement 1 ; en bas, extension sur des échantillons en forme de bobine.

proche du grès pécédent, a été étudié jusqu'à des confinements de 130 MPa. De la tomographie à rayons X (IFP Rueil-Malmaison) a été mise en œuvre pour caractériser en 3D les structures de localisation, permettant d'observer des organisations complexes décrites auparavant dans du sable (Desrues *et al.*, 1996), et qui consiste en un cône central de localisation et des bandes conjuguées en forme de V orientés radialement. De la microscopie quantitative a permit de décrire l'endommagement du matériau dans les bandes de localisation (Fig. 4). Des bandes de compaction ont été observées, à savoir des bandes quasi perpendiculaires à la direction de contrainte majeure.

Collaborations : Jacques Desrues (3S), Suzanne Raynaud (Géosciences Montpellier), Patrick Baud (EOST Strasbourg), Teng-fong Wong (SUNY Stony Brook, USA)
Publications : [6, 3, 71, 20, 48, 40, 39, 18]
Références in-extenso (en fin de chapître) :

- P. Bésuelle, J. Desrues, and S. Raynaud, *Experimental characterisation of the localisation phenomenon inside a Vosges sandstone in a triaxial cell*, Int. J. Rock Mech. Min. Sci. **37** (2000), no. 8, 1223–1237.

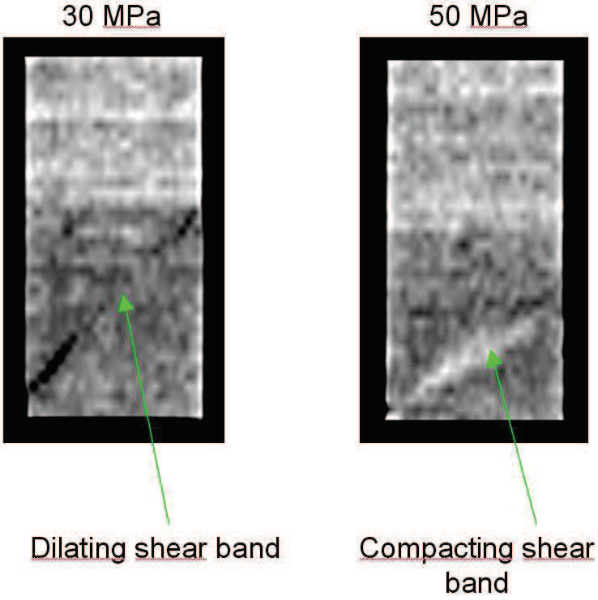

FIGURE 3 – Coupes tomographiques (rayons X) : à gauche, échantillon comprimé sous un confinement de 30 MPa, montrant une augmentation de la pososité dans la bande de localisation (bande de cisaillement dilatante) ; à droite, échantillon comprimé sous un confinement de 50 MPa, montrant une diminution de la pososité dans la bande de localisation (bande de cisaillement compactante).

- P. Bésuelle, *Evolution of strain localisation with stress in a sandstone : brittle and semi-brittle regimes*, Phys. Chem. Earth, Part A **26** (2001), no. 1-2, 101–106.
- P. Bésuelle, P. Baud, and T.-f. Wong, *Spatial distribution of damage in Rothbach sandstone in the brittle ductile transition*, Pure Appl. Geophys. **160** (2003), no. 5-6, 851–868.

Références externes :

Antonellini M.A., Aydin A., Pollard D.D., 1994, Microstructure of deformation bands in porous sanstones at Arches National Park, Utah, *J. Struct. Geol.*, vol. 16, pp. 941-959.

Chambon R., Desrues J., Tillard D., 1994, Shear modulus identifcation versus experimental localisation data. In : Chambon R, Desrues J, Vardoulakis I, editors. Localisation and bifurcation theory for soils and rocks. Rotterdam : Balkema, pp. 101-111.

Colliat-Dangus J.L., 1986, Comportement des matériaux granulaires sous fortes contraintes. Influence de la nature minéralogique du matériau étudié, PhD thesis, INPG et USMG, Grenoble, France.

Desrues J., Chambon R., 1989, Shear band analysis for granular materials : the

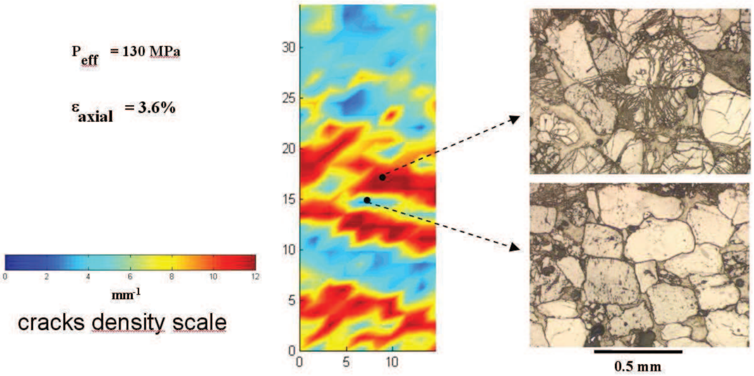

FIGURE 4 – Carte de densité de la microfissuration dans un échantillon de grès de Rothbach après essai de compression sous 130 MPa de confinement, et photographies prises au microscope optique d'une zone fortement endommagée et d'une zone peu endomagée.

question of incremental non-linearity. *Ing.-Arch.*, vol. 59, pp. 187-196.

Desrues J., Chambon R., Mokni M., Mazerolle F., 1996, Void ratio evolution inside shear bands in triaxial sand specimens studied by computed tomography, *Géotechnique*, vol. 46, No. 3, pp. 529-546.

Desrues J., 1998, Localisation patterns in ductile and brittle geomaterials. In : de Borst R, van der Giessen E, editors. Material instabilities in solids. New York : Wiley, pp. 137-158.

Dunn D.E., LaFountain L.J., Jackson R.E., 1973, Porosity dependence and mechanism of brittle fracture in sandstones. *J. Geophys. Res.*, vol. 78, pp. 2403-2417.

Menéndez B., Zhu W., Wong T.-f., 1996, Micromechanics of brittle faulting and cataclastic flow in Berea sandstone. *J. Struct. Geol.*, vol. 18, pp. 1-16.

Hicher P.Y., Wahyudi H., 1994, Microstructural analysis of strain localisation in clay. *Comput. Geotech.*, vol. 16, pp. 205-222.

Kolymbas D., 1981, Bifurcation analysis for sand sample with non-linear constitutive equation. *Ing.-Arch.*, vol. 50, pp. 131-140.

Rice JR., 1973, The initiation and growth of shear bands. In : Palmer AC, editor. International Congress of Theoretical and Applied Mechanics, Cambridge, pp. 263-274.

Sulem J., Vardoulakis I., Papamichos E., Oulahna A., Tronvoll J., 1999, Elastoplastic modelling of red Wildmoor sandstone. *Mech. Cohesive-Frictional Mater.*, vol. 4, pp. 215-245.

Tillard-Ngan D., Desrues J., Raynaud S., Mazerolle F., 1993, Strain localisation in Beaucaire marl. Proc. Geotechnical Engineering of Hard Soils and Soft Rocks, Rotterdam : Balkema, pp. 1679-1686.

Vardoulakis I., Goldscheider M., Gudehus G., 1978, Formation of shear bands in sand bodies as a bifurcation problem. *Int. J. Numer. Anal. Methods Geomech.*, vol. 2, pp. 99-128.

Vardoulakis I., 1984, Rock bursting as a surface instability phenomenon. *Int J Rock Mech Min Sci Geomech Abstr*, vol. 21, pp. 137-144.

Wawersik W.R., Fairhurst C., 1970, A study of brittle rock fracture in laboratory compression experiments. *Int J Rock Mech Min Sci*, vol. 7, pp. 561-575.

### 4.1.2 Localisation par compaction

Un cas extrême de localisation dans les roches poreuses sollicitées sous un niveau de confinement relativement élevé est une localisation par bande de compaction (bande orthogonale à la direction de contrainte majeure et abscence de glissement relatif des bords de la bande). Ce sujet fait florès dans la littérature depuis une dizaine d'années (*e.g.*, Mollema et Antonellini, 1996 ; Olsson, 1999 ; Baud *et al.*, 2004). Pour autant, les bandes présentant une compaction ont tendance à se saturer (le matériau ne peut se compacter indéfiniment), ce qui peut entrainer une modification des structures de localisation au cours du chargement. Les études que l'on trouve dans la littérature sont des observations *post-mortem*, qui ne permettent pas bien de comprendre le processus évolutif, mais qui laisse penser que les modifications peuvent se faire soit par création de nouvelles bandes, soit par élargissement de la structure initiale. Nous nous sommes intéressé ici aux processus évolutifs qui font que les structures de localisation avec compaction se modifient au cours du chargement en mettant en œuvre de la tomographie à rayons X *in situ* (au cours des essais).

Nous avons choisi de travailler sur un tuffeau prélevé aux environs de Maastricht (Baxevanis *et al.*, 2006), roche calcaire extrêmement poreuse, avec un seuil de plastification (par effondrement des pores) sous chargement isotrope de l'ordre de 7 MPa. Nous avons mené une campagne d'essais, dans notre tomographe à rayons X et notre cellule triaxiale axisymmétrique transparente aux RX, à différents niveaux de confinement (jusqu'à 7 MPa), mettant en évidence différentes formes de localisation. Pour les essais à 'fort' confinement, nous avons observé une localisation par bandes de compaction, et nous avons pu mettre en évidence que les bandes s'élargissaient progressivement au cours de l'essai, avec une vitesse de propagation liée directement à la vitesse de chargement de l'échantillon, jusqu'à envahir tout l'échantillon. A partir du moment où les bandes s'initient et jusqu'à ce qu'elles recouvrent l'intégralité de l'échantillon, on observe un palier de résistance de l'échantillon (Fig. 5). Une fois que les bandes se sont propagées dans tout l'échantillon, celui-ci redevient à nouveau homogène, il est constitué alors, non plus du matériau initial, mais d'un nouveau matériau plus com-

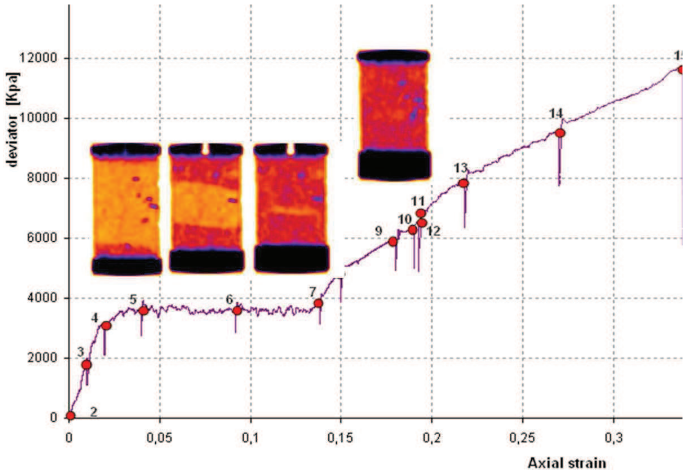

FIGURE 5 – Réponse d'un échantillon de tuffeau de Maastricht, en compression axisymmétrique, sous un confinement de 4 MPa. Les figures montrent l'évolution du champ de porosité le long d'une coupe verticale. La phase de propagation des bandes de compaction (l'une depuis le bas, l'autre depuis le haut de l'échantillon) correspond au palier de contrainte.

pact. La résistance se met alors à augmenter si l'on continue à solliciter l'échantillon. Une nouvelle localisation peut ensuite se former, moins ductile que la précédente, sous forme de bandes de cisaillement inclinées. Une étude des micromécanismes de déformation à l'échelle des grains est actuellement en cours.

Collaborations : Alexandra Raluca Moldovan (stagiaire Master), Daiki Takano (postdoc), Pascal Charrier (AI au 3SR), Steve Hall (3SR), Cino Viggiani (3SR), Patrick Baud (EOST Strasbourg), Teng-fong Wong (SUNY Stony Brook, USA)
Publications : un article de revue en préparation et [66]

Références externes :

Baud P., Klein E., Wong T.-f., 2004, Compaction localization in porous sandstones : spatial evolution of damage and acoustic emission activity, *J. Struct. Geol.*, vol. 26, pp. 603-624.

Baxevanis T., Papamichos E., Flornes O., Larsen I., 2006, Compaction bands and induced permeability reduction in Tuffeau de Maastricht calcarenite, *Acta Geotechnica*, vol. 1, pp. 123-135.

Mollema P.N., Antonellini M.A., 1996, Compaction bands : A structural analog for anti-mode I cracks in aeolian sandstone, *Tectonophysics*, vol. 267, pp. 209-228.

Olsson W.A., 1999, Theoretical and Experimental Investigation of Compaction Bands in Porous Rock, *J. Geophys. Res.*, vol. 104, pp. 7219-7228.

### 4.1.3 Localisation dans une argilite

Notre ambition pour cette étude était d'étendre des méthodes précédemment utilisées dans l'équipe pour caractériser la localisation dans les sables, à savoir la tomographie (médicale) à rayons X, à des roches tendres de structures fines. Les matériaux étudiés sont d'une part une marne (déjà étudiée quelques années auparavant) puis une roche argileuse, dans le cadre d'un partenariat avec l'ANDRA autour de la problématique de l'endommagement des roches par fissuration autour des galeries de stockage. Du fait de la microstructure très fine de ces roches, il nous fallait obtenir des images avec une résolution bien meilleure que pour le sable et avec des temps d'acquisition courts, ce qui nous a conduit à utiliser la ligne de micro-tomographie ID15A de l'ESRF.

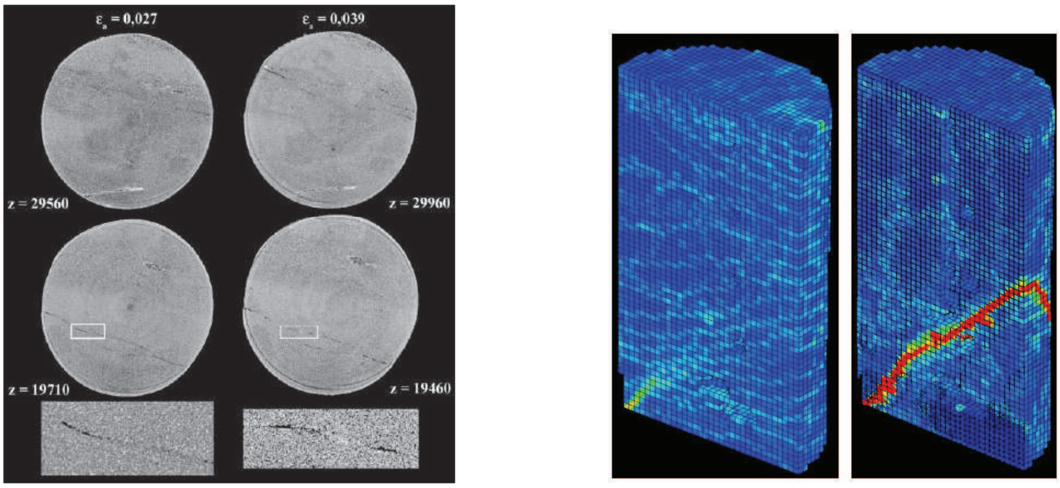

FIGURE 6 – Exemple d'images de microtomographie RX réalisées *in situ* à l'ESRF sur une marne argileuse (gauche). Champs 3D de déformation de cisaillement maximum lors de deux incréments de chargement (avant et après pic de contrainte) sur une argilite (droite).

Des essais de type compression axisymmétrique ont été conduits, avec une installation expérimentale développée spécifiquement pour réaliser des essais directement dans le faisceau RX. La figure 6a donne un exemple d'image obtenue, où une fissure est visible de par le vide créé entre les lèvres de la fissure. Comme la localisation de la déformation se produit avec peu de variation de porosité, elle se détecte assez mal en tomographie (sensible à la variation de densité massique), ou alors très tardivement, par exemple quand une fissure est activée et que des vides se crééent du fait d'effets de forme de la fissure. De ce fait, nous avons cherché à étendre les analyses en corrélation d'image 2D aux milieux 3D afin d'obtenir le champ du tenseur de déformation (complet). Ce travail s'est fait via une collaboration avec M. Bornert. On a pu obtenir des champs 3D du tenseur complet de déformation montrant la naissance de la localisation dans un échantillon (Fig.

6b). Il apparait très clairement que la localisation de la déformation est déjà initiée au moment du pic de contrainte, et que la bande se propage pleinement après le pic de contrainte. Ces premiers travaux nous ont conduit par la suite à développer l'imagerie 3D pour les géomatériaux, concrétisé par l'achat d'un tomographe en 1998 par mon équipe de recherche, afin de nous offrir une meilleure accessibilité qu'à l'ESRF. Par ailleurs, nous avons depuis développé notre propre code de corrélation d'image 3D (en volume).

Collaborations : Cino Viggiani (3SR), Jacques Desrues (3SR), Nicolas Lenoir (3SR), Michel Bornert (LMS-X)
Publications : [12, 10, 23, 31, 33, 69, 64, 62, 63, 59, 60, 68, 50]
Référence in-extenso (en fin de chapître) :

- P. Bésuelle, G. Viggiani, N. Lenoir, J. Desrues, and M. Bornert, *X-ray micro CT for studying strain localization in clay rocks under triaxial compression (keynote lecture)*, Advances in X-Ray Tomography for Geomaterials, Proc. 2nd International Workshop on X-Ray CT for Geomaterials, GeoX 2006 (Grenoble & Aussois, France, October 4-7), 2006.

## 4.2 Etude des micro-mécanismes de déformation dans un sable

On a montré précédemment tout l'intérêt qu'il y avait à mesurer le champ de déformation cinématique pour étudier la localisation de la déformation, seul moyen d'interpréter correctement un essai. Les premières analyses de champ pour étudier la localisation dans les sables ont commencé à la fin des années 60 à Cambridge (*e.g.*, Roscoe *et al.*, 1963 ; Roscoe, 1970) et ont été poursuivies dans les dernières décennies par plusieurs groupes (voir une synthèse par Desrues et Viggiani, 2004). La plupart de ces travaux ont été conduits sur des appareils de déformation plane, avec diverses méthodes d'analyse de champs, dont les méthodes basées sur l'imagerie en visuel (stéréophotogrammétrie, corrélation d'image). Dans les années 60, la radiographie par rayons X a été utilisée pour mesurer le champ de déformation bi-dimmensionnel dans un sable (*e.g.*, Roscoe, 1970). Dans les années 80, la tomographie par rayons X a été mise en œuvre par Desrues (Desrues, 1984 ; Desrues *et al.*, 1996), puis ultérieurement par Alshibli *et al.* (2000). Ces études ont permis d'obtenir des informations tri-dimensionnelles sur les structures de localisation dans les sables, et en particulier des informations quantitatives sur l'évolution de l'indice des vides à l'intérieur des bandes, en lien avec l'état critique appliqué au matériau dans les bandes (Desrues *et al.*, 1996). Avec la tomographie synchrotron, et maintenant les progrès de la tomographie industrielle, la résolution spatiale des images s'est nettement accrue, offrant de nouvelles possibilités pour comprendre la mécanique des milieux granulaires, en 3D, à l'échelle des grains. Oda *et al.* (2004) ont présenté des images tomographiques, prises en *post mortem*, sur l'organisation des grains à l'intérieur d'une bande de localisation. La compréhension des mécanismes de déformation requiert toutefois que les processus de déformation puissent être suivis dans le temps, tout au long de l'essai mécanique. On a vu que cela était possible en utilisant la tomographie *in situ* (scans éffectués durant le chargement, ce qui nécesite d'avoir une cellule d'essai transparente aux rayons X). De telles études ont été effectuées, avec des tomographes médicaux ou industriels (*e.g.*, Desrues *et al.*, 1996 ; Alshibli *et al.*, 2000 ; Otani *et al.*, 2002). Plus récemment, Matsushima *et al.* (2006, 2007) ont utilisé la tomographie synchrotron, ce qui leur a permis, grâce à la résolution des images, d'identifier et de suivre la trajectoire de grains pendant le chargement (cette analyse de trajectoire n'a été faite qu'en 2D). Dans l'étude présentée ci-avant (Lenoir *et al.*, 2007 [10]), nous avons associé l'imagerie tomographique à la corrélation d'image en volume, pour étudier une roche argileuse. Ici, nous avons appliqué les mêmes outils, mais compte tenu que la résolution des images permet d'identier chaque grain, la correlation a été adaptée aux milieux discrets, afin d'obtenir la cinématique complète de chaque grain (vecteur déplacement et rotation - axe de rotation et angle).

Cette activité rentre dans le cadre du projet ANR non thématique 'Micromodex' (période 2005-2008). Les principales thématiques de ce projet concernent d'une part la modélisation des milieux granulaires vu comme milieu à double échelle par une homogénéisation numérique MEF-MED (modélisation par éléments discrets à l'échelle micro), et d'autre part, la caractérisation expérimentale du comportement d'un milieu granulaire avec description exhaustive du mouvement des grains. J'ai apporté ma contribution à ce second thème, qui a mobilisé également mes collègues expérimentateurs.

Le premier essai expérimental a été réalisé à l'ESRF sous lumière synchrotron (ID15A), il s'agit d'un essai *in situ* sur échantillon de sable (échantillon de 11 mm de diamètre, 22 mm de hauteur, avec des grains de taille moyenne 0,3 mm, soit de l'ordre de 50 000 grains). Nous avons pu obtenir à plusieurs stades de chargement des reconstructions 3D avec une résolution de 14 micromètres. Le stade ultérieur a été de développer des outils de suivi des grains par corrélation d'image, adapté au cadre des milieux granulaires. Ce dernier travail a été réalisé en collaboration avec le groupe du LMS (Ecole polytechnique), qui ont adapté leur code de corrélation en volume pour les milieux discrets, simplement en adaptant les fenêtres de corrélation à chaque grain, après avoir définit pour chaque grain un masque épousant la forme individuelle des grains. Ces outils fonctionnent bien, et permettent notamment d'analyser les mécanismes de déformation à l'échelle des grains (évolution du nombre de contact entre grains, contacts avec glissement relatif ou adhésion). Ces résultats sont sans précédent. En particulier, nous avons

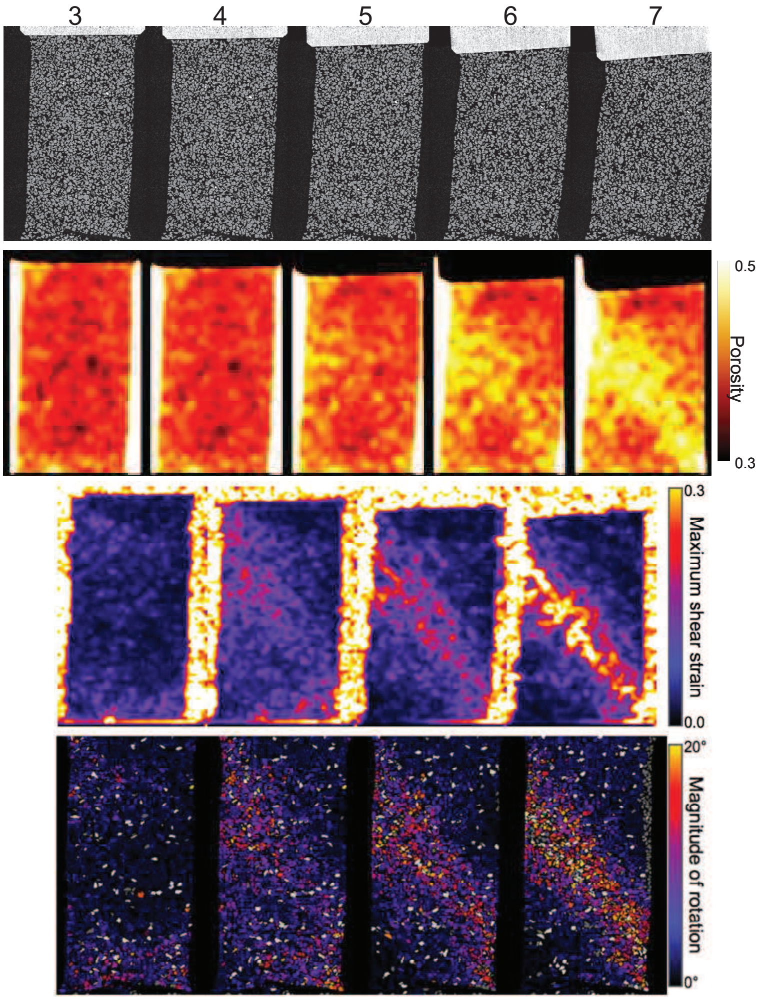

FIGURE 7 – Synthèse de l'analyse menée sur une échantillon de sable, depuis les images tomographique RX de l'échantillon durant l'essai in situ (1ère ligne), le champ de porosité (2ème ligne), jusqu'à la corrélation d'image en volume continue (3ème ligne) et la corrélation discrète (rotation des grains, dernière ligne).

montré le rôle important de la rotation des grains à l'intérieur d'une bande de localisation où la rotation se concentre (voir la figure 7, rangée inférieure). Nous travaillons à présent avec notre propre tomographe à rayons X de laboratoire (achat en 2008), et nous avons commencé une campagne d'essai sur deux types de sable dont les grains sont anguleux dans l'un, et arrondis dans l'autre, afin d'étudier l'effet de la forme de grain sur les mécanismes de déformation.

Collaborations : Jacques Desrues (3SR), Steve Hall (3SR), Nicolas Lenoir (Postdoc), Cino Viggiani (3SR), Michel Bornert (LMS-X), Yannick Pannier (LMS-X), Christophe Rousseau (AI au 3SR), Pascal Charrier (AI au 3SR), Edward Andò (en thèse depuis sept. 2009)

Publications : [7, 11, 28, 35, 27, 17, 61, 53, 55, 42, 43, 51, 36, 72, 76]
Référence in-extenso (en fin de chapître) :

- S.A. Hall, M. Bornert, J. Desrues, Pannier Y., N. Lenoir, G. Viggiani, and P. Bésuelle, *Discrete and continuum analysis of localised deformation in sand using X-ray micro CT and volumetric digital image correlation*, Géotechnique **60** (2010), no. 5, 315–322.

Références externes :

Alshibli K.A., Sture S., Costes N.C., Franck M.L., Lankton M.R., Batiste S.N., Swanson R.A., 2000, Assessment of localized deformation in sand using X-ray computed tomography, *Geotech. Testing J.*, vol. 23, pp. 274-299.

Desrues J., 1984, La localisation de la déformation dans les matériaux granulaires, Thèse d'état, USMG and INPG, Grenoble, France.

Desrues J., Chambon R., Mokni M., Mazerolle F., 1996, Void ratio evolution inside shear bands in triaxial sand specimens studied by computed tomography, *Géotechnique*, vol. 46, No. 3, pp. 529-546.

Desrues J. et Viggiani G., 2004, Strain localization in sand : an overview of the experimental results obtained in Grenoble using stereophotogrammetry. *Int. J. Numer. Analyt. Methods Geomech.*, vol. 28, No. 4, pp. 279-321.

Matsushima T., Uesugi K., Nakano T., Tsuchiyama A., 2006, Visualization of grain motion inside a triaxial specimen by micro X-ray CT at SPring-8. In Advances in X-ray tomography for geomaterials (eds J. Desrues, G. Viggiani and P. Bésuelle), pp. 35-52. London : ISTE.

Matsushima T., Katagiri J., Uesugi K., Nakano T., Tsuchiyama A., 2007, Micro X-ray CT at SPring-8 for granular mechanics, In Soil stress-strain behavior : measurement, modeling and analysis (eds H. I. Ling, L. Castillo, D. Leshchinsky and J. Koseki), pp. 225-234. The Netherlands : Springer.

Oda M., Takemura T., Takahashi M., 2004, Microstructure in shear band observed by microfocus X-ray computed tomography, *Géotechnique*, vol. 54, No. 8, pp. 539-542.

Otani J., Mukunoki T., Obara Y., 2002, Characterization of failure in sand under triaxial compression using an industrial X-ray scanner. *Int. J. Phys. Modelling Geotech.*, vol. 2, No. 1, pp. 15-22.

Roscoe K.H., 1970, The influence of strains in soil mechanics, *Géotechnique*, vol. 20, No. 2, pp. 129-170. 129.

Roscoe K.H., Arthur J.R.F., James R.G., 1963, The determination of strains in soils by an X-ray method. *Civ. Engng Public Works Rev.*, vol. 58, No. 7, pp. 873-876 and No. 8, pp. 1009-1012.

### 4.3 Naissance de la localisation et comportement en régime localisé

Les résultats présentés précédemment sont basées pour ce qui est des roches tendres, sur des observations de la localisation qui sont *post-mortem* (en fin d'essai). Pour des roches très tendres (tuffeau, argilite), nous avons pu caractériser la localisation par des mesures *in situ* par de la tomographie à rayons X associée à la corrélation d'image en volume, et ainsi observer l'initiation de la localisation. L'utilisation de la tomographie RX pour étudier les roches plus raides est encore peu étendue, en partie pour des aspects de rigidité et résistance des matériaux de fabrication pour les cellules d'essai, ils doivent être transparents aux rayons X (Takemura *et al.*, 2004). Par ailleurs, il n'est pas encore envisageable d'obtenir des images suffisamment rapprochées dans le temps lors du chargement de l'échantillon pour caractériser finement la transition entre déformation diffuse et localisée qui est souvent un phénomème relativement rapide.

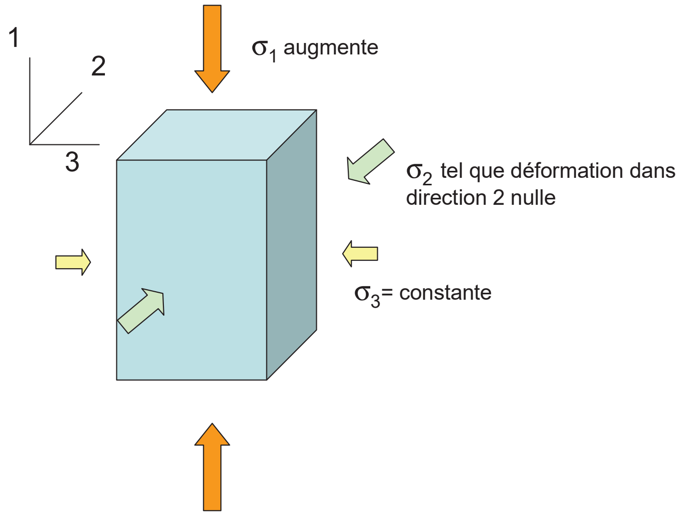

FIGURE 8 – Principe de l'appareil triaxial vrai utilisé dans le cadre d'un contrôle en déformation plane.

Nous avons fait le choix de développer pour les roches tendres un appareil de type triaxial vrai avec dispositif de visualisation sous chargement, de manière à pouvoir caractériser pendant le chargement le champ cinématique dans l'échantillon, et cela de manière très rapprochée dans le temps (petits incréments de chargement). Cet appareil est unique sur le plan internationnal (voir le principe figures 8 et 9 et les illustrations figure 10). Quelques appareils triaxiaux vrais pour roches existent dans la littérature, mais aucun ne permet une visualisation de l'échantillon (Mogi, 1967 ; Atkinson et Ko, 1973 ; Michelis, 1985 ; Wawersik et al., 1997 ; Haimson et Chang, 2000 ; King, 2002 ; Naumann *et al.*, 2007 ; Popp et Salzer, 2007). La nouvelle installation expérimentale que j'ai développé a pour objectif de

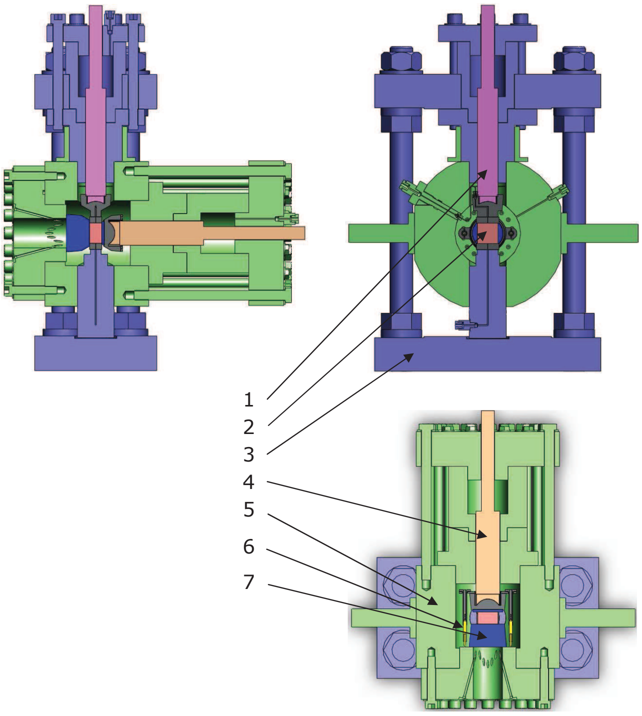

FIGURE 9 – Schémas de principe de l'appareil développé : 1) piston axial, 2) échantillon, 3) bâti axial flottant, 4) piston horizontal, 5) chambre de confinement et bâti fixe, 6) capteurs de déplacement internes, 7) fenêtre en saphir.

pouvoir étudier le phénomène de localisation de la déformation dans les roches en situation de chargement mécanique que l'on peut trouver dans les premiers kilomètres de lithosphère (la pression de confinement supportée par l'appareil est de 100 MPa). Il s'agit de pouvoir réaliser des essais mécaniques bien contrôlés dont en particulier sur des chemins de compression en déformation plane, en associant plusieurs types d'analyse : mesure de champs cinématiques, mesure des propriétés de transfert hydraulique, mesure des émissions acoustiques et des vitesses de propagation d'ondes 'élastiques', toutes ces mesures devant se faire en cours de chargement. Les mesures qui se font *in situ* représentent un réel progrès pour étudier la naissance et le comportement localisé. Par ailleurs, dans le cas d'une utilisation pour essais en déformation plane, le contrôle de la déformation plane est actif (via un piston) contrairement aux autres systèmes dits passifs car reposants sur une rigidité de cellule. La solution retenue offre une bien meilleure maitrise du chemin de chargement et donne la perspective aussi de travailler sur des chemins autres qu'en déformation plane, puisqu'il s'agit de fait d'un vrai appareil triaxial (les trois contraintes principales sont indépendantes). De plus, dans ce nouveau dispositif, à l'instar des appareils biaxiaux (*e.g.*, Ord *et al.*, 1991, Labuz *et al.*, 1996), les surfaces de ruptures peuvent s'initier et se propager de manière

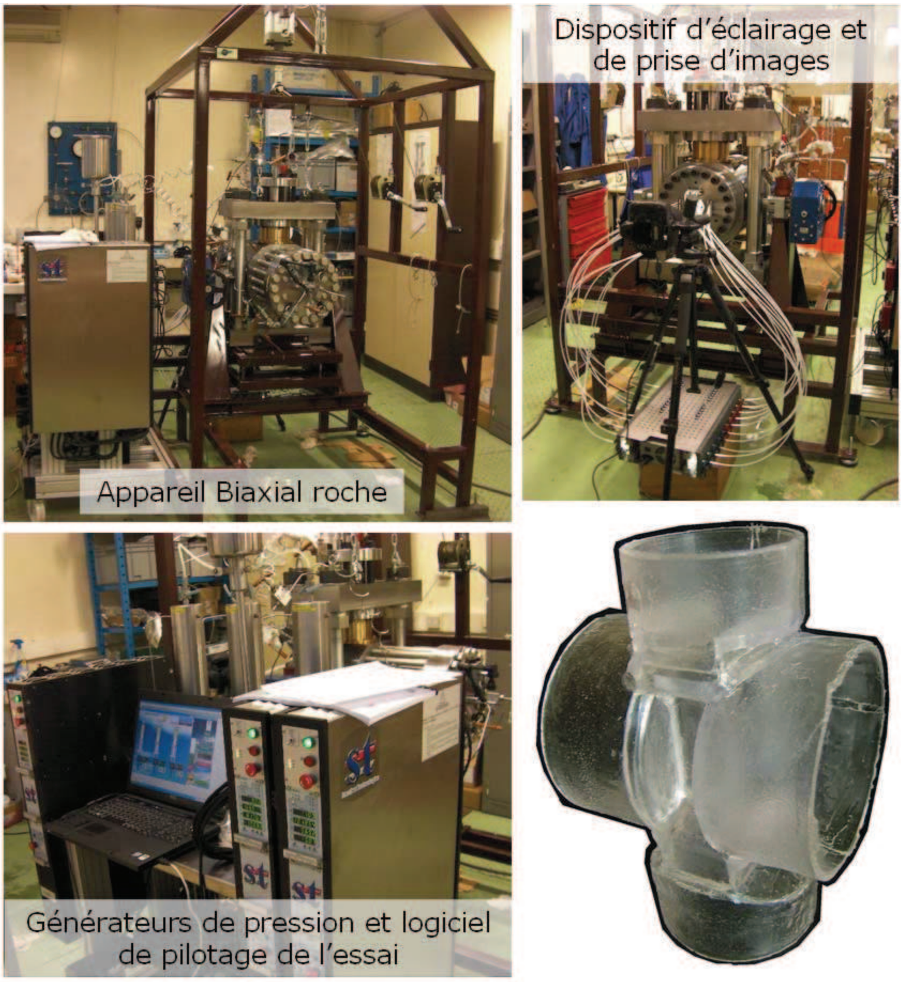

FIGURE 10 – Photographies du nouvel appareil biaxial roche lors du premier essai, du dispositif d'éclairage de l'échantillon par fibres optiques, et des trois générateurs de pression, ainsi que d'une membrane d'étanchéité en silicone devant protéger l'échantillon de l'huile de confinement.

non restreintes car deux des surfaces sont des surfaces libres (application d'une pression par un fluide, et non via un plateau rigide), même s'il a été montré dans les sols que des conditions de type plateaux rigides n'empéchaient pas la localisation, mais rendaient les structures de localisation un peu plus complexes (réflexion des bandes sur les plateaux).

Le premier essai de validation sur un grès des Vosges a été effectué à un confinement de 20 MPa. Tout au long du chargement, des photographies de l'échantillon ont été prises. Entre paires d'images, une analyse par corrélation d'image a été effectuée, permettant de mesurer le champ de déplacement incrémental sur la face de l'échantillon en appui contre le hublot. La figure 11 montre la courbe de chargement de l'échantillon en terme de force axiale (contribution au déviateur

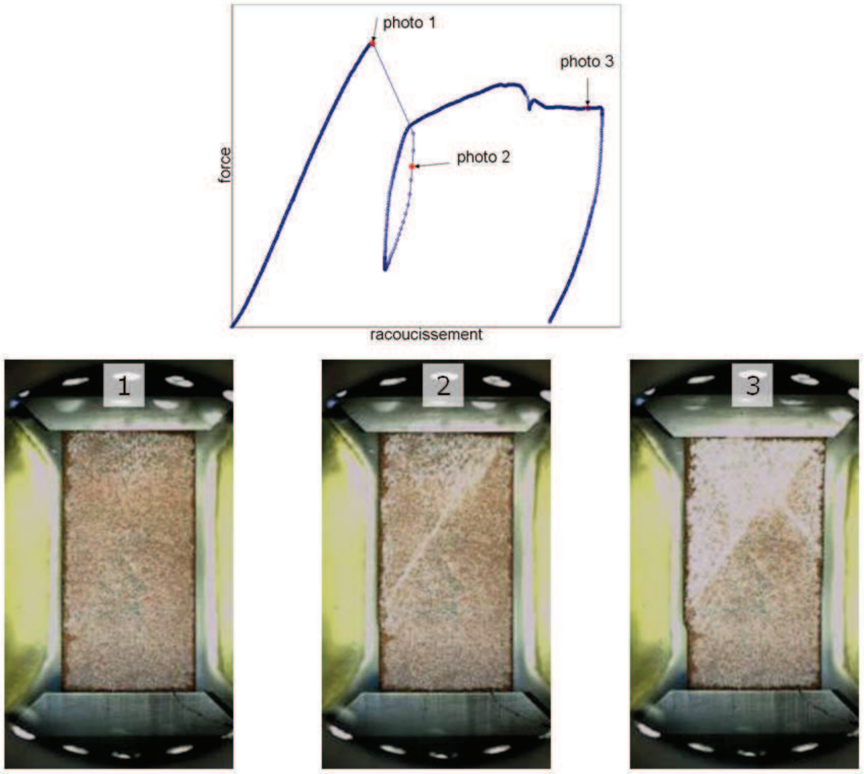

FIGURE 11 – Premier test de validation : courbe de chargement de l'échantillon de grès en terme de force *vs* raccourcissement, sous un confinement de 20 MPa, et trois photographies de l'échantillon prises aux trois instants mentionnés sur la courbe par des flèches (les dimensions de l'échantillon sont de l'ordre de 50 mm de hauteur, 25 mm de largeur et 30 mm de profondeur).

de contrainte) en fonction du raccourcissement de l'échantillon, ainsi que trois photographies de l'échantillon prises aux instants indiqués par les flèches sur la courbe de chargement. Rappelons que du fait de la condition de déformation plane, la mesure de surface du champ cinématique est représentative du champ de déplacement dans tout l'échantillon, y compris en régime localisé, car la bande se forme naturellement parallèlement à la contrainte principale intermédiaire, soit ici la direction de déformation plane ou encore la direction perpendiculaire au hublot (fait que nous avons pu vérifier après démontage de l'échantillon). Cela peut se montrer théoriquement par une analyse en bifurcation, démontrant que la bande est parallèle à la direction de contrainte intermédiaire (voir par exemple Bésuelle et Rudnicki, 2004 [13]), et a été également observé expérimentalement sur les sables (*e.g.*, Desrues, 1984) et roches (*e.g.*, Ord *et al.*, 1991 ; Labuz *et al.*, 1996)

Une campagne d'essais a débuté, en commençant par l'étude de la rupture dans une argilite à différents niveaux de confinement. Lors d'un essai, l'échantillon est photographié à intervalles réguliers (quelques centaines de photographies par essai) et une analyse par corrélation d'image, sur une sélection de photographies, est effectuée. La figure 12 montre la réponse type d'un échantillon (confinement latéral de 6 MPa), avec l'emplacement des photogaphies utilisées pour l'analyse de la cinématique.

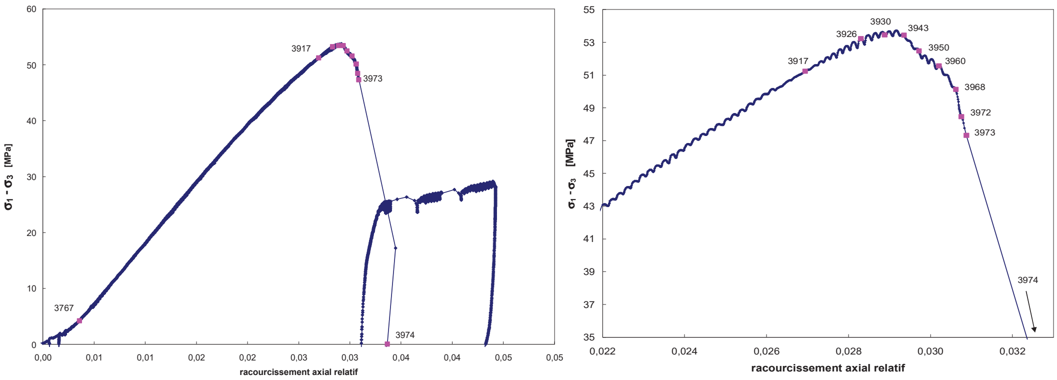

FIGURE 12 – Réponse d'un échantillon de roche argileuse comprimé en déformation plane avec un confinement latéral de 6 MPa. A gauche, vue d'ensemble ; à droite, vue de détail près du pic de contrainte avec position des photographies sélectionnées pour l'analyse en corrélation.

La figure 13 montre les différents résultats obtenus sur les différents incréments de chargement. Le premier incrément correspond à la première phase de chargement, du début vers un peu avant le pic de contrainte, les autres incréments concernent la région autour du pic de contrainte de la figure 12. Les résultats sont montrés en terme de champ de déplacement ou champ de déformations (cisaillement maximum et volume). Les mesures des incréments de déplacement étant de très faibles valeurs lors des petits incréments près du pic (quelques dixièmes de pixel grâce à un algorithme de corrélation sub-pixel, avec une taille de pixel de l'ordre de 10 microns) et donc perturbées par un bruit, les gradients de déplacement se perçoivent mieux à l'oeil sur le champ de déplacement que sur le champ de déformation (des améliorations sont en cours pour réduire le bruit). Ces résultats montrent très clairement qu'après un régime de déformation relativement homogène (avec un peu de frottement au niveau des têtes de chargement), la localisation de la déformation sous forme d'une bande s'initie peu avant le pic de contrainte, cette bande inclinée traverse l'échantillon de part en part. Apparait alors à l'emplacement de la bande une fissure (en haut à droite de l'échantillon) qui se propage progressivement, jusqu'à traverser entièrement l'échantillon, cette propagation complète étant associée à une forte chute de résistance de l'échantillon. Lors de la propagation de la fissure, on distingue en amont de la pointe de fissure une bande de déformation (plutôt qu'une zone de 'process' car son extension est très importante), cette bande suit la pointe de la fissure lorsque cette dernière se propage.

Ces premiers résultats sont à notre connaissance uniques et permettent de mieux comprendre le processus de rupture. Pour la roche étudiée ici, elle se présente d'abord par une localisation de la déformation, donc aussi par une rapide augmentation de l'amplitude de déformation dans la bande. Lorsque celle-ci devient importante, on observe la naissance et la propagation d'une macro-fissure en lieu et place de la bande.

Collaboration : Steve Hall (3SR)
Publication : [22]
référence in-extenso :

- P. Bésuelle and S.A. Hall, *Characterization of the strain localization in a porous rock in plane strain condition using a new true-triaxial apparatus*, Proc. 9th International Workshop on Bifurcation and Degradation in Geomaterials, IWBDG 2011 (Porquerolles, France, may 23-26) (S. Bonelli, C. Dascalu, and F. Nicot, eds.), 2011, in print.

Références externes :

Atkinson R.H., Ko H.-Y., 1973, A fluid cushion, multiaxial cell for testing rock specimens. *Int J Rock Mech Mining Sci Geomech Abstr.*, vol. 10, pp. 351-361.

Desrues J., 1984, La localisation de la déformation dans les matériaux granulaires, Thèse d'état, USMG and INPG, Grenoble, France.

Haimson B., Chang C., 2000, A new true triaxial cell for testing mechanical properties of rock, and its use to determine rock strength and deformability of Westerly granite. *Int J Rock Mech Mining Sci.*, vol. 37, pp. 285-296.

King M.S., 2002, Elastic wave propagation in and permeability for rocks with multiple parallel fracture. *Int J Rock Mech Mining Sci.*, vol. 39, pp. 1033-1043.

Labuz J.F., Dai S.-T., Papamichos E., 1996, Plane-strain compression of rock-like materials. *Int J Rock Mech Mining Sci Geomech Abstr.*, vol. 33, pp. 573-578.

Michelis P, 1985, A true triaxial cell for low and high pressure experiments. *Int J Rock Mech Mining Sci Geomech abstr.*, vol. 22, pp. 193-188.

Mogi K., 1967, Effect of the intermediate principal stress on rock failure. *J Geophys Res*, vol. 72, pp. 5117-5131.

Naumann M., Hunsche U., Schulze O., 2007, Experimental investigations on anisotropy in dilatancy, failure and creep of Opalinus Clay. *Phys Chemistry Earth*, vol. 32, pp. 889-895.

Ord A., Vardoulakis I., Kajewski R., 1991, Shear band formation in Gosford sandstone. *Int J Rock Mech Mining Sci Geomech Abstr.*, vol. 28, pp. 397-409.

Popp T., Salzer K., 2007, Anisotropy of seismic and mechanical properties of Opalinus clay during triaxial deformation in a multi-anvil apparatus. *Phys. Chemistry Earth*, vol. 32, pp. 879-888.

Takemura T., Oda M., Takahashi M., 2004, Microstructure observation in deformed geomaterials using microfocus X-ray computed tomography. In : Otani J, Obara Y (eds) *X-ray CT for Geomaterials, GeoX2004*, Balkema.

Wawersik W.R., Carlson L.W., Holcomb D.J., Williams R.J., 1997, New method for true-triaxial rock testing. *Int J Rock Mech Mining Sci.*, vol. 34, pp. 330.

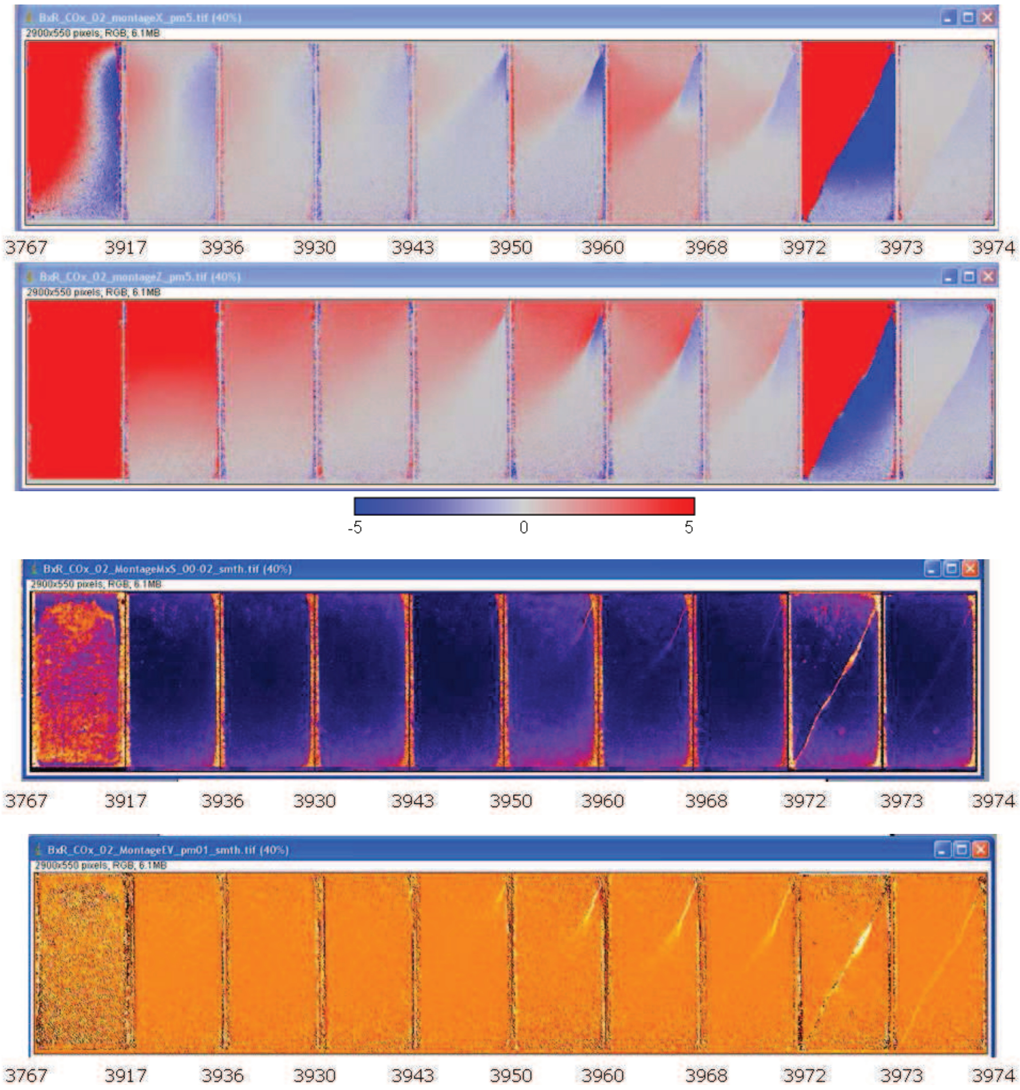

FIGURE 13 – Analyse par corrélation d'image du champ cinématique incrémental au cours du chargement (les incréments de chargement n'ont pas tous la même amplitude). 1ère ligne, champ de déplacement horizontal ; 2ème ligne, déplacement vertical ; 3ème ligne, déformation de cisaillement maximum ; 4ème ligne, déformation volumique.

# 5 Travaux de modélisation

## 5.1 Mode de localisation dans la transition fragile ductile

Si nous considérons un problème initialement homogène, la naissance de la localisation de la déformation peut être considérée comme une perte d'unicité du problème aux limites. Une solution au problème, présentant une localisation sous forme de bande de déformation, devient possible et alternative à une solution initiale homogène. Une approche pionière basée sur une analyse en bifurcation a été introduite pour les géomatériaux par Rice au début des années 70 (Rice, 1973). La condition de naissance de la localisation est intimement dépendante à la fois de la loi constitutive et du chargement subit par le matériau. Ces travaux initiaux ont fait l'objet par la suite de nombreuses analyses, avec pour principaux points d'intérêt l'effet de la loi de comportement sur la condition de localisation (Vardoulakis *et al.*, 1978 ; Desrues et Chambon, 2002 ; Molenkamp, 1985 ; Ottosen et Runesson, 1991, pour n'en citer que quelques uns). On peut retenir que d'une manière générale, le caractère non standard d'une loi (dans le contexte des lois élasto-plastiques), ou encore l'anisotropie ou la non coaxialité d'un modèle sont des facteurs favorisant la localisation de la déformation.

Dans la suite des travaux de Rudnicki et Rice (1975), Issen et Rudnicki (2000) ont étendu l'analyse initiale basée sur un modèle élasto-plastique avec une surface ouverte, à un modèle à surface fermée adapté aux roches fortement poreuses, pour lesquelles une augmentation de la contrainte moyenne, quand celle-ci est forte, peut induire de la déformation irréversible. Le mode de localisation dans la zone de fermeture de la surface d'écoulement (*i.e.*, correspondant aux forts niveaux de contrainte moyenne) correspond à ce qui est appelé dans la littérature 'bandes de compaction', mode particulier de localisation où les bords opposés de la bande se rapprochent l'un de l'autre, sans glissement relatif comme c'est le cas en général pour les bandes de cisaillement (notons cependant que la déformation dans une bande de compaction contient une composant volumique, mais aussi de cisaillement) et qui sont orientées orthogonalement à la direction de la contrainte la plus compressive. Le lecteur intéressé pourra trouver une synthèse étendue dans Bésuelle et Rudnicki (2004) [13].

L'objectif de cette étude était d'analyser les modes de rupture dans la transition fragile-ductile. Une analyse théorique des conditions de localisation dans le cadre des modèles de comportement élasto-plastiques a été menée en utilisant une approche en bifurcation (Bésuelle, 2001a [1]). L'étude concerne les matériaux poreux, présentant une grande sensibilité du comportement vis-à-vis de la contrainte moyenne, avec d'une part un comportement dilatant à faible contrain-

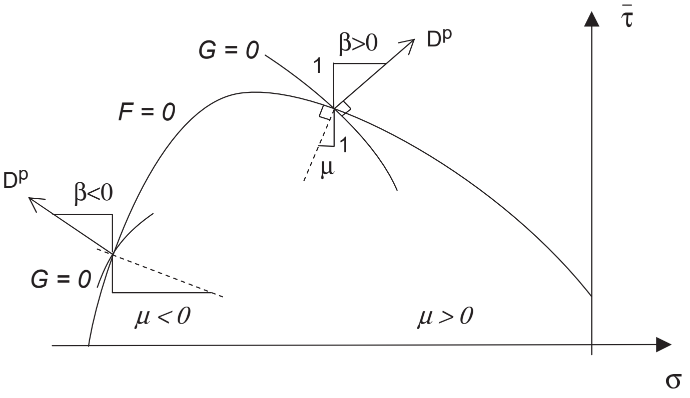

FIGURE 14 – Illustration d'une surface d'écoulement fermée dans le plan de Mohr. L'angle de frottement est positif et le matériau dilatant à faible contrainte moyenne, et inversement aux plus forts confinements.

te et un comportement contractant à forte contrainte et d'autre part une surface d'écrouissage fermée dans le plan deuxième *vs* premier invariant (cap model) (Fig. 14). L'expression analytique de la déformation dans les bandes de localisation naissantes est exprimée, en décomposant la composante de cisaillement et la composante en volume (Fig. 15), introduisant la notion de bandes de cisaillement dilatante ou compactante (Fig. 16). La limite entre ces deux catégories, nommée bande de cisaillement pure (sans variation de volume) est également formulée, elle fait intervenir notamment la pente de la courbe enveloppe du domaine élastique (coefficient de frottement $\mu$) ainsi que le coefficient de dilatance $\beta$ :

$$3(1-2\nu)(1-\nu)N = (1+\nu)\left[(1-2\nu)(\beta+\mu)+2\beta\right],$$

où $N$ correspond à la contrainte intermédiaire du tenseur déviatorique normalisé[3] et $\nu$ est le coefficient de Poisson. Les modes de localisation évoluent de manière continue (Fig. 17), en termes d'orientation et de mode de déformation intérieur à la bande, selon de niveau de contrainte moyenne, allant des bandes de dilatance (à rapprocher de la fissuration par axial splitting caractérisée par des structures parallèles à la direction de compression), aux bandes de compaction, en passant par les bandes de cisaillement dilatantes et les bandes de cisaillement compactantes (toutes deux inclinées par rapport à la direction de compression). La comparaison avec des résultats expérimentaux obtenus pour un grès poreux (grès des Vosges) montre la bonne adéquation du modèle pour ce qui est de l'orientation des bandes et du comportement en volume des bandes détecté par tomographie à rayons X (Bésuelle, 2001b [2]). On constate qu'aux forts

---

[3] Les bornes maximum et minimum de $N$ sont respectivement $1/\sqrt{3}$ en compression axisymétrique et $-1/\sqrt{3}$ en extension axisymétrique

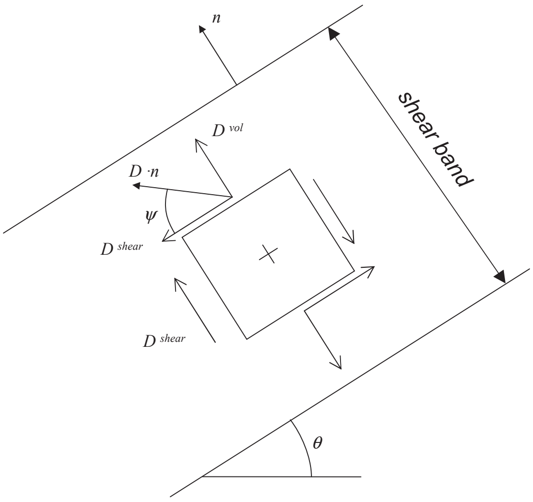

FIGURE 15 – Représentation de la différence de la vitesse de déformation entre l'intérieur de la bande et l'extérieur de la bande, dans le plan défini par la contrainte majeure et la contrainte mineure. $\psi$ est l'angle de dilatance de bande.

confinements, il y a eut réduction de porosité dans la bande alors que les paramètres constitifs correspondent à une bande de cisaillement compactante, réciproquement, aux faibles confinements, on observe une augmentation de la porosité, avec des paramètres constitutifs correspondant à une bande de cisaillement dilatante (Fig. 18). L'évolution de ces prédictions avec le niveau de contrainte moyenne fournit également une interprétation de la transition fragile-ductile du mode de rupture. Les bandes exhibant un cisaillement avec compaction ont tendance à être moins radoucissantes que les bandes avec dilatance, car des mécanismes de durcissement associés à la compaction contre-balancent l'éventuel radoucissement associé au cisaillement. De ce fait, la réponse post-localisation avec des bandes de cisaillement compactantes (se développant à forte contrainte moyenne) est moins radoucissante (moins fragile) que la réponse avec des bandes dilatantes (à faible contrainte moyenne) (Fig. 17).

Publications : [1, 2, 37, 39]
Référence in-extenso (en fin de chapître) :

- P. Bésuelle, *Compacting and dilating shear bands in porous rock : Theoretical and experimental conditions*, J. Geophys. Res. **106** (2001), no. B7, 13435–13442.

Références externes :

Desrues J. and Chambon R., 2002, Shear bands analysis and shear moduli calibration, *Int. J. Solids Struct.*, vol. 39, pp. 3757-3776.

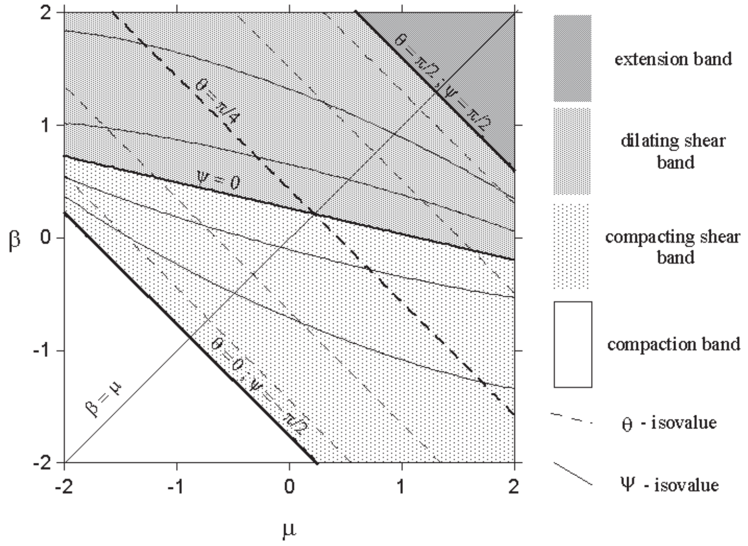

FIGURE 16 – Nature des bandes de localisation (compaction pure, cisaillement avec compaction, cisaillement avec dilatance et extension pure) en fonction du coefficient de frottement $\mu$ et du coefficient de dilatance $\beta$. L'angle $\theta$ est l'angle entre la normale à la bande et la direction de la contrainte la plus compressive, et $\psi$ l'angle de dilatance de bande.

Issen K.A. and Rudnicki J.W., 2000, Conditions for Compaction Bands in Porous Rock, *J. Geophys. Res.*, vol. 105, 21529-21536.

Molenkamp F., 1985, Comparison of frictional material models with respect to shear band initiation, *Géotechnique*, vol. 35, pp. 127-143.

Ottossen N.S. and Runesson K., 1991, Properties of discontinuous bifurcation solutions in elasto-plasticity, *Int. J. Solids Struct.*, vol. 27, pp. 401-421.

Rice J.R., 1973, The initiation and growth of shear bands. In : Palmer AC, editor. *International Congress of Theoretical and Applied Mechanics*, Cambridge, p. 263-274.

Rudnicki J.W. and Rice J.R., 1975, Conditions for the Localization of Deformation in Pressure Sensitive Dilatant Materials, *J. Mech. Phys. Solids*, 23, 371-394.

Vardoulakis I., Goldscheider M. and Gudehus G., 1978, Formation of shear bands in sand bodies as a bifurcation problem, *Int. J. Numer. Anal. Meth Geomech.*, vol 2, pp. 99-128.

## 5.2 Comportement en régime localisé

**Milieux enrichis et implémentation numérique** Les observations expérimentales sur les géomatériaux (sables, roches) réalisées sur des essais conduits en laboratoire montrent une assez bonne reproductibilité pour ce qui concerne les

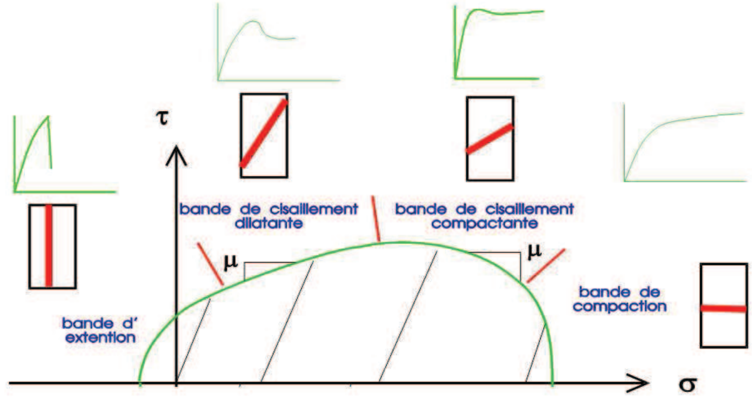

FIGURE 17 – Shématisation des modes de localisation en compression axiale en fonction du niveau de contrainte moyenne pour un modèle à surface fermée, dans le plan de Mohr, et illustration des différentes catégories de réponse de l'échantillon qui y sont associées, du fragile au ductile.

orientations et les épaisseurs des bandes de localisation. Le phénomène de localisation de la déformation fait apparaître, de par l'épaisseur des bandes, des longueurs caractéristiques aux matériaux, en général en relation étroite avec la taille des grains (une bande dans un sable a une largeur de l'ordre de 5 à 20 grains, voir Bésuelle et Rudnicki, 2004, [13], pour une synthèse). A contrario, les modélisations numériques de la localisation dans un milieu continu classique montre une dépendance de la largeur de bande avec la taille du maillage, plus le maillage se raffine, moins la bande est épaisse, convergeant dans le cas ultime à une bande de largeur nulle et sans dissipation d'énergie (Pijaudier-Cabot et Bazant, 1987).

Afin de modéliser proprement le phénomène de localisation, il est nécessaire de mettre en œuvre une démarche de régularisation mathématique qui permettra d'empécher ce problème de dépendance au maillage. Plusieurs cadres ont été développés dans la littérature, par exemple en ajoutant une dépendance au temps dans la loi constitutive (*e.g.*, Loret et Prevost, 1990), ou bien en développant des lois constitutives enrichies, disposant d'une longueur interne (*e.g.*, Bazant *et al.*, 1987 ; Vardoulakis et Aifantis, 1991 ; de Borst et Muehlhaus, 1992 ; Chambon *et al.*, 1998, pour n'en citer que quelques uns).

Un travail théorique a été mené dans le cadre des modèles à microstructure (Cosserat et Cosserat, 1909 ; Toupin, 1962 ; Mindlin, 1964 ; Germain, 1973) par R. Chambon et D. Caillerie (Chambon *et al.*, 1998) sur des modèles dits de second gradient locaux, cas particulier des modèles à microstructure (certaines hypothèses sont faites sur la macrocinématique et la microcinématique). Pour ce for-

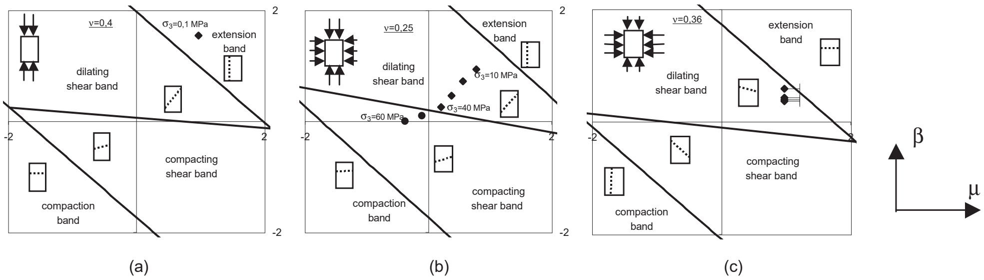

FIGURE 18 – Comparaison entrez théorie et expériences sur le grès des Vosges : on a reporté les données expérimentales ([6]) sur le graphe de la figure 16, pour la compression uniaxiale (a), pour la compression axisymétrique (b) et pour l'extension axisymétrique (c). Pour la compression axisymétrique, la tomographie *post-mortem* a confirmé une dilatance dans la bande à 30 MPa de confinement et une compaction à 50 MPa, en conformité avec l'analyse théorique.

malisme de milieux continus, le principe des travaux virtuels peut s'écrire :

$$\int_\Omega \left( \sigma_{ij}\varepsilon^\star_{ij} + \Sigma_{ijk}\frac{\partial^2 u^\star_i}{\partial x_j\,\partial x_k} \right) dv = \int_\Omega G_i u^\star_i \, dv + \int_{\partial\Omega} \left( p_i u^\star_i + P_i D u^\star_i \right) ds \;, \qquad (1)$$

où $\sigma_{ij}$ est la contrainte de Cauchy, $\varepsilon^\star_{ij}$ la macro-déformation virtuelle, $\Sigma_{ijk}$ le terme dual associé au second gradient du déplacement virtuel, encore appelé double contrainte. $G_i$ est la densité de force de volume, $p_i$ et $P_i$ sont respectivements des conditions de surfaces, liées à la densité de force surfacique et double force surfacique et la dérivée normale à la surface est définie par $Du_i = n_k\,\partial u_i/\partial x_k$, avec $n_k$ la normale à la surface.

Ces modèles mettent en œuvre une double relation de comportement, contrainte histoire du gradient du déplacement (loi classique) et relation double contrainte - second gradient du déplacement, celle-ci étant supposée linéaire dans les applications qui suivent. Les solutions analytiques, par exemple pour un problème unidimensionnel (Chambon *et al.*, 1998), montrent que la largeur d'une bande s'exprime par certains des paramètres du modèle constitutif, à savoir les modules de rigidité tangents de la loi premier gradient $K_{ijkl}$ et les modules de la loi second gradient $A_{ijklmn}$ (voir le paragraphe suivant pour une extension au cas général).

Pour mettre en œuvre ces lois d'un point de vue numérique par la méthode des éléments finis, il a été nécessaire de passer à une formulation faible du problème, en employant deux champs cinématiques, l'un pour le déplacement, l'autre pour le gradient du déplacement, les deux étant reliés par l'intermédiaire de multiplicateurs de Lagrange (Matsushima *et al.*, 2002). Un tel élément comporte alors 36 degrés de liberté (cf. Fig. 19).

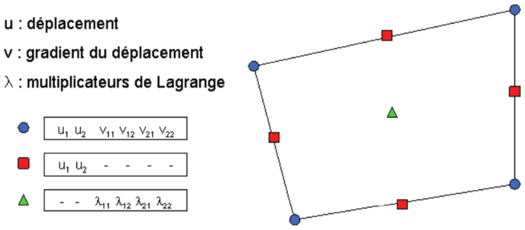

FIGURE 19 – Caractérisation de l'élément tel qu'il a été implémenté dans le code Lagamine. Le champ $u$ représente le déplacement, le champ $v$ le gradient du déplacement et le champ $\lambda$ les multiplicateurs de Lagrange.

J'ai contribué, en collaboration avec l'Université de Liège (équipe de R. Charlier), à l'implémentation de ce nouvel élément fini 2D dans le code E.F. *Lagamine*. Cet élément a fait l'objet d'une validation, d'abord à partir de résultats analytiques 1D. Dans le cadre de la modélisation d'un essai de compression en déformation plane (2D), on a pu montrer que ce type d'élément permet bien de rendre les calculs indépendants vis-à-vis de la finesse du maillage en régime post-localisation, tant du point de vue de la dissipation d'énergie de déformation (courbe force-raccourcissement, Fig. 20) que de la déformée (Fig. 21). On peut considérer que dès que l'on a deux à trois éléments dans la largeur de bande définie par le modèle, la modélisation est indépendante du maillage ([73]).

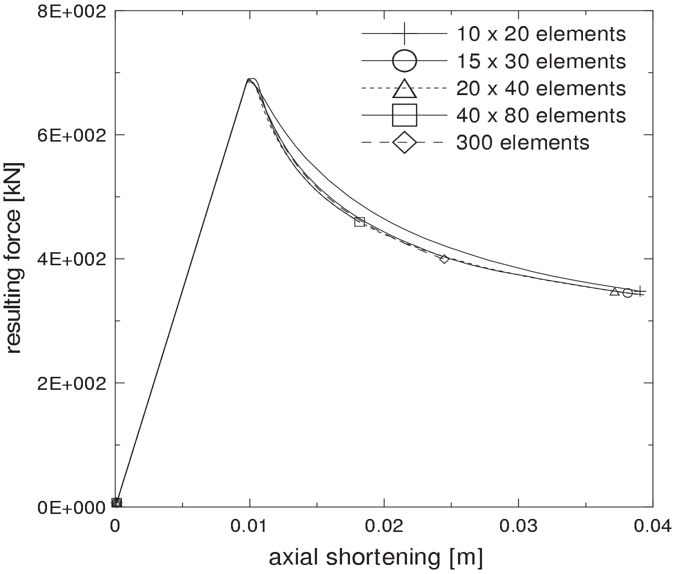

FIGURE 20 – Comparaison de l'évolution de la force résultante-racoucissement pour un essai biaxial simulé avec 4 tailles de maillage régulier et un maillage non structuré (cf. Fig. 21), avec le nouvel élément fini implémenté dans Lagamine.

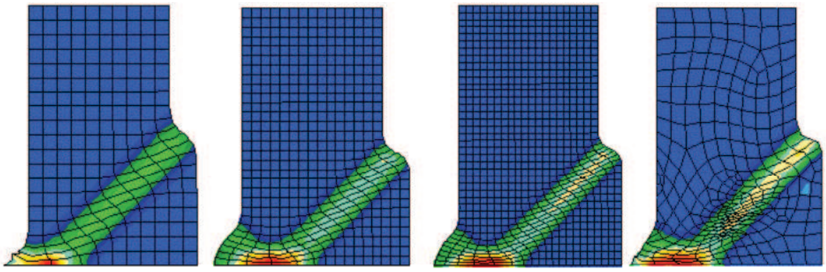

FIGURE 21 – Comparaison de la déformée réelle d'un essai biaxial après localisation (raccourcissement de 10 %) pour trois tailles de maillage réguliers (10x20, 15x30 et 20x40) et un maillage non structuré. Simulations obtenues avec le nouvel élément fini implémenté dans Lagamine (un défaut a été placé en bas à gauche de l'échantillon pour 'forcer' la localisation).

**Unicité des solutions en régime localisé** Disposant d'un outil numérique opérationnel, il était possible de commencer à explorer par des expériences numériques le comportement post-localisation. L'aspect de non-unicité des solutions à un problème aux conditions limites est une notion importante. Elle permet de valider un résultat numérique obtenu, ou au contraire de le relativiser compte tenu que d'autres solutions au même problème mathématique existent. A ce titre, j'ai généralisé aux milieux second gradient locaux l'analyse théorique en bifurcation de Rice (1973) afin d'expliciter un seuil de localisation théorique dans ces milieux (recherche de perte d'unicité sous forme de bande de déformation)(Bésuelle *et al.*, 2006 [4]). Si l'on désigne $K^{ep}_{ijkl}$ le tenseur constitutif de la partie premier gradient de la loi en vitesse, $A_{ijklmn}$ le tenseur de la partie second gradient de la loi en vitesse et $n_i$ le vecteur unitaire normal à la bande naissante, alors on peut montrer qu'il y a localisation s'il existe une solution à l'équation :

$$\det(\mathcal{K}^{ep}_{ij} - \Lambda\ \mathcal{A}_{ij}) = 0,$$

avec $\mathcal{K}^{ep}_{ik} = K^{ep}_{ijkl}\, n_j n_l$ et $\mathcal{A}_{il} = A_{ijklmn}\, n_j n_k n_m n_n$, l'indice $^{ep}$ désignant le domaine de chargement élasto-plastique et $\Lambda = \lambda^2$, $\lambda$ étant une longueur caractéristique de la largeur de bande. L'équation précédente étant une équation du troisième degré, alors on obtient, en notant $\Lambda_a$, $\Lambda_b$, $\Lambda_c$ les trois solutions :

$$\det(\mathcal{A})\Lambda_a\ \Lambda_b\ \Lambda_c = \det(\mathcal{K}^{ep})\ .$$

Pour qu'il y ai localisation, une des solutions doit être négative (profil de déformation de type harmonique), aussi nous obtenons que la condition de localisation se résume alors à la condition :

$$\det(\mathcal{K}^{\mathbf{ep}}) \leq 0 \,.$$

Celui-ci s'avère être identique aux milieux classiques (signe du tenseur acoustique de la partie classique de la loi constitutive), sauf qu'un effet d'échelle apparaît en plus et qui a tendance à retarder le seuil de localisation, en rapport avec la dimension du domaine d'étude du problème aux limites considéré. En effet, la longueur caractéristique dépend du déterminant du tenseur de la partie second gradient $\det(\mathcal{A})$ (considéré positif) et de l'inverse du déterminant du tenseur acoustique $\det(\mathcal{K}^{\mathbf{ep}})$. Pour la première condition de localisation possible $\det(\mathcal{K}^{\mathbf{ep}}) = 0$ , la bande a une largeur infinie. Dans un domaine d'étude de dimension finie, la localisation ne devient possible que si le déterminant du tenseur acoustique devient suffisamment négatif.

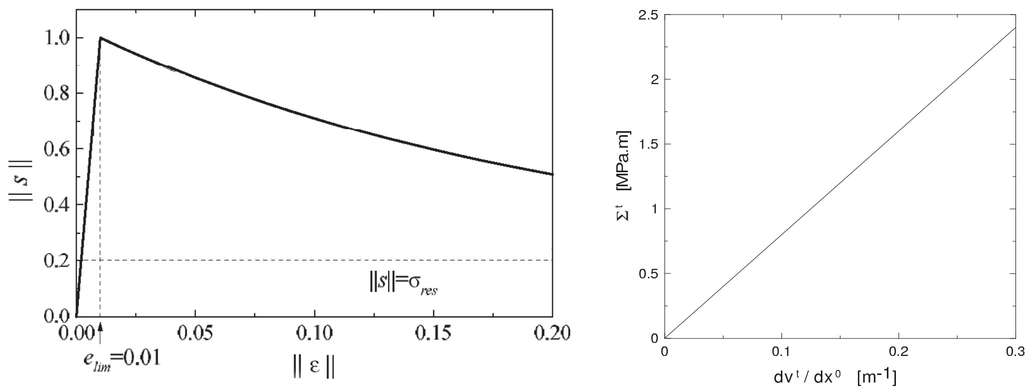

FIGURE 22 – Loi constitutive utilisée pour les calculs 2D : à gauche, partie classique premier gradient montrant un régime durcissant puis un régime radoucissant, à droite, partie second gradient de type élastique linéaire.

A partir d'un certain seuil de chargement, il y a donc souvent perte d'unicité des solutions du problème aux conditions limites. Pour les essais biaxiaux numériques précédents, et compte tenu de la loi constitutive utilisée (Fig. 22), on peut dire qu'à partir du pic de contrainte, il existe une infinité de solutions. Si l'on considère cette question cette fois-ci d'un point de vue expérimental, il a été constaté que les essais de laboratoire menés proprement étaient faiblement reproductibles dès lors que la localisation se mettait en place. Sont bien reproductibles les épaisseurs et orientation de bandes, mais leur nombre et leurs positions, de même que la persitance des bandes ne le sont pas toujours (Desrues et Viggiani, 2004), cela pouvant entrainer des différentes de réponse sur la courbe force-racourcissement de l'échantillon. Cette diversité de réponse est généralement attribuée aux détails microstructuraux du matériau constituant l'échantillon (détails parfois difficilement observables), les petites imperfections du matériau (associées également aux imperfections des conditions limites appliquées à l'échantillon) contrôlant les zones de naissance des bandes de localisation.

Si l'on revient du point de vue numérique au problème, une façon de contrôler de manière déterministe les structures de localisation est d'introduire dans le milieu un champ d'imperfections via les paramètres constitutifs du modèle. Néanmoins rien ne garantit que l'unicité du problème est restaurée de cette manière. Il est aussi possible de considérer cette question en considérant un milieu parfait (sans imperfection) et en cherchant différentes solutions au problème. De cette manière, on associe la non reproductibilité expérimentale, liée à l'incertitude des petites hétérogénéités inhérentes aux matériaux naturels, à la non unicité numérique du problème posé. La méthode que nous avons adopté pour cela est d'utiliser l'algoritme de recherche directionnelle initialement développé par R. Chambon (2001) pour les milieux classiques, qui se défini par un tirage aléatoire des vitesses nodales au début du calcul de la solution d'un pas donné pour lequel on cherche à initier une solution alternative (initialisation aléatoire de la méthode de Newton-Raphson). Cet algorithme a été introduit dans le code *Lagamine* pour les milieux second gradient. Nous montrons ainsi que nous pouvons obtenir plusieurs solutions non homogènes à partir d'un même problème initialement homogène. Les solutions trouvées sont généralement des solutions présentant une ou plusieurs bandes (Fig. 23). La réponse force-déplacement est quant à elle entièrement contrôlée par le nombre de bandes de déformation (Fig. 24.a).

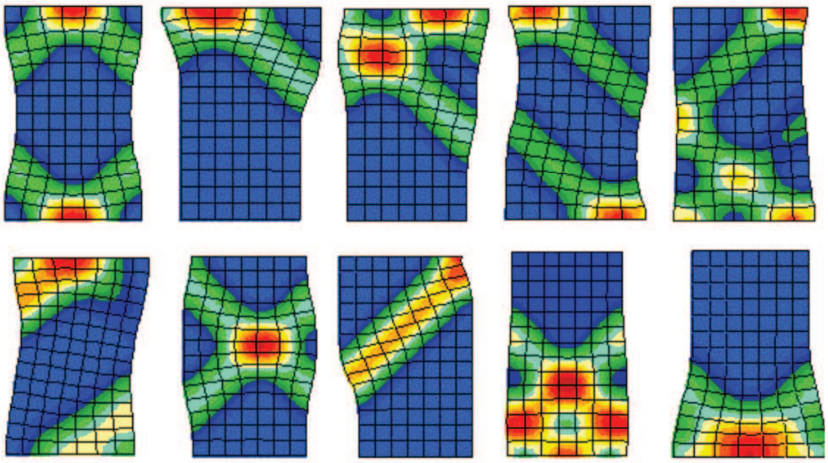

FIGURE 23 – Exemples de solutions non homogènes obtenues par tirage aléatoire après le pic de contrainte (à partir de la solution homogène). Les solutions montrées (après 10% de raccourcissement total pour la plupart) comportent 1, 2 ou 3 bandes, certaines bandes pouvant disparaîtrent (en se désactivant) lors du chargement.

Une fois qu'une structure de localisation est apparue, il était intéressant d'en étudier la pérennité, peut-elle évoluer au cours du chargement ? J'ai montré numériquement que celle-ci peut en effet évoluer, notamment en désactivant (de manière *ad hoc*, ou alors spontanément) des bandes de déformation (Bésuelle *et al.*, 2006 [4]). Cette réduction du nombre de bandes actives implique un changement brutale de la réponse de l'échantillon numérique (Fig. 24.b), ce qui est tout à fait logique sur les principes. Là aussi, on retrouve numériquement des observations expérimentales de blocage de bandes.

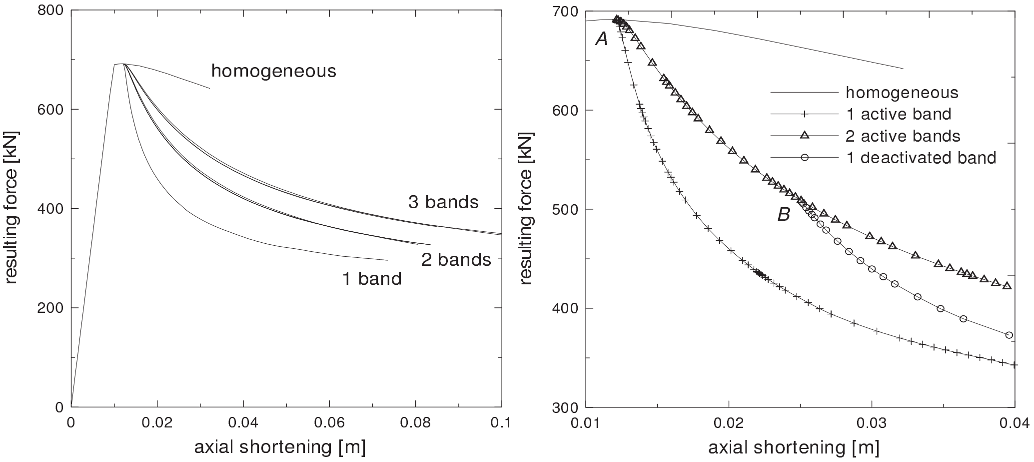

FIGURE 24 – Comparaison des réponses force-racourcissement de dix calculs du même problème initial, en fonction du nombre de bandes de déformation (à gauche). La désactivation d'une bande de déformation en cours de chargement implique une rupture de pente dans la réponse (point B sur la figure de droite).

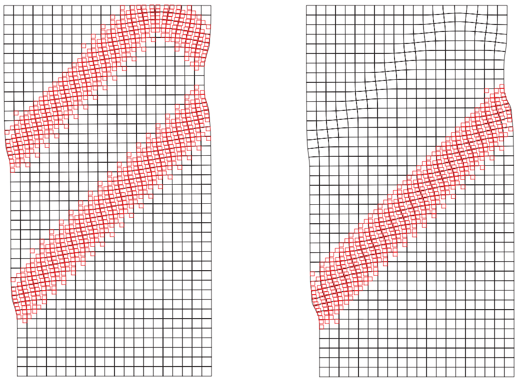

FIGURE 25 – Exemples de solutions après un tirage aléatoire au point A de la Figure 24.b exhibant initialement deux bandes : à gauche, les bandes sont restées actives ; à droite, une des bandes a été désactivée au point B. Le racourcissement axial est de 4% dans les deux cas.

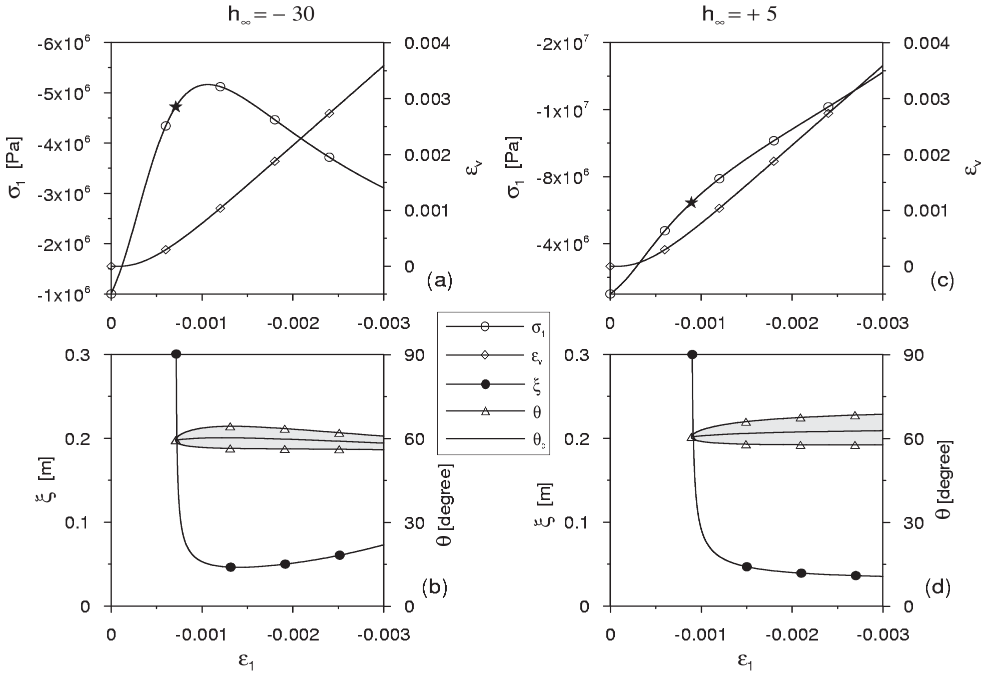

FIGURE 26 – Réponse de loi utilisée sur un chemin de compression plane, avec un régime radoucissant (a), ou sans phase de radoucissement (c). Les courbes de la contrainte de compression $\sigma_1$ et de la déformation volumique $\varepsilon_v$ sont représentées en fonction de la déformation axiale $\varepsilon_1$. Les caractéristiques résultants de l'analyse en bifurcation sont représentées dans la partie inférieure. Le domaine des orientations possibles $\theta$ de la bande et la longueur spécifique $\xi$ correspondant à l'angle critique $\theta_c$ (b) et (d) sont représentés en fonction de $\varepsilon_1$. Les étoiles en (a) et (c) correspondent au premier seuil de localisation possible.

**Influence de la loi constitutive sur la réponse post-localisation** Après cette première exploration, il me semblait important de commencer à s'orienter vers des lois de comportement plus réalistes que celle utilisée jusqu'à présent, qui avait justement pour avantage d'être 'simple' en terme de déclenchement de la localisation car elle présente une discontinuité de pente sur la courbe contrainte-déformation avec radoucissement. Au contraire, les lois ordinaires sont continues, elles ne présentent pas de discontinuité de pente. De ce fait, au premier seuil théorique de localisation, la largeur de bande est infinie puis décroît assez rapidement vers une longueur propre. Cet aspect de l'évolution de la largeur de bande illustre, comme nous l'avons mentionné auparavant, un effet d'échelle dans les milieux second gradient (le seuil de localisation est influencé par la taille du domaine d'étude considéré). J'ai utilisé un modèle de comportement élastoplastique avec une surface d'écoulement de type Drucker-Prager écrouissable sur

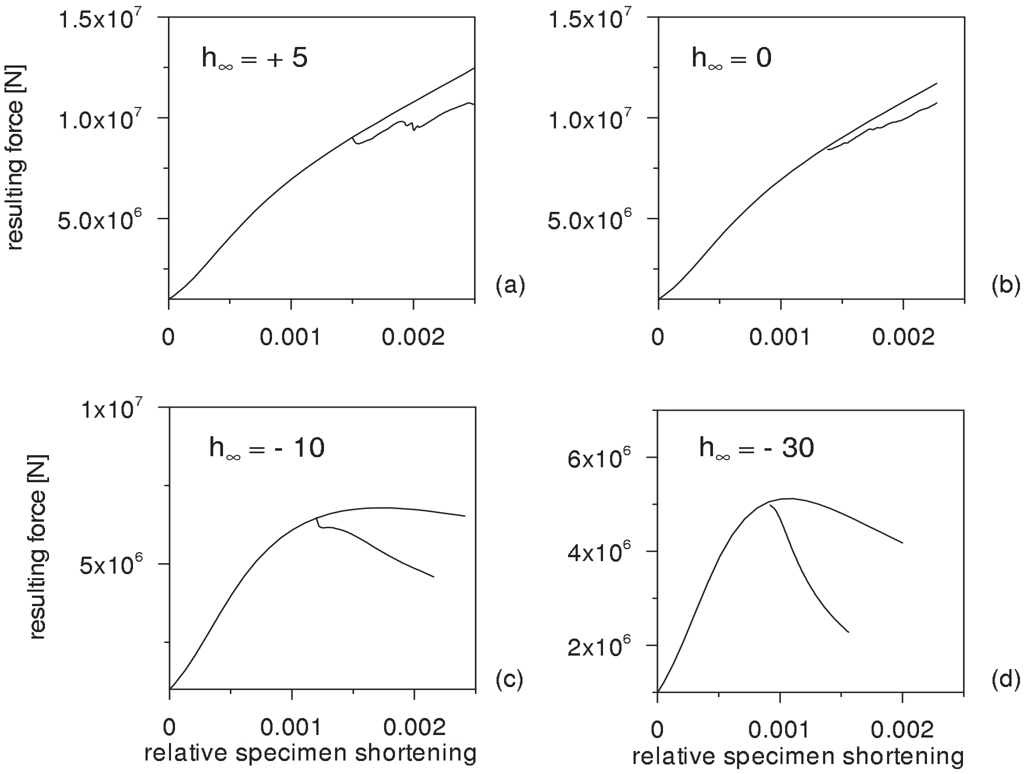

FIGURE 27 – Comparaison entre les solutions homogènes et des exemples de solutions localisées obtenues, soit pour un modèle durcissant $h_\infty > 0$ (a et b), soit pour un modèle présentant du radoucissement $h_\infty < 0$ (c et d). Les fluctuations dans le cas durcissant correspondent à des blocages de bandes et formation de nouvelles bandes de déformation.

l'angle de frottement avec une déformation de cisaillement plastique équivalente. En fonction du choix des paramètres constitutifs, cette loi est entièrement de type durcissante, ou bien comporte une première phase durcissante puis une seconde phase radoucissante (Fig. 26). Un enjeu important était de montrer que la localisation, conformément aux prédictions théoriques, pouvait apparaître en régime durcissant. Cette étude a permis par ailleurs d'explorer les comportements post-localisation, suivant que du radoucissement existe ou non dans le modèle et de les comparer de manière qualitative avec les observations expérimentales (Bésuelle et Chambon, 2005 [19]). De manière schématique (Fig. 27), si le modèle présente du radoucissement, on retrouve des réponses de type régime quasi-fragile, et si le modèle est uniquement durcissant, on trouve des réponses de type régime de transition fragile-ductile (bien connu dans les roches assez poreuses sous forte contrainte moyenne). La réponse avec localisation se situe dans tous les cas en dessous (en terme de résistance) de la réponse homogène. Quand la loi est durcissante, elle continue à augmenter au cours du chargement et présente des fluctuations (comme on peut aussi l'observer expérimentalement). Cela est lié à la non persistance des bandes de déformation. Celles-ci ont tendance à se 'saturer', et donc à s'éteindre spontanément pour que d'autres bandes de localisation apparaissent ailleurs. Une fois de plus, on remarque une forte similitude avec les expériences sur les roches dans le régime fragile-ductile dans lesquelles on peut trouver ce genre d'observations (Fig. 28).

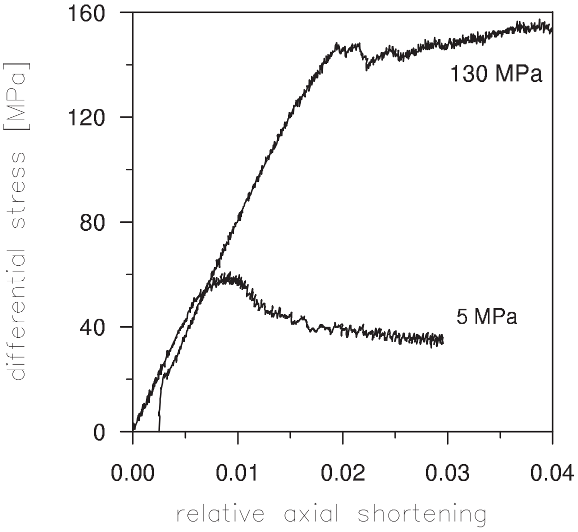

FIGURE 28 – Réponses de deux échantillons du grès de Rothbach sollicités en compression axisymmétrique avec un confinement, respectivement, de 5 MPa et 130 MPa, correspondant à un comportement plutôt fragile et un comportement de transition fragile-ductile (Bésuelle *et al.*, 2003 [3]).

Collaborations : René Chambon (3SR), Frédéric Collin (FNRS-Université de Liège), Robert Charlier (Université de Liège), Panos Kotronis (3SR)
Publications : [4, 19, 38, 74, 73, 8, 30, 58]
références in-extenso :

- P. Bésuelle, R. Chambon, and F. Collin, *Switching mode of deformation in post- localization solutions with a quasi brittle material*, J. Mech. Mater. Struct. **1** (2007), no. 7, 1115–1134.
- P. Bésuelle and R. Chambon, *Modelling the post-localization regime with local second gradient models : Non uniqueness of solutions and non persistent shear bands*, Modern Trends in Geomechanics (Proc. Int. Workshop, Vienna, Austria, june 27-29, 2005) (W. Wu and H.-S. Yu, eds.), Springer, Berlin, 2006, pp. 209–221.

Références externes :

Bažant Z., Lin F.-B. and Pijaudier-Cabot G., 1987, Yield limit degradation : Nonlocal continuum model with local strain, In *Computational Plasticity. Models,* *Software and Applications*, D.R. Owen, E. Hinton, and E. Oñate, edts, pp. 1757-1780. Pineridge Press, Swansea.

Chambon R., Caillerie D. and El Hassan N., 1998, One-dimensional localisation studied with second grade model, *Eur. J. Mech. A/Solids*, vol. 17, pp. 637-656.

Chambon R., Crochepeyre S. and Charlier R., 2001, An algortithm and a method to search bifurcation point in non linear problems, *Int. J. Numer. Meth. Engng.*, vol. 51, pp. 315-332.

Cosserat E. and Cosserat F., 1909, Théorie des corps déformables, Hermann, Paris.

Desrues J. and Viggiani G., 2004, Strain localization in sand : an overview of the experimental results obtained in Grenoble using stereophotogrammetry, *Int. J. Numer. Anal. Meth. Geomech.*,vol. 28,pp. 279-321.

de Borst R. and Mühlhaus H.-B., 1992, Gradient-dependent plasticity : Formulation and algorithmic aspects, *Int. J. Numer. Meth. Engng.*, vol. 35, pp. 521-539.

Germain P., 1973, La méthode des puissances virtuelles en mécanique des milieux continus, première partie : Théorie du second gradient, *J. Méc.*, vol. 12, pp. 235-274.

Loret B. and Prevost J.H., 1990, Dynamic strain localization in elasto-(visco-) plastic solids, Part 1. General formulation and one dimensional examples, *Comput. Meth. Appl. Mech. Engng*, vol. 83, 247-273.

Matsushima T., Chambon R. and Caillerie D., 2002, Large strain finite element analysis of a local second gradient model : application to localization, *Int. J. Numer. Meth. Engng.*, vol. 54, pp. 499-521.

Mindlin R.D., 1964, Micro-structure in linear elasticity, *Arch. Rat. Mech. Anal.*, vol. 4, pp. 50-78.

Pijaudier-Cabot G. and Bažant Z., 1987, Nonlocal damage theory, *J. Engng. Mech.*, vol. 113, pp. 1512-1533.

Rice J.R., 1973, The initiation and growth of shear bands. In : Palmer A.C., editor. *Int. Congress of Theoretical and Applied Mechanics*, Cambridge, pp. 263-274.

Toupin R. A., 1962, Elastic materials with couple-stresses, *Arch. Rat. Mech. Anal.*, vol. 11, pp. 385-414.

Vardoulakis I. and Aifantis E.C., 1991, A gradient flow theory of plasticity for granular materials, *Acta Mechanica*, vol. 387, pp. 197-217.

# 6 Conclusions et perspectives

Nous avons montré un certain nombre de résultats, à la fois sur le plan expérimental et de la modélisation. Sur les observations expérimentales, nous avons à présent une bonne compréhension des modes de rupture dans les roches poreuses, en particulier dans le régime de transition fragile - ductile. Les informations recueillies, seuil d'initiation des bandes de localisation, orientation des bandes, nature de la déformation dans les bandes, micromécanismes dans les bandes, sont très précieuses pour la modélisation. Suivant le niveau de contrainte moyenne, les micro-mécanismes de déformation changent. A faible confinement, ils sont plutôt induits par un accroissement de l'anisotropie de la contrainte, à fort confinement, ils peuvent être également induits par un accroissement de la contrainte moyenne. Nous avons vu que cette sensibilité vis-à-vis de la contrainte moyenne était à l'origine d'une évolution des modes de localisation, de fragiles à faible confinement, associés à de la dilatance, à ductiles à fort confinement, associés à de la contractance : bandes de dilatance, bandes de cisaillement dilatantes ou compactantes, bandes de compaction. Ces observations ont été confrontées à une approche théorique de la localisation de la déformation par une analyse en bifurcation. Nous avons montrés que la dépendance du comportement vis-à-vis du premier invariant de contrainte était le facteur prépondérant pour expliquer cette transition fragile-ductile. Nous retrouvons les tendances observées en terme d'orientation des bandes et de variation de volume à l'intérieur des bandes.

Nous nous sommes intéressés à plusieurs types de matériaux, grès, calcarénite, roches argileuses, sables. Dans ces derniers, la qualité de nos méthodes d'imagerie nous ont permis d'étudier les mécanismes à l'échelle du grain, par une description exhaustive de la cinématique de chaques grains constituants l'échantillon. Nous avons montré que la rotation des grains à l'intérieur de la bande jouait un rôle crucial.

Dans nos travaux expérimentaux, nous avons mis en œuvre des techniques ou installations expérimentales modernes voire même tout à fait innovantes. Nous utilisons de manière courante les essais mécaniques *in situ* sous rayons X pour réaliser de la tomographie RX pendant les essais, initialement à l'ESRF et maintenant dans notre tomographe de laboratoire. Nous avons développé un appareil d'essai triaxial vrai pour les roches avec dispositif de visualisation de l'échantillon en cours de chargement, prototype unique à l'échelle internationnal. Nos méthodes d'imagerie, en 2D ou en 3D (en volume), sont systématiquement associées à du traitement d'images par corrélation, afin de calculer la transformation permettant de passer d'une image à une autre, et d'en déduire le champ de déformation associé à cette transformation. Cette combinaison d'outils est particulièrement pertinente pour étudier la localisation de la déformation, et permet d'éviter de fausses interprétions d'essais qui négligeraient cette localisation de la déformation. On l'aura compris, nous nous intéressons particulièrement à la caractérisation fine des *processus évolutifs* dans le temps, pour décrire la transition entre un mode de déformation diffus à localisé.

Nous n'avons pas fait état dans ce mémoire de tout un travail effectué sur l'étude des couplages hydro-mécaniques dans les roches argileuses, très faiblement perméables, et en particulier du lien entre rupture et évolution des propriétés de transfert. Ce sujet est expérimentalement difficile, il est néanmoins d'actualité car nombre de problèmes de l'ingénieur en géomécanique implique ce type de roche : problématique du stockage de déchets nucléaires dans les couches géologiques profondes, stockage de dioxyde de carbone en profondeur, forages pétroliers, etc... Ce domaine est peu souvent abordé dans la littérature, notre expertise s'est fortement consolidée ces dernières années, en parallèle avec d'autres équipes de recherche européennes dans le cadre de collaborations et projets conjoints. Nous avons à présent une assez bonne confiance dans nos mesures et pensons aboutir à une bonne compréhension des phénomènes de couplages et localisation dans les années à venir.

Sur le plan de la modélisation, nos travaux ont consolidés les travaux antérieurs dans le cadre des milieux enrichis, dits de second gradient, développés pour modéliser proprement la localisation de la déformation (présence d'une longueur interne au modèle pour limiter les dépendances vis-à-vis du maillage). Nous avons étudier la rôle de la loi constitutive sur la réponse post-localisation, en particulier de l'effet du durcissement ou du radoucissement dans la bande, pour interpéter la transition fragile-ductile de la rupture. Nous nous sommes par ailleurs intéressé à la question épineuse de la non unicité des solutions, et avons fait un parallèle entre non unicité et non reproductibilité des expériences en laboratoire dès lors que la localisation apparait. Trouver une solution à un problème n'est plus suffisant, il convient de se poser la question de la multiplicité éventuelle de solutions.

Nos projets de recherche sont en continuité avec les travaux entrepris ces dernières années, que nous pouvons décomposer en quatre parties : étude de la localisation de la déformation, études des couplages hydro-mécaniques, micromécanique des géomatériaux, comportement et localisation dans les matériaux non saturés.

**Localisation de la déformation** L'étude initiée à l'aide de notre nouvel appareil triaxial vrai pour roches va être poursuivi. Grâce au dispositif de visualisation de l'échantillon en cours d'essai, nous pouvons analyser en continu l'évolution du champ de déformation. C'est un élément essentiel pour pouvoir interpréter le comportement post-localisation dans les géomatériaux. Notre objectif est la prise en compte explicite de la localisation dans ce régime de comportement. Nous pouvons également combiner aux mesures de champ les mesures de perméabilité au travers l'échantillon pour mettre en évidence le rôle de la localisation ou fissuration dans l'évolution des propriétés de transfert d'un domaine d'étude considéré.

A ces travaux expérimentaux innovants, nous allons associer des outils de modélisation très performants pour modéliser le régime localisé, par des approches en milieux enrichis. Notre projet est le rapprochement intime entre expériences et modélisations avancées pour développer une méthodologie d'identification des modèles enrichis, en s'appuyant sur les méthodes de mesure de champs cinématiques à partir des expériences. L'idée est d'identifier la loi de comportement dans les bandes, qui n'est pas accessible directement, mais qui pourtant contrôle fortement la réponse d'une structure en présence de localisation. Ce travail vient de commencer dans le cadre d'une thèse de doctorat.

Nos premier résultats expérimentaux ont montrés, du moins pour certaines roches, que la rupture se développait dans un premier temps par une localisation de la déformation, puis dans un second temps par une fissuration s'initiant à l'intérieur de la bande de localisation. Ces observations méritent à notre sens des approches théoriques nouvelles de la rupture. Savoir modéliser proprement à la fois localisation et fissuration nous semble une piste de travail pertinente. Cela nécessitera de travailler dans le contexte des milieux de second gradient et d'y incorporer des éléments nouveaux pour décrire la fissuration.

**Couplages hydro-mécaniques** Nous l'avons déjà dit, nous avons développé nos protocoles d'essais dans les roches saturées et très faiblement perméables. Ce sujet est difficile et nous avons à présent une assez bonne confiance quant à nos mesures. Nous pensons là-aussi aboutir à une bonne compréhension des phénomènes de couplages et localisation dans les années à venir.

Par ailleurs, nous souhaitons mettre en place de nouvelles méthodes, basées sur l'imagerie 3D, pour estimer le champs de perméabilité dans un échantillon en présence d'une localisation, pour mettre en évidence le rôle éventuel de drain ou de barrière d'écoulement de la bande. Ces approches combineront mesures en volume de front d'écoulement, la modélisation d'expériences de drainage et l'analyse inverse pour relier les deux.

**Micromécanique des géomatériaux** La tendance récente de nos travaux expérimentaux est d'aller vers une description des mécanismes à la petite échelle. Nous l'avons vu pour les milieux granulaires, où il est désormais possible, en combinant tomographie à rayons X et corrélation d'image, d'obtenir une description exhaustive de la cinématique de tous les grains composant un échantillon. Nous l'étendons actuellement aux roches de type granulaire cohésive (genre grès). Les méthodes sont en place, les travaux se poursuivent. Le développement récent des méthodes d'imagerie, avec en particulier l'amélioration des résolutions spatiales, devrait nous permettre dans les années à venir d'étendre cette étude des micromécanismes de déformation à la petite échelle dans des matériaux à microstructure fine, par exemple pour les roches argileuses. Le projet est ambitieux, il nous semble pertinent.

Il apparait alors de plus en plus judicieux d'aller aussi dans la direction de la modélisation multi - échelles pour les géomatériaux, c'est un des objectifs pour les prochaines années. En particulier, l'homogénéisation numérique offre une grande souplesse dans le choix de la microstructure pour obtenir des lois macroscopiques résultant directement d'un calcul à la petite échelle. Il y a là une perspective de rapprochements intéressants avec les observations expérimentales et la modélisation. Un travail de thèse va commencer sur l'association d'une approche double échelle numérique prenant en compte le couplage hydro-mécanique à l'échelle microscopique avec le formalisme de second gradient à l'échelle macroscopique.

**Comportement des matériaux non-saturés** La présence de plusieurs phases dans la porosité d'un matériau (gaz-liquide ou deux liquides non miscibles) induits des effets capillaires qui peuvent modifier le comportement du matériau. Assez peu de travaux ont été réalisés sur les intéractions avec le phénomène de localisation. Les forces capillaires dépendent de la microstructure du matériau, du degré de saturation des phases fluides et de la succion (différence de pression entre les phases fluides). On sait que lorsqu'il y a localisation de la déformation, il y a généralement variation de la porosité du matériau et changement de microstructure (plus ou moins fort selon les matériaux). Dans ces conditions, la localisation de la déformation est associée à un écoulement des phases fluides et un changement des forces capillaires, ce qui implique un couplage fort entre comportement non saturé et condition de localisation. Nous projettons d'étudier expérimentalement ces phenomènes dans un sable, en tant que matériau modèle, en s'appuyant sur nos outils d'imagerie pour visualiser l'évolution de l'organisation des phases fluides. Ces informations seront utilisées pour la modélisation, soit dans un cadre de milieu continu, soit dans un cadre de milieu discret.

On l'aura compris, la combinaison entre expérimentations et modélisations est un élément important de mon activité et que je tiens à maintenir dans les années à venir.

# Sélection de publications :
# Travaux Expérimentaux

PERGAMON
International Journal of Rock Mechanics & Mining Sciences 37 (2000) 1223–1237
International Journal of
Rock Mechanics
and Mining Sciences
www.elsevier.com/locate/ijrmms

# Experimental characterisation of the localisation phenomenon inside a Vosges sandstone in a triaxial cell

P. Bésuelle[a,b,*], J. Desrues[b], S. Raynaud[c]

[a] Laboratoire de Géologie, Ecole Normale Supérieure, 24 rue Lhomond, F-75231 Paris Cedex 05, France
[b] Laboratoire 3S-IMG, Grenoble, France
[c] Laboratoire Hydrosciences, Montpellier, France

Accepted 12 September 2000

## Abstract

The behaviour of a Vosges sandstone is studied, including quasi-homogeneous deformation, incipient strain localisation and localised rupture. The homogeneous behaviour is first presented from about 60 experiments in triaxial compression with two slenderness ratios ($H/D = 1$ and 2), in triaxial extension, and in isotropic compression. A large range of confining pressures (0–60 MPa) is investigated, showing a significant evolution of material response. A strong positive dilatancy is observed at lower pressure, decreasing to become negative (contractancy) at higher pressure. Simultaneously, the strength decreases with increasing confining pressure. The localisation is described in terms of onset of localisation, shear band orientation and patterning. The volumetric strain is analysed inside the band with computed X-ray tomography and electron microscopy. We observed the formation of a gouge layer, and around it, a dilating shear band at lower confining pressure and a compacting shear band at higher pressure. This compacting shear band seems to be the transition mechanism between the brittle and semi-brittle regime. © 2000 Elsevier Science Ltd. All rights reserved.

## 1. Introduction

Failure in porous soft rocks is associated in most cases with the phenomenon of localisation, at least under conditions of low stress and low temperature. If we observe the behaviour of the rock at a macroscopic scale, these failure zones can be considered as strain localisation bands. This description of failure is classical in soils (sands, clays). In laboratory tests on the latter materials, one usually observes a stress peak in the specimen's response, while the strain is concentrated in shear bands. Outside the bands, the strain is very small [1].

Following these experimental observations, failure in soils can be considered as generally associated with the development of shear bands, which in turn explains the strain softening of the specimen's response. The softening step in rocks can be stable or unstable depending on the elastic energy stored inside the specimen [2]. To predict the onset of appearance of the bands the so-called bifurcation theory has been developed by Rice [3] and Rudnicki [4] (see also [5] for a review). In this theory, the shear bands are treated as a problem of instability of the mechanical system. This approach has subsequently been intensively developed for soils [6–9], and for soft rocks [10–13]. From an experimental point of view, a macroscopic description of the localisation in porous soft rock like sandstone, tested at laboratory conditions, is necessary.

However, the microscopic description of the localisation phenomenon cannot be ignored. Localisation bands in soft porous rocks are defined at the micro-scale by a strong increase of the local density of microcracking in comparison to the material outside the bands [14–16]. Inside, the material becomes strongly damaged, which rapidly degrades its mechanical characteristic (local strain softening). Therefore, the behaviour of the bands strongly influences the specimen's response, and it is important to evaluate it. It is well recognised that dilating volumetric strain can take place inside the shear bands, but the existence of contractant shear bands is still under question. Nevertheless, contractant shear

---

*Corresponding author. Tel.: +33-1-4432-2209; fax: +33-1-4432-2000.
*E-mail address:* besuelle@geologie.ens.fr (P. Bésuelle).

1365-1609/00/$ - see front matter © 2000 Elsevier Science Ltd. All rights reserved.
PII: S1365-1609(00)00057-5

bands have been observed in soils [17,18], in natural geological structures [19] and in laboratory experiments on soft rocks [20–22].

In this paper, we analyse the behaviour of a porous Vosges sandstone under a range of stress, under axisymmetric test conditions (compression, extension and isotropic). Firstly, the homogeneous behaviour is presented, which shows a strong change from the low-pressure range, with a dilating volumetric strain at failure, to the high-pressure range (60 MPa) with a contracting behaviour at failure. Then, a detailed description of the localisation is presented, analysing the following characteristics: the onset of localisation, the orientation and the patterning of the shear bands, and their volumetric behaviour, using computed X-ray tomography (CT) and scanning electron microscopy (SEM). These characteristics change strongly with confining pressure.

## 2. Experimental device

### 2.1. Triaxial apparatus

The triaxial cell was designed to be autonomous, which means that it does not require an external load press. The axial load device is integrated into the cell. This cell is able to sustain a confining pressure up to 60 MPa and a deviatoric pressure up to 270 MPa. The apparatus (Fig. 1) comprises: a lower cell (1), which allows us to apply a confining pressure and a back pressure to the specimen (2); and an upper cell (3), hosting the axial load self-compensated piston (4). The piston is pushed from the top chamber (5) by oil pressure. The pressure is transmitted to the specimen with a multiplication of about 4.5 due to the surface ratio of the piston. The two cells are joined by eight bolts (6). In the lower cell, a neoprene membrane (thickness of 0.7 mm) (7) is placed around the specimen to avoid a confining oil penetration. Both upper and lower load caps (8) are connected to drainage lines. Different pore pressures can be imposed at the ends of the specimen, in order to allow fluid flow and measurement of the rock permeability under load. Two intermediate smooth enlarged plates (9) are placed between the specimen ends and the loads caps. These plates are hardened by thermal treatment and rectified; they are used to insure a frictionless interface and avoid edge effects. We use two internal tight connectors (10) each with 12 signal conductors each other for the internal instrumentation. A steel sheath (11) protects a thermo-couple used for measuring oil temperature.

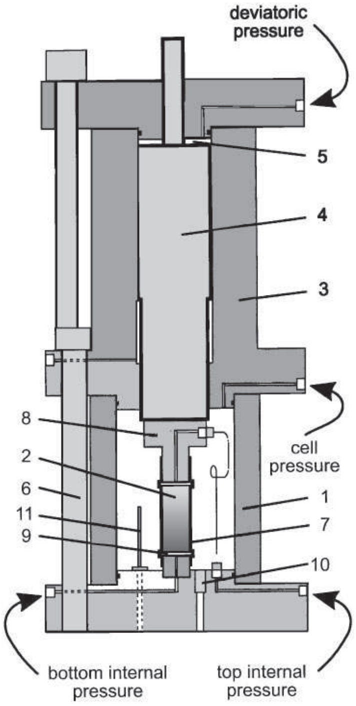

Fig. 1. Schematic of the triaxial cell: (1) lower cell, (2) specimen, (3) upper cell, (4) self-compensated load piston, (5) deviatoric pressure chamber, (6) bolts, (7) neoprene membrane, (8) load caps, (9) enlarged platen, (10) internal tight connectors, (11) steel sheath.

The four pressures (deviatoric, cell, top and bottom pore pressure) are supplied by four identical and independent generators. A generator consists of a piston moving in a pressure chamber. A DC electrical motor controls a screw-nut device and translates the piston. Each pressure generator is guided by an electronic regulator receiving an analogical signal from an external transducer. The regulators are programmed by a PC computer. The volumes of the water injected by the two pore pressure generators are measured by an angular transducer on the motors. The deviatoric pressure is regulated from a LVDT signal measuring the axial displacement of the cell piston. Such displacement control is necessary in order to experimentally follow the post-peak portion of the specimen response. The mechanical rigidity of the cell with respect to the axial load applied on the specimen is 0.45 MN/mm.

### 2.2. Instrumentation

The axial and lateral strains are measured with three axial transducers and four radial transducers which are regularly spaced around the specimen (120 and 90°, respectively, between each transducer). They were designed on the principle of a flexible strip equipped with strain gauges [23,24] (Fig. 2), inspired from the LDT developed in Japan [25].

An axial transducer measures the axial shortening between two points on the membrane, corresponding to the middle of the pseudo-hinged attachment glued on the membrane. An axial strain is deduced from the shortening divided by the initial distance between the

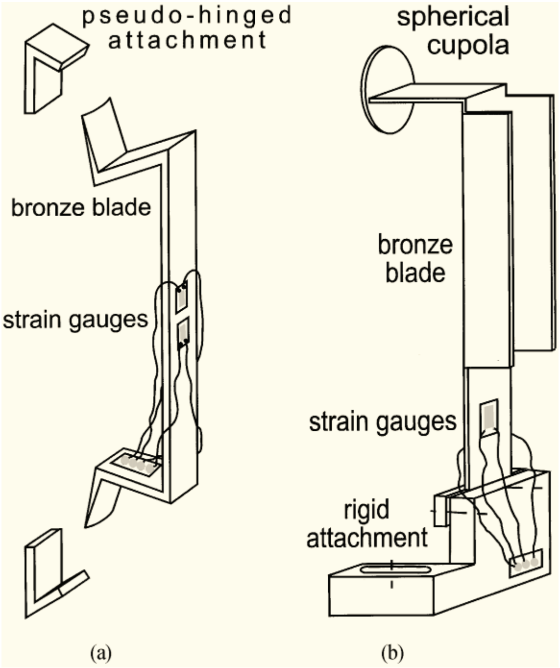

Fig. 2. Schematic of the internal instrumentation for the (a) axial and (b) radial strain measurement. The flexible strips are equipped with strain gauges and deformation of the specimen induces changes in the electrical response of the gauges.

two points. The mean axial strain is defined as the average of the three measurements from the three axial transducers.

A radial transducer measures the lateral displacement of the point of contact between the transducer and the membrane, at the mid-height of the specimen. A lateral strain can be computed from two opposite transducers as the sum of the two displacements divided by the initial diameter. Therefore one has two lateral strains in two orthogonal directions. The difference between two opposite displacements is also computed to obtain the displacement of the centre of the mid-height section of the specimen. This displacement can be non-zero if the lateral deformation of the specimen is not symmetrical with respect to the specimen's axis. One obtains a measure of the displacement of the centre in two orthogonal directions and so a radial orientation of this displacement.

## 3. Tested rock

The tested rock is a natural sandstone coming from the Woustviller quarry in the Vosges mountains, France. It is a pink quartz sandstone (quartz = 93%), with a few percent of feldspar and white mica. The sandstone is poorly cemented; the cohesion is due to the interpenetration between grains. The porosity is about 22%. The dimension of grains measured by optical microscope is between 100 and 300 μm. To estimate the true size of grains in three dimensions, we use the statistical factor of $\frac{3}{2}$ which, for spherical grains [26], can be rigorously derived. The dimension of grains fluctuates between 150 and 450 μm with a mean value of about 300 μm. Specimens are tested dry, after exposing them to a temperature of 100°C for a few days.

## 4. Experiments

Specimen ends are rectified to have a good parallelism, better than ±0.04 mm [27]. To reduce the friction at the ends, a mixture of vaseline and stearic acid was used [28]. Specimens are loaded at a strain rate of $10^{-5}\,\mathrm{s}^{-1}$ from nearly unconfined conditions to a confining pressure of 60 MPa. The deviatoric stress is computed as the major principal stress minus the minor principal stress. Specimens are tested with two types of test (compression and extension tests), from an isotropic stress state up to failure. During the compression test, the lateral stress is equal to the confining pressure, and is kept constant while the axial stress is increased, the latter stress being the major principal stress. During the extension test, the lateral stress is also kept constant, but the axial stress is decreased; this is the minor principal stress. At the beginning of the extension test, the axial load is positive (compressive force) but can become zero and then negative. Depending on the material and on the initial isotropic stress, in some tests failure in extension can occur with a compressive axial stress, and in other tests failure in extension can be achieved only with a tensile stress.

### 4.1. Compression tests

The behaviour of the sandstone is presented in Fig. 3. The stress–strain curves show that the loading modulus and the deviatoric strength at stress peak increase with confining pressure. However, at 60 MPa the response is similar to the response at 50 MPa, up to the stress peak which occurs earlier at 60 MPa. The deviatoric strength is smaller than at 50 MPa. As far as volumetric curves are concerned (lower Fig. 3), one observes first an initial contractancy at all confining pressures. Then, up to the peak stress, depending on the confining pressure, one gets either dilatancy (stronger at low confining pressure), or contractancy (small, only at 60 MPa). Similar evolution has been observed on porous rocks (sandstone and limestone) for example by Cornet and Fairhurst [29]. After peak stress, the measurements must be considered insignificant, at least in terms of the global response. The curve of strength at failure in the Mohr diagram is strongly non-linear (Fig. 4), which is classical for a number of sedimentary rocks (e.g. [30]). Indeed,

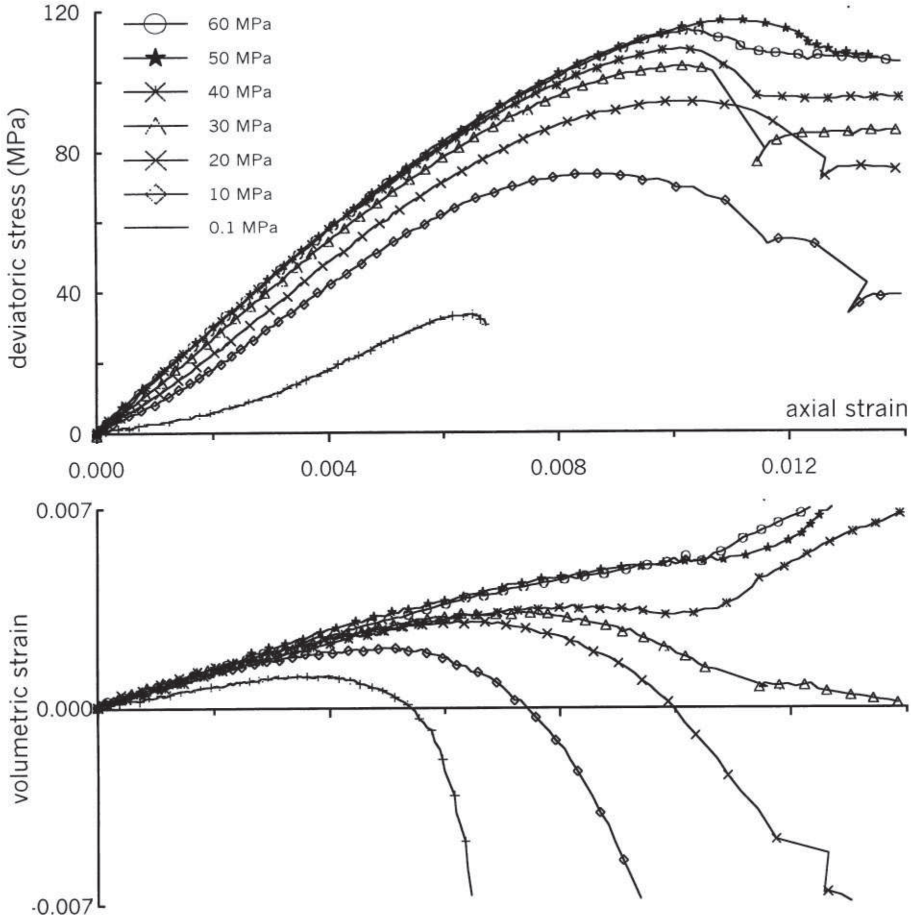

Fig. 3. Deviatoric stress and volumetric strain versus axial strain in compression tests for the $H/D = 2$ specimens.

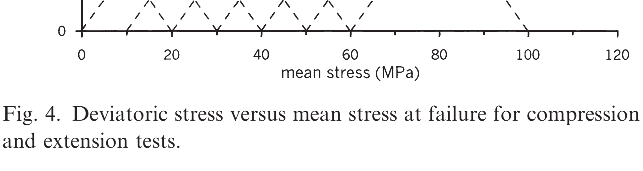

Fig. 4. Deviatoric stress versus mean stress at failure for compression and extension tests.

the slope corresponding to failure for a confining pressure between 50 and 60 MPa is slightly negative.

A parallel series of tests have been performed on specimens with a slenderness ratio of 1. The strength of the shorter specimens $H/D = 1$ is in general greater by 10% than for the conventional specimen $H/D = 2$ (Fig. 4). This seems to be due to the residual friction at the ends of the specimen, which remains finite despite the lubrication of the specimen's ends, and disturbs the shorter specimens more than the longer ones.

### *4.2. Extension tests*

In the investigated range of confining pressure, the failure of Vosges sandstone in triaxial extension does not occur with positive axial stresses. In order to get failure in extension with positive axial stresses, higher values of confining pressure would be necessary for this material. A solution to this problem is to use specimens having a so-called "bobbin-shape", as already suggested by Brace [31] and Millar and Murray [32]. With this setup, it is possible to have a negative axial stress in the middle portion of the specimen while having a positive stress at its ends. The axial stress $\sigma_c$ in the central part of the specimen is derived from the axial stress at the end of the specimen $\sigma_e$ and the confining pressure $\sigma_{cp}$ by: $\sigma_c = \sigma_e - (\sigma_{cp} - \sigma_e)(\alpha^2 - 1)$ where $\alpha$ is the ratio of the diameter at the end by the diameter in the middle part of the specimen ($\alpha > 1$). In the present experiments, the diameter and height of the middle portion of the specimen are 30 mm and about 45 mm, respectively; the total height of the specimen is 75 mm and the larger

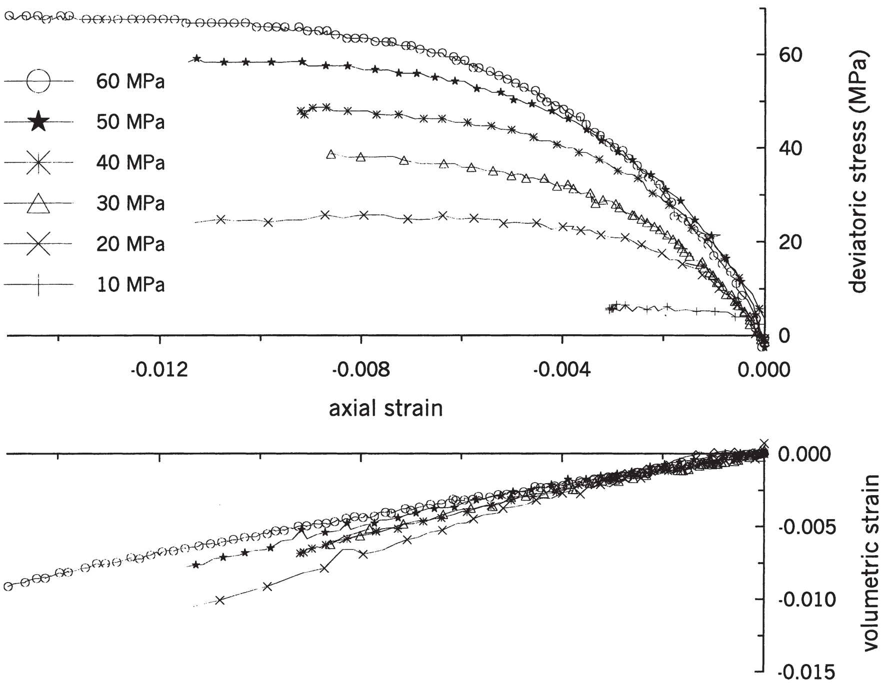

Fig. 5. Deviatoric stress and volumetric strain versus axial strain in extension tests.

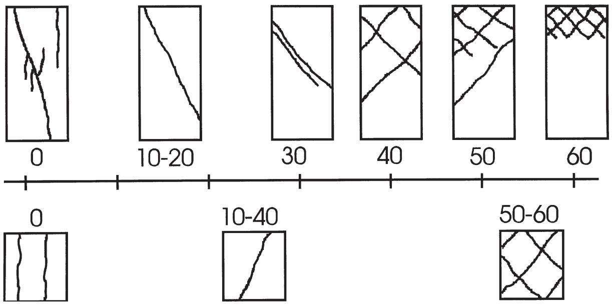

Fig. 6. Observed shear band patterns versus confining pressure for compression test with $H/D = 2$ and 1. The angle of the bands with respect to the major principal stress increases with the confining pressure, and bands become more and more numerous and close.

Fig. 7. Sandstone specimens tested in compression, at low (right) to high (left) values of the confining pressure.

diameter 40 mm. The bobbin-shape was obtained by turning with a carbide tool to achieve a good surface, as less perturbed as possible. Strains are measured on the central portion of the specimen using the measuring devices described above.

The behaviour of the sandstone in the extension tests is shown in Fig. 5. The axial stress at failure for the different confining pressures are the same, about $-10$ MPa in traction, which implies a quasi-linear failure curve in the Mohr diagram. However, a test performed in a stronger cell at 100 MPa confining pressure shows that the curve becomes non-linear at higher stress, such as for the compression test (Fig. 4). The volumetric dilatancy is quasi-linear with the axial strain, and depends only slightly on the confining pressure.

### 4.3. Failure pattern

In all the tests, specimens failed with the appearance of one or several shear bands through the specimen. Typical patterns of shear bands observed at the end of the tests are shown schematically in Fig. 6 (see also Fig. 7). We observe a combination of axial splitting and inclined failure surfaces at zero confining pressure. At a confining pressure $\geqslant 10$ MPa, inclined white lines are visible on the lateral surface of the specimen. Similar observations were made by Ord et al. [16], who described these lines as "white, chalky zones" and identified them as the trace of shear bands or failure surfaces. The number of these failure surfaces increases with confining pressure. Between 10 and 30 MPa, there are one or two parallel bands visible throughout the specimen. Conjugate shear bands occur from 40 to 60 MPa, and the distance between the bands decreases with pressure, as the number of shear bands increases. The orientation of the shear bands with respect to the loading axis increases with confining pressure, and for the higher pressure, all the bands are concentrated in half of the specimen. The observed patterns are similar in the short specimens ($H/D = 1$) with respect to the classical specimens, but the number of shear bands is smaller for the same confining pressure.

The angle between the shear band and the axial direction (major principal stress) is measured from the trace appearing on the membrane after the compression tests. The angle is very sensitive to the pressure, and increases almost linearly from about 35° at 10 MPa confining pressure to 55° at 60 MPa, with a slope of about 0.29°/MPa of mean stress (Fig. 8). The angle in the short specimens ($H/D = 1$) is smaller than in the classical specimens ($H/D = 2$), but the slope of the evolution of the angle versus the mean stress is equivalent. The friction at the ends of the specimen could explain this difference, since the local stress is disturbed inside this zone, and this effect is more important on a short specimen [33].

The evolution of the failure pattern in extension tests is similar (Fig. 9). However, the mean stress at failure is less than the mean stress at failure by compression for the same confining pressure. This is due to the fact that in extension tests, the axial stress is reduced up to failure, while in compression tests, it is increased. Thus, in extension tests we observe the formation of a unique shear band through the specimen, as observed in compression tests at the same mean stress. The orientation with respect to the major principal stress (horizontal direction) increases with confining pressure (Fig. 8). In this case, the failure of the specimen can be suggested to occur by shearing. At lower confining pressure, the band is parallel to the major stress direction, like axial splitting in compression, which suggests failure by an extensional fracture. In most of the tests, the shear band intercepts the surface of the specimen at the place where the diameter changes, which is likely to be due to stress concentration effects.

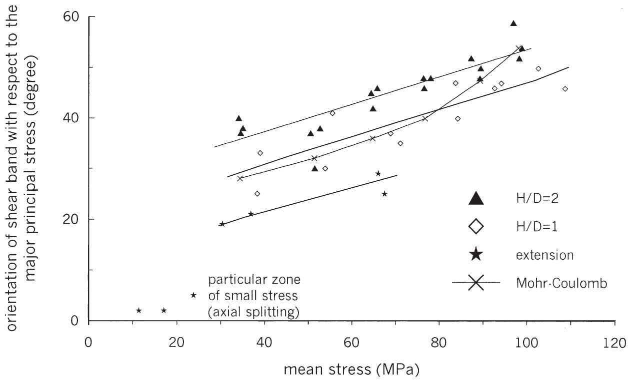

Fig. 8. Orientation of the shear bands with respect to the major principal stress axis versus the mean stress at failure, for compression ($H/D = 1$ and 2) and extension test. Solid line shows the prediction with the Mohr–Coulomb criterion: $\theta = 45° - \phi/2$, for the $H/D = 2$ compression tests.

## 5. Detection of localisation

Prospective precursors of failure have been studied using the independent axial and lateral displacement measurements on the specimen. Two types of detection have been compared: the first one uses the comparison of the three axial measures, and the second one uses the comparison of the four lateral transducers.

We investigated the difference between each of three axial transducers and the mean axial strain, which is defined itself as the average of the three axial measurements. These differences should be equal to zero if the strain field is perfectly homogeneous and the three strains are the same, which is not the case in reality. If the differences stay constant during part of the specimen loading, then the axial strain field can be considered to be reasonably homogeneous in this part of the loading.

In general, the three axial strains diverge strongly in the initial part of the test (Fig. 10), due to the bedding error effects (small residual default of parallelism between the ends of the specimen and the load caps). After this initial adjustment, the differences are fairly constant, up to the onset of a strong divergence. This threshold is considered as the point of loss of homogeneity of the strain field [34]. It indicates the limit after which the specimen's response can no longer be

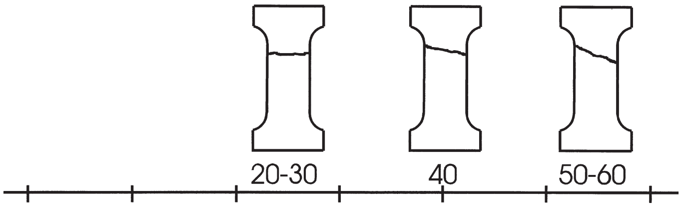

Fig. 9. Observed shear band patterns versus confining pressure for extension test.

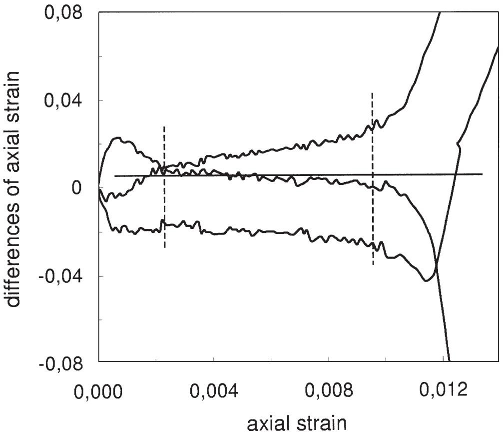

Fig. 10. Example of the evolution of the three differences of the axial strain measurements with respect to the mean strain computed as the average of the three measurements. The first part of the test shows a divergence corresponding to the setting up of the specimen, the second part shows a homogeneous axial strain field, and the last one shows a strong divergence which is a loss of the homogeneity.

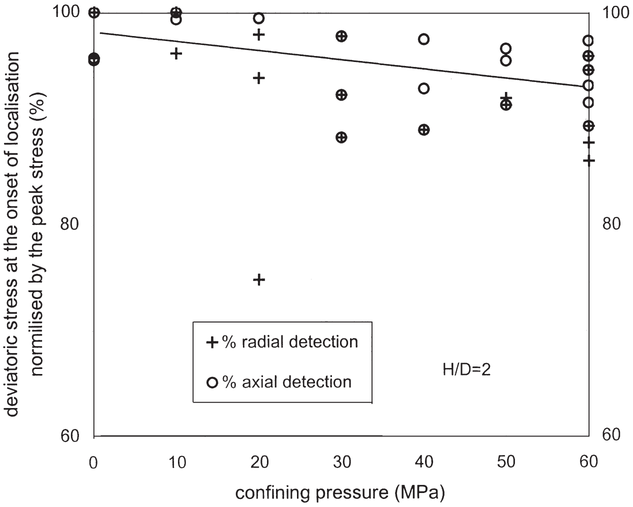

Fig. 11. Evolution of the ratio of the deviatoric stress at the onset of loss of homogeneity to the deviator at the stress peak, versus the confining pressure. The onsets are detected independently with axial and lateral transducers.

considered as representative of the material behaviour, but of a structural response of the specimen [35,36].

The evolution of the two perpendicular diameters defined by the four lateral transducers is also compared. If the strain field is homogeneous, the radial strain evolution of one diameter is linear with respect to the other radial strain, and even equal for a transversely isotropic material. We consider than the radial strain field become inhomogeneous when the evolution becomes non-linear [35,37]. For a clearer observation, we computed the root mean square of the linear regression of the previous evolution along the loading. This measure shows a threshold when linearity is lost.

Furthermore, we observed the displacement of the centre of the mid-height section of the specimen, computed from the difference between the two opposite lateral transducers. This displacement is initially small before increasing to take on a preferential azimuthal direction. This direction is, in most cases, perpendicular to the shear band observed after the test. The onset corresponds to a loss of symmetry of the lateral deformation of the specimen with respect to the axis of the specimen, and we compare it with the two first observations (axial and radial divergence).

The deviatoric stress at the loss of homogeneity, normalised by the deviatoric peak stress, is represented in Fig. 11. This onset occurs at a progressively lower normalised deviatoric stress as the confining pressure is increased. The evolution of the onset with respect to the confining pressure is almost linear.

## 6. Shear band observations

Some specimens tested up to the residual stress step were observed unloaded using computed X-ray tomography (CT). This technique provides a spatial view of the local density distribution inside the specimen and reveals the localised zones which have a density different from the rest of the specimen. Afterwards, the same specimens were observed by microscopy to quantify the deformation of the microstructure.

### 6.1. X-ray CT apparatus

As far as the CT technique is concerned, only a brief summary is given here. More details on the apparatus used in the present study are given by Latiere et al. [38] and Raynaud et al. [39].

This non-destructive method is based on the measurement of the attenuation of a X-ray beam through the body. The attenuation is physically proportional to the electron density inside the body, which is itself proportional to the mass density if the material is chemically homogeneous.

A set of 1D projections of the attenuation through a slice of the specimen is measured for different angular positions (Fig. 12). The 2D slice is reconstructed by a mathematical algorithm. From several adjacent slices, the 3D specimen can be reconstructed to visualise 2D projections on any plane, in particular on a parallel-to-axis plane.

In the ND8000 apparatus, each pixel represents a $0.7 \times 0.7\,\mathrm{mm}^2$ projected onto the medium plane of the slice which has a thickness of 2 mm. The measurement of the local density in one or several pixels is possible. Nevertheless, in the case of thin structure with a high-density gradient such as a shear band, the averaging in a pixel and the dispersion of the CT response disturb this measurement [40,41]. An appropriate analysis should be necessary to validate the density measurements in the shear bands. In this study, we used the CT apparatus essentially for a qualitative response.

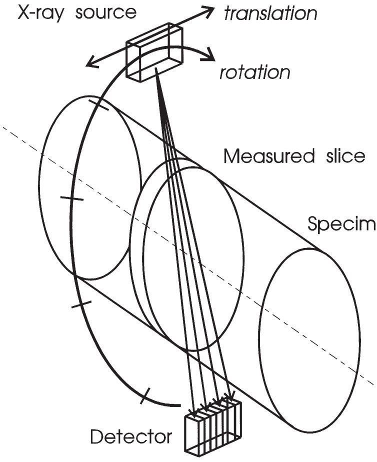

Fig. 12. Schematic of the scanner. X-ray beam translates and rotates around the specimen to characterise a 2 mm thickness slice.

### 6.2. CT observations

One specimen tested at a confining pressure of 30 MPa up to an axial strain of 0.019, and one tested at 50 MPa up to an axial strain of 0.015, have been observed by CT. Fig. 13a–c shows three slices of the specimen tested at 30 MPa, at different positions along the specimen's axis. The shear band appears as a black area, which implies that it has a higher porosity than the material outside the band. The position of the band in the slice changes in the three slices due to the inclination of the shear band relative to the specimen's axis. The shear band is not a perfect plane as we can see in Figs. 13a and b, and the density in the band is not homogeneous. In the central part of the specimen (Fig. 13b), the density in the band far from the surface of the specimen is higher than the density near the surface.

The reconstruction of the specimen in a plane parallel to the axis and perpendicular to the shear band is presented in Fig. 13d. The view shows a heterogeneity of the specimen where the top half is less dense than the lower half. The heterogeneity, which is not visible by simple observation of the specimen, existed prior to the test, and the densities measured by water impregnation were 1.955 and 1.982 g/cm$^3$ in the upper and lower half,

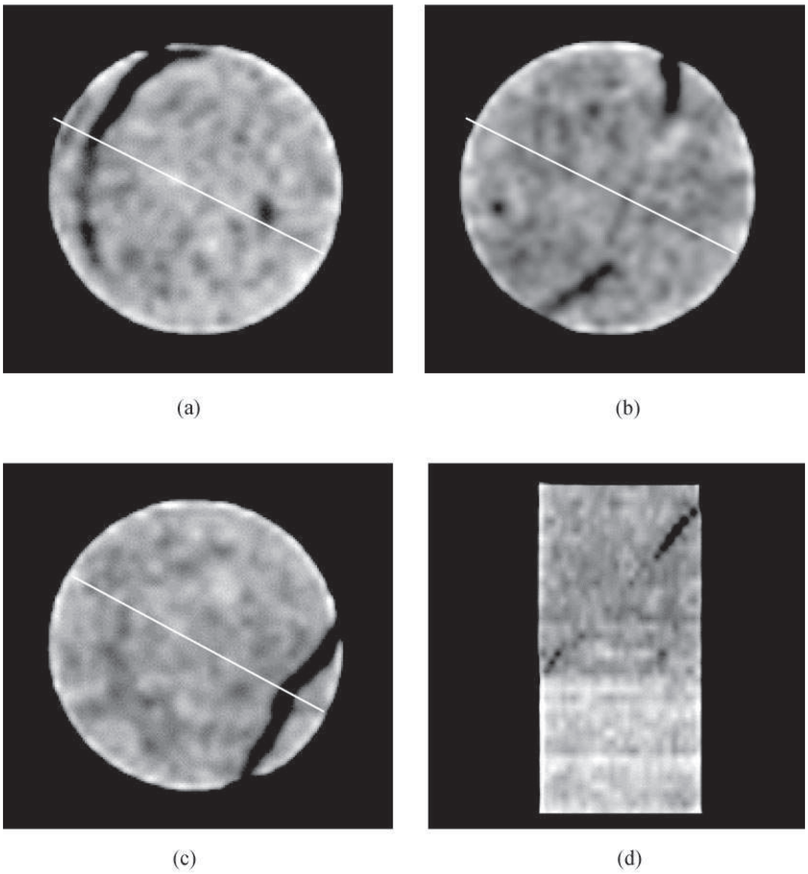

Fig. 13. Localisation pattern inside a specimen tested at a confining pressure of 30 MPa in compression. Dark area corresponds to a shear band more porous than the mean porosity of the specimen. The white lines in (a), (b) and (c) show the position of the plane of reconstruction (d).

respectively. The interface between the two halves seems to have had an important role for the position of the shear band. In all specimens, shear bands take place preferentially in the less dense part which is likely to have a lower strength. In the plane of Fig. 13d, the shear band seems to be linear, with an angle with respect to the specimen's axis equal to the angle measured from the trace on the neoprene membrane used for the test.

Fig. 14 shows the same views for the specimen tested at 50 MPa. Whereas in the previous specimen, only one (maybe two parallel) shear band was visible from direct observation, in the present case the external observation of the specimen shows several conjugated shear bands (Fig. 6). However, the CT reconstruction (Fig. 14d) shows a single band. It is larger than the shear band of the preview specimen and not as well defined. In the core of the specimen, the density in the band is higher (lighter) than the material outside the band. On the other hand, near the surface of the specimen, the band has a lower density than outside the band (Fig. 14c). This predominance of one shear band over the others was also detected by the internal lateral transducers. Indeed, the displacement of the centre of the mid-height section of the specimen developed a preferential orientation slightly before the stress peak [42], with a likely orientation perpendicular to the azimuthal orientation of the principal shear band. This suggest that, if several shear bands take place before the stress peak, one of them may become kinematically dominant sometime after the initiation.

### *6.3. Microstructural measurements*

In the intact material, there is little cement and it is the lay out of the grains which provide the cohesion of the sandstone (Fig. 15). At the microscopic scale in the failed specimen, one observes intergranular as well as intragranular cracks. In Fig. 16, several bands of cracked grains (intragranular) can been distinguished. Due to the intensity of the cracks, grains can even be crushed, indicating a cataclastic deformation. A fracture exists inside a shear band in the specimen tested at 30 MPa, but it is suspected to have been created during the preparation of the thin section.

The thickness of the bands are in the range from 360 to 1200 μm. An intermediate zone exists around the bands between the band and the uncracked area which is only one or two grains thick (about 300–600 μm) and which contains fewer cracks (intra and inter-granular).

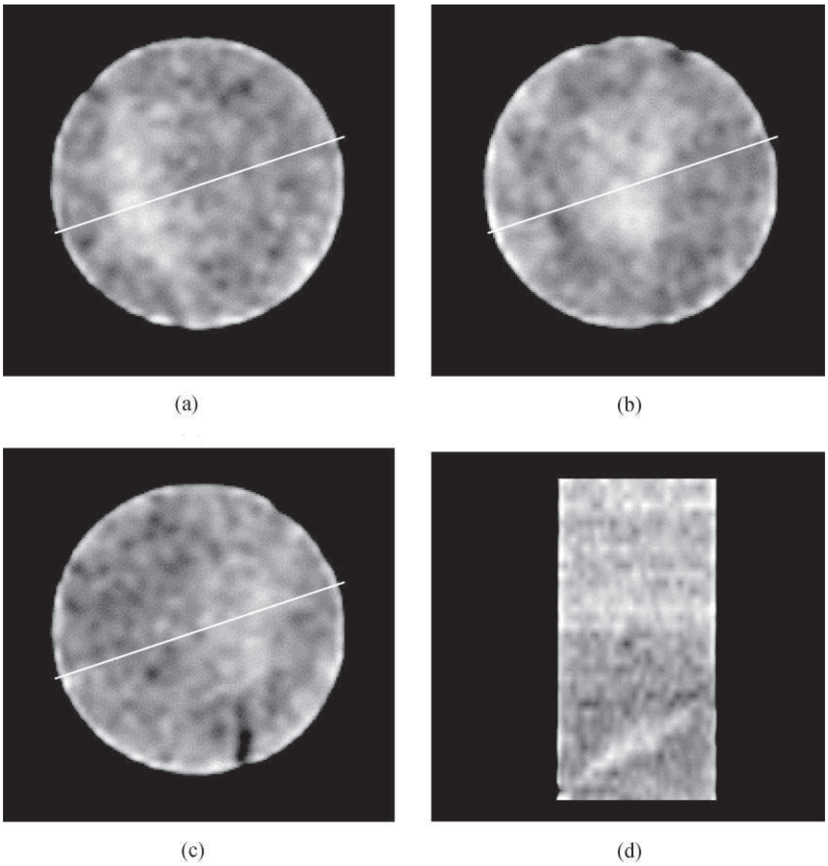

Fig. 14. Localisation pattern inside a specimen tested at a confining pressure of 50 MPa in compression. Light area corresponds to a shear band less porous than the mean porosity of the specimen. The white lines in (a), (b) and (c) show the position of the plane of reconstruction (d).

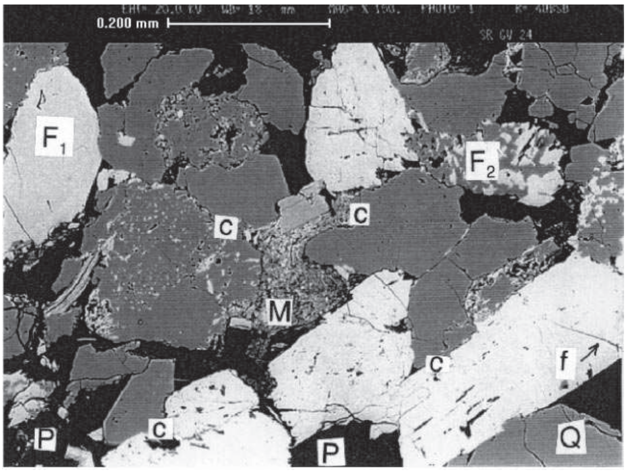

Fig. 15. Scanning electron micrograph of intact material. The interconnectedness of the grains improves the cohesion of the sandstone.

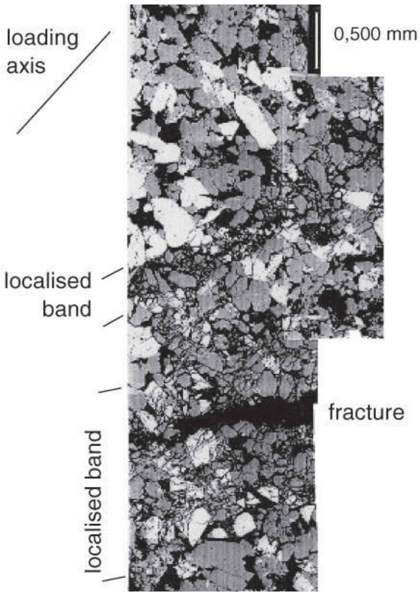

Fig. 16. Scanning electron micrograph of shear zone of the specimen tested at a confining pressure of 30 MPa. The bands are characterised by a cataclastic deformation.

The density of cracks have been measured as the number of cracks inside a 1 mm$^2$ with an optical microscope. The density decreases rapidly with the distance from the central part of the band (Fig. 17). In the shear bands, the statistical orientation of the cracks show a preferential orientation around the loading axis in the specimen tested at 30 MPa confining pressure (Fig. 18a). In the specimen tested at 50 MPa confining pressure there is no preferential orientation (Fig. 18b).

The porosity measured by mercury injection in pieces (about 1 cm$^3$ in size) of undeformed and failed specimens is about 20–22%, with the same peak of pore threshold size: 25 μm. At the cm$^3$ scale, deformation does not produce a significant variation of porosity in

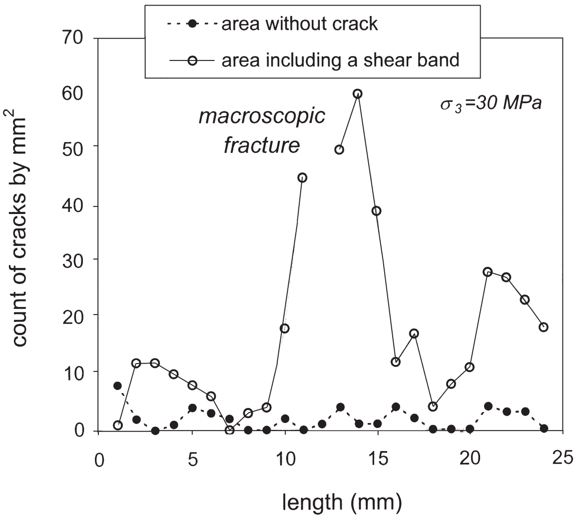

Fig. 17. Number of cracks by millimetre square in area including a shear band. $X$-axis is the length perpendicular to the shear band in millimetres.

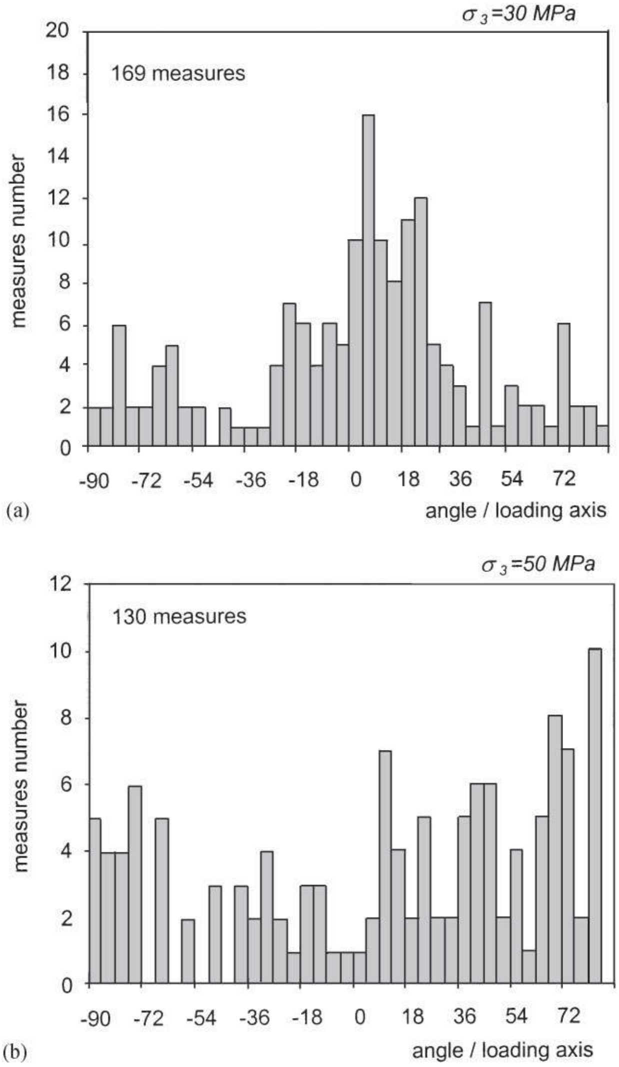

Fig. 18. Statistical orientation of the cracks with respect to the loading axis.

comparison with the resolution of the mercury injection measurement.

To measure the microscopic shear band porosity, the surface porosity has been measured with a scanning electronic microscope (SEM) and software; it is defined as the pore surface inside a 1 $mm^2$. The surface porosity far from the shear bands has a mean value of 25%.

For the specimen tested at 30 MPa, a shear band and a fracture are observed, characterised by a strong surface porosity over a thickness less than 1 mm in Fig. 19a. There is a transitional zone, in which the porosity is intermediate between the porosity inside the band and the porosity outside.

For the specimen tested at 50 MPa, several shear bands have been formed, and three of them with a strong porosity can be observed in Fig. 19b. Near the microscopic bands, the porosity is less than the porosity far from the bands, showing that a compaction mechanism exists in the localised zone between the dilating shear bands. Although this result seems contradictory, it is in fact consistent with the X-rays CT measurements which show an average contractancy in the localised deformation zone. Indeed, with CT, the dilating shear bands cannot be viewed because they are too thin (relative to the resolution of the apparatus). In this case, only one compacted zone appears in place of the shear band, resulting from the averaging of the thin dilating bands and the larger contracting ones.

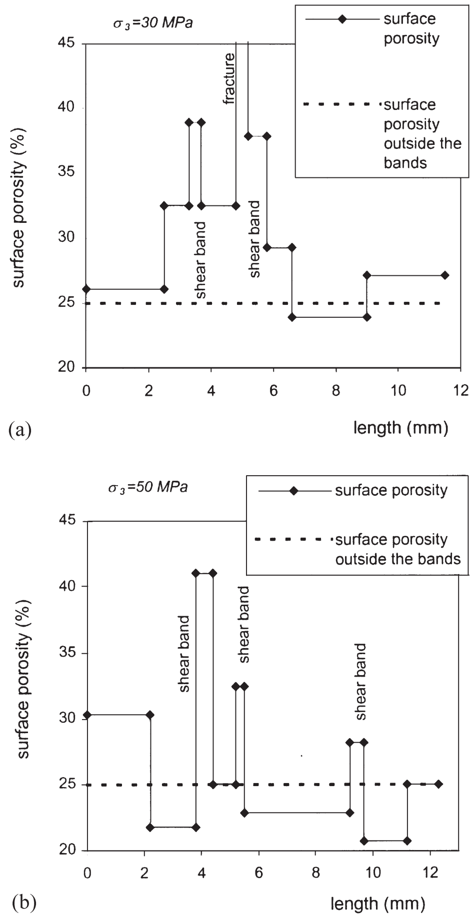

(a)

(b)

Fig. 19. Surface porosity near (solid lines) and far from (dotted lines) the shear bands.

The trapped porosity measured by mercury porosity is 69% of the global porosity of the intact specimen, and decreases to 58% in the specimen tested at 50 MPa confining pressure, and 47% of the global porosity in the specimen tested at 30 MPa confining pressure. These results show an increase of the connectivity of the pores during the tests.

## 7. Discussion

### 7.1. Shear band angle

The orientation of the shear bands with respect to the major principal stress can be predicted theoretically by the model of Mohr as: $\theta = 45^\circ - \phi/2$ where $\phi$ is the internal friction angle of the material [33]. This orientation corresponds to the plane of maximum stress vector obliquity. It is the most critical in terms of stress. Roscoe [43] has also discussed the orientation of $\theta = 45^\circ - \nu/2$, with $\sin(\nu) = -(\dot{\varepsilon}_a + \dot{\varepsilon}_l)/(\dot{\varepsilon}_a - \dot{\varepsilon}_l)$, where $\dot{\varepsilon}_a$ and $\dot{\varepsilon}_l$ are the axial and lateral strain rates (global) at the onset of localisation. This orientation corresponds to the plane embedding zero extension lines or the pure shear strain plane in the Mohr circle of strain transformation. Later, Arthur et al. [44] proposed the intermediate angle of $\theta = 45^\circ - \phi/4 - \nu/4$ on the basis of physical arguments. Several authors, e.g. Vardoulakis [45] or Vermeer [46], investigating the prediction of bifurcation theory for an elasto-plastic Mohr–Coulomb model, have shown that Arthur's orientation is approximately matched by the bifurcation prediction for this model.

In the case of the Mohr orientation, for a material with a non-linear failure envelope, $\phi$ should be defined as the angle of the failure envelope at the stress state corresponding to the failure (Fig. 20), which is the

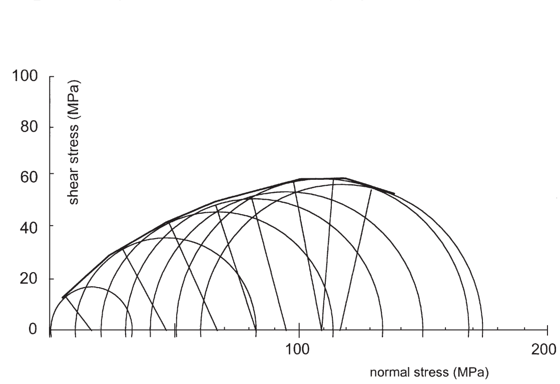

Fig. 20. Failure envelope in the Mohr diagram. Lines show the inclination of the curve tangent to the Mohr circles of the different triaxial compression tests.

orientation of the more critical plane, i.e., the plane of the stress state in the Mohr circle which first touches the failure envelope. This Mohr prediction of the angle of the shear bands, obtained from the strength curve for the $H/D = 2$ specimens tested in compression, gives an angle of about 25° at lower pressure and about 55° at 60 MPa (as the slope of the failure envelope is negative). The prediction is lower than reality for low confining pressure, but is more accurate at higher confining pressure (Fig. 8).

### 7.2. Brittle to semi-brittle transition

Failure in porous rock is generally classified by a brittle regime, a ductile regime and a transitional semi-brittle regime. In the ductile regime, when temperature and pressures are high, plastic deformation mechanisms such as dislocation flow, twinning or diffusive mass transfer are considered to occur homogeneously [33]. At medium pressure, a quasi-homogeneous cataclastic flow represents the semi-brittle regime. At lower pressure, strain localisation occurs, which is considered characteristic of the brittle regime. However, deformation inside the localised zone is cataclastic. Comparing the volumetric strain inside the specimen during an axisymmetric triaxial compression test (deviatoric + isotropic loading) with the volumetric strain recorded during a purely isotropic test shows a *relative* dilatancy in the brittle regime, but a *relative* compactancy, the so-called “shear-enhanced compaction” in the semi-brittle regime [47].

From the authors’ knowledge, the transition between configurations leading to a localised strain with dilatancy inside a shear band to configurations showing a quasi-homogeneous strain with compactancy, is not well understood. Our results suggest that the transition occurs by localised shear strain with compactancy inside large bands, becoming more and more numerous and closely spaced (Fig. 21). We observed a *relative* global dilatancy before the onset of localisation in triaxial compression tests where dilating shear bands occur, and conversely a neutral effect of the deviatoric stress on the volumetric strain where compacting shear band occur. During the extension tests, we observe a *relative* dilatancy in comparison with the volumetric strain during unloading of the isotropic test. For higher confining pressure, Zhu et al. [48] have observed a relative global compactancy in several sandstones, which suggest that compacting shear bands could exist in specimens deformed in triaxial extension tests.

Compaction inside bands has been already observed in geological structures by Antonellini et al. [19], Mollema and Antonellini [49], and in laboratory triaxial tests by Tillard [21] (stiff clay), Colliat-Dangus [17] (offshore calcareous sand), Olsson [22] (porous sandstone). The later observed bands with a very large angle with respect to the major principal stress, which is different from our observation, suggests that there is essentially a normal compaction mechanism, without shear strain.

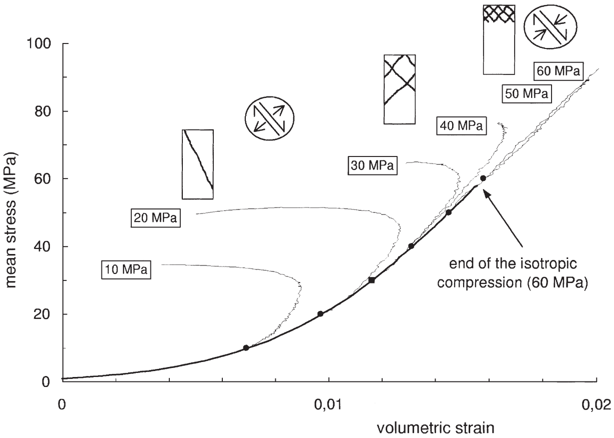

Fig. 21. Experimental curves of the compression test in the mean stress versus volumetric strain plane. The origins of the curves of the compression tests are arbitrarily placed on the curve of the isotropic compression test.

### 7.3. Shear band observations

The loss of homogeneity was observed to occur in the hardening regime, i.e., before peak stress. This loss of homogeneity is currently recognised as associated with localisation phenomenon [16,50]. However, as observed by other authors [50,51] shear bands become fully developed throughout the specimen only in the softening regime of the specimen’s response. Menéndez et al. [15] observed in the Berea sandstone some isolated clusters of Hertzian fractures before the stress peak, and a coalescence of these clusters to form a shear band in the post peak step.

When shear bands are well-developed, they are composed of a dilatant band in the central part, where the deformation is cataclastic, and lateral bands. The mean grain size is significantly reduced inside the central layer. In the lateral bands, the material is damaged by intergranular and intragranular microcracking and the density of the cracks decreases with distance from the central band. This structure of the shear bands is similar to faults observed in the geological structures at a larger scale [52]. The band where the deformation is cataclastic is generally called a “gouge layer” in the latter case.

The porosity of the material in the side bands is dependent on the confining pressure. We observed a dilating behaviour at lower pressure and a contracting behaviour during the shearing at higher pressure. Mechanisms of deformation at the microscopic scale are essentially cracking and grains movements. Crystal plastic phenomenon such as twinning and dislocation creep should be absent at our stress and temperature conditions [33]. The mean size of the grains is not changed in this zone, in contrast to the grains' size inside the gouge layer. The development and opening of microcracks could be associated with dilatancy, as it is classically admitted [53], and porosity reduction around the gouge should be due to grain movements.

Our idea on the appearance of this complex structure of localisation in intact material is that localisation initiates by formation of a large band, where the volumetric behaviour depends on the confining pressure of the test. A second-order localisation could then occur inside this first band, on the central axe and parallel to this one. The appearance of second-order localisation with a cataclastic deformation was already observed in artificial or natural gouges [54–56], which constitute an argument in favour of our interpretation. A shear band with cataclastic deformation seems to be a structure which is able to sustain large shear strain and which could be stable. The concept of a critical state in these bands needs to be examined [56], as it was observed by Desrues et al. [41] in granular materials.

## 8. Conclusion

The confining pressure has a strong influence on the behaviour of the Vosges sandstone and on the localised deformation structure that emerges at failure. We observe two distinct types of failure by localisation, in the brittle regime and in the transition between the brittle and semi-brittle regime.

For confining pressures up to 40 MPa, the deviatoric strength increases with confining pressure and the global volumetric strain dilates before failure. The angle of the shear bands with respect to the major principal stress direction increases, and the number of shear bands increases from one to several. The localised band is composed of a central part characterised by a cataclastic deformation which is dilating, and around it by a band with many intragranular and intergranulars cracks, which also has a dilating behaviour.

For confining pressures in the range from 50 to 60 MPa, the deviatoric strength decreases with confining pressure, and the global volumetric strain is continuously compacting up to the onset of localisation (although only sligthly at the end). The angle of the shear band keeps on increasing, the number of bands increases and their spacing decreases, while their thickness increases too. In the central part of the shear band, there is always a cataclastic dilatant gouge-like layer, but besides this central band, the adjacent microcracked bands have a compacting behaviour. At the macroscopic scale, shear bands in this pressure range appear as compacting zones.

Compacting shear bands are a challenging subject in the context of the theoretical analysis of the localisation by bifurcation theory. Can such objects be predicted by theory? The response will essentially depend on the structure of the constitutive equation used to describe the material behaviour. The strain type inside localisation bands predicted by the bifurcation theory can be divided between dilating and compacting shear bands [57]. Compacting shear bands could have important implications in field applications. For example, local permeability reduction in a layer or a set of parallel layers produced as a result of localisation could produce important changes in the permeability of a global structure.

## Acknowledgements

We are grateful to Dominique Fourmaintraux (Elf Aquitaine) for providing the Vosges sandstone. The experiments on the CT apparatus, at the Laboratoire de Mécanique et Acoustique in Marseille (France), were performed by Frédéric Mazerolle.

The work reported herein was supported by the groupement de recherche CNRS, GdR 914 "Géomécanique des Roches Profondes" (CNRS, Elf, Total, ANDRA, IFP), by the Alliance of Laboratories in Europe for Research and Technology (ALERT Geomaterials), and by University Joseph Fourier (Special Grant BQR-UJF).

## References

[1] Desrues J. Localisation patterns in ductile and brittle geomaterials. In: de Borst R, van der Giessen E, editors. Material instabilities in solids. New York: Wiley, 1998. p. 137–58

[2] Wawersik WR, Fairhurst C. A study of brittle rock fracture in laboratory compression experiments. Int J Rock Mech Min Sci 1970;7:561–75.

[3] Rice JR.The initiation and growth of shear bands. In: Palmer AC, editor. International Congress of Theoretical and Applied Mechanics, Cambridge, 1973. p. 263–74.

[4] Rudnicki JW, Rice JR. Conditions for the localisation of the deformation in pressure sensitive dilatant materials. J Mech Phys Solids 1975;23:371–94.

[5] Hobbs BE, Mühlhaus H-B, Ord A. Instability, softening and localisation of deformation. In: Knipe RJ, Rutter EH, editors. Deformation mechanisms, rheology and tectonics. Geological Society Special Publication No. 54, 1990. p. 143–65.

[6] Vardoulakis I, Goldscheider M, Gudehus G. Formation of shear bands in sand bodies as a bifurcation problem. Int J Numer Anal Methods Geomech 1978;2:99–128.

[7] Kolymbas D. Bifurcation analysis for sand sample with non-linear constitutive equation. Ing-Arch 1981;50:131–40.

[8] Darve F. An incrementally non-linear constitutive law of the second order and its application to localisation. International Conference on Laws Engineering Materials, Tuscon, 1987.

[9] Desrues J, Chambon R. Shear band analysis for granular materials: the question of incremental non-linearity. Ing-Arch 1989;59:187–96.

[10] Vardoulakis I. Rock bursting as a surface instability phenomenon. Int J Rock Mech Min Sci Geomech Abstr 1984;21:137–44.

[11] Chambon R, Desrues J, Tillard D. Shear modulus identification versus experimental localisation data. In: Chambon R, Desrues J, Vardoulakis I, editors. Localisation and bifurcation theory for soils and rocks. Rotterdam: Balkema, 1994. p. 101–11.

[12] Sulem J, Vardoulakis I, Papamichos E, Oulahna A, Tronvoll J. Elasto-plastic modelling of red Wildmoor sandstone. Mech Cohesive-Frictional Mater 1999;4:215–45.

[13] Bésuelle P. Déformation et rupture dans les roches tendres et les sols indurés: comportement homogène et localisation. PhD thesis, University of Grenoble, France, 1999. p. 370.

[14] Dunn DE, LaFountain LJ, Jackson RE. Porosity dependence and mechanism of brittle fracture in sandstones. J Geophys Res 1973;78:2403–17.

[15] Menéndez B, Zhu W, Wong T-f. Micromechanics of brittle faulting and cataclastic flow in Berea sandstone. J Struct Geol 1996;18:1–16.

[16] Ord A, Vardoulakis I, Kajewski R. Shear band formation in Gosford sandstone. Int J Rock Mech Min Sci Geomech Abstr 1991;28:397–409.

[17] Colliat-Dangus JL. Comportement des matériaux granulaires sous fortes contraintes. Influence de la nature minéralogique du matériau étudié. PhD thesis, INPG & USMG, Grenoble, France, 1986.

[18] Hicher PY, Wahyudi H. Microstructural analysis of strain localisation in clay. Comput Geotech 1994;16:205–22.

[19] Antonellini MA, Aydin A, Pollard DD. Microstructure of deformation bands in porous sanstones at Arches National Park, Utah. J Struct Geol 1994;16:941–59.

[20] Tillard D. Etude de la rupture dans les géomatériaux cohésifs. Application à la marne de Beaucaire. PhD thesis, University of Grenoble, France, 1992. p. 297.

[21] Tillard-Ngan D, Desrues J, Raynaud S, Mazerolle F. Strain localisation in beaucaire marl. Proceedings of Geotechnical Engineering of Hard Soils — Soft Rocks, Rotterdam: Balkema, 1993. p. 1679–86.

[22] Olsson WA. Theoretical and experimental investigation of compaction bands in porous rock. J Geophys Res 1999; 104:7219–28.

[23] Bésuelle P, Desrues J. An internal instrumentation for axial and radial strain measurements in triaxial tests. Geotech Testing J, to appear.

[24] Bésuelle P, Desrues J. Internal instrumentation for strain measurements on soft rocks tested in an axisymmetric triaxial cell. Proceedings of The Geotechnics of Hard Soils — Soft Rocks, Napoli, vol. 1. Rotterdam: Balkema, 1998. p. 45–8.

[25] Goto EC, Tatsuoka F, Shibuya S, Kim Y-S, Sato T. A simple gauge for local small strain measurements in the laboratory. Soils Found 1991;31:169–80.

[26] Underwood EE. Quantitative stereology. Reading MA: Addison-Wesley, 1970. p. 274.

[27] ISRM. Suggested methods for determining the strength of rock materials in triaxial compression: revised version. Int J Rock Mech Min Sci Geomech Abstr 1983;20:283–90.

[28] Labuz JF, Bridel JM. Reducing frictional constraint in compression testing through lubrification. Int J Rock Mech Min Sci Geomech Abstr 1993;30:451–5.

[29] Cornet FH, Fairhurst C. Influence of pore pressure on the deformation behavior of saturated rocks. Advances in rock mechanics, Proceedings of Third Congress on International Society Rock Mechanics, vol. 2, part A, Washington, 1974. p. 638–44.

[30] Handin J, Hager RV, Friedman M, Feather JN. Experimental deformation of sedimentary rocks under confining pressure: pore pressure tests. Bull Am Assoc Petrol Geol 1963;47:717–55.

[31] Brace WF. Brittle fracture of rocks. In: Judd WR, editor. State of stress in the Earth's crust. New York: Elsevier, 1964. p. 111–74.

[32] Millar PJ, Murray DR. Triaxial testing of weak rocks including use of triaxial extension test. In: Chaney RC, Silver ML, editors. Advanced triaxial testing of soil and rock, ASTM STP977. Philadelphia: ASTM, 1988. p. 376–86.

[33] Paterson MS. Experimental rock deformation, the brittle field. Berlin: Springer, 1978. p. 251.

[34] Tatsuoka F, Kim Y-S. Deformation of shear zone in sedimentary soft rock observed in triaxial compression. In: Chambon R, Desrues J, Vardoulakis I, editors. Localisation and bifurcation theory for soils and rocks. Rotterdam: Balkema, 1994. p. 181–7.

[35] Santarelli FJ, Brown ET. Failure of three sedimentary rocks in triaxial and hollow cylinder compression tests. Int J Rock Mech Min Sci Geomech Abstr 1989;26:401–13.

[36] Read HE, Hegemier GA. Strain softening of rock, soil and concrete — A review article. Mech Mater 1984;3:271–94.

[37] Hadley K. Azimuthal variation of dilatancy. J Geophys Res 1975;80:4845–50.

[38] Latière HJ, Mazerolle F. The X-ray scanner. A tool for the examination of the intravoluminal crystaline state of aluminum. Engng Fract Mech 1987;27:413–63.

[39] Raynaud S, Fabre D, Mazerolle F. Analysis of the internal structure of rocks and characterisation of mechanical deformation by a non-destructive method: X-ray tomodensitometry. Tectonophysics 1989;159:149–59.

[40] Johns RA, Steude JS, Castanier LM, Roberts PV. Nondestructive measurements of fracture aperture in crystaline rock cores using X-ray computed tomography. J Geophys Res 1993;98:1889–900.

[41] Desrues J, Chambon R, Mokni M, Mazerolle F. Void ratio evolution inside shear bands in triaxial sand specimens studied by computed tomography. Géotechnique 1996;46:529–46.

[42] Bésuelle P, Desrues J. Homogeneous and localised deformation in sandstone specimens tested in a triaxial cell. Proceedings of the Geotechnics of Hard Soils — Soft Rocks, Napoli, vol. 1. Rotterdam: Balkema, 1998. p. 37–43.

[43] Roscoe KH. The influence of strains in soil mechanics. Géotechnique 1970;20:129–70.

[44] Arthur JFR, Chua KS, Dunstan T. Induced anisotropy in a sand. Géotechnique 1977;27:13–30.

[45] Vardoulakis I. Shear band inclination and shear modulus of sand in biaxial tests. Int J Numer Anal Methods Geomech 1980;4:103–19.

[46] Vermeer PA. A simple shear band analysis using compliances. IUTAM Conference on Def Fail Gran Materials, Delft, 1982. p. 493–9.

[47] Wong T-f, David C, Zhu W. The transition from brittle faulting to cataclastic flow in porous sandstones: mechanical deformation. J Geophys Res 1997;102:3009–25.

[48] Zhu W, Montesi LGJ, Wong T-f. Shear-enhanced compaction and permeability reduction: triaxial extension tests on porous sandstone. Mech Mater 1997;25:199–214.

[49] Mollema PN, Antonellini MA. Compaction bands: a structural analog for anti-mode I cracks in aeolian sandstone. Tectonophysics 1996;267:209–28.

[50] Labuz JF, Dai S-T, Papamichos E. Plane-strain compression of rock-like materials. Int J Rock Mech Min Sci Geomech Abstr 1996;33:573–84.

[51] Lockner DA, Byerlee JD, Kuksenko V, Ponomarev A, Sidorin A. Quasi-static fault growth and shear fracture energy in granite. Nature 1991;350:39–42.

[52] Chester FM, Logan JM. Implications for mechanical properties of brittle faults from observations of the Punchbowl fault zone, California. Pure Appl Geophys 1986;124:78–106.

[53] Teufel LW. Pore volume changes during frictional sliding of simulated faults. In: Carter NL, Friedman M, Logan J, Stearns D, editors. Mechanical behaviour of crustal rocks. Geophysical

Monographs, vol. 24. Washington, DC: American Geophysical Union, 1981. p. 135–45.

[54] Cox SJD. Velocity-dependent friction in a large direct shear experiment on gabbro. In: Knipe RJ, Rutter EH, editors. Deformation mechanisms, rheology and tectonics. Geological Society Special Publications No. 54, 1990. p. 63–70.

[55] Marone C, Scholz CH. Particle-size distribution and microstructures within simulated fault gouge. J Struct Geol 1989;11:799–814.

[56] Morrow CA, Byerlee JD. Experimental studies of compaction and dilatancy during frictional sliding on faults containing gouge. J Struct Geol 1989;11:815–25.

[57] Bésuelle P. Compacting and dilating shear bands in porous rock: theoretical and experimental conditions. J Geophys Res, submitted for publication.

Pergamon

*Phys. Chem. Earth (A)*, Vol. 26, No. 1-2, pp. 101–106, 2001

1464-1895/01/$ - see front matter

PII: S1464-1895(01)00032-1

# Evolution of Strain Localisation with Stress in a Sandstone: Brittle and Semi-Brittle Regimes

**P. Bésuelle**

Laboratoire de Géologie, Ecole Normale Supérieure, Paris, France

*Received 15 June 2000; accepted 15 November 2000*

**Abstract.** The experimental characterisation of strain localisation in a porous sandstone is presented for the brittle and the transition between the brittle and semi-brittle regimes. Localisation occurs through bands and the observations show a continuous evolution from a dilative strain type inside the bands at low mean stress to a compactive strain type at higher mean stress. The orientation of the bands changes also with the stress level and the onset of localisation is systematically detected before the peak stress. Microscope observations suggest two steps during the localisation process. A theoretical analysis of the localised strain inside bands is presented using the framework of bifurcation theory. The notion of dilating and compacting shear bands is introduced and this allows to show that a continuous transition from pure extension bands to dilating and compacting shear bands and to pure compaction bands is expected. These theoretical predictions are in accordance with the experimental observations, providing an interesting framework to investigate the brittle to semi-brittle transition regime.

## 1 Introduction

The failure of porous rocks evolves notably with the mean stress. The failure is generally associated with localisation bands. These bands are planar zones with a non zero thickness where the strain is concentrated. At low mean stress, deviatoric loading behaviour is characterised by shear-induced dilatancy and planar strain localisation is accompanied by strain softening, this is the brittle regime. At higher confining pressure, in the semi-brittle regime, deviatoric loading behaviour is characterised by shear-enhanced compaction, the cataclastic flow is a quasi homogeneous compaction accompanied by strain hardening (Menéndez et al., 1996; Wong et al., 1997). It is well recognised that strain localisation can be dilative, but the existence of contracting shear bands is still under question. Such compactive bands have been observed in natural geological structures (Antonellini et al., 1994; Mollema and Antonellini, 1996) and laboratory experiments (e.g., Bésuelle et al., 2000; Olsson, 1999; Tillard et al., 1993). They could represent a transitional failure mode between the brittle and the semi-brittle regimes.

Rudnicki and Rice (1975) proposed a bifurcation analysis to predict the onset of planar localisation. Olsson (1999) and Issen and Rudnicki (2000) used this model to analyse pure compaction bands in porous rock. The bifurcation analysis also allows to specify the strain type within a localisation band. A shear band can be dilative or compactive. There exists a continuous evolution from pure extension bands to pure compaction bands via dilating and compacting shear bands, with respect to the constitutive parameters of the law (Bésuelle, 2000).

The first section of this paper summarises the experimental results of strain localisation observed in a porous Vosges sandstone, showing dilating and compacting shear bands. A more complete investigation is given in Bésuelle et al. (2000). The second section presents the theoretical analysis of the localised strain inside bands, relying on the analysis of Bésuelle (2000). The third part proposes a comparison between the experimental and theoretical results, to understand the evolution of the strain localisation with respect to the mean stress.

## 2 Experimental characterisation of strain localisation

### 2.1 Specimen behaviour

The investigated Vosges sandstone has a porosity of 22% and mean grain size of about 0.3 mm. It is a pink quartz sandstone (quartz=93%) with few percents of feldspar and white mica and which is poorly cemented. The cohesion is due to the interpenetration between grains. Cylindrical specimens have been cored with a diameter of 40 mm and a length of 80 mm and are tested in dried condition in a triaxial cell using isotropic compression tests, axisymmetic compression tests

---

*Correspondence to:* P. Bésuelle

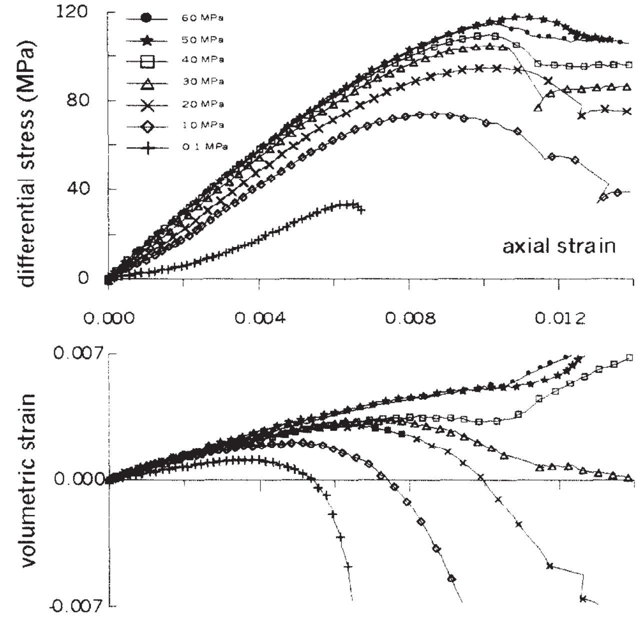

**Fig. 1.** Differential stress and volumetric strain versus axial strain, for several confining pressures. Compactive strains are assumed to be positive.

(the axial stress is the maximum compressive stress) and axisymmetric extension tests (the axial stress is the minimum compressive stress).

The axial and lateral strains of specimen are measured with specific global internal transducers fixed on the specimen inside the cell (Bésuelle and Desrues, 2000). The comparison of three axial transducers and of four lateral transducers allows to detect a loss of the homogeneity of the strain field, which is associated to the strain localisation. This onset of localisation is systematically detected before the peak stress of the specimen response. The differential stress at the onset of localisation is about 98% of the differential peak stress for uniaxial compression tests (zero confining pressure) and about 93% of the peak stress for a confining pressure of 60 MPa, with a quasi-linear evolution for intermediate confining pressures (Bésuelle et al., 2000; Bésuelle, 1999). The volumetric strain is computed from the axial and radial transducers.

The specimen response tested in axisymmetric compression is represented in Fig.1 for several confining pressures (from 0 to 60 MPa). Strain-stress curves show that strength at peak stress increases with confining pressure. Note however, the peak stress at 60 MPa is lower than the peak stress at 50 MPa. As far as volumetric strains are concerned, the specimens show a global compaction at the beginning of the axial loading. Then, up to the peak stress, one gets either dilatancy (strong at low confining pressure) or compaction (at 50 and 60 MPa). The failure envelope is strongly non linear, the slope is positive at low confining pressure, decreases with confining pressure and becomes negative between 50 and 60 MPa. The failure envelope observed in axisymmetric extension tests is similar.

## 2.2 Description of deformation bands

In all tests, specimens fail with development of localised deformation bands through the specimen. In uniaxial compression tests, one observes a combination of axial splitting and inclined failure surfaces. Between 10 and 30 MPa in compression tests, there is one or two parallel shear bands. Conjugated shear bands occur from 40 to 60 MPa, and the distance between the bands decreases with pressure as the number of shear bands increases. The angle between the bands (the line of steeper slope) and the axial stress direction (the most compressive principal stress) increases with the confining pressure and becomes greater than $\pi/4$ at 50 MPa.

The observation of failure surfaces is similar for extension tests. Between 40 and 60 MPa confining pressure, there is one shear band with a small angle with respect to the lateral stress direction (the most compressive principal stress). Between 20 and 30 MPa, the failure surface is parallel to the most compressive stress direction.

Two specimens tested in axisymmetric compression tests (30 and 50 MPa confining pressure) up to the residual stress step were observed unloaded using X-rays CT. This technique provides a spatial view of the bulk density distribution inside the specimen. Figure 2 shows the reconstruction of a specimen tested at 30 MPa (left) and a specimen tested at 50 MPa (right) in a plane parallel to the specimen axis. The denser zones inside the specimen are the brighter areas in the figure. Note that the samples are not perfectly homogeneous since the upper half of the left image is darker, pointing to a less dense material. This heterogeneity existed before the test and the shear bands take place principally in the less dense part. At 30 MPa confining pressure, the shear band is darker than the surrounding material, which shows that the porosity is greater inside the band than outside. At 50 MPa, the band is clearer, the porosity is lower inside the band than outside. A dilative volumetric strain is associated to the shear band at 30 MPa and a compactive volumetric strain is associated to the shear band at 50 MPa.

Observation by optical and electronic microscopy and a measurement of the surface porosity on thin slices of the previous specimens shows a similar result. However, the structure of localisation appears to be more complex than suggested by X-rays CT. Microscopy shows a central part where grains are crushed and where the porosity is higher than outside the bands. On the lateral part of the band, crack density is high. The surface porosity at 30 MPa in these lateral parts is intermediate between the porosity in the central part of the band and outside the band. At 50 MPa, the surface porosity on the lateral part of the band is lower than outside the band and than in the central part of the band. These results suggest that two steps occur during the strain localisation process. A first step of localisation is associated with a specific volumetric behaviour of the band, which itself depends on the confining pressure. A second step of localisation takes place inside the bands and is always associated with a dilative and cataclastic deformation. This second step probably occurs at larger strains, beyond the peak stress.

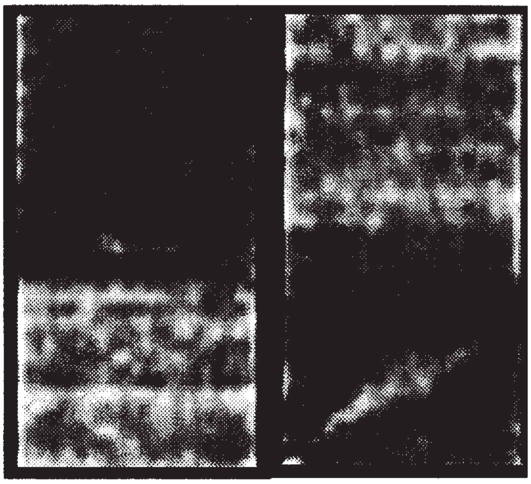

Fig. 2. X-rays CT reconstructions of specimens tested at 30 MPa (left) and 50 MPa (right) confining pressure. The dilating shear band is inclined and darker, and the compacting shear band is inclined and clearer than the average grey level of the specimen.

## 2.3 Brittle and semi-brittle regimes

The volumetric strain during axisymmetric compression tests (deviatoric + isotropic loading) is compared up to the axial peak stress with volumetric strain during isotropic tests, with respect to the mean stress (Fig. 3). The deviatoric stress in compression tests at confining pressure between 0 to 40 MPa induced a relative dilatancy of the specimen response in comparison with the isotropic response, and it is showed that the shear bands at 30 MPa are dilating. At 50 and 60 MPa, the volumetric strain in compression tests is similar to the response in isotropic test, which means that the deviatoric stress has a neutral effect on the volumetric response. It is showed that the shear bands are compacting at 50 MPa. It was shown by others (Wong et al., 1997) that at higher confining pressure, deviatoric stress induces a relative compaction, called shear-enhanced compaction, with a quasi homogeneous compaction inside the specimen. This latter case corresponds to the semi brittle regime, while the relative dilatancy corresponds to the brittle regime.

To summarise our results, we observed that in the brittle regime (from 0 to 40 MPa), the localisation bands have a dilative volumetric strain behaviour. In the transition between the brittle regime and the semi brittle regime, corresponding to a neutral effect of the deviatoric stress, shear bands have a compactive volumetric strain behaviour and are more numerous. These observations seem to bridge the gap between the brittle failure and the semi brittle failure.

## 3 Theoretical analysis of the localised strain

Rudnicki and Rice (1975) proposed a constitutive model and a bifurcation analysis to predict the onset of planar strain localisation in pressure-sensitive materials. Strain localisation is considered as a non-uniqueness of the strain field from a homogeneous strain state. The model assumes an elastoplastic law with a Drucker-Prager yield surface and a non-associated flow rule. The constitutive relation is expressed by: $\overset{\nabla}{\sigma}_{ij} = \mathcal{L}_{ijkl} D_{kl}$ where $D_{ij} = 1/2(v_{i,j} + v_{j,i})$ is the symmetric part of the velocity gradient tensor and $\overset{\nabla}{\sigma}$ is the co-rotational Jaumann stress rate. The constitutive tensor $\mathcal{L}$ can be expressed with elastic parameters (e.g., the Young modulus E and the Poisson ratio $\nu$) and plastic parameters (the friction coefficient $\mu$ and the dilatancy factor $\beta$) and a hardening modulus $h$.

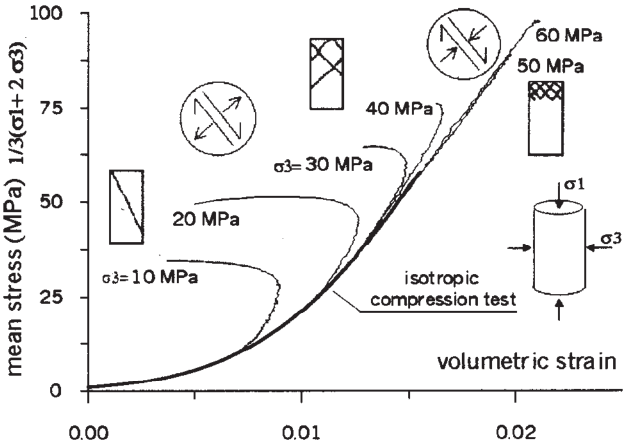

Fig. 3. Mean stress versus volumetric strain: comparison of axisymetric compression test paths with respect to the isotropic test path.

The strain inside the band is assumed to be equal to the strain outside the band plus an additional strain expressed by: $\Delta D_{ij} = 1/2\,(g_i n_j + g_j n_i)$, where $n$ is the unit vector normal to the band and $g$ an arbitrary vector. The equilibrium conditions on the band can be written as: $(n_i \mathcal{L}_{ijkl} n_l) g_k = 0$. This equation admits a non-trivial solution (i.e. a non homogeneous strain field) if: $det(n_i \mathcal{L}_{ijkl} n_l) = 0$, which is the bifurcation condition. This latter condition depends on the constitutive relation, which depends itself on the stress and strain state, and on the orientation of the band (i.e. $n$). The above analysis allows to determine the most critical orientation of the band, which is the orientation corresponding to the first bifurcation during the loading of the material. This orientation of the band can be determined with respect to the principal stress directions.

The band is parallel only to the second principal stress direction if (Perrin and Leblond, 1993):

$$(1-2\nu)N - \sqrt{4-3N^2} \le \tfrac{2}{3}(1+\nu)(\beta+\mu) \le (1-2\nu)N + \sqrt{4-3N^2}$$

where $N$ is the intermediate principal deviatoric stress normalised by the von Misès equivalent stress, and is equal to $1/\sqrt{3}$ in axisymmetric compression stress state and $-1/\sqrt{3}$ in axisymmetric extension stress state.

This condition corresponds to the existence of the so-called shear bands. If the lower inequality is violated, then the band is parallel to the second and to the least compressive principal

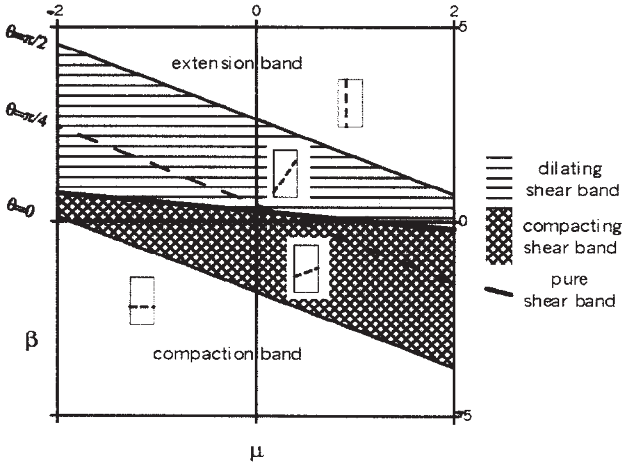

**Fig. 4.** Distinction in the plane $(\mu, \beta)$ of the domains of pure extension bands, dilating shear bands, compacting shear bands and pure compaction bands, for an axisymmetric compression stress state and $\nu = 0.2$

| $g_n > 0$<br>$g_s = 0$ | $> 0$<br>$> 0$ | $= 0$<br>$> 0$ | $< 0$<br>$> 0$ | $< 0$<br>$= 0$ |
|---|---|---|---|---|
| extension band | dilating shear b. | pure shear b. | compacting shear b. | compaction band |

**Table 1.** Distinction of the different strain types inside bands. $g_n$ is the normal component and $g_s$ the shear component of the additional strain inside bands.

stress direction (i.e. perpendicular to the most compressive stress direction). In that case, the band is a compaction band as defined by Olsson (1999) and Issen and Rudnicki (2000). The condition for compaction bands to exist is that $(\beta + \mu)$ is negative. If the upper inequality is violated, then the band is parallel to the most compressive and to the second principal stress direction, and is called an extension band.

At the onset of localisation, if: $det(\mathcal{N}) = 0$ with $\mathcal{N}_{jk} = n_i \mathcal{L}_{ijkl} n_l$, then $g$ is a eigenvector of the tensor $\mathcal{N}$ and characterises the strain type inside the band. The additional strain inside the band has a shear component $g_s$ and a normal component $g_n$. The component $g_n$ can be dilative or compressive (Bésuelle, 2000). Four cases can be distinguished with respect to the constitutive parameters, according to the nature of both components $g_s$ and $g_n$ (Fig. 4 and Table 1). If the shear component is zero and the normal component is dilative, this case corresponds to pure extension bands as expressed above. If the shear component is non-zero and the normal component is dilative, then this case is a particular case of shear bands and is termed here *dilating shear bands*. If the shear component is non-zero and the normal component is compressive, this case is the complementary case of the latter over the shear bands domain, and is called here *compacting shear bands*. The last case is characterised by a zero shear component and a non-zero compressive normal component and corresponds to the pure compaction bands cited above. The transition of one case to the other is continuous and the strain type inside the band evolves gradually with respect to the constitutive parameters.

The limit between the dilating and compacting shear bands is the case of pure shear band (no normal component of the additional strain) and is expressed by:

$$3(1 - 2\nu)(1 - \nu)N = (1 + \nu)\left[(1 - 2\nu)(\beta + \mu) + 2\beta\right]$$

This case delimits the conditions between dilative volumetric strain and compactive volumetric strain localised inside a band. For an associated model (i.e. $\mu = \beta$), this case corresponds also to a band inclined of $\pi/4$ with respect to the most compressive stress direction. Figure 4 represents the four domains with respect to the friction coefficient $\mu$ and the dilatancy factor $\beta$, for an axisymmetric compression stress state and a Poisson ratio equal to 0.2. The angle $\theta$ is the angle between the normal to the band and the most compressive principal stress direction. At the transition between compacting shear bands and compaction bands, $\theta = 0$, and at the transition between the dilating shear bands and extension bands, $\theta = \pi/2$.

## 4 Comparison between the experimental and theoretical results

In this part, experimental observations are compared with theoretical localised strain and critical orientation of the band The dilatancy factor $\beta$ which is proportional to the rate of plastic volume strain divided by the rate of plastic shear strain is measured at the onset of bifurcation. This onset of bifurcation is determined as the onset of divergence of the three internal axial transducers measurements and of divergence of the four radial transducers measurements. The Poisson ratio $\nu$ and the Young modulus $E$ are determined at the beginning of the axial loading, when the stress-strain curve is quasi-linear, they depend on the confining pressure. The friction coefficient $\mu$ is determined as the slope of the failure envelope in the von Misès equivalent stress versus mean stress plane. This parameter $\mu$ and the parameter $\beta$ are positive at low confining pressure and decrease when the confining pressure increases. At highest confining pressure (60 MPa) $\mu$ is negative and $\beta$ is zero (Fig.1). Note that at high pressures, it seems that the plastic parameter $\mu$ should not be identified to an internal friction coefficient.

The experimental points $(\mu, \beta)$ are reported in Fig. 5. Figure 5.a corresponds to the uniaxial compression ($\nu \approx 0.4$). The experimental point is in the theoretical domain of pure extension bands, where bands are parallel to the most compressive principal stress direction. This theoretical prediction of the localisation bands is very similar to the observed axial splitting failure mode, where opening cracks are parallel to the axial direction. Figure 5.b corresponds to the axisymmetric compression ($\nu \approx 0.25$). The four points corresponding to confining pressure between 10 and 40 MPa are in the domain of dilating shear bands, while experimental results show dilative volumetric strain inside the bands. The two points corresponding to confining pressure of 50 and 60 MPa

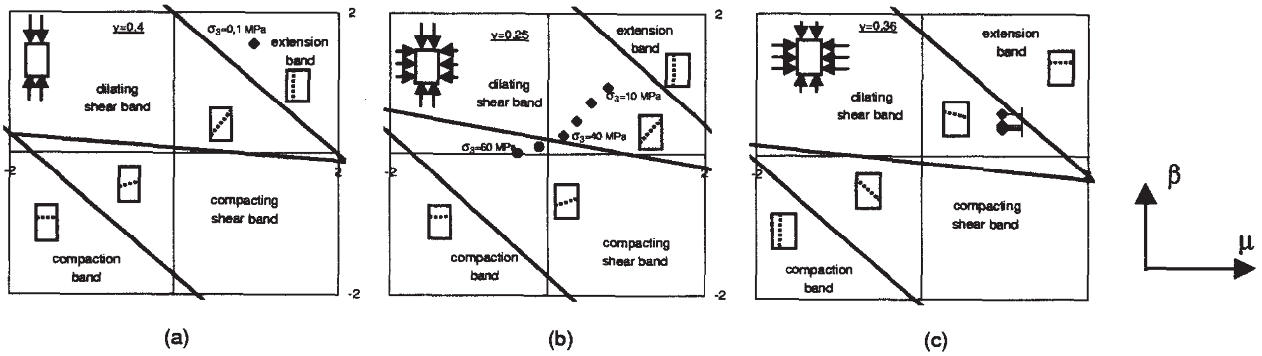

**Fig. 5.** Comparison between the theoretical analysis and the experimental results. (a) for uniaxial compression test (axial splitting: full diamond), (b) for axisymmetric compression tests (dilating shear bands: full diamonds, compacting shear bands: full circles), (c) axisymmetric extension tests (dilating shear bands: full diamonds).

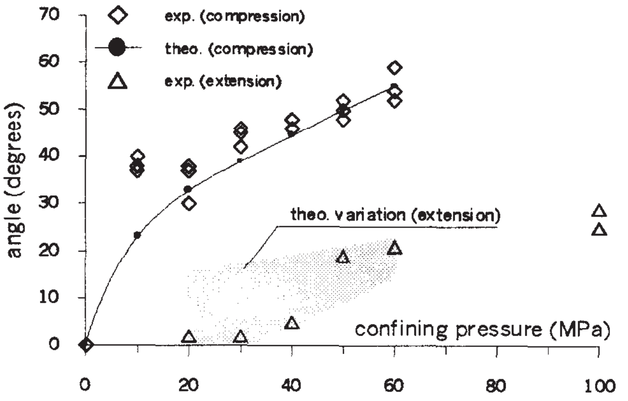

**Fig. 6.** Comparison of the experimental angle between the shear bands and the most compressive principal stress direction, and the theoretical angle computed from the experimental values of $\mu$ and $\beta$.

are in the domain of compacting shear bands, while experimental results show a compactive volumetric strain inside the bands. Figure 6 shows the experimentally observed angles between the shear bands (the line of steeper slope) and the maximum compressive principal stress direction, and theoretical predictions computed from the values of $\mu$ and $\beta$. Experimental and theoretical values are in close agreement for compression tests.

Figure 5.c corresponds to an extension stress state and is more speculative because experimental determination of the friction coefficient $\mu$ is problematic. It is expected to be higher than the friction coefficient measured in the uniaxial compression, especially for the extension tests at low confining pressure. The experimental points are in the domain of dilating shear bands, with a small angle between the band and the horizontal direction, as it was observed on specimens. However, at 20 and 30 MPa confining pressure, horizontal bands are observed and experimental points (corresponding to the highest values of $\beta$) could be in the theoretical domain of pure extension bands because of the experimental error on $\mu$. Failure mode at these low confining pressures in extension tests could be the equivalent of axial splitting observed in uniaxial compression. The grey area in Fig. 6 corresponds to a possible variation of the theoretical angle of bands in extension tests, the upper limit corresponding to the value of $\mu$ measured in uniaxial compression.

The comparison of the onset of localisation is less conclusive. Rudnicki and Rice (1975) pointed as suspect the fact that, in axisymmetric compression stress state, the onset of localisation is predicted to occur in the strain softening regime. Experimental results show that localisation appears in the strain hardening regime, before the peak stress of the specimen response. The onset of localisation depends in fact on the constitutive relation that it is used to describe the rock behaviour. Bifurcation analysis with other constitutive relations predict localisation in the hardening regime (e.g., Chambon et al., 1994)

## 5 Conclusions

Experimental characterisation of the failure mode of a porous sandstone has shown a strong evolution with respect to the stress level. Two steps of localisation seem to exist. A first step of localisation is clearly evidenced, the behaviour of which depends strongly of the mean stress. A second localisation step is suggested, where the deformation is cataclastic and dilative. The present work focuses on the first localisation step. At low mean stress, in compression or extension tests, bands occur parallel to the most compressive stress direction, with a pure extension strain type. When the mean stress increases, strain in the bands develops a shear component, while the volumetric strain is dilative and the angle between the band and the most compressive stress direction increases. At higher mean stress, the volumetric component becomes compactive and shear bands evolve from dilating shear bands to compacting shear bands through an important intermediate case, that of pure shear bands. If mean stress increases more, compaction bands would be expected.

Theoretical analysis using bifurcation theory confirms this description of the localisation process. Pure extension bands correspond to the axial splitting, dilating and compacting shear bands are observed as predicted. The cell capacity was not sufficient however to observe pure compaction bands, which should develop at higher confining pressure (above 60 MPa). Detailed observation of pure compaction bands in laboratory tests is needed to determine the corresponding constitutive parameters and to understand the relation between compaction bands and quasi homogenous compaction inside specimen in the semi brittle regime failure.

The existence of pure shear bands is important for permeability analysis in field applications. On one side of this limit, shear bands are dilative, on the other side, there are compactive. As it was already suggested by Issen and Rudnicki (2000) for pure compaction band, the reduction of the porosity inside a band can act as a permeability barrier which has a preferential orientation with respect to the principal stress directions.

*Acknowledgements.* Experimental tests were performed at laboratory 3S, Grenoble. I am grateful to J. Desrues, S. Raynaud and F. Mazerolle for their contributions in this experimental program. I thank also Y. Guéguen for interesting discussions on the theoretical results.

## References

Antonellini, M. A., Aydin, A., and Pollard, P. P., Microstructure of deformation bands in porous sandstones at Arches National Park, Utah, *J. Struct. Geol.*, *16*, 941–959, 1994.

Bésuelle, P., Compacting and dilating shear bands in porous rock: theoretical and experimental conditions, *submitted to J. Geophys. Res.*

Bésuelle, P., Desrues, J., and Raynaud, S., Experimental characterisation of the localisation phenomenon inside a Vosges sandstone in a triaxial cell, *Int. J. Rock Mech. Mining Sci.*, in print.

Bésuelle, P., and Desrues, J., An internal instrumentation for axial and radial strain measurements in triaxial tests, *Geotechnical Testing J.*, in print.

Bésuelle, P., Déformation et rupture dans les roches tendres et les sols indurés : comportement homogène et localisation, *PhD thesis University of Grenoble, France*, p. 370, 1999.

Chambon, R., Desrues, J., and Hammad, W., CloE, a new rate-type constitutive model for geomaterials theoretical basis and implementation, *Int. J. Num. Ana. Methods in Geomechanics*, *18*, 253–278, 1994.

Issen, K. A., and Rudnicki, J. W., Conditions for compaction bands in porous rock, *J. Geophys. Res.*, *105*, 21529–536, 2000.

Menéndez, B., Zhu, W. and Wong, T.-F., Micromechanics of brittle faulting and cataclastic flow in Berea sandstone, *J. Struct. Geology*, *18*, 1–16, 1996.

Mollema, P. N., and Antonellini, M. A., Compaction bands: a structural analog for anti-mode I cracks in aeolian sandstone, *Tectonophysics*, *267*, 209–228, 1996.

Olsson, W. A., Theoretical and experimental investigation of compaction bands in porous Rock, *J. Geophys. Res.*, *104*, 7219–7228, 1999.

Perrin, G., and Leblond, J. B., Rudnicki and Rice's analysis of strain localization revisited, *J. Applied Mech.*, *4*, 842–846, 1993.

Rudnicki, J. W., and Rice, J. R., Conditions for the localization of deformation in pressure- sensitive dilatant materials, *J. Mech. Phys. Solids*, *23*, 371–394, 1975.

Tillard-Ngan, D., Desrues, J., and Raynaud, S., Strain localisation in beaucaire marl, *Proceeding Geotechnical Engineering of Hard Soils - Soft Rocks, Balkema*, 1679–1686, 1993.

Wong, T.-F., David, C. and Zhu, W., The transition from brittle faulting to cataclastic flow in porous sandstone: mechanical deformation, *J. Geophys. Res.*, *102*, 3009–3025, 1997.

Pure appl. geophys. 160 (2003) 851–868
0033–4553/03/060851–18

**Pure and Applied Geophysics**

# Failure Mode and Spatial Distribution of Damage in Rothbach Sandstone in the Brittle-ductile Transition

PIERRE BÉSUELLE,[1] PATRICK BAUD,[2]
and TENG-FONG WONG[3]

*Abstract*—To elucidate the spatial complexity of damage and evolution of localized failure in the transitional regime from brittle faulting to cataclastic ductile flow in a porous sandstone, we performed a series of triaxial compression experiments on Rothbach sandstone (20% porosity). Quantitative microstructural analysis and X-ray computed tomography (CT) imaging were conducted on deformed samples. Localized failure was observed in samples at effective pressures ranging from 5 MPa to 130 MPa. In the brittle faulting regime, dilating shear bands were observed. The CT images and stereological measurements reveal the geometric complexity and spatial heterogeneity of damage in the failed samples. In the transitional regime (at effective pressures between 45 MPa and 130 MPa), compacting shear bands at high angles and compaction bands perpendicular to the maximum compression direction were observed. The laboratory results suggest that these complex localized features can be pervasive in sandstone formations, not just limited to the very porous aeolian sandstone in which they were first documented. The microstructural observations are in qualitative agreement with theoretical predictions of bifurcation analyses, except for the occurrence of compaction bands in the sample deformed at effective pressure of 130 MPa. The bifurcation analysis with the constitutive model used in this paper is nonadequate to predict compaction band formation, may be due to the neglect of bedding anisotropy of the rock and multiple yield mechanisms in the constitutive model.

**Key words:** Damage, sandstone, brittle-ductile transition, microscopy, X-ray computed tomography, bifurcation theory.

## *1. Introduction*

In porous sandstones, a transition in failure mode from brittle faulting to cataclastic flow occurs as effective pressure increases. Under a relatively low pressure the differential stress attains a peak before it undergoes strain softening; the failure of sample occurs by shear localization. On the other hand, under high confinement the

---

[1] Ecole Normale Supérieure, Laboratoire de Géologie, Paris, France. Now, Laboratoire Sols, Solides, Structures (CNRS, UJF, INPG), BP53, 38041 Grenoble Cedex 9, France. E-mail: Pierre.Besuelle@inpg.fr

[2] E.O.S.T., Laboratoire de Physique des Roches, 5 rue René Descartes, 67084 Strasbourg Cedex, France.

[3] State University of New York at Stony Brook, Department of Geosciences, Stony Brook, NY 11794-2100, U.S.A.

sample strain hardens and fails by delocalized cataclastic flow (PATERSON, 1978; WONG *et al.*, 1997).

Some intriguing field observations and new theoretical analysis have focused on the mechanical behavior in the *transitional* regime: historically the failure mode in this regime is described as a mosaic of conjugate shear bands and yet recent field and experimental observations indicate the development of discrete compaction bands orthogonal to the maximum compressive stress $\sigma_1$ (MOLLEMA and ANTONELLINI, 1996; OLSSON, 1999). This agrees with recent bifurcation analyses (ISSEN and RUDNICKI, 2000) which predict a continuous transition of the localization mode from extension bands (parallel to $\sigma_1$) to compaction bands as a function of the constitutive parameters that characterize porosity change and frictional dependence of plastic yield. In the transitional regime between these two failure modes, localization develops by shear bands (inclined with respect to $\sigma_1$ at angles ranging from $0^{\mathrm{o}}$ to $90^{\mathrm{o}}$) which may be dilating or compacting (BÉSUELLE, 2001).

Since they can act as barriers to fluid transport and influence the stress field and strain partitioning in sedimentary formations, it is important to gain a fundamental understanding of the extent of and conditions under which these localized compactant structures would occur. Preliminary microstructural studies (DIGIOVANNI *et al.*, 2000; WONG *et al.*, 2001) have shown that such complex development of localization can occur in sandstones with porosities ranging from 13% to 28%. Acoustic emission locations (OLSSON and HOLCOMB, 2000) have also mapped out the three-dimensional complexity of the localization development in the Castlegate sandstone (with 28% porosity). In this study we systematically conducted mechanical tests on the Rothbach sandstone (with a porosity of 20%), and characterized the spatial heterogeneity in porosity change and damage using X-ray computed tomography (CT) imaging and stereological measurements on optical micrographs, respectively. These two types of complementary measurements provide useful insights into the geometric complexity and micromechanics associated with the development of compaction and shear bands in the brittle-ductile transition.

## *2. Experimental Procedure*

Rothbach sandstone from the Vosges mountains in eastern France was used is this study. Our samples came from the same block studied by DAVID *et al.* (1994) and WONG *et al.* (1997), who have provided the petrophysical description. Cylindrical samples (of diameter 18.1 mm and length 38.1 mm) were cored perpendicular to the sedimentary bedding. The arithmetic mean of connected porosities (measured on each sample) was 20.3%.

The samples were saturated with distilled water and deformed in conventional triaxial conditions following procedures described in detail by BAUD *et al.* (2000). The samples were deformed at a nominal strain rate of $1.3 \times 10^{-5}$ $\mathrm{s}^{-1}$ under fully drained conditions at a fixed pore pressure of 10 MPa. Each end of the specimen was in contact with a stainless steel spacer with a central hole for fluid inlet. To uniformly distribute the pore fluid, several shallow grooves were made on the spacer surface that was touching the sample. The interfaces with the sample ends were lubricated with a mixture of stearic acid and vaseline (LABUZ and BRIDEL, 1993). Axial strain, differential stress, confining pressure, porosity change as well as acoustic emission activity were monitored during the tests. Axial strain was computed from the displacement of the cell piston measured by an external transducer. Adjustment of a pressure generator kept the pore pressure constant, and the pore volume change was recorded by monitoring the piston displacement of the pressure generator with a displacement transducer. The porosity change was calculated from the ratio of the pore volume change to the initial bulk volume of the sample.

Samples at different stages of deformation were unloaded and retrieved from the pressure vessel for X-ray CT imaging conducted at the Institut Français du Pétrole (Rueil-Malmaison, France). The CT-scanner measures the X-ray attenuation coefficient, which increases with increasing bulk density and atomic number (WELLINGTON and VINEGAR, 1987; ANTONELLINI *et al.*, 1994). In a homogeneous sample the attenuation coefficient is proportional to the bulk density. X-ray radiographs taken from different angles provide a cross-sectional image, and a multiplicity of such slices can be combined to visualize the three-dimensional distribution of density in the deformed specimen. The CT apparatus measured the average X-ray attenuation value in a voxel of $0.2 \times 0.2 \times 1.5$ mm$^3$. CT imaging has been used to characterize the three-dimensional development of strain localization in sandstone (VINEGAR *et al.*, 1991; BÉSUELLE *et al.*, 2000) and granite (RAYNAUD *et al.*, 1989; KAWAKATA *et al.*, 1999).

Petrographic thin sections of selected samples were also prepared. The deformed samples were first impregnated with epoxy and then sawed along a plane parallel to the axial direction. Using optical microscopy the damage states in the thin sections were characterized quantitatively. For each sample, the spatial distribution of crack density over a total area of $16.3 \times 35.4$ mm$^2$ was characterized. The area centrally located in a thin section was further divided into $10 \times 29$ subregions, each of which had an area of $1.63 \times 1.22$ mm$^2$. The reflected images were all acquired at a magnification of 100x. Using stereological techniques (MENÉNDEZ *et al.*, 1996; WU *et al.*, 1999), we counted the number of crack intersections with a test array of 5 parallel lines (spaced at 0.33 mm or 0.24 mm apart) in two orthogonal directions parallel and perpendicular to $\sigma_1$, respectively. We denote the linear intercept density (number of crack intersections per unit length) for the array oriented parallel to $\sigma_1$ by $P_L^{\|}$, and that for the perpendicular array by $P_L^{\perp}$.

For each sample, 290 pairs of stereological parameters ($P_L^{\|}$ and $P_L^{\perp}$) were measured to map out the spatial evolution of damage and stress-induced anisotropy.

Since the spatial distribution of damage is approximately axisymmetric in a triaxially compressed sample, the crack surface area per unit volume ($S_v$) is given by

$$S_v = \frac{\pi}{2} P_L^{\perp} + \left(2 - \frac{\pi}{2}\right) P_L^{\|} \tag{1}$$

and the anisotropy of crack distribution (UNDERWOOD, 1970) can be characterized by the parameter

$$\Omega_{23} = \frac{P_L^{\perp} - P_L^{\|}}{P_L^{\perp} + (4/\pi - 1) P_L^{\|}} \tag{2}$$

that represents the ratio between the surface area of cracks parallel to $\sigma_1$ and the total crack surface area.

## *3. Mechanical Data*

The compressive stresses and compactive strains will be taken positive. The maximum and minimum (compressive) principal stresses will be denoted by $\sigma_1$ and $\sigma_3$, respectively. The pore pressure will be denoted by $P_p$, and the difference between the confining pressure ($P_c = \sigma_2 = \sigma_3$) and pore pressure will be referred to as "effective pressure."

The mechanical behavior and failure mode of porous sandstones have several common attributes (WONG *et al.*, 1997). At low pressures, failure involves dilatancy and faulting, with a failure envelope described by the Coulomb surface, with positive pressure dependence. At high pressures, the samples fail by strain hardening and shear-enhanced compaction. The compactive yield is characterized by an elliptical cap that has negative pressure dependence. The brittle-ductile transition occurs in the regime where these two envelopes meet.

Guided by the mechanical data of WONG *et al.* (1997) on Rothbach sandstone, we performed 15 triaxial experiments at effective pressures ranging from 5 to 130 MPa to capture the evolution of the failure modes in the transitional regime. Representative mechanical data for selected experiments are presented in Figure 1. At effective pressure up to 20 MPa, the mechanical response and failure mode were typical of the brittle faulting regime. The differential stress ($\sigma_1 - \sigma_3$) attained a peak, beyond which strain softening was observed (Fig. 1a). The peak stress showed a positive correlation with the confining pressure and effective mean stress (Fig. 2), and macroscopic shear bands oriented at ~30° with respect to the $\sigma_1$ direction were observed in the failed samples. Whereas dilatancy initiated before the stress peak was attained at 5 MPa of effective pressure, continuous compaction was observed beyond about 20 MPa of effective pressure (Fig. 1b).

At effective pressure $P_{\text{eff}} \geq 40$ MPa, visual examination of the failed samples did not discern features that would suggest localized failure. All the samples showed

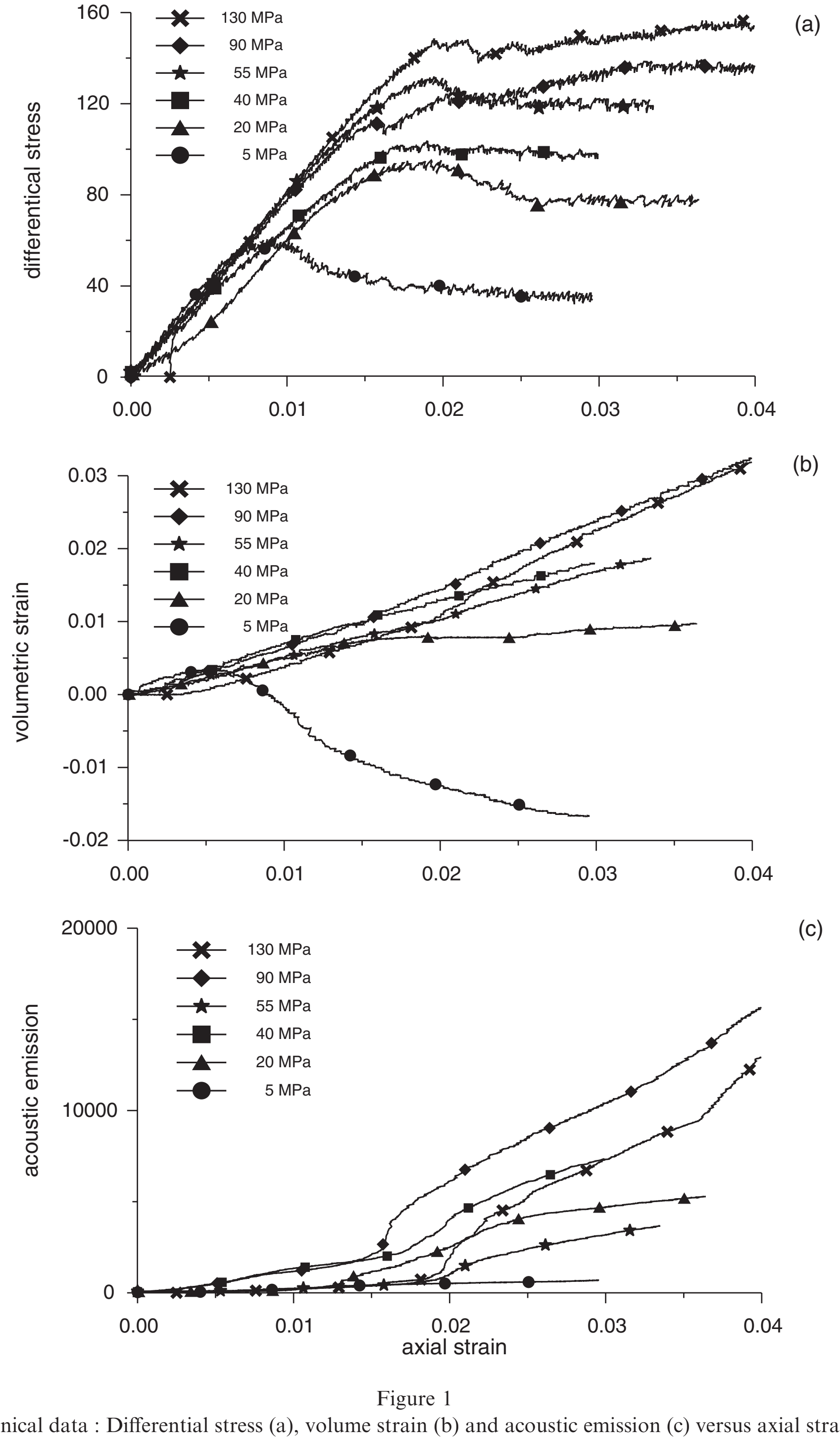

Figure 1
Mechanical data : Differential stress (a), volume strain (b) and acoustic emission (c) versus axial strain for effective pressure between 5 and 130 MPa.

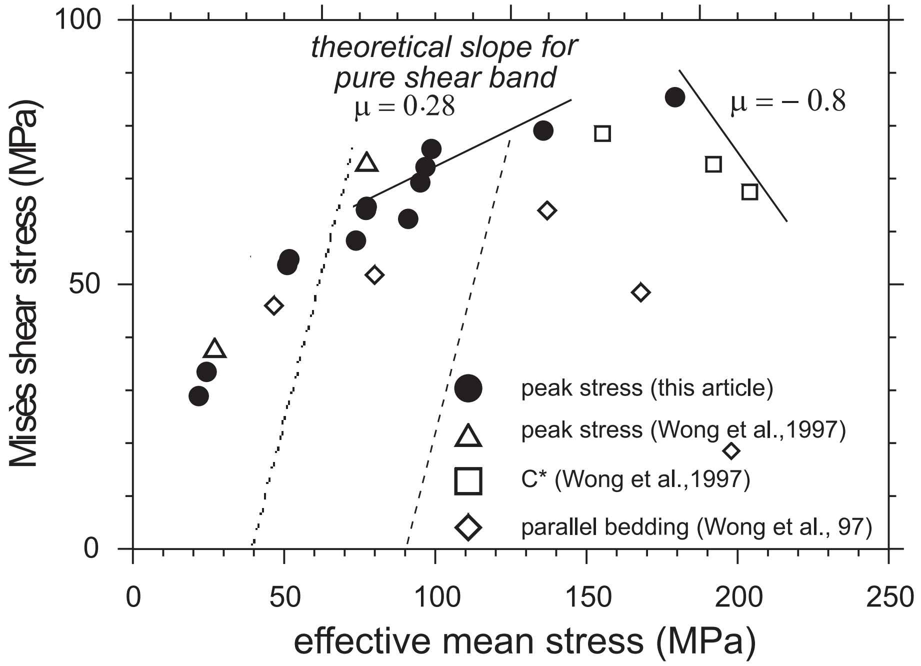

Figure 2
Peak stress and onset of shear enhanced compaction in the Misès shear stress versus effective mean stress plane. $\mu$ denotes the friction coefficient.

shear-enhanced compaction (CURRAN and CARROLL, 1979) that initiated at a stress level $C^*$, beyond which there was an accelerated decrease in volume in comparison to the hydrostat (Fig. 1b). A peak stress followed by a small amount of strain softening was still observed in most of the samples (Fig. 1a). A surge in acoustic emission activity was commonly observed beyond $C^*$ (Fig. 1c).

We compiled the yield stress data in Figure 2. The equivalent Misès shear stress and effective mean stresses for a compressive axisymmetric stress state are defined by $(\sigma_1 - \sigma_3)/\sqrt{3}$ and $(\sigma_1 + 2\sigma_3) - P_p$, respectively. Our data (solid circles) correspond to the peak stresses at effective pressures between 5 and 130 MPa. Data of WONG *et al.* (1997) for the brittle strength and stresses at the onset of shear-enhanced compaction are also included. In the transitional regime (corresponding to effective pressures between 45 MPa and 130 MPa) dilatancy was inhibited even though the differential stress attained a peak. Duplicate experiments indicate appreciable variability in the peak stresses in the transitional regime, which is possibly due to local variations of the bedding direction in our sample block. The sensitivity of strength and yield stress to bedding was documented by WONG *et al.* (1997), who showed that samples cored parallel to bedding (open diamonds in Fig. 2) had significantly lower strengths and yield stresses.

## *4. Spatial Pattern of Strain Localization—CT Analysis*

Altogether twelve deformed samples were prepared for CT imaging. Zones with higher attenuation coefficients are shown in lighter color. For all the specimens analyzed, a number of sub-parallel planar zones with somewhat higher attenuation than the average were observed (Fig. 3). These zones are almost perpendicular to the axial direction and probably associated with the natural sedimentary bedding. In a homogeneous material the brighter zones would correspond to denser materials. However, since the Rothbach sandstone (with modal composition of 68% quartz, 16% feldspar, ~12% clay, and 3% oxides and mica) is by no means monomineralic, the localized anomalies in attenuation may also arise from mineralogical heterogeneity.

At effective pressures of 5 and 20 MPa, the development of dilating shear bands was manifested as inclined planar zones of darker color in the CT images (Figs. 3 and 4). The geometric complexity of these shear bands is illustrated by the images of four circular slices perpendicular to the sample axis (Fig. 4). In each slice several dilatant zones were observed to radiate from an approximately circular zone. The diameter of the concentric zone and spacing between the radial zones both vary with the axial position of the slice.

Although we had expected to observe localized compactant features in samples deformed at effective pressure higher than 40 MPa, our CT images revealed no obvious signs of strain localization. In some specimens a cone of slightly higher density seems to have developed near the ends of the specimens (Fig. 5). Given the low resolution, it is difficult to unambiguously evaluate to what extent these represent strain localization features.

At 130 MPa effective pressure, if present, these localized zones are expected to be at very high angles to the sample axis and almost parallel to the bedding.

Figure 3
X-ray CT measurement of the whole sample at 20 MPa effective pressure. The imaged plane is parallel to the specimen axis. Shear band are inclined and dilating (darker than the average grey level) and sedimentary bedding is close to perpendicular of the specimen axis.

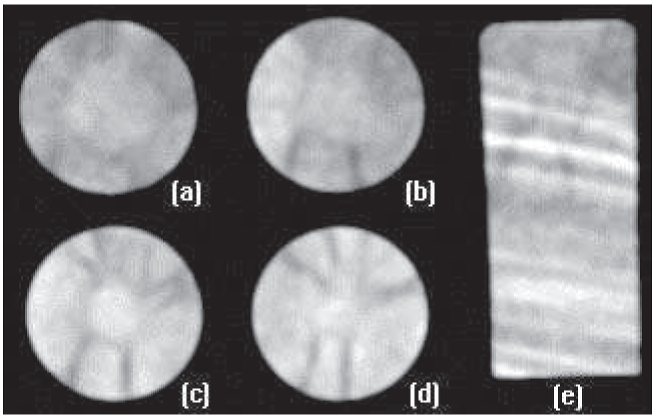

Figure 4
X-ray CT measurements of the whole sample at 5 MPa effective pressure : (a–d) in planes perpendicular to the specimen axis, the size and the spacing out of localisation traces (a circular zone and several radial bands) depend on the position in the specimen; (e) in a vertical mid-section of the specimen, the previous circular zone corresponds to a central V shape and the radial traces to several inclined bands.

Figure 5
X-ray CT measurements of the whole sample at 55 MPa effective pressure. A cone of compactive strain (slightly brighter than the average grey level) is observed at the top of the specimen.

Consequently it is difficult to differentiate such localized features in a failed sample from the pre-existing bedding heterogeneities.

## 5. *Spatial Evolution of Anisotropic Damage—Microstructural Observation*

Microstructural observations were conducted to characterize the spatial distribution of cracking and damage localization in the deformed samples. For reference, we first studied a sample deformed in the brittle faulting regime at $P_{\text{eff}} = 20$ MPa : sample B1 was deformed to the post-failure stage (to about 3% of axial strain), where the differential stress reached a residual level (Fig. 1a). Shear localization developed from a corner of the sample along a planar zone inclined at an angle of ~40° to $\sigma_1$ (Figs. 3 and 6). The width of the shear band varied by a factor of ~3, with a minimum of ~ 0.5 mm (which is comparable to the average grain diameter of 0.6 mm). Its central part was subject to intense grain crushing. In the periphery of the band extensive inter- and intra-granular cracking occurred. Crack density decreased quickly and transversely to the band. Beyond a distance of 4 or 5 grains, damage became very slight. A few intra-granular cracks preferentially aligned in an approximately axial direction were observed in grains neighboring the shear zone (Fig. 7). Damage anisotropy in Rothbach sandstone is qualitatively similar to what was observed in Berea sandstone (21% porosity) by MENÉNDEZ *et al.* (1996).

Stereological measurements were performed on four samples deformed in the transitional regime at effective pressures 40, 55, 90 and 130 MPa. Using equation (1) the crack surface area per unit volume ($S_v$) was inferred from linear intercept measurements along two orthogonal directions. The samples deformed at 40 and 55 MPa effective pressures showed similar spatial distributions of damage (Fig. 8). In

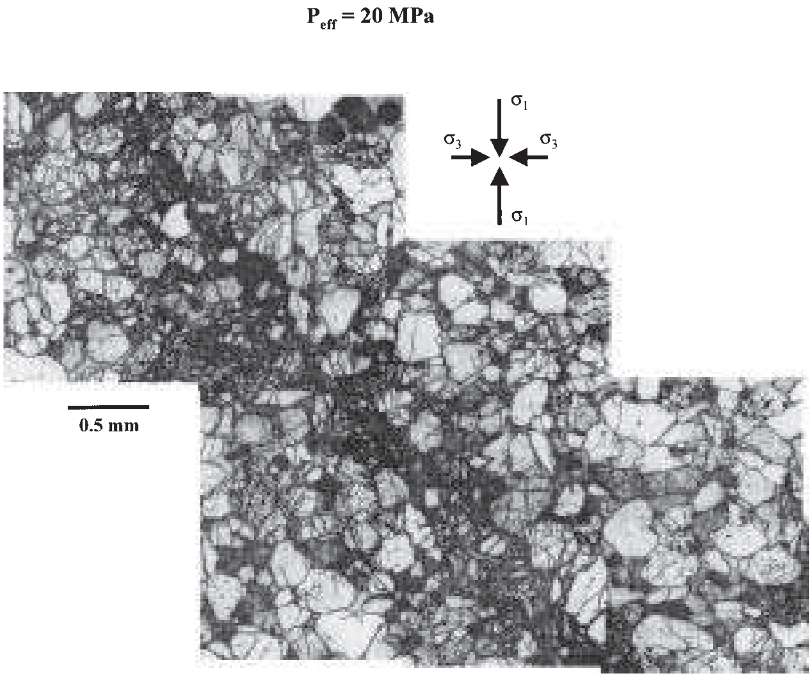

Figure 6
Mosaic of optical (reflexion) micrographs showing part of the shear band that developed in sample $B_1$ deformed in the brittle regime.

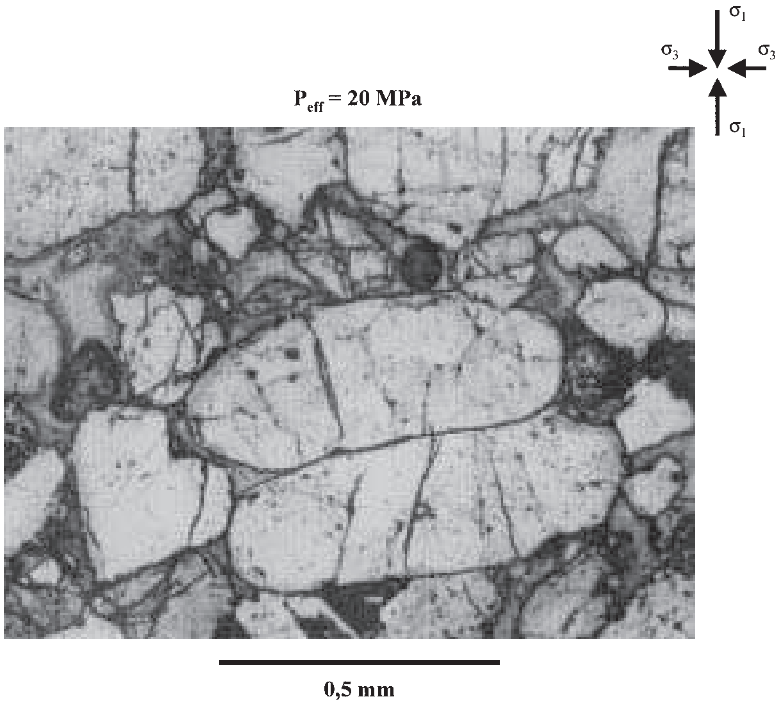

Figure 7
Intragranular cracks outside the shear band in sample $B_1$ deformed in the brittle regime.

all cases damage affected near one or both ends of the sample, and the cumulative area of the localized zones did not exceed 1/3 of the total surface of the sample. Within the high damage areas, the crack density is higher than the background by as much as a factor of 5. For example, we found in sample $T_2$ an average of 4.3 $m^{-1}$ for $S_v$ and a maximum of 14.6 $m^{-1}$. These values are in the range found by MENÉNDEZ *et al.* (1996) in shear compacted samples of Berea sandstone. Qualitatively similar distributions of damage were observed in samples $T_2$ and $T_3$ from two experiments conducted at effective pressure 55 MPa. High-angle conjugate zones initiated from the sample corners and intersected at a sub-horizontal tabular zone of variable length, where maximum crack density was measured in most cases. In sample $T_2$ deformed at 55 MPa effective pressure, the length of this tubular zone was $\sim$4 mm. The thin section $T_3$ was taken from the sample shown in Figure 5. Locations of the high-angle conjugate zones in the thin section roughly correspond to those where an axi-symmetric compacting cone was vaguely resolved by CT.

In Figure 9, we present micrographs corresponding to different areas of sample $T_3$ (deformed to 3% of axial strain). Intensive grain crushing occured in the upper part of the sample (Figure 9a). Numerous "Hertzian fractures" radiating from grain contacts (MENÉNDEZ *et al.*, 1996; WU *et al.*, 1999) were observed. The damage

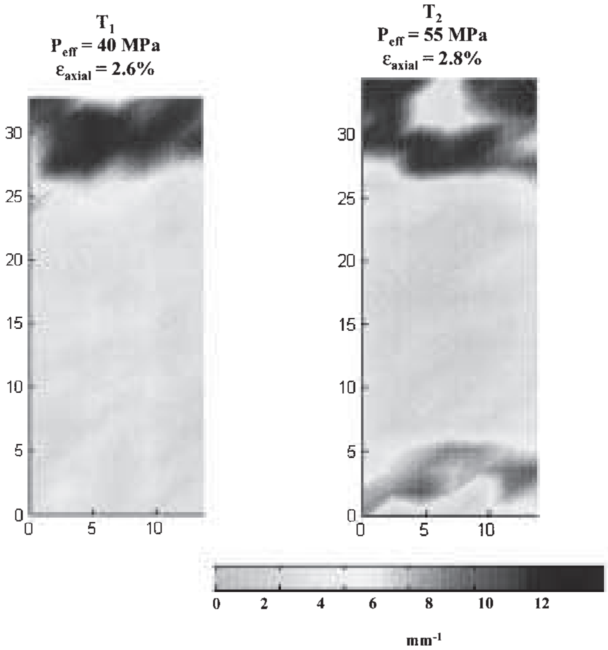

Figure 8
Spatial distribution of specific surface area in sample $T_1$ deformed at $P_{\mathrm{eff}} = 40$ MPa (a), and in samples $T_2$ (b) and $T_3$ (c) deformed at $P_{\mathrm{eff}} = 55$ MPa. The $\sigma_1$ direction is vertical.

anisotropy (evaluated using equation 2) was negligible in this sample, with $\Omega_{23} = 0.1$ within the localized zone and an average value $\sim$0 in the whole sample. In Figure 9b pore collapse was evident, and part of the pore space was filled with comminuted particles. This suggests an overall decrease of the porosity in the damaged part of the sample. Figures 9c and 9d depict two different regions of the sample that did not have intensive cracking. Minor damage was in fact observed in both areas, and some of the visible cracks were likely to be present prior to deformation. Figures 9c and 9d show the strong heterogeneity in grain size and porosity that is typical for different layers of the bedding in Rothbach sandstone. Bedding layers were found in most of the thin sections, except in the damaged zones where grain crushing "homogenized" the material. It is therefore unclear, at this point, if the bedding heterogeneity promotes or inhibits damage localization.

At 90 MPa effective pressure (Fig. 10), intensive cracking was observed in a larger portion of the sample (about 1/2), at both ends. The highest crack densities ($S_v = 14.6\,\mathrm{mm}^{-1}$) were measured in association with grain crushing and pore collapse (Fig. 10b). In this area we found an anisotropy factor of about 0.1. In other regions, mostly close to the periphery of the damaged area, subvertical cracking was dominant (Fig. 10c). We consistently measured a maximum of $\Omega_{23} = 0.4$ in these zones. In the central part of the sample, significant differences

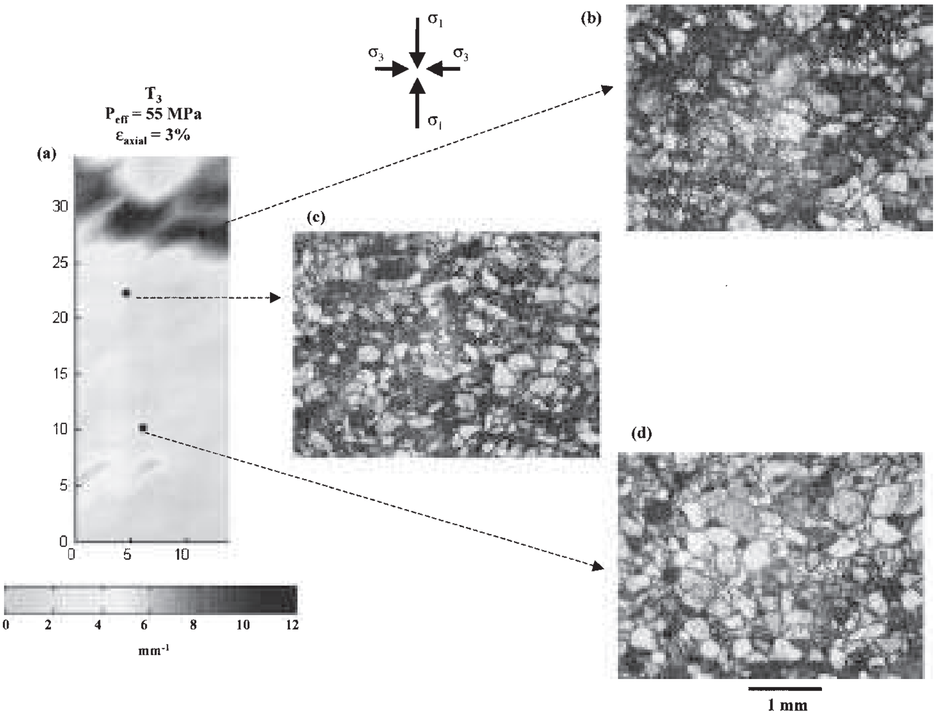

Figure 9
(a) Spatial distribution of specific surface area in sample $T_3$ deformed at $P_{\text{eff}} = 55$ MPa. (b) Extensive grain crushing where crack density is high. (c) No damage in a compact layer of the sample. (d) No damage in a more porous layer of the sample.

in porosity could be observed (Figs. 10d and 10e). Axial cracking such as observed in Figure 10c appeared to be predominant in the less compact layers of the sample.

At 130 MPa effective pressure, damage was spatially distributed in a clearly different way (Fig. 11). Intensive cracking was observed in about 2/3 of the sample, including the central area. Several localized and elongated clusters were identified (Fig. 11a). In all of them, grain crushing was evident (Fig. 11b). The orientations of these clusters were mainly sub-horizontal (perpendicular to $\sigma_1$), and the crack surface area reached a maximum of $S_v = 15.3\,\text{mm}^{-1}$. These localized structures can be interpreted as compaction bands or compacting shear bands at a relatively high angle of $\sim 80°$ degrees with respect to the axial direction. As they are almost parallel to the bedding, it may have been difficult to resolve them in the CT images. We found a relatively low anisotropy factor of $\Omega_{23} = 0.02$ in these compaction bands. Damage level was appreciably less in grains outside the compaction bands (Fig. 11c) and the overall spatial distribution of damage remained anisotropic even at high effective pressure (Fig. 11d).

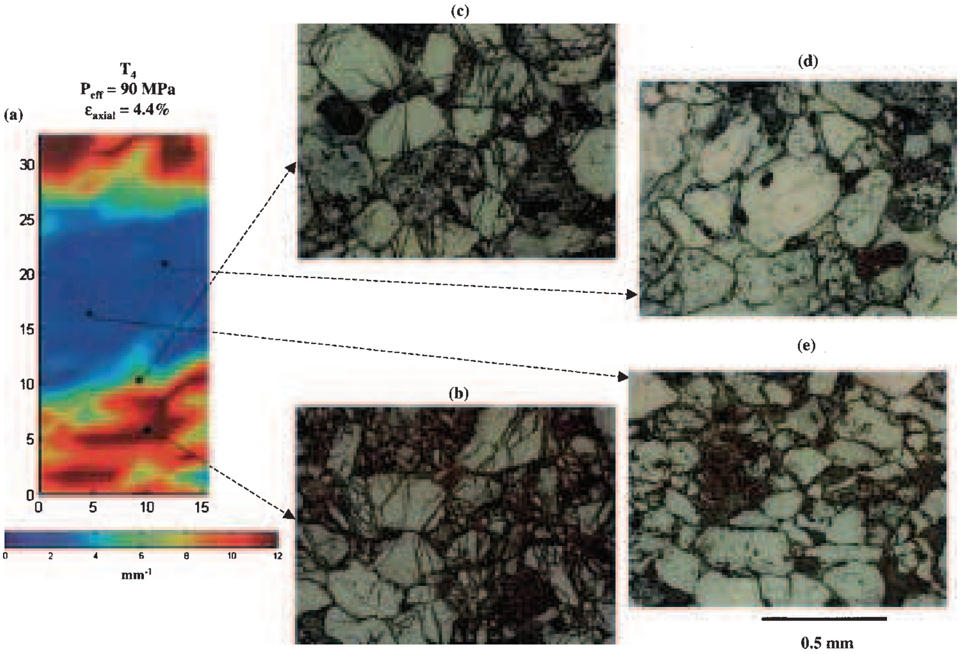

Figure 10
(a) Spatial distribution of specific surface area in sample $T_4$ deformed at $P_{\mathrm{eff}} = 90$ MPa. (b) Extensive grain crushing in a localized cluster of intense damage. (c) Area where axial cracking is dominant. (d) No damage in a compact layer of the sample. (e) No damage in a more porous layer of the sample. The $\sigma_1$ direction is vertical.

## 6. Discussion and Conclusion

### 6.1. Strain Localization and Failure Mode in the Brittle-Ductile Transition

Our data on the Rothbach sandstone are in qualitative agreement with recent studies by OLSSON (1999) and WONG *et al.* (2001) who have documented the development of high-angle shear bands and compaction bands in sandstones with porosities ranging from 13% to 28%. The localized failure modes are associated with stress states in the transitional regime from brittle faulting to compactive cataclastic flow. These laboratory results suggest that such complex features can be pervasive in sandstone formations, not just in the very porous aeolian sandstone in which they were first documented (MOLLEMA and ANTONELLINI, 1996). Recognition of such structures in the field would elucidate the complex development of localization in sandstone formations (AYDIN and JOHNSON, 1978) and accretionary prisms (BYRNE *et al.*, 1993).

Our microstructural observations and stereological data underscore the spatial heterogeneity of damage associated with the development of high-angle shear and

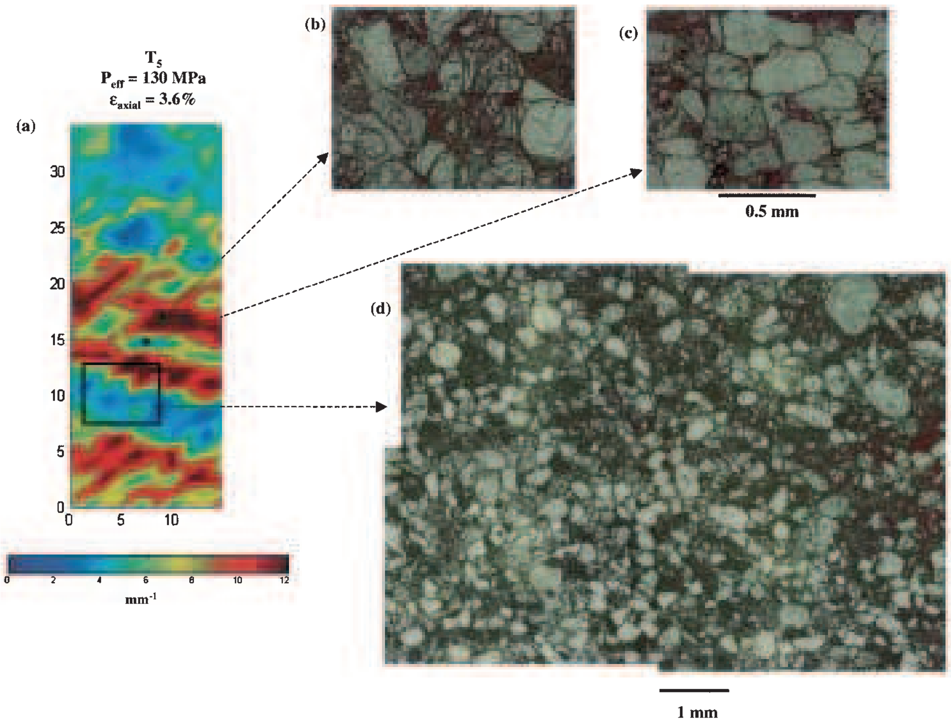

Figure 11
(a) Spatial distribution of specific surface area in sample $T_5$ deformed at $P_{\text{eff}} = 130$ MPa. (b) Detail of grain crushing in a compaction band. (c) No damage in an area between two compaction bands. (d) Mosaic of micrographs showing the transition between a compaction band and an undamaged zone. The $\sigma_1$ direction is vertical.

compaction bands. In the localized bands intensive grain crushing and pore collapse were observed. Similar micromechanical processes were documented by DIGIOVANNI *et al.* (2000) in laboratory deformed Castlegate sandstone and by MOLLEMA and ANTONELLINI (1996) in naturally deformed Navajo sandstone. Previous laboratory data show that bedding in Rothbach sandstone has significant influence on the failure and yield behavior. Our microstructural observations presented here suggest that the development of compaction band is promoted along planar zones parallel to the bedding.

The CT data have provided preliminary images of the three-dimensional geometric complexity associated with strain localization. At 5 MPa effective pressure, a complex pattern of localization was observed (Fig. 4). Axisymmetric loading and frictional constraints at the specimen ends appear to promote the development of such an axisymmetric pattern, and to inhibit the initiation of a single shear band (which is intrinsically a plane-strain mechanism). The pattern we observed is analogous to that in axisymmetrically compressed specimens of Hostun

RF sand, which was studied by DESRUES *et al.* (1996) as a combination of a cone centered on the axis of the specimen and on a set a plane strain mechanism associated with V-shape pairs.

Since compaction bands have an intrinsically axisymmetric geometry, their development should be promoted by axisymmetrical loading if the constitutive parameters attain the critical conditions for inception of such a localization mode. Since the compaction bands that developed at 130 MPa confining pressure were observed in the mid-section of the sample, we believe frictional end-effects to be minimal in our tests. However, the conical shape of the high-angle shear bands at effective pressures between 40 and 55 MPa may have been influenced by stress heterogeneity from frictional constraints, since they initiated in the proximity of the specimen ends.

### *6.2. Comparison with Localization Analysis*

Bifurcation analyses (RUDNICKI and RICE, 1975; OLSSON, 1999; ISSEN and RUDNICKI, 2000; BÉSUELLE, 2001) specify the mechanical conditions under which such localized failure modes may develop. The simplest approach is to adopt a constitutive framework (RUDNICKI and RICE, 1975) whereby the yield envelope and inelastic volumetric change can be characterized by the pressure-sensitivity parameter $\mu$ and dilatancy factor $\beta$, respectively. The parameter $\mu$ can be inferred from the slope of the yield stress data as indicated in Figure 2. Our data together with those of WONG *et al.* (1997) for samples cored perpendicular to the bedding indicate that $-0.8 \leq \mu \leq 0.28$ in the transitional regime. For this range of $\mu$ values and Poisson ratio equal to 0.14 (inferred from our laboratory data), the bifurcation analyses predict that localized failure occurs by three possible modes :

1. A *pure shear* band (with negligible volumetric change throughout the sample) may develop for an associated model (i.e., $\mu = \beta$) for $\mu = 0.28$ (BÉSUELLE, 2001).
2. A *compaction* band perpendicular to $\sigma_1$ may develop for negative values of $\mu$ and $\beta$ such that $\beta + \mu < -\sqrt{3}$ (ISSEN and RUDNICKI, 2000).
3. A *compacting shear* band at high angle may develop for intermediate values of $\mu$ and $\beta$ such that $\beta + \mu \geq -\sqrt{3}$.

WONG *et al.* (2001) recently showed that the dilatancy factors for Bentheim, Berea and Darley Dale sandstones (deformed in the brittle-ductile transitional regime) fall in the range $-\sqrt{3}/2 < \beta < 0$. They argued that these limiting values arise from the plastic strain field in this regime which is characterized by axial shortening (probably dominated by pore collapse) and lateral expansion (probably induced by axial microcracking). Values of $\beta$ for Rothbach sandstone in the transitional regime are expected to also fall within these limits, which imply that $\beta + \mu \geq -(\sqrt{3}/2 + 0.8) > -\sqrt{3}$. Accordingly, the bifurcation analysis would rule out the possibility of compaction band formation (mode 2) and predict the development of localization by either mode 1 or mode 3. These two localization modes correspond to the mosaics of high-angle shear bands revealed in our microstructural observations of samples deformed at effective pressures less than 130 MPa (Figs. 8–10). The bifurcation analysis also predicts that such localization modes develop during the strain softening stage (Fig. 1). To explore this further we should conduct observations on samples deformed to different stages to study the progressive development of localization.

Moreover, the bifurcation analysis (BÉSUELLE, 2001) predicts the development of dilating shear bands during the post-peak stage for $\mu > 0.28$ (if $\beta \approx \mu$). Constitutive parameters for Rothbach sandstone deformed at effective pressures of 5 MPa and 20 MPa satisfy these conditions. Our CT and microstructural observations indicate that the localized bands developed as dilating shear bands.

However, there is an apparent discrepancy in that our microstructural observations indicate formation of compaction bands in the sample failed at the effective pressure of 130 MPa (Fig. 11), even though the bifurcation analysis rules out this localization mode (mode 2). The discrepancy may arise from several intrinsic limitations in the constitutive framework of RUDNICKI and RICE (1975) that was adopted in the localization analyses. First, the plastic yield behavior is assumed to be isotropic, even though the mechanical data for Rothbach sandstone (WONG *et al.*, 1997; MILLIEN, 1993) and our microstructrual observations both indicate significant anisotropy due to the sedimentary bedding. RUDNICKI's (1977) theoretical analysis has shown that the onset of localization is sensitive to mechanical anisotropy. Second, the constitutive model does not adequately account for plastic yield and volume change induced by the mean stress (AYDIN and JOHNSON, 1983). ISSEN and RUDNICKI (2000) recently proposed a constitutive model that incorporates multiple yield surfaces and damage mechanisms, with predictions on compaction band formation that seem to be in better agreement with laboratory and microstructural observations (WONG *et al.*, 2001). More systematic studies are necessary before we can make quantitative comparisons with such a more elaborate model.

## *Acknowledgements*

We are grateful to Maurice Boutéca who allowed us to use the X-ray apparatus at the Institut Français du Pétrole and to Camille Schlitter who performed the measurements. We thank Yves Guéguen who stimulated this work. We have benefited from discussions with John Rudnicki and Kathleen Issen. The research programs at Paris and Stony Brook were partially supported by joint program Centre National de la Recherche Scientifique (CNRS) and National Sciences Foundation (NSF) under grants EAR9805072, EAR0006932 and INT9815570.

## REFERENCES

ANTONELLINI, M., AYDIN, A., POLLARD, D. D., and D'ONFRO, P. (1994), *Petrophysical Study of Faults in Sandstone Using Petrographic Image Analysis and X-Ray Computerized Tomography*, Pure Appl. Geophys. *143*, 181–201.

AYDIN, A. and JOHNSON, A. M. (1978), *Development of Faults as Zones of Deformation Bands and as Slip Surfaces in Sandstone*, Pure Appl. Geophys. *116*, 931–942.

AYDIN, A. and JOHNSON, A. M. (1983), *Analysis of Faulting in Porous Sandstones*, J. Struct. Geol. *5*, 19–31.

BAUD, P., ZHU, W., and WONG, T.-f. (2000), *Failure Mode and Weakening Effect of Water on Sandstone*, J. Geophys. Res. *105*, 16371–16389.

BÉSUELLE, P. (2001), *Compacting and Dilating Shear Bands in Porous Rocks: Theoretical and Experimental Conditions*, J. Geophys. Res., 106, 13435–13442.

BÉSUELLE, P., DESRUES, J., and RAYNAUD, S. (2000), *Experimental Characterisation of the Localisation Phenomenon Inside a Vosges Sandstone in a Triaxial Cell*, Int. J. Rock Mech. Min. Sci. *37*, 1223–1237.

BYRNE, T., MALTMAN, A., STEPHENSON, E., SOH, W., and KNIPE, R. (1993), *Deformation Structures and Fluid Flow in the Toe Region of the Nankai Accretionary Prism*, Proc. of the ODP, Scientific Results *131*, 83–192.

CURRAN, J. H. and CARROLL, M. M. (1979), *Shear Stress Enhancement of Void Compaction*, J. Geophys. Res. *84*, 1105–1112.

DAVID, C., WONG T.-f., ZHU, W., and ZHANG, J. (1994), *Laboratory Measurement of Compaction-Induced Permeability Change in Porous Rock: Implications For the Generation and Maintenance of Pore Pressure Excess in the Crust*, Pure Appl. Geophys. *143*, 425–456.

DESRUES, J., CHAMBON, R., MOKNI, M., and MAZEROLLE, F. (1996), *Void Ratio Evolution Inside Shear Bands in Triaxial Sand Specimens Studied by Computed Tomography*, Géotechnique *46*, 529–546.

DIGIOVANNI, A. A., FREDRICH, J. T., HOLCOMB, D. J., and OLSSON, W. A. (2000), *Micromechanics of Compaction in an Analogue Reservoir Sandstone*, Proc. 4th North Am. Rock Mech. Symp. 1153–1160.

ISSEN, K. A. and RUDNICKI, R. J. (2000), *Conditions for Compaction Bands in Porous Rock*, J. Geophys. Res. *105*, 21529–21536.

KAWAKATA, H., CHO, A., KIYAMA, T., YANAGIDANI, T., KUSUNOSE, K., and SHIMADA, M. (1999), *Three-dimensional Observations of Faulting Process in Westerly Granite Under Uniaxial and Triaxial Conditions by X-Ray CT Scan*, Tectonophysics *313*, 293–305.

LABUZ, J. F. and BRIDEL, J. M. (1993), *Reducing Frictional Constraint in Compression Testing through Lubrication*, Int. J. Rock Mech. Min. Sci. *20*, 451–455.

MENÉNDEZ, B. ZHU, W., and WONG, T.-f. (1996), *Micromechanics of Brittle Faulting and Cataclastic Flow in Berea Sandstone*, J. Struct. Geol. *18*, 1–16.

MILLIEN, A. (1993), *Comportement anisotrope du grès des Vosges: élasto-plasticité, localisation, rupture*, Ph.D. Thesis, Univ. of Grenoble, Grenoble, France, 220 pp.

MOLLEMA, P. N. and ANTONELLINI, M. A. (1996), *Compaction Bands: A Structural Analog For Anti-Mode I Cracks in Aeolian Sandstone*, Tectonophysics *267*, 209–228.

OLSSON, W. A. (1999), *Theoretical and Experimental Investigation of Compaction Bands in Porous Rock*, J. Geophys. Res. *104*, 7219–7228.

OLSSON, W. A. and HOLCOMB, D. J. (2000), *Compaction Localization in Porous Rock*, Geophys. Res. Lett. *27*, 3537–3540.

PATERSON, M. S., *Experimental Rock Deformation-The Brittle Field* (Spinger-Verlag, New York 1978).

RAYNAUD, S., FABRE, D., MAZEROLLE, F., GERAUD, Y., and LATIERE, H. J. (1989), *Analysis of the Internal Structure of Rocks and Characterization of Mechanical Deformation by a Non-destructive Method: X-ray Tomodensitometry*, Tectonophysics *159*, 149–159.

RUDNICKI, J. W. (1977), *The effect of stress-induced anisotropy on a model of brittle rock failure as localization of deformation*. In *Energy Resources and Excavation Technology*, Proc. 18th U.S. Symp. on Rock Mechanics, pp. 1–8, Keystone, Colorado.

RUDNICKI, J. W. and RICE, J. R. (1975), *Conditions for the Localization of Deformation in Pressure Sensitive Dilatant Materials*, J. Mech. Phys. Solids *23*, 371–394.

UNDERWOOD, E. E., *Quantitative Stereology* (Addison Wesley, Reading 1970).

Vinegar, H. J., de Waal, J. A., and Wellington, S. L. (1991), *CT Studies of Brittle Failure in Castlegate Sandstone*, Int. J. Rock Mech. Min. Sci. *28*, 441–448.

Wellington, S. L. and Vinegar, H. J. (1987), *X-Ray Computerized Tomography*, J. Pet. Tech. *39*, 885–898.

Wong, T.-f., David, C., and Zhu, W. (1997), *The Transition From Brittle Faulting To Cataclastic Flow in Porous Sandstones: Mechanical Deformation*, J. Geophys. Res. *102*, 3009–3025.

Wong, T.-f., Baud, P., and Klein, E. (2001), *Localised Failure Modes in a Compactant Porous Rock*, Geophys. Res. Lett., *28*, 2521–2524.

Wu, X. Y., Baud, P., and Wong, T.-f. (1999), *Micromechanics of Compressive Failure and Spatial Evolution of Anisotropic Damage in Darley Dale Sandstone*, Int. J. Rock Mech. Min. Sci. *37*, 1–18.

(Received March 7, 2001, revised June 1, 2001, accepted August 1, 2001)

# X-ray Micro CT for Studying Strain Localization in Clay Rocks under Triaxial Compression

**Bésuelle P.* — Viggiani G.* — Lenoir N.** — Desrues J.* — Bornert M.*****

** Laboratoire 3S, BP 53, 38041 Grenoble cedex 9, France*
*Pierre.Besuelle@hmg.inpg.fr, Cino.Viggiani@hmg.inpg.fr,*
*Jacques.Desrues@hmg.inpg.fr*

*** formerly at ANDRA and Laboratoire 3S*
*now at University of Kumamoto, Japan*
*Nicolas.Lenoir@hmg.inpg.fr*

**** Laboratoire de Mécanique des Solides, 91128 Palaiseau cedex, France*
*bornert@lms.polytechnique.fr*

ABSTRACT: *The paper presents selected results from an experimental testing program recently performed at the ESRF, where high resolution, fast X-ray micro tomography was used to evaluate the onset and evolution of strain localization in Callovo-Oxfordian argillite under deviatoric loading. In situ micro tomography allowed detailed observations of strain localization at different load levels. X-ray CT was complimented with 3D digital image correlation to obtain a sequence of incremental 3D strain fields of a deforming specimen.*

KEY WORDS: *in situ micro tomography, synchrotron, triaxial compression, strain localization, cracks, 3D digital image correlation*

## 1. Introduction

Strain localization, the concentration of deformation into narrow zones of intense shearing, is a phenomenon commonly observed in virtually all geomaterials, including rocks, soils and concrete. Experimental investigations represent an essential ingredient for improving the understanding of the mechanics and physics of shear banding. A wide range of experimental techniques have been applied over the years, which include optical and electronic microscopy, radiographic analysis, ultrasonic and acoustic techniques, multiple stress and strain local measurements, stereophotogrammetry and digital image analysis to name but a few. The challenge here, and the possible reason why so many different techniques have been used is the fact that one wants to measure deformations in a region the size of which, upon strain localization, reduces abruptly and dramatically, say from the scale of the specimen to the shear band scale. Measuring deformations throughout a test, that is: prior to, at, and after the onset of strain localization is then a formidable task, which can only be accomplished by using *field measurements*. In fact, it should be stressed that when strains are (highly) localized, stress and strain variables cannot be derived from boundary measurements of loads and displacements.

In principle, direct three dimensional (3D) observation of the internal structure of a specimen while it deforms under applied load can provide substantial advances in the understanding of shear banding in geomaterials. In this respect, the recent, rapid development of non destructive 3D imaging techniques such as X-ray tomography (*e.g.*, Baruchel *et al.*, 2000) offers new experimental possibilities, which have been indeed used in recent years for studying shear banding and failure in geomaterials. However, several requirements specific to geomaterials – confining pressure and pore pressure control – make it quite difficult to properly run a test within a typical X-ray tomography set up, especially if one intends to perform *in situ* tomography, *i.e.*, to load the specimen and to scan it in the same setting and at the same time (*e.g.*, Otani *et al.*, 2002; Raynaud *et al.*, 1989; Desrues *et al.*, 1996; Otani *et al.*, 2000; Alshibli *et al.*, 2000; Vinegard *et al.* 1991; Kawakata *et al.*, 1999).

It should be noted that all the above experimental studies have been performed with conventional Computed Tomography (CT) systems used in medical and industrial applications. However, another, much more powerful source of X-rays can be provided by the synchrotron radiation, for which the X-ray beam is a thousand billion times “brighter” than the beam produced by a hospital X-ray machine. The higher energy and photon flux of synchrotron radiation allow for a much higher resolution, down to the micrometric scale.

Such a resolution is probably unnecessary for coarse-grained geomaterials such as sand, in which the width of a shear band is known to be roughly 10 to 20 times the mean grain diameter size (*i.e.*, within a few millimeters). However, it becomes crucial for characterizing strain localization in fine-grained materials such as clays, marls and clayey rocks, in which shear bands are much thinner, and are often described as displacement discontinuities, or slip surfaces (Viggiani *et al.*, 2004). This is apparent from the relatively poor quality of the (few) available tomographic images of shear zones in fine-grained geomaterials obtained so far (Otani *et al.*, 2000; Tillard-Ngan, 1992; Hicher *et al.*, 1994).

Another difficulty with experimentally detecting strain localization is associated to the very nature of localized strain. In fact, while localization can sometimes induce large volumetric deformation – either dilatancy (or crack opening) or compaction (compaction bands), depending on the material and loading conditions – in general *volumetric* strain in a shear band is small compared to the *shear* strain. Unfortunately, X-ray CT is based on transmission measurement, hence it is sensible to density variations only. Therefore, in the absence of measurable volumetric strain in the region of localized deformation, X-ray CT may fail to detect the phenomenon, especially in its early stage (Bésuelle, 2003). As it will be shown in the paper, such a limitation can be overcome by complimenting X-ray CT with digital image correlation (DIC). Through the comparison of couples of reconstructed 3D images of a specimen at two successive steps of loading, this allows to measure an incremental displacement field, from which a strain tensor field can be obtained.

This paper presents a few selected results from a recent, unique experimental testing program where synchrotron radiation micro tomography has been used to evaluate the onset and evolution of localized deformation in a fine-grained clayey rock under deviatoric loading. A brief description of the material tested is first given in Section 2. Section 3 describes the apparatus which was specifically designed to be placed in the X-ray beam (*in-situ* tomography) at the ESRF. A few results from X-ray CT are discussed in Section 4. Then, DIC is presented in Section 5 together with a few representative results. Finally, some conclusions are drawn in Section 6.

## 2. Material Tested

The argillite tested for this study was provided by ANDRA (*Agence Nationale pour la Gestion des Déchets Radioactifs*) from their underground research laboratory (URL) site at Bure (Meuse/Haute Marne, Eastern France).

It belongs to the Callovo-Oxfordian Formation (Jurassic), which is about 130 m thick in the area of the URL, with its base at about 550 m below the ground surface. Core samples of 100 mm diameter and 320 mm length were taken at different depths between 476 and 479 m below the surface from the drill core of the boreholes EST212 and EST361 drilled at the axis of the auxiliary shaft of the URL. A candidate for the geological disposal of radioactive waste, the Callovo-Oxfordian argillite has been in recent years the object of many detailed studies (*e.g.*, Escoffier 2002, Zhang *et al.* 2004, Escoffier *et al.* 2005, Fabre and Pellet 2006). At the investigated depth, the material has an extremely low intrinsic permeability ($10^{-20}$ to $10^{-22}$ $m^2$) and a uniaxial compressive strength ranging from 20 to 30 MPa. Its water content is equal to about 6%, and clay content is in range 40 to 45%, the other minerals being essentially calcite and quartz. In order to prevent loss of water and possible damages, the samples after drilling were stored in sealing cells. Cylindrical specimens (10 mm in diameter and 20 mm in height) were prepared by cutting from the cores by means of a diamond wire saw, which minimizes material disturbance during preparation (see Lenoir 2006 for details).

## 3. Experimental Set-up

### 3.1. *Micro tomography Device*

The experiments were carried out at the high energy beamline ID15A at the European Synchrotron Radiation Facility (ESRF) in Grenoble, a third generation storage ring. This beamline has been recently equipped with a fast three-dimensional X-ray micro tomography system (Di Michiel *et al.*, 2005). In fact, the work presented in this paper is one of the first applications of fast micro tomography at ID15A. The setup is schematically shown in Figure 1a. The X-ray white radiation was generated by an 11 poles wiggler, in order to get a high photon flux. The X-ray energy used for this study ranged from 50 to 70 keV, and the radiation was filtered using a stack of polymer pieces, in order to avoid beam hardening artifacts. The triaxial apparatus (including the loading system, confining cell and specimen) was moved and rotated by a high precision positioning device in order to get a sequence of digital radiographs at different angular positions and different elevations. The X-rays transmitted through the two polycarbonate cell walls, the confining fluid, and the claystone specimen, were converted into visible light by a phosphor screen scintillator. A 1024×1024 *Dalstar* CCD camera captured the raw digital images from the phosphor screen. The pixel size was $14\times14$ $\mu m^2$, and a 1X objective was used for the scans described hereafter. The size of the beam was $14\times3.65$ $mm^2$, which allows to get, for each radiograph, 261 slices of the specimen (10 mm in diameter). The exposure time was equal to 0.04 s for each radiograph, and the complete scan of a section, obtained by taking 1200 radiographs at different equally spaced angles covering a range of 180°, took approximately 2.5 minutes. The acquisition of the entire specimen height (20 mm) took no more than 15 minutes, with a voxel size of $14\times14\times14\ \mu m^3$.

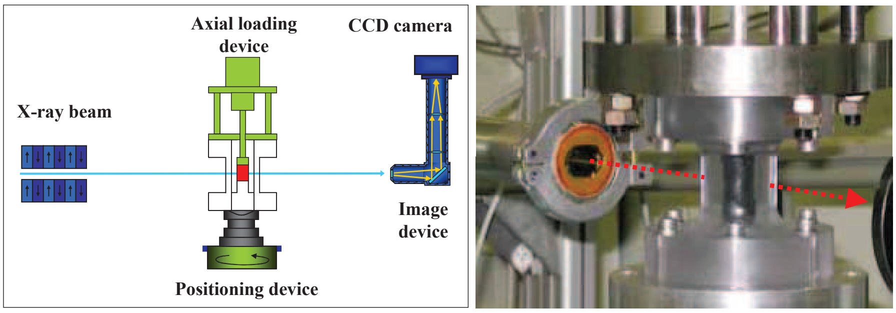

(a) (b)

**Figure 1.** *(a) scheme of the micro-CT device; (b) experimental setup showing a specimen inside the transparent triaxial cell*

### 3.2. *Triaxial Apparatus and Testing Program*

The apparatus includes a small triaxial cell and a loading device designed specifically for this program (Viggiani *et al*., 2004). The triaxial apparatus is practically the same as a conventional triaxial testing system, except for its much smaller size and the shape of the confining cell, which was designed to be as transparent as possible to the X-rays. The rock specimen is a cylinder with height twice the diameter (20 and 10 mm, respectively). The top and bottom rigid platens are enlarged and lubricated to minimize friction at the ends of the specimen. The specimen is enclosed in a thin neoprene sleeve sealed to the top and bottom platens, and placed in an oil-filled cell, which can sustain up to 10 MPa. A frictionless ram passes through the top of the cell and allows applying a stress deviator $q = (\sigma_a - \sigma_r)$, $\sigma_a$ and $\sigma_r$ being the axial and radial total stress, respectively. The axial strain, $\varepsilon_a$, is obtained by measuring the movement of the ram using a LVDT.

The axial load and hence the deviator stress is applied in a displacement-controlled manner using a motor-driven screw actuator. The loading system was designed in cooperation with CSP (*Composants et Systèmes de Précision*) and can be placed in the X-ray beamline without interfering with the tomographic scans. It is quite compact and light (less than 30 kg), which is important since it directly sits on the translation and rotation stage during the experiment. The system has a maximum loading capacity of 7.5 kN, and allows to move the ram at a constant rate in the range of 1 to 100 µm/min. It is worth noting that while in a conventional triaxial system the tensile reaction force is carried by a loading frame, in this case it is carried by the cell walls, which therefore are subjected to traction in the axial direction. This allows a clear path, free of any obstacle (apart from the cell walls), for the X-ray beam within the region to be scanned. X-ray absorption through the apparatus must be small, so the walls of the cell have to be as thin as possible. In the mean time, they cannot be too thin, as they must resist the axial traction — in addition to the cell pressure. The solution adopted was to reduce the thickness of the polycarbonate walls to a value of 10 mm only where needed, *i.e.* in the central region of the cell. The output signals of all transducers (for axial load, cell pressure, and axial strain) are conditioned by a 16 bit process interface unit which is linked to a laptop computer, which also controls the loading actuator. The experiments are remotely controlled from a control cabin, because the shield room, the so-called *experimental hutch*, is obviously inaccessible when the shutter is open.

A total of four triaxial compression tests on Callovo-Oxfordian argillite were performed, at three different values of the confining stress (1, 5 and 10 MPa). The tests were carried out under undrained conditions, *i.e.*, no drainage of the pore fluid into, or out of, the specimen was allowed. See Lenoir (2006) for further details.

## 4. Selected Results

Results from only two tests (*ESTSYN01* and *ESTSYN02*) are presented herein. The confining pressure (total mean stress) was equal to 10 MPa and 1 MPa, respectively. Deviatoric loading was performed under displacement control, by advancing the loading ram at a rate of 3.0 µm/min, which corresponds to a nominal axial strain rate of $2.5.10^{-6}$ $s^{-1}$ for a 20 mm specimen height. For each test, the specimen was scanned at different steps: before and right after applying the confining pressure (steps 0 and 1, respectively), and then at different levels of axial strain during deviatoric loading (steps 2-7 for test *ESTSYN01* and steps 2-5 for test *ESTSYN02*). One last scan of the specimen was performed at the end of the test, after removal of the confining pressure (step 8 for test *ESTSYN01* and step 6 for test *ESTSYN02*). It is worth to note that the ram displacement was stopped at those points of the test when a tomographic scan of the specimen was required. The specimen was scanned while the axial strain was held constant, which unavoidably caused some amount of axial load relaxation during scanning. However, the scanning operations were fast enough (approximately 15 minutes for six sections, *i.e.*, the full specimen height) for this relaxation to be relatively small.

Deviator stress $q$ is plotted as a function of axial strain $\varepsilon_a$ in Figure 2 for both tests. All stresses and strains are positive in compression. The numbers noted on each curve are the scanning step numbers. In test *ESTSYN01*, the deviator stress first increases (almost linearly up to step 2), then attains a peak value of 28 MPa around step 3 and finally decreases, essentially leveling off at about 19 MPa after step 5. A single shear band formed in the specimen during the test, which could be clearly observed by the eye at the end of the test.

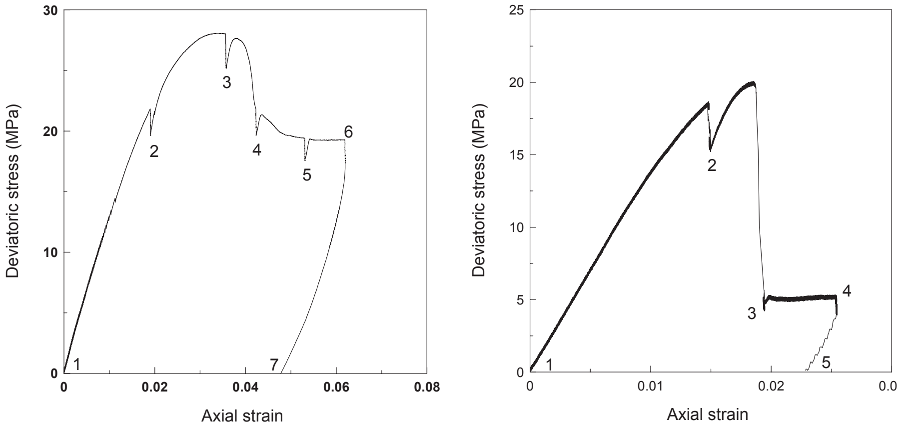

**Figure 2.** *Deviator stress vs. axial strain for test ESTSYN01 (10MPa confining stress, left) and test ESTSYN02 (1MPa confining stress, right)*

We focus now on the X-ray CT scans of specimen *ESTSYN01* during loading. Figure 3 shows the reconstruction of a tomographic slice perpendicular to the specimen's axis for each scanning step. Note that the elevation of a given slice decreases from one scan to the next, to take into account the specimen shortening during loading. Strain localization becomes visible at step 4 as a very narrow band in the upper left part of the slice. The band of localized deformation appears as a darker zone (2-3 pixels, *i.e.*, 30-40 µm thick), which means that the material is dilating inside the band (darker indicates lower mass density). In the subsequent scanning steps, the band becomes increasingly visible in term of both length and thickness (about 60 µm at step 7), essentially in the outer region of the slice. A material shift can be observed at the intersection of the band with the external surface of the specimen. The size of such shift increases with specimen shortening, which is due to the relative sliding on the band. When the confining pressure is removed (step 8), the band of localization opens up in the outer region of the specimen and it looks like an open crack. However, no trace of localization is visible in the central region of the slice.

By performing a 3D reconstruction, it is possible to obtain a virtual slice in a plane orthogonal to the slices in Figure 3, *i.e.*, parallel to the specimen's axis. In such a plane, the region of localization appears as a straight band. Interestingly, the existence of distinct inclusions of calcite in the argillite turned out to be particularly helpful for characterizing shear sliding along the band. In fact, some of these inclusions, which are due to the activity of bio-organisms during sedimentation of the clay particles, have a quite elongated vein shape and a length of a few millimeters (Figure 4a), thus appearing as distinct thin white bands in a CT image. A specific analysis based on a gray level separation, allowed to recognize these inclusions as well as the open fissures (respectively shown in yellow and in red in Figure 4b). It appears that upon loading, the vein-shaped inclusion shown in Figure 4 was strongly deformed by the band of localization (compare Figure 4a at step 1 and Figure 4b at step 8).

The evolution of the inclusion geometry throughout test *ESTSYN01* is shown in Figure 4c. Some shearing of the inclusion is apparent starting from step 5, and becomes more and more pronounced for increasing deformation (steps 6 through 8). However, the region of intense shearing in the shale is not associated to a measurable variation of density (at least within the X-ray CT resolution, which is based on X-ray absorption). This implies that the band of localization in the central zone of the specimen is essentially a shear band without substantial volumetric deformation, whereas some localized volume changes (eventually, crack opening) can be observed as the region of localized deformation is closer to the edge of the slice.

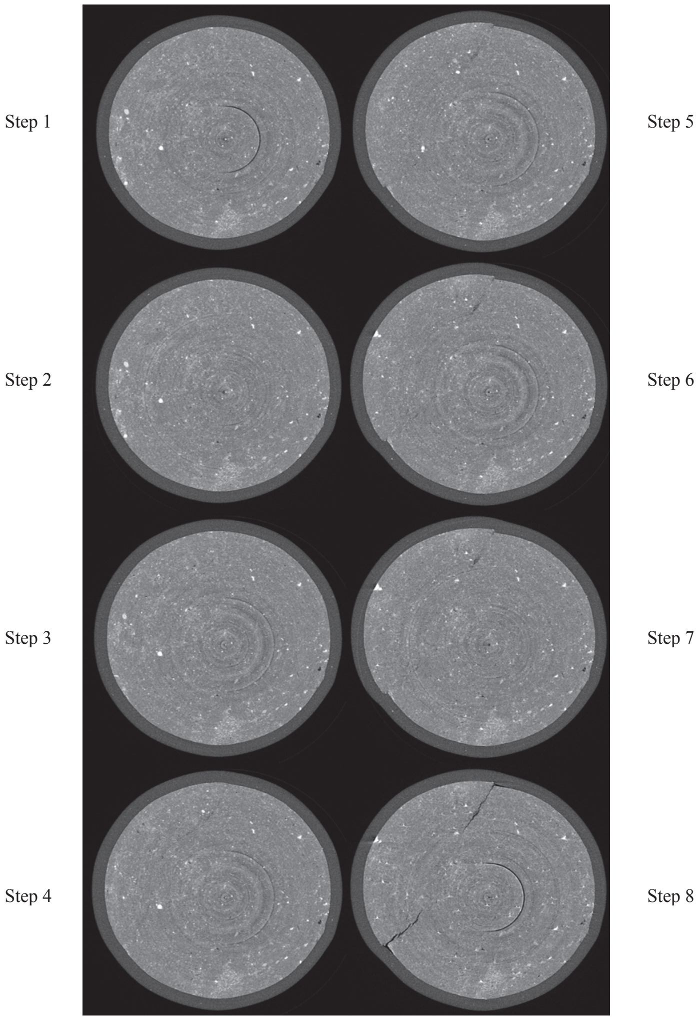

**Figure 3.** *A horizontal CT slice of specimen ESTSYN01 at different steps*

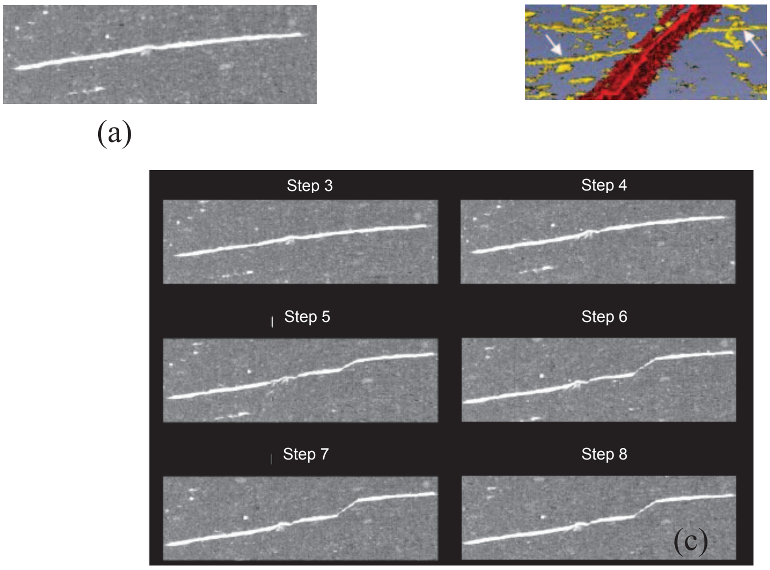

**Figure 4.** *A natural vein-shaped inclusion in specimen ESTSYN01: (a) CT image in a vertical plane before loading (step 1), (b) 3D reconstruction after unloading (step 8), and (c) CT image in a vertical plane at different steps of loading*

Test *ESTSYN02* exhibited a much more brittle behavior, see Figure 2. The deviator stress drops from 20 MPa down to about 5 MPa immediately after the peak, and stays constant in the post-peak portion of the test. At the end of the test, the specimen was split into several pieces. Figure 5 shows the evolution of three tomographic slices at different elevations (11.0, 7.2 and 3.6 mm from the bottom of the specimen, respectively) throughout the test. At the lower elevation, localized deformation is visible already at step 2, appearing as two dark (*i.e.*, dilating) zones a few pixels wide. These bands include a few segments which can be also interpreted as open cracks. The regions of localization are in any case extremely thin with respect to the spatial resolution, which sometime makes it difficult to discriminate between a dilating band and an opening crack. At step 3, several fissures can be observed on all three slices. Their opening increases thereafter, especially after the removal of confining pressure (step 6), when a well developed network of fissures has developed at the lower elevation. A 3D reconstruction of the data for test *ESTSYN02* (not shown herein) allowed to recognize that while some of these fissures are vertical (axial splitting), also inclined fissures developed in the specimen, so that the overall spatial organization of the fissures is quite complex (see Lenoir 2006 for details).

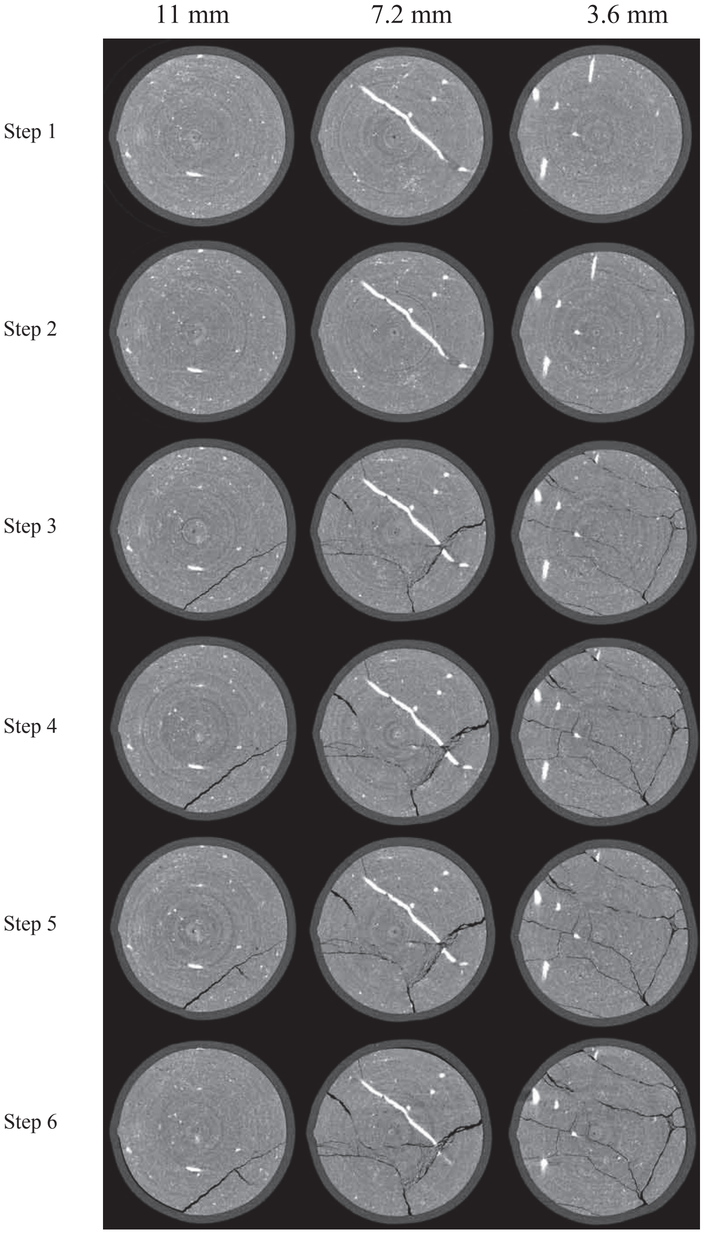

**Figure 5.** *Horizontal CT slices of specimen ESTSYN02 at different steps and for three different elevations*

## 5. Strain Field Measurement by Digital Image Correlation

Direct observation of X-ray micro tomography images allows for immediately detecting volumetric strain, since dilation (contraction) corresponds to a change of mass density, which in turn results in a decrease (increase) of X-ray attenuation. However, as far as shear (deviatoric) strain is concerned, this does not necessarily induce any volume change and therefore it cannot be directly detected by measuring changes in X-ray attenuation. In this study, we have developed a general method for obtaining the distribution of both the volumetric and deviatoric components of strain increment between two reconstructions of a specimen at two different steps of deformation. The method, which is based on the correlation of digital volume (3D) tomographic images, is thoroughly described elsewhere (Lenoir *et al.*, 2006). Herein, only a short explanation of the method will be given, along with some background on 3D DIC. Then, a few representative results will be shown of 3D strain fields obtained for test *ESTSYN01*.

Digital Image Correlation (DIC, hereafter) is a mathematical method which essentially consist in recognizing the same material point on a pair of digital images of an object. A material point is assumed to be fully identified by its local pattern (*e.g.*, the gray level distribution around the point in a black and white image). Such a local pattern is assumed to be unique for a given point, *i.e.*, it cannot be found elsewhere on the image. By optimizing an appropriate correlation function, DIC allows for determining for each point/pattern on the first image, the most likely location of such a point/pattern on the second image. Note that from one image to the other, a pattern is in general subject to translation, rotation and distortion. By repeating this procedure for a number of points, a full displacement and deformation field can be obtained for the pair of images.

Such a method was applied to measure 2D displacement and deformation fields on the surface of a specimen already back in the 80s (Chu *et al.*, 1985; Bruck *et al.*, 1989). Since, DIC techniques have become widely used in geomechanics (*e.g.*, Gudehus and Nübel, 2004; Bhandari and Inoue, 2005 – to mention just a few recent studies). Note that using two rather than just one digital camera, one can measure 3D displacements on the surface of a specimen (*e.g.*, Helm *et al.*, 1996). However, surface displacement fields are not necessarily representative of the deformation inside a specimen, except in some particular cases (*e.g.*, specimens loaded in plane strain).

DIC has also been applied to X-ray photographs (Russel and Sutton, 1989; Synnergen *et al.*, 1999). In this case, the pattern is the X-ray attenuation distribution through the specimen in the direction of propagation of the rays. More recently, full three dimensional displacement and strain fields have been measured based on X-ray (micro-) CT reconstructions (Bay *et al*., 1999, Smith *et al.*, 2002; Verhulp *et al*., 2004; Bornert *et al*. 2004b; Forsberg and Sjödahl, 2004). The particular 3D DIC method used in the present study is similar to that described by Bornert *et al.* (2004a). Additional information on its application to the present CT images of clayey rocks are given elsewhere (Lenoir *et al*., 2006). Herein it will be sufficient to bear in mind that each 3D image is decomposed in several subsets, which are cubes in the reference image, each of them containing $20^3$ voxels. The center of a subset is identified by the gray level distribution inside the subset. Also note that due to the small deformation experienced by the argillite specimens, for this study the transformation between two images was assumed to be a rigid translation, without any rotation and distortion. While such an approximation substantially reduced the computing time, it still provided a fair resolution (see Lenoir *et al*., 2006 for further details).

Hereafter, a few results are presented where DIC was applied to the 3D tomographic images from test *ESTSYN01*. Only the two increments between steps 2 and 3 and between steps 3 and 4 are discussed herein (see Figures 2 and 3). Hereafter, these two increments will be referred to as the pre-peak and the post-peak increment, respectively. Figures 6 and 7 show the (incremental) strain field as obtained by DIC. More precisely, these fields represent the second invariant of the strain tensor, in the sense of von Mises, which is a measure of shear strain. To better appreciate the computed 3D fields, these are also shown by a few horizontal and vertical cuts (see respectively left and right images on Figures 6 and 7). The maximum strain plotted in these figures equals 0.15, which means that the red color indicates shear strain values equal to, or greater than 0.15.

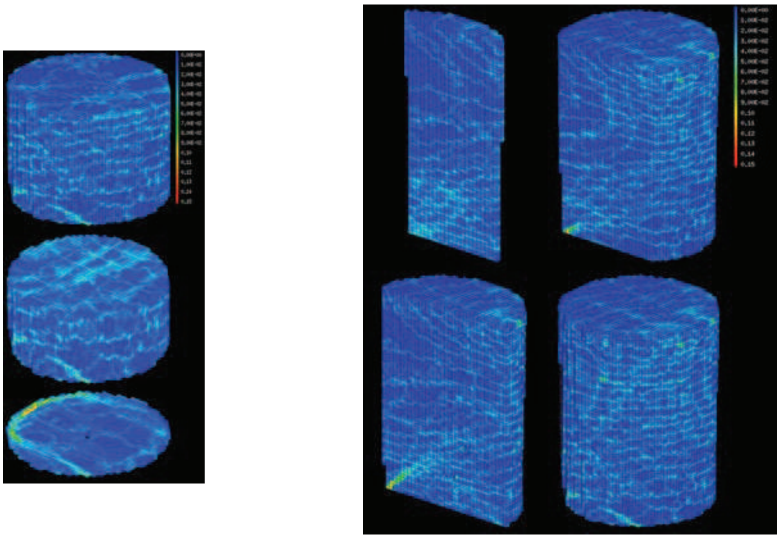

**Figure 6.** *Three dimensional shear strain increment field in the pre-peak increment, represented by horizontal cuts at different heights (left), and vertical cuts (right)*

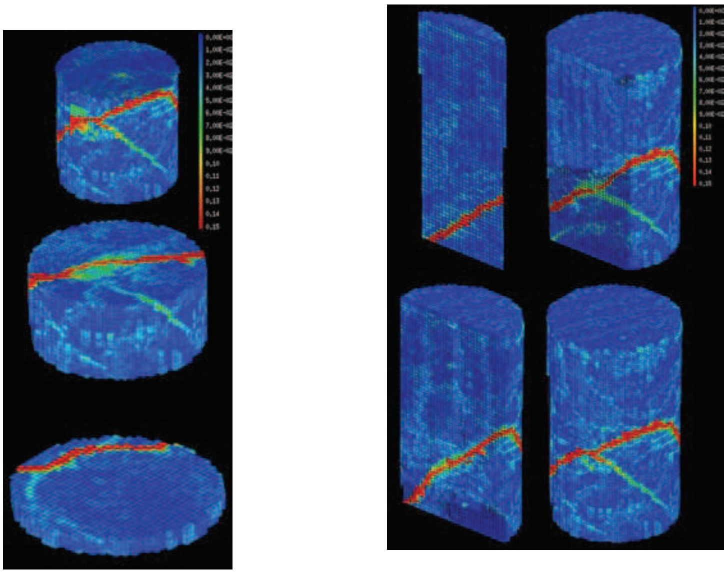

**Figure 7.** *Three dimensional shear strain increment field in the post-peak increment, represented by horizontal cuts at different heights (left), and vertical cuts (right)*

Strain localization is distinctly visible already in the pre-peak increment (Figure 6), close to the bottom edge of the specimen. Such a shear zone appears as a narrow, straight band in the vertical cuts. The shape of the shear zone is circular in the horizontal bottom cut, which suggests that the overall shape of the zone of localized deformation is influenced to some extent by the boundary conditions. In the post-peak increment (Figure 7), the shear band has entirely propagated through the specimen. As compared to the pre-peak increment, the zone of localized deformation appears straight (planar) both in the vertical and in the horizontal cuts. A second shear band can also be observed, which is characterized by lower values of the (incremental) shear strain. A closer scrutiny of the 3D tomographic images revealed that very close to the intersection of these two bands, in the external part of the specimen, a large inclusion of calcite and pyrite existed in the argillite. This inclusion is in fact also revealed by the green volume (a few subsets in size) which appeared on the 3D strain fields in Figure 7 (see top left and bottom right images). Such an inclusion was most likely stiffer than the matrix, which induced a shear strain concentration. Therefore, it can be concluded that in test *ESTSYN01*, the pattern of localization was influenced by both the boundary conditions (at the specimen bottom) and natural inclusions in the specimen. Fields of the first invariant of the strain tensor (*i.e.*, the volumetric strain) were also computed for test *ESTSYN01*, which are not reported herein (see Lenoir, 2006). These fields indicate that volume changes localized only in the post-peak increment. Just like the simple observation of CT images (without any DIC analysis), the inspection of volumetric strain fields allows to detect shear banding only at a later stage of the test, when dilatancy and/or crack opening induced measurable mass density variations.

Finally, it is worth to note that the thickness of the shear bands as it appears in these DIC-based shear strain fields is largely over evaluated, because it cannot be smaller than the subset size. Recall that the side of the subset was equal to 20 voxels (*i.e.*, 280 μm) in this analysis, whereas CT images indicate that the thickness of the zones of localized deformation in the tested specimens was typically less than 70 μm (see Lenoir, 2006).

## 6. Conclusions

An original loading system has been developed for testing argillaceous rocks at a relatively high confining pressure (10 MPa), which allows for micro tomography observation of the specimen under deviatoric loading. The high energy synchrotron radiation used for this study allowed to combine both *fast* tomography and *high resolution* micro tomography. This is essential for argillites, due to the fine micro structure (with zones of localized deformation which can be only a few microns wide) and their susceptibility to creep, which makes it difficult to have a stable specimen configuration if the radiation period is too long.

X-ray tomography essentially measures material density distribution. During a test, changes of X-ray attenuation are therefore due to volumetric deformation. If the material in a zone of localized deformation is essentially strained in shear, without significant volumetric strain, then the phenomenon can be hard to detect. However, it has been shown in this study that X-ray 3D imaging can be effectively complimented with 3D digital image correlation, which allows for measuring a 3D displacement field in a specimen. From the displacement field, a 3D strain field can then be obtained, including the shear and volumetric strain components. The quality of the results that can be obtained by digital image correlation crucially depend on the quality of the images (which need to be well contrasted) as well as on the signal-to-noise ratio, that must be sufficiently high. In this study, while the use of synchrotron light allowed to meet the latter requirement, the contrast in the images directly results from the natural heterogeneity of the tested material.

Different regimes of behavior were obtained for the Callovo-Oxfordian argillite in the investigated confining stress range, from brittle (at 1 MPa) to ductile (at 10 MPa). This paper has mainly focused on the ductile behavior at higher confining stress, where a single band of localized deformation was observed and there was little to very little volumetric strain in such a band. At lower confining stresses, failure was associated to the appearance of several open cracks, both parallel to the direction of loading (axial splitting) and inclined. In this case, the application of digital image correlation is more difficult because the specimen splits into several pieces.

## 7. Acknowledgements

The authors are very grateful to Marco Di Michiel from the ESRF at Grenoble for his invaluable contribution to the experimental program. We also wish to thank ANDRA for financially supporting this project and for supplying core samples from their site at *Bure*.

## 8. References

Alshibli K.A., Sture S., Costes N.C., Franck M.L., Lankton M.R., Batiste S.N., Swanson R.A., “Assessment of localized deformation in sand using X-ray computed tomography”, *Geotechnical Testing Journal*, vol. 23, p. 274-299, 2000.

Baruchel J., Buffière J.Y., Maire E., Merle P., Peix G, *X-ray Tomography in Materials Science*, Paris, Editions Hermes, 2000.

Bay B.K., Smith T.S., Fyhrie D.P., Saad M., “Digital volume correlation: three-dimensional strain mapping using X-ray tomography”, *Experimental Mechanics*, vol. 39 no. 3, p. 217-226, 1999.

Bésuelle P., “X-ray CT observations of strain localization and failure in two porous sandstones”, *Proc. 1st Int. Workshop X-ray CT for Geomaterials, GeoX 2003*, Kumamoto, Japan, p. 287-292, 6-7 november 2003.

Bhandari A.R., Inoue J., “Strain localization in soft rocks – a typical rate-dependent solid: experimental and numerical studies”, *International Journal for Numerical and Analytical Methods in Geomechanics*, vol. 29, p. 1087-1107, 2005.

Bornert M., Chaix J.M., Doumalin P., Dupré J.C., Fournel T., Jeulin D., Maire E., Moreaud M. and Moulinec H., “Mesure tridimensionnelle de champs cinématiques par imagerie volumique pour l'analyse des matériaux et des structures”, *Instrumentation, Mesure, Métrologie*, vol. 4, p. 43-88, 2004.

Bornert M., Doumalin P., Maire E., Moulinec H., “Full 3D investigation of the local straint field in particulate metal matrix composites”, *Proc. 12th Int. Conf. on Experimental Mechanics ICEM12*, Bari, Italy, p. 1-8, 29 August-2 Sept. 2004.

Bruck H.A., McNeill S.R., Sutton M.A., Peters W.H., “Digital image correlation using Newton-Raphson method of partial differential correction”, *Experimental Mechanics*, vol. 29 no. 3, p. 261-267, 1989.

Chu T.C., Ranson W.F., Sutton M.A., Peters W.H., “Applications of digital-image-correlation techniques to experimental mechanics”, *Experimental Mechanics*, vol. 25 no. 3, p. 232-244, 1985.

Desrues J., Chambon R., Mokni M., Mazerolle F., “Void ratio evolution inside shear bands in triaxial sand specimens studied by computed tomography”, *Géotechnique*, vol. 46, p. 529-546, 1996.

Di Michiel M., Merino J.M., Fernandez-Carreiras D., Buslaps T., Honkimäki V., Falus P., Martins T., Svensson O., “Fast microtomography using high energy synchrotron radiation”, *Review of Scientific Instruments*, vol. 76, 2005.

Escoffier S., Caractérisation expérimentale du comportement hydromécanique des argilites Meuse/Haute Marne, PhD thesis, Institut National Polytechnique de Lorraine, 2002.

Escoffier S., Homand F., Giraud A ., Hoteit N., Su K., “Under stress permeability determination of the Meuse/Haute-Marne mudstone”, *Engineering Geology*, vol. 81, no. 3, p. 329-340, 2005.

Fabre G., Pellet F., “Creep and time-dependent damage in argillaceous rocks”, *International Journal of Rock Mechanics and Mining Sciences*, vol. 43, no. 6, p. 950-960, 2006.

Forsberg F., Sjödahl M., “Tomographic 3D-DSP: measurement of internal deformations”, *Proc. 12th Int. Conf. on Experimental Mechanics ICEM12*, Bari, Italy, p. 217-226, 29 august-2 sept. 2004.

Gudehus G. and Nübel K., “Evolution of shear bands in sand”, *Géotechnique*, vol. 54, p. 187-201, 2004.

Helm J.D., McNeill S.R., Sutton M.A., “Improved three-dimensional image correlation for surface displacement measurement”, *Optical Engineering*, vol. 35 no. 7, p. 1911-1920, 1996.

Hicher P.Y., Wahyudi H., Tessier D., “Microstructural analysis of strain localisation in clay”, *Computers and Geotechnics*, vol. 16, p. 205-222, 1994.

Kawakata H., Cho A., Kiyama T., Yanagidani T., Kusunose K., Shimada H., “Three-dimensional observations of faulting process in Westerly granite under uniaxial and triaxial conditions by X-ray CT scan”, *Tectonophysics*, vol. 313, p. 293-305, 1999.

Lenoir N., Comportement mécanique et rupture dans les roches argileuses étudiés par micro tomographie à rayons X, PhD thesis, Grenoble University (http://tel.ccsd.cnrs.fr/tel-00011996), 2006.

Lenoir N., Bornert M., Desrues J., Bésuelle P., Viggiani G., “3D digital image correlation applied to X-ray micro tomography images from triaxial compression tests on argillaceous rock”, *Strain* (submitted), 2006.

Otani J., Mukunoki T., Obara Y., "Characterization of failure in sand under triaxial compression using an industrial X-ray scanner", *International Journal of Physical Modelling in Geotechnics*, vol. 1, p. 15-22, 2002.

Otani J., Mukunoki T., Obara Y., "Application of X-ray CT method for characterization of failure in soils", *Soils and Foundations*, vol. 40, p. 111-118, 2000.

Raynaud S., Fabre D., Mazerolle F., Géraud Y., Latière H.J., "Analysis of the internal structure of rocks and characterization of mechanical deformation by a non-destructive method: X-ray tomodensitometry", *Tectonophysics*, vol. 159, p.149-159, 1989.

Russel S.S., Sutton M.A., "Strain-field analysis acquired through correlation of X-ray radiographs of a fiber-reinforced composite laminate", *Experimental Mechanics*, vol. 29 no. 2, p. 237-240, 1989.

Smith T.S., Bay B.K., Rashid M.M., "Digital volume correlation incliding rotational degrees of freedom during minimization", *Experimental Mechanics*, vol. 42 no. 3, p. 272-278, 2002.

Synnergren P., Goldrein H.T., Proud W.G., "Application of digital speckle photography to flash x-ray studies of internal deformation fields in impact experiments", *Applied Optics*, vol. 38 no. 19, p. 4030-4036, 1999.

Tillard-Ngan D., Etude de la rupture dans les géomatériaux cohésifs. Application à la marne de Beaucaire, PhD thesis, Grenoble University, 1992.

Verhulp E., van Rietbergen B., Huiskes R., "A three-dimensional digital image correlation technique for strain measurements in microstructures", *Journal of Biomechanics*, vol. 37, p. 1313-1320, 2004.

Viggiani G., Lenoir N., Bésuelle P., Di Michiel M., Marello S., Desrues J., Kretzschmer M., "X-ray microtomography for studying localized deformation in fine-grained geomaterials under triaxial compression", *C. R. Mécanique*, vol. 332, p. 819-826, 2004.

Vinegard H.J., de Waal J.A., Wellington S.L., "CT studies of brittle failure in Castlegate sandstone", *International Journal of Rock Mechanics and Mining Sciences*, vol. 28, 1991, p. 441-448.

Zhang C., Rothfuchs T., "Experimental study of the hydro-mechanical behaviour of the Callovo-Oxfordian argillite", *Applied Clay Science*, vol. 26, no. 1-4, p. 325-336, 2004.

Hall, S. A. *et al.* (2010). *Géotechnique* **60**, No. 5, 315–322 [**doi:** 10.1680/geot.2010.60.5.315]

# Discrete and continuum analysis of localised deformation in sand using X-ray μCT and volumetric digital image correlation

S. A. HALL*, M. BORNERT†‡, J. DESRUES*, Y. PANNIER†, N. LENOIR*, G. VIGGIANI*
and P. BÉSUELLE*

**The objective of this work was to observe and quantify the onset and evolution of localised deformation processes in sand with grain-scale resolution. The key element of the proposed approach is combining state-of-the-art X-ray micro tomography imaging with three-dimensional volumetric digital image correlation techniques. This allows not only the grain-scale details of a deforming sand specimen to be viewed, but also, and more importantly, the evolving three-dimensional displacement and strain fields throughout loading to be assessed. X-ray imaging and digital image correlation have been in the past applied individually to study sand deformation, but the combination of these two methods to study the kinematics of shear band formation at the grain scale is the first novel aspect of this work. Moreover, the authors have developed a completely original grain-scale volumetric digital image correlation method that permits the characterisation of the full kinematics (i.e. three-dimensional displacements and rotations) of all the individual sand grains in a specimen. The results obtained using the discrete volumetric digital image correlation confirm the importance of grain rotations associated with strain localisation.**

**KEYWORDS:** deformation; fabric/structure of soils; failure; laboratory tests; sands

**L'objectif du travail présenté était d'observer et de quantifier le processus de localisation de la déformation dans un sable, à l'échelle des grains. La clé de l'approche proposée est la combinaison de la tomographie à rayons X de dernière génération, avec la généralisation des techniques de corrélation d'images numériques aux images volumiques 3D (V-DIC). Cette approche permet non seulement d'observer les détails à l'échelle des grains pour l'ensemble d'un échantillon soumis à un processus de déformation, mais aussi et surtout de mesurer les champs de déplacement et de déformation associés, tout au long du chargement. Bien que l'imagerie X et la corrélation d'images numériques aient déjà été appliquées séparément pour l'étude de la déformation du sable, la combinaison de ces deux méthodes pour l'étude de la cinématique de formation de bande de cisaillement dans le sable observé comme milieu granulaire est inédite, et c'est le premier aspect novateur des travaux présentés ici. De plus, nous avons développé une méthode de V-DIC discrète entièrement originale, permettant de caractériser la cinématique individuelle complète (à savoir déplacements et rotations tridimensionnels) de tous les grains de sable dans l'échantillon. Les résultats obtenus en utilisant la V-DIC discrète confirment l'importance de la rotation individuelle des grains, associée à la localisation de la déformation.**

## INTRODUCTION

The importance of strain localisation in soil behaviour has been known for a long time, and it has been thoroughly investigated in the laboratory. However, it should be kept in mind that in the presence of localised deformations, the meaning of stress and strain variables derived from boundary measurements of loads and displacements is only nominal, or conventional. Therefore, the most valuable experimental contributions to the understanding of localised deformation are those measuring, in one way or another, the full field of deformation in the specimen, which is the only means by which test results can be appropriately interpreted (Viggiani & Hall, 2008). Full-field analysis of strain localisation in sand started with work in the late 1960s in Cambridge (e.g. Roscoe *et al.*, 1963; Roscoe, 1970) and has been continued over the last decades in the work of a number of groups (see a review by Desrues & Viggiani (2004)). Most of these works were conducted using specifically designed plane strain devices, and used a range of full-field methods, the more advanced of which allowed observation of the specimen throughout loading by optical methods, thereby permitting measurement of the evolving strain field. In the 1960s, X-ray radiography was first used to measure two-dimensional (2D) strain fields in sand (e.g. Roscoe, 1970). From the early 1980s, X-ray tomography was used by Desrues and coworkers (Desrues, 1984; Colliat-Dangus *et al.*, 1988; Desrues *et al.*, 1996) and later by Alshibli *et al.* (2000); see Desrues (2004) for a review. These studies provided valuable three-dimensional (3D) information on localisation patterning in sand, and demonstrated the potential of X-ray tomography as a quantitative tool, for example for measuring the evolution of void ratio inside a shear band and its relation to critical state (Desrues *et al.*, 1996).

The recent advent of X-ray micro tomography, originally with synchrotron sources and now with laboratory scanners, has provided much finer spatial resolution, which opens up new possibilities for understanding the mechanics of granular media (in three dimensions) at the scale of the grain. Oda *et al.* (2004) presented micro tomography images of sand grains inside a shear band, showing organised structures that would not have been seen in standard X-ray tomography images (because of insufficient resolution) and that had only previously been observed in 2D thin sections (Oda & Kazama, 1998).

It should be noted that the images by Oda *et al.* (2004) were obtained post-mortem, that is after testing. However, a full understanding of the mechanisms of deformation, in particular localisation, can only be achieved if the entire deformation process is followed throughout a test while the

---

Manuscript received 13 February 2009; revised manuscript accepted 12 October 2009.
Discussion on this paper closes on 1 October 2010, for further details see p. ii.

* Laboratoire 3S-R, CNRS, Université Joseph Fourier, Grenoble, France.
† LMS, CNRS, École Polytechnique, Palaiseau, France.
‡ UR Navier, École des Ponts ParisTech, Marne-la-Vallée, France.

specimen deforms. This is possible by using in-situ X-ray tomography (in situ meaning X-ray scanning at the same time as loading). A number of such in-situ studies for triaxial tests on sand have been performed using medical or industrial tomography systems (e.g. Desrues *et al.*, 1996; Alshibli *et al.*, 2000; Otani *et al.*, 2002). More recently, Matsushima *et al.* (2006, 2007) have used synchrotron X-ray in-situ micro tomography, which allowed them to identify individual sand grains and track their displacements throughout a triaxial test – note that this tracking was carried out only in two dimensions for a section through the specimen.

In the present authors' previous work 3D volumetric digital image correlation (V-DIC) has been applied to a sequence of X-ray tomography images taken during a triaxial test on a clay–rock specimen (Lenoir *et al.*, 2007). In the present paper, results are shown of a similar DIC-based analysis of deformation for a sand specimen under triaxial compression. In addition a new grain-scale V-DIC method is developed that permits the characterisation of the full kinematics (i.e. 3D displacements and rotations) of all the individual sand grains in a specimen.

The structure of the paper is as follows. First, the experimental set-up for triaxial testing with concurrent X-ray micro tomography is described. The main features of the DIC methodologies (continuum and discrete) used in this study and present results from one triaxial compression test on Hostun sand are then described. Complete 3D images of the specimen were recorded at several stages throughout the test, which were subsequently analysed using the two different V-DIC approaches. The evolution of full-field incremental kinematics (at both the continuum level and the grain scale) is presented, with special emphasis on strain localisation. Different features of localised deformation are identified at different scales and their spatial and temporal development is characterised.

## EXPERIMENTAL SET-UP AND MATERIAL TESTED

The experimental results presented in this work come from a testing programme carried out at the European Synchrotron Radiation Facility (ESRF) in Grenoble on beamline ID15A. X-ray micro tomography allows high spatial resolution (in the order of a few microns), which is crucial for understanding mechanics down to the grain scale. Using a synchrotron source also provides, thanks to the high photon flux, very fast scanning (minutes, as opposed to hours for laboratory X-ray scanners). In these experiments, acquisition times were 12 min for a scan of the entire sample.

The tests were conducted using a specifically built in-situ set-up that could be placed in the X-ray beam allowing the specimens to be scanned under load, see Fig. 1. The triaxial apparatus, made from poly(methyl methacrylate) (PMMA) (very transparent to X-rays), is practically the same as a conventional system, except the much smaller size and the shape of the confining cell. Note that the tensile reaction force is carried by the cell walls and not by tie bars (which avoids having any obstacles to the X-ray beam). The axial load and hence the deviator stress are applied using a motor-driven screw actuator, which also does not interfere with the tomographic X-ray scans. See Lenoir (2006) and Viggiani *et al.* (2004) for full details.

The triaxial compression test discussed herein was performed on a dry specimen of Hostun sand under a confining pressure of 100 kPa. Deviatoric loading was strain controlled, with a screw-driven piston descending at 60 μm/min, which corresponds to quite a low strain rate (0·05%/min for a 11 mm high specimen). Hostun sand is a fine-grained, angular siliceous sand with a mean grain size ($D_{50}$) of about 300 μm. The specimen was 11 mm in diameter, 22 mm high and had an initially dense packing. It should be noted that despite the small sample size (in comparison to standard triaxial tests on sands), the specimen can be considered large enough to be mechanically pertinent (i.e. its response can be considered representative of that of a larger mass of the material); in fact the sample comprises roughly 50 000 grains. These reduced dimensions were imposed by the X-ray imager width, which was just 14 mm (the sample needed to be smaller than this in order not to risk passing out of the field of view, although this does occur by the end of the test; see later). The spatial resolution (i.e. the voxel size) was set to $14 \times 14 \times 14$ μm$^3$, which was enough to

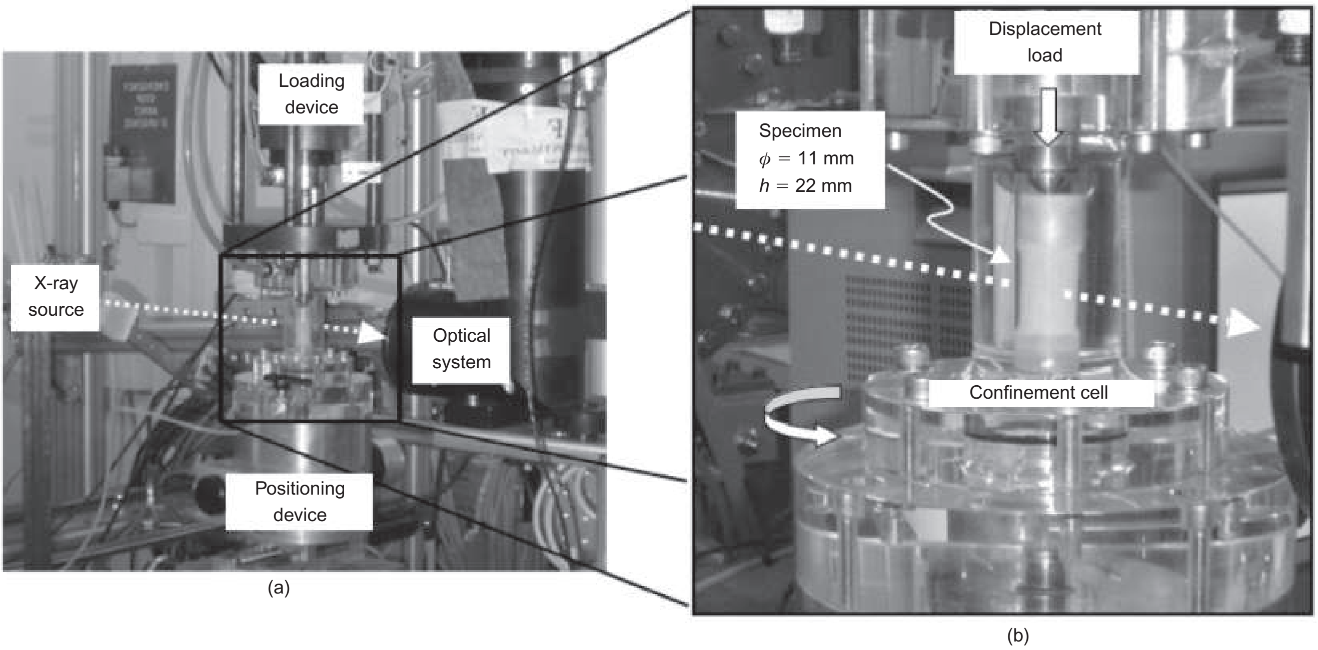

(a)

(b)

**Fig. 1. Tomography set-up for triaxial testing at the beam-line ID15A at ESRF. (a) Complete set-up on the beam-line and (b) zoom on the specimen inside the triaxial cell**

identify clearly the individual grains (recall that the mean grain size is around 300 μm or 21 voxels; each grain contained about 5500 voxels in the tomography images).

## CONTINUUM AND DISCRETE VOLUMETRIC DIGITAL IMAGE CORRELATION

Surface full-field strain measurement by digital image correlation (DIC) techniques was pioneered in the 1980s (e.g. Sutton *et al.*, 1983; Chu *et al.*, 1985). The availability of increasingly efficient optical sensors and the increase of computer power (at a much lower cost) have made DIC techniques almost standard in experimental mechanics. Numerous applications have been reported for a wide range of materials and structures, loading conditions, scales and imaging techniques, see for example the recent review by Withers (2008). DIC can be used to determine surface displacements and strains in two dimensions using a single camera, or in three dimensions using two cameras (stereovision and stereo-correlation, where out-of-plane surface displacements can be measured, see Orteu (2009)). The extension of DIC to measure displacement and strain fields within solid objects, for example using 3D images acquired by X-ray tomography, is more recent (e.g. Bay *et al.*, 1999; Bornert *et al.*, 2004; Verhulp *et al.*, 2004; Lenoir *et al.*, 2007; also see Bay (2008) for a review).

The theoretical formulation of *volume* DIC is a straightforward extension of *surface* DIC. Whatever dimension (2D or 3D), DIC is a mathematical tool to define the best mapping of an image into another. More precisely, the aim is to determine the transformation $\Phi$ that relates reference and deformed configurations of an evolving system. The method is based on the fundamental assumption that at any point $x$ the grey levels in the first image, $f(x)$, are convected into the grey levels of the second image, $g(x)$, by the transformation $\Phi$, that is, $g(\Phi(x)) = f(x)$. In practice this relation is never fully satisfied, because of systematic and random noise. For the case of images acquired by X-ray micro tomography, random noise can be high and systematic reconstruction artefacts are often present.

Implementations of DIC usually involve local evaluations of the transformation $\Phi$ over cubic (for the volume case) subsets that are regularly distributed over the reference image. The evaluation requires solving an optimisation problem for each subset, in which essentially some measure of the similarity of $f(x)$ and $g(\Phi(x))$ in the considered subset is maximised over a parametric set of transformations. As a digital image is a discrete representation of grey levels, any integral over subsets is in fact discretised into a sum over *voxels* (the 3D version of pixels). Some interpolation is therefore necessary to evaluate the transformation with subvoxel accuracy.

It should be noted that standard implementations of the approach described above assume a continuous displacement field, at least within each subset. Locally, the transformation is assumed to be a rigid translation, or a low-order (usually linear or quadratic) polynomial expansion of the actual transformation. When deriving strain from the displacements of separate subsets, continuity between subsets is assumed. For this reason, this DIC analysis is referred to as 'continuum DIC'. Such a procedure can be applied to study the deformation of a granular material such as sand as long as the spatial scale of the investigation remains large with respect to the grain size. It may also be used at somewhat smaller scales (a few grains within the correlation subsets) under the condition that only small deformation increments are considered. However, a different DIC approach is possible, which recognises the granular character both of the images and the mechanical response, and has therefore the specific objective of investigating the kinematics of *individual* sand grains. In this work, a 'discrete DIC' procedure has been developed with the specific aspect that the regularly shaped and spaced subsets are replaced by subsets centred on each individual grain, with a shape following the actual shape of the grain. In practice, the subsets include a grain plus a small surrounding layer a few voxels thick (the reason for this layer is that, possibly because of the relatively high noise level in the X-ray images and an almost uniform X-ray absorption of the sand grains, the grey level variation within a grain was not enough for DIC; adding a layer provided the extra information of grain shape, which is characteristic of each individual grain). If the grains are assumed to be rigid, then the transformation of each subset is a rigid motion, that is it involves a three-component translation vector plus a rotation. The latter is represented by a rotation axis and a positive angle of rotation about this axis (the axis is parameterised by two polar angles, a longitude with respect to the specimen axis, and a latitude in the cross-sectional plane).

The practical implementation of this discrete DIC comprises the following four consecutive steps.

(*a*) The image of the undeformed specimen is segmented in order to identify and label individual grains. This is performed using a watershed algorithm in the image-processing package Visilog (copyright Noesis, see http://www.noesisvision.com/).

(*b*) A mask is defined for each grain, covering the grain plus a three-voxel wide layer around the grain. This was implemented within the code CMV-3D (Bornert *et al.*, 2004) using the ITK image-processing library (see http://www.itk.org/).

(*c*) Standard DIC procedures of CMV-3D are applied to determine a first evaluation of the translation of each grain, making use of sufficiently large cubic subsets centred on the grains.

(*d*) Starting from these initial estimates, the translation and rotation of each grain are determined using the discrete DIC algorithm, that is by applying optimisation to the subsets defined in step (*b*). Also this step has been integrated into the CMV-3D software, using the generic registration algorithms in ITK.

The final output of the discrete DIC procedure is a set of six transformation parameters for each grain. As an indication of the computational cost of this procedure: step (*a*) took about 7 h to extract about 50 000 grains from an 8 bit 900 × 900 × 1542 image; step (*b*) took about 45 min, while steps (*c*) and (*d*) took slightly less than 1 s per grain, on a Linux-based workstation with a 2·3 GHz Xeon processor. Memory-wise, step (*c*) required about 3 Gb internal memory, whereas more than 8 Gb were needed for step (*d*). Note that several deformation steps can be run concurrently, therefore in principle the entire test could be processed in about 24 h on a dual-quadricore computer with enough memory (64 Gb).

In the following, the results obtained using both continuum and discrete V-DIC are presented. The former uses the code TomoWarp, which is based on the work of Hall (2006) (see Hall *et al.* (2010) for a 2D application to a granular material). Discrete V-DIC has been integrated into CMV-3D, a code developed by Bornert *et al.* (2004) (see also Lenoir *et al.* (2007) for further details and an application to geomechanics).

## SELECTED RESULTS

X-ray tomography scans were carried out at key moments throughout the test, which are marked by (small) relaxations

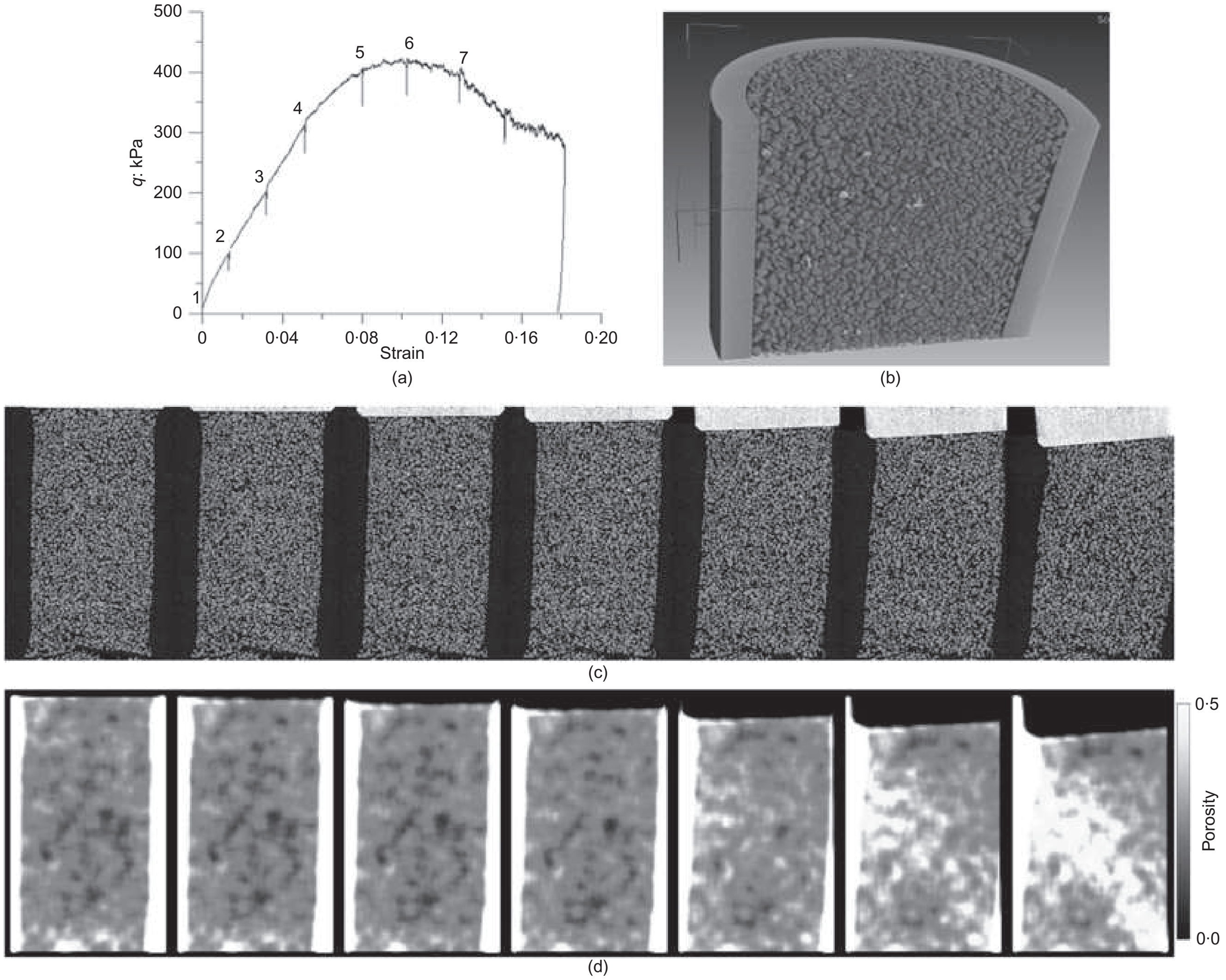

(a) (b)

(c)

(d)

**Fig. 2. (a) Deviator stress plotted against axial strain curve for the deviatoric loading part of the triaxial compression test. (b) 3D rendering of a specimen of Hostun sand showing the grain detail. (c) Vertical slices extracted from the seven 3D X-ray micro tomography images of the sand specimen acquired throughout the triaxial compression. (d) Equivalent slices through the 3D volumes of calculated porosity. For scale, note that the initial sample diameter was 11 mm**

in the loading curve in Fig. 2(a). The sample stress–strain response shows a roughly linear initial trend followed by a curvature to the peak stress at around 11% nominal axial strain, after which the stress drops, to what is probably the beginning of a plateau, after which the test was stopped and the sample unloaded.

Figure 2(b) shows the grain detail which is possible to obtain for Hostun sand through X-ray tomography. For the sake of clarity, in the following only 2D slices through this volumetric data and the subsequent V-DIC results are shown. Fig. 2(c) shows a series of vertical slices through the X-ray tomography images at different stages in the test (see Fig. 2(a)). These slices, which are roughly perpendicular to the planar band of localised strain that developed during the test, show that the specimen gradually leans to one side, with a rotation of the upper platen in the latter part of the test. However, there is no clear evidence of localised deformation in these images. Porosity maps shown in Fig. 2(d) were obtained from the grey-scale images based on overlapping cubic windows of side 61 voxels (854 μm) throughout the sample volume. From these porosity fields an evolving inclined zone of localised dilation can be seen.

Continuum V-DIC has been carried out on consecutive pairs of 3D images to provide the incremental displacement and strain fields (the results are thus averages over the given time interval). The key DIC parameters are the distances between the calculation nodes (which also represent the reference length for subsequent strain calculation) and the correlation window sizes; in this analysis these were, respectively, 20 voxels (or 280 μm) and a cube with sides of 21 voxels (or 294 μm) reduced to 11 voxels (or 154 μm) for the sub-voxel derivation. Results from this analysis indicate that, despite the granular nature of the material, smooth and relatively continuous displacement fields are measured. Fig. 3 shows vertical slices through the 3D field of maximum shear strain $(\varepsilon_1 - \varepsilon_3)/2$ (where $\varepsilon_1$ and $\varepsilon_3$ are the major and minor principal strains) for increments 3–4, 4–5, 5–6 and 6–7. These strain images clearly show the evolution of a localised band that traverses the sample diagonally from left to right. It is worth noting that this is an incremental analysis, indicating that the deformation is active in each strain increment. This is different from what can be seen with accumulated porosity changes shown in Fig. 2(d). As such it is seen from these incremental maps that the localisation possibly initiated in increment 4–5, and was clearly developed in 5–6, that is before the peak load. Note that localisation is visible in these maps before it becomes clear in the porosity images (Fig. 2(d)). The general picture is of a localisation of shear strain and dilatancy which starts as a broad zone and

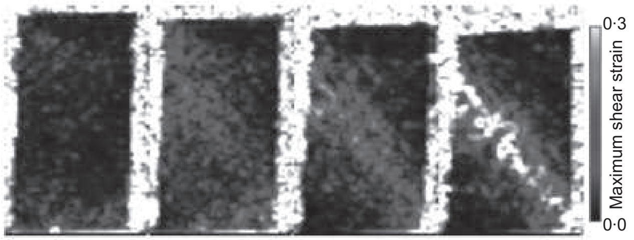

**Fig 3. Continuum V-DIC derived incremental maximum shear strains (as defined in text) for increments 3–4, 4–5, 5–6 and 6–7 (previous increments showed much the same picture as 3–4). The images show vertical slices through the shear strain volume near the middle of the specimen at an equivalent position to Fig. 2**

then progressively thins with loading. In increment 6–7, this zone has a width of about 5 mm (i.e. about 17 $D_{50}$). It is also clear that the localised zone is not uniform, showing a degree of structure.

Discrete V-DIC has been applied to provide incremental analysis of grain kinematics. Following the procedure detailed earlier, a set of six scalar quantities (three displacements and three rotations) describing the kinematics of each sand grain are determined. From these results, displacement components at any position within a grain can be deduced. As an example, in Fig. 4 the field of incremental vertical displacements is viewed in three orthogonal slices through the volume for increment 3–4, before the onset of localisation, and increment 6–7, when a shear band is well developed in the specimen – as clearly portrayed in all three viewing planes. Despite these results having been derived from a discrete analysis, they indicate a relatively continuous field of displacements, even in the presence of strain localisation, which explains why continuum V-DIC performs well. However, locally the field can be discontinuous, as discussed later.

Figure 5(a) shows a 3D view of the rotation vectors for each grain in increments 3–4, 4–5, 5–6 and 6–7. Fig. 5(b) shows, for the same increments, the magnitude of rotation for each grain about its rotation axis (recall this is specific for a grain) in a vertical slice corresponding to the middle of the specimen, as in Fig. 3. Note that the grains in Fig. 5(b) are represented in the configuration that existed at the beginning of the test, and not in their displaced positions. Both sets of images in Fig. 5 indicate that grain rotations become progressively more intense into a zone that roughly corresponds to where shear strain localises (see Fig. 3).

## DISCUSSION AND CONCLUSIONS

The objective of this work was to observe and quantify the onset and evolution of localised deformation processes in sand with grain-scale resolution. The key element of the proposed approach is combining state-of-the-art X-ray micro tomography imaging with 3D V-DIC techniques. This makes it possible not only to view the grain-scale details of a deforming sand specimen, but also and more importantly to assess the evolving 3D displacement and strain fields throughout loading. While X-ray imaging and DIC have been in the past applied individually to study sand deformation, the combination of these two methods to study the kinematics of shear band formation at the scale of the grains is the first novel aspect of this work. Moreover, a completely original grain-scale V-DIC method has been developed that permits the characterisation of the full kinematics (i.e. 3D displacements and rotations) of all the individual sand grains in a specimen.

The application of continuum V-DIC has allowed the development of a localised shear band to be characterised throughout a test. Incremental analysis of consecutive steps reveals that strain localisation begins before the peak stress, and indicates a diffuse, wide band progressively thinning to a 17 $D_{50}$ wide band after peak. It also appears that the shear band contains a narrower internal core of much higher strain, and that within the band there are aligned zones of either reduced or elevated strains at angles 'conjugate' to the main band direction.

The results obtained using the discrete V-DIC confirm the importance of grain rotations associated to strain localisation. A clear correspondence can be established between the zones of the specimen experiencing localisation of (continuum) shear strain and the zones where grain rotations are more intense. Fig. 6 shows the history of rotation throughout the test for a few selected grains, indicating contrasting behaviour for grains positioned inside and outside the region where shear strain localises. Grains inside the band show a rapid acceleration of rotation as the shear band initiates,

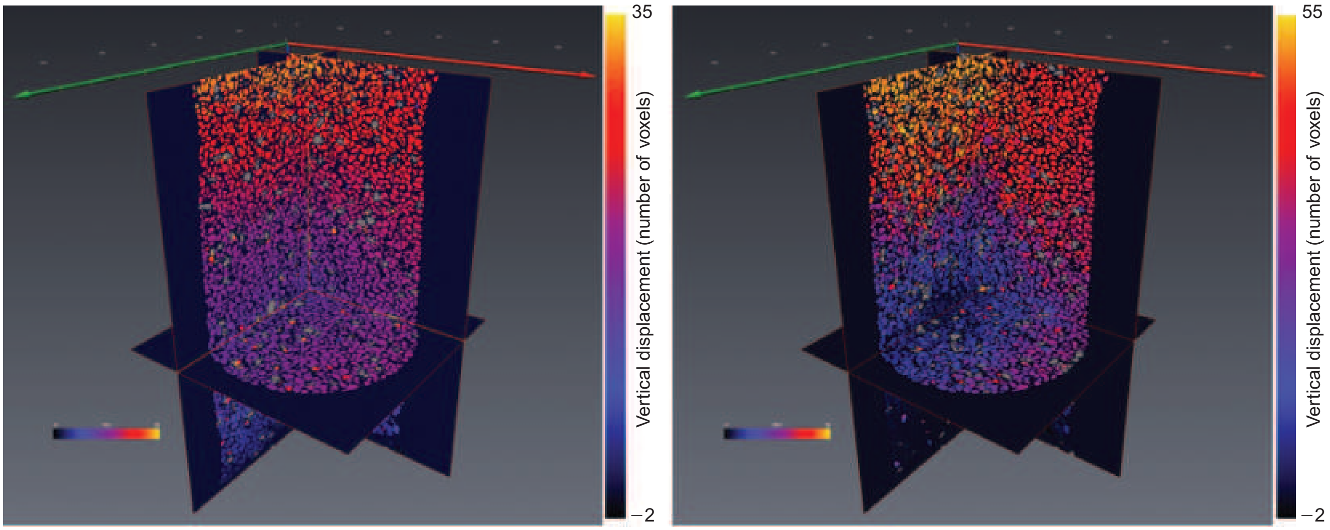

**Fig 4. Discrete V-DIC derived grain displacements (vertical component) viewed in three orthogonal slices through the volume for strain increments 3–4 and 6–7 (before and after peak stress, respectively). Grains coloured grey are those for which the image correlation was not successful (about 2% and 5% of the grains for 3–4 and 6–7, respectively)**

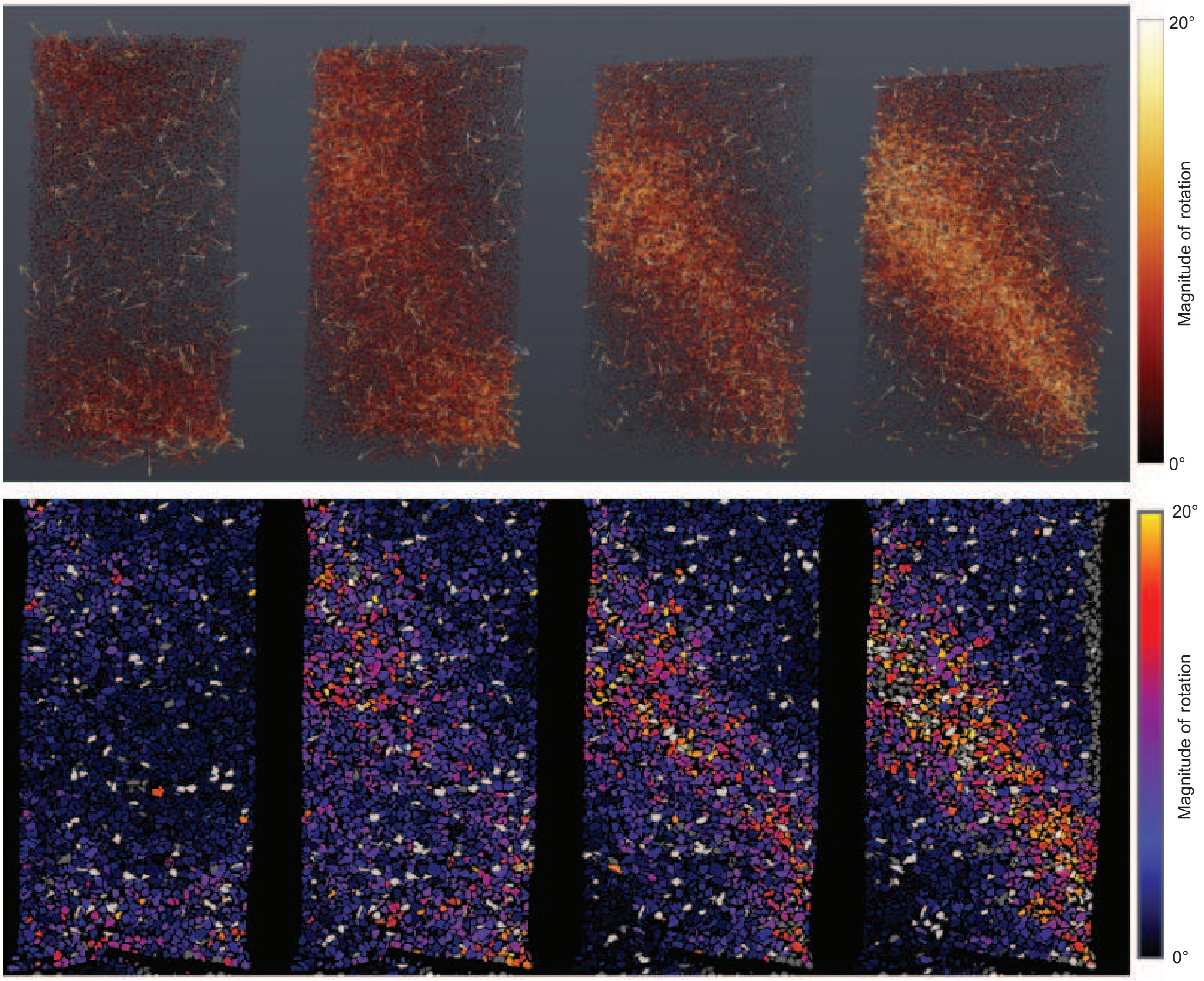

**Fig 5. Discrete V-DIC derived incremental grain rotations for increments 3–4, 4–5, 5–6 and 6–7 (previous increments showed much the same picture as 3–4). Top: 3D volume view of the rotation vectors (axes of rotation for each grain are plotted with their length and colour indicating the magnitude of the rotation about these axes). Bottom: magnitude of the grain rotations plotted for vertical slices through the middle of the specimen at an equivalent position to Figs 2 and 3; note that the grains are plotted in the configuration at the start of the test for all increments. Grains coloured grey are those for which the image correlation was not successful and those coloured white are those with a rotation above a threshold value of 20° (corresponding also to the long white vectors in the upper images)**

whereas grains elsewhere show relatively constant increase of rotation as the test progresses.

Figure 7 shows the discrete V-DIC vertical component of total displacement from start to image 7 (note that these displacements include the contribution due to the grain rotations). The overall impression from the left image in the figure is that discrete V-DIC yields a relatively continuous displacement field, even at this stage of the test when strain localisation has developed. However, the zoomed images reveal that local discontinuities exist at the scale of the grains. While only a few such examples of discontinuities are noted in the figure, it is clear that a deeper analysis of continuities/discontinuities at grain contacts and their evolution is now possible, and will be investigated in future work. It should also be noted that the grain images in Fig. 7 are those resulting from image segmentation, that is grains that are in contact will not appear so as they have been artificially separated. Therefore, it is not possible to differentiate from such segmented images grains that are in contact from those that are not. A more detailed study of grain contact evolution in space and time would require defining contacts based on the original, non-segmented images.

In constitutive modelling, it is necessary to understand the physics governing material behaviour – from the micro scale to the continuum scale. This is particularly true when modelling emergent fine-scale mechanisms whose characteristic length scales are only a few particles wide, for example shear bands. Since their initial development by Cundall & Strack (1979), discrete element methods have been gaining popularity as a numerical means to explore the mechanical behaviour of sand and other granular media at the scale of the grains. On the experimental side, micro mechanics studies are few in number, and most of them are restricted either to two dimensions or to artificial granular media such as glass beads. The few experimental studies exploring sand deformation at the scale of the grains have provided limited quantitative information so far. With the tools presented in this paper, the capability has now been provided to capture experimentally and at a pertinent level of resolution the details of grain-scale processes, including those that underlie the localisation phenomena of interest here. However, the potential of the approach has still to be fully exploited. Future directions of this research include more detailed analysis of: kinematics across grain contacts

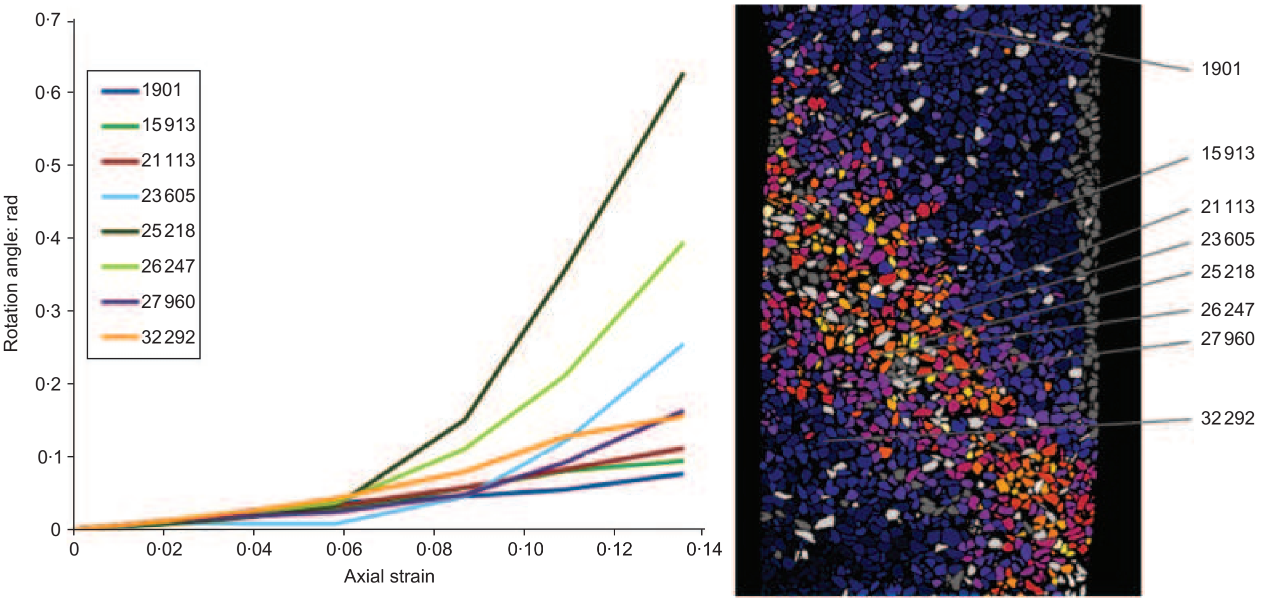

**Fig 6. History of rotation for a few selected grains positioned inside and outside the localised deformation band – left: plot of total rotations for each selected grain as a function of nominal axial strain of the specimen; right: the selected grains indicated on the slice of incremental rotation for step 6–7, as in Fig. 5**

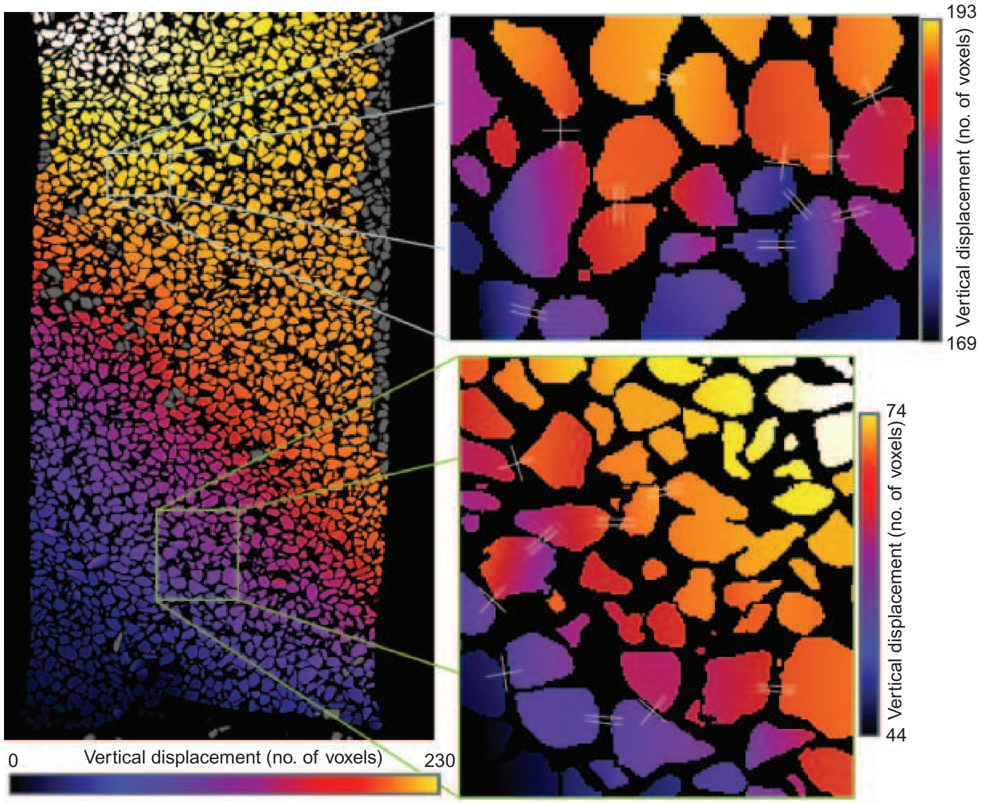

**Fig 7. Vertical slice (as in previous figures) through the total *z* component displacement field up to image 7 from the discrete V-DIC with displacements derived at all points, within the grains, from the grain displacements and rotations. While the displacement field appears relatively continuous, the zoomed images (right) highlight that locally there exists both continuity and discontinuity of displacements between adjacent grains, as indicated by = and + respectively**

and its evolution with strain localisation at the macro scale; emergence of grain-scale structures inside a shear band (e.g. the 'columns' of aligned grains observed by Oda *et al.* (2004) and also advocated by Rechenmacher (2006) based on continuum 2D DIC); organised kinematics, in particular grain rotation, at the onset of shear banding and through its evolution.

## ACKNOWLEDGEMENTS

This work was carried out within the framework of the project MicroModEx funded by the French research agency, ANR (contract number: ANR-05-BLAN-0192). The authors acknowledge Christophe Rousseau (Laboratoire 3S-R) and Marco di Michel (ESRF), for their contributions to the experimental programme.

## REFERENCES

Alshibli, K. A., Sture, S., Costes, N. C., Franck, M. L., Lankton, M. R., Batiste, S. N. & Swanson, R. A. (2000). Assessment of localized deformation in sand using X-ray computed tomography. *Geotech. Testing J.* **23**, 274–299.

Bay, B. K. (2008). Methods and applications of digital volume correlation. *J. Strain Anal.* **43**, 745–760.

Bay, B. K., Smith, T. S., Fyhrie, D. P. & Saad, M. (1999). Digital volume correlation: three-dimensional strain mapping using X-ray tomography. *Expl Mech*. **39**, No. 3, 217–226.

Bornert, M., Chaix, J. M., Doumalin, P., Dupré, J. C., Fournel, T., Jeulin, D., Maire, E., Moreaud, M. & Moulinec, H. (2004). Mesure tridimensionnelle de champs cinématiques par imagerie volumique pour l'analyse des matériaux et des structures. *Instrumn Measmt Metrology* **4**, 43–88.

Chu, T. C., Ranson, W. F., Sutton, M. A. & Peters, W. H. (1985). Applications of digital-image-correlation techniques to experimental mechanics. *Expl Mech*. **25**, No. 3, 232–244.

Colliat-Dangus, J. L., Desrues, J. & Foray, P. (1988). Triaxial testing of granular soil under elevated cell pressure. *Proceedings of a conference on advanced triaxial testing for soil and rocks* (eds R. T. Donaghe, R. C. Chaney and M. L. Silver), STP977, pp. 290–310. Philadelphia: American Society for Testing and Materials.

Cundall, P. A. & Strack, O. D. L. (1979). A discrete numerical model for granular assemblies. *Géotechnique* **29**, No. 1, 47–65, **doi**: 10.1680/geot.1979.29.1.47.

Desrues, J. (1984). *La localisation de la déformation dans les matériaux granulaires*. PhD thesis, USMG and INPG, Grenoble, France.

Desrues, J. (2004). Tracking strain localization in geomaterials using computerized tomography. *Proc. 1st Int. Workshop X-ray Tomography for Geomater., Kumamoto, Japan* **1**, 15–41. Lisse, The Netherlands: Balkema.

Desrues, J., Chambon, R., Mokni, M. & Mazerolle, F. (1996). Void ratio evolution inside shear bands in triaxial sand specimens studied by computed tomography. *Géotechnique* **46**, No. 3, 529–546, **doi**: 10.1680/geot.1996.46.3.529.

Desrues, J. & Viggiani, G. (2004). Strain localization in sand: an overview of the experimental results obtained in Grenoble using stereophotogrammetry. *Int. J. Numer. Analyt. Methods Geomech*. **28**, No. 4, 279–321.

Hall, S. A. (2006). A methodology for 7D warping and deformation monitoring using time-lapse seismic data. *Geophysics* **71**, No. 4, O21–O31.

Hall, S. A., Muir Wood, D., Ibraim, E. & Viggiani, G. (2010). Localised deformation patterning in 2D granular materials revealed by digital image correlation. *Granular Matter* **12**, No. 1, 1–14.

Lenoir, N. (2006). *Comportement mécanique et rupture dans les roches argileuses étudiés par micro tomographie à rayons X*. PhD thesis, University of Grenoble, France (http://tel.ccsd.cnrs.fr/tel-00011996).

Lenoir, N., Bornert, M., Desrues, J., Bésuelle, P. & Viggiani, G. (2007). Volumetric digital image correlation applied to X-ray micro tomography images from triaxial compression tests on argillaceous rocks. *Strain* **43**, No. 3, 193–205.

Matsushima, T., Uesugi, K., Nakano, T. & Tsuchiyama, A. (2006). Visualization of grain motion inside a triaxial specimen by micro X-ray CT at SPring-8. In *Advances in X-ray tomography for geomaterials* (eds J. Desrues, G. Viggiani and P. Bésuelle), pp. 35–52. London: ISTE.

Matsushima, T., Katagiri, J., Uesugi, K., Nakano, T. & Tsuchiyama, A. (2007). Micro X-ray CT at SPring-8 for granular mechanics. In *Soil stress–strain behavior: measurement, modeling and analysis* (eds H. I. Ling, L. Castillo, D. Leshchinsky and J. Koseki), pp. 225–234. The Netherlands: Springer.

Oda, M. & Kazama, H. (1998). Microstructure of shear band and its relation to the mechanism of dilatancy and failure of granular soils. *Géotechnique* **48**, No. 4, 465–481, **doi**: 10.1680/geot.1998.48.4.465.

Oda, M., Takemura, T. & Takahashi, M. (2004). Microstructure in shear band observed by microfocus X-ray computed tomography. *Géotechnique* **54**, No. 8, 539–542, **doi**: 10.1680/geot.2004.54.8.539.

Orteu, J. J. (2009). 3-D computer vision in experimental mechanics. *Optics and Lasers in Engineering* **47**, No. 3–4, 282–291.

Otani, J., Mukunoki, T. & Obara, Y. (2002). Characterization of failure in sand under triaxial compression using an industrial X-ray scanner. *Int. J. Phys. Modelling Geotech*. **2**, No. 1, 15–22.

Rechenmacher, A. L. (2006). Grain-scale processes governing shear band initiation and evolution in sands. *J. Mech. Phys. Solids* **54**, No. 1, 22–45.

Roscoe, K. H. (1970). The influence of strains in soil mechanics. *Géotechnique* **20**, No. 2, 129–170, **doi**: 10.1680/geot.1970.20.2.129.

Roscoe, K. H., Arthur, J. R. F. & James, R. G. (1963). The determination of strains in soils by an X-ray method. *Civ. Engng Public Works Rev.* **58**, No. 7, 873–876 and No. 8, 1009–1012.

Sutton, M. A., Wolters, W. J., Peters, W. H., Ranson, W. F. & McNeill, S. R. (1983). Determination of displacements using an improved digital correlation method. *Image and Vision Comput*. **1**, No. 3, 133–139.

Verhulp, E., van Rietbergen, B. & Huiskes, R. (2004). A three-dimensional digital image correlation technique for strain measurements in microstructures. *J. Biomech*. **37**, No. 9, 1313–1320.

Viggiani, G. & Hall, S. A. (2008). Full-field measurements, a new tool for laboratory experimental geomechanics. Keynote paper. *Proc. 4th Int. Symp. Deformation Characteristics Geomater*. (eds S. E. Burns, P. W. Mayne and J. C. Santamarina) **1**, 3–26. Atlanta: IOS Press.

Viggiani, G., Lenoir, N., Bésuelle, P., Di Michiel, M., Marello, S., Desrues, J. & Kretzschmer, M. (2004). X-ray micro tomography for studying localized deformation in fine-grained geomaterials under triaxial compression. *C. R. Mécanique* **332**, No. 10, 819–826.

Withers, P. J. (2008). Strain measurement by digital image correlation. *Strain* **44**, No. 6, 421–422.

# Characterization of the strain localization in a porous rock in plane strain condition using a new true-triaxial apparatus

Bésuelle P. and Hall S.A.

## 1 Introduction

Failure by strain localization is commonly observed in geomaterials. In a previous workshop (IWBI Minneapolis St Paul, 2002), we presented an experimental characterization of strain localization in a porous sandstone [2]. This study was performed with classical axisymmetric triaxial compression tests. The effect of the confining pressure was observed on several aspects: onset of localization; pattern of localization; porosity evolution inside the localized bands. Complex patterns of localization were observed at high confining pressure in the transition between the brittle and ductile regimes, showing several deformation bands in the specimens. However the history (time evolution) of the localization was not accessible because the observations were post-mortem.

Measurements of strain fields and their evolution in time are particularly useful to study strain localization (initiation of deformation bands) and post-localization regimes. Such tools have been developed for soils (e.g., sand specimens in plane strain conditions [3] or in triaxial conditions using X-ray tomography [5]). Similar developments for rocks are still difficult, especially because the pertinent confining pressure to reproduce in-situ stresses and material stiffnesses are higher than for soils; only a very few devices exist (*e.g.*, [15]).

We present here first results obtained in a new true-triaxial apparatus that allows observation of rock specimens under loading. Whilst several triaxial apparatuses exist that allow the application of three different principal stresses, they do not allow observation of specimens under load and such analysis is only possible post-mortem (*e.g.*, [11, 1, 10, 16, 4, 7, 12, 14]). Furthermore, in this new device, as for biaxial apparatuses (*e.g.*, [13] and [8]), failure surfaces can develop and propagate in a sample in an unrestricted manner; this can be under true-triaxial or plane-strain (biaxial) conditions as, if required, the intermediate stress can be controlled (with active con-

---

CNRS - UJF - Grenoble INP, Laboratoire 3SR, BP53, 38041 Grenoble Cedex 9, France. e-mail: Pierre.Besuelle@hmg.inpg.fr

trol) to impose a plane strain condition during a test. The observation of a specimen under load is possible as one surface of the prismatic specimen, which is orthogonal to the plane strain direction, is in contact with a hard transparent window. The deformation of this surface should representative of the deformation in the whole specimen (due to the plane-strain condition), up to and beyond strain localization. Therefore the evolution of the strain field in a sample can be measured by digital image correlation (DIC) of photographs taken of this surface.

The next section describes briefly the new apparatus. We present in a third section preliminary results obtained with a porous clay rock, focusing on strain localisation and crack initiation.

## 2 Description of the true triaxial cell

The true-triaxial apparatus has been developped in Laboratoire 3SR (Grenoble) with the aim to charaterize the initiation of localization and the post-localization regime in rocks. With this device three independant stresses can be applied in the three space directions on prismatic rock specimens, with the ability to visualise the specimen under load. The surfaces perpendicular to the major and intermediate stresses (compression) are in contact with rigid platens, which are moved by two perpendicular pistons, while the two surfaces perpendicular to the minor stress are free to deform because the stress is applied by a confining fluid (through a soft membrane). As deformation bands and cracks are generally parallel to the intermediate stress, the specimen has the freedom to deform and fail with no kinematic constraints imposed on the formation of the failure zone. Moreover, one of the two surfaces perpendicular to the intermediate stress is in contact with a hard window to observe the specimen under load. The two pistons can be controlled in stress or displacement. The intermediate stress can be controlled such that there is no deformation in this direction, which allows application of plane strain loading. In such a case, the kinematics over the surface in contact with the window is representative of the kinematics in the whole specimen up to and beyond strain localization.

A simplified schema of the apparatus is presented in figure 1. The hydraulic axial piston (1) applies the axial loading on the specimen (2). This is self-compensated with respect to the confining pressure, *i.e.*, it is in equilibrium whatever the confining pressure. The axial loading is controlled in displacement by an external displacement transducer linked to a pressure generator that adapts the pressure applied to the top of the piston to keep a constant displacement rate. The axial piston moves inside a floating axial frame (3), when the piston moves down, the frame and the bottom loading cap move up by about the same value. In such a way, if the specimen deforms homogeneously, the middle of the specimen does not move (or only very slightly). The weight of the floating frame is compensated by an external air piston.

The horizontal piston (4) applies the intermediate stress. This is also self-compensated with respect to the confining pressure inside the confining chamber (5).

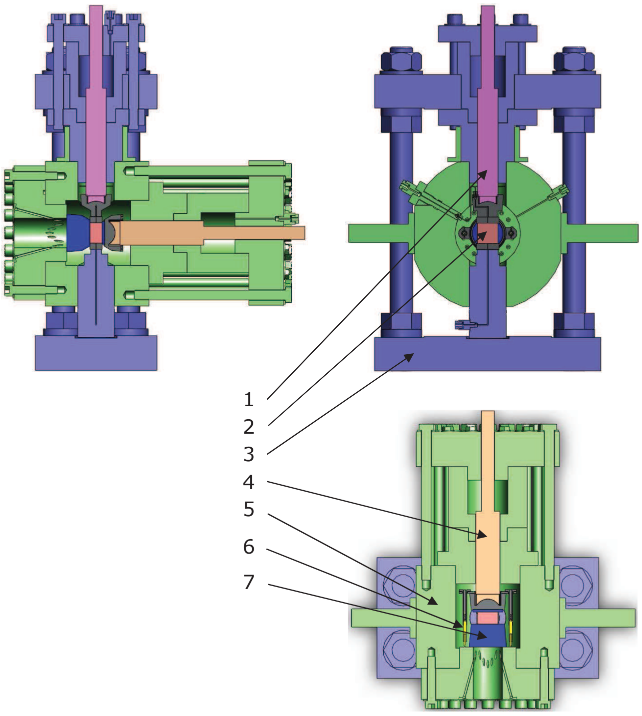

**Fig. 1** Scheme of the true triaxial cell with an observation window: 1) axial piston, 2) specimen, 3) floating axial frame, 4) horizontal piston, 5) confining chamber and fixed frame, 6) internal displacement tranducers, 7) sapphire window

The piston can be controlled in displacement by the internal displacement transducers (6). One possible mode of operation is to adapt the pressure sent by its generator pressure to keep a zero displacement, *i.e.*, a plane strain condition on the specimen, although all other controls in displacement or stress are possible. The surface of the specimen, opposed to the horizontal piston, is in contact with a thick, transparent sapphire window. This surface can be observed and photographs of the surface can be taken. For a symmetry of the contact, the surface on the side of the horizontal piston is in contact with a thin sapphire platen, to have the same boundaries conditions.

The minor stress is applied by the confining fluid on the two lateral surfaces of the specimen. The specimen is separated from the fluid by a silicone membrane. The membrane wraps around both the specimen and the four loading caps. In such a way, there is a direct contact between the specimen and the window. Note that in the axial direction, a special device of wedges between the specimen and the loading caps ensures that they have the same thickness as the specimen in the direction of intermediate stress. If a compression or extension of specimen in this direction

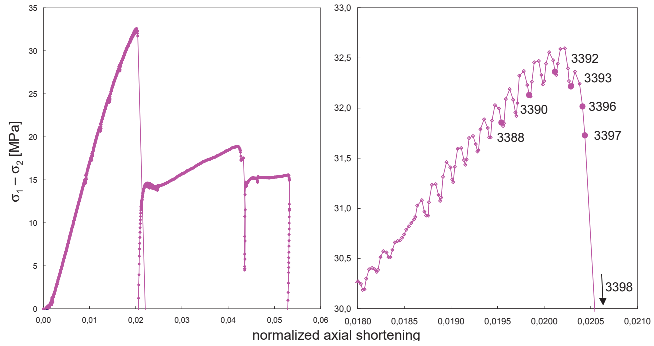

**Fig. 2** Evolution of the differential stress (major stress minus minor stress) versus axial strain. At right, detail of the full curve at left, close to the stress peak. Numbers correspond to the photographs. (The small oscillations of the right curve have been induced by an imperfect regulation of the axial piston pressure generator)

occurs, the set of wedges automatically follow this change. This avoids an extrusion of the membrane during the deformation of the specimen.

A set a three pressure generators (syringe pumps with electronic control) is associated to the apparatus, to apply the loading in the three space directions. Further development is a control of the bottom and top pore pressure inside the specimen to impose a fluid flux. Note also that numerous electrical connectors in the cell allow to put several internal transducers, *e.g.*, for acoustic emissions measurement.

The surface of the specimen is illuminated through the sapphire window by light from a set of LEDs focussed onto the sample surface through optical fibers; this provides a good and homogenous luminosity to take photographs. Photographs of the visible surface of the specimen were taken throughout the loading with a high resolution camera (providing images of 6080 × 4044 pixels). DIC analysis can thus be carried out on the resultant images to yield displacement and strain fields over the observed surface; for details on the DIC procedure see [6]. However, it is important to note that for the DIC, it is necessary to have a pattern over the surface of the sample that varies such that different parts of the surface can be uniquely distinguished. Depending on the test specimen, this pattern can be natural (as with some sandstones for example) or artificial (in this case it was necessary to add this pattern as discussed later).

The size of the specimen is 50 mm in the axial direction, 30 mm in the direction of intermediate stress, and 25 or 50 mm in the direction of minor stress, which corresponds to slenderness ratios (the ratio of the height to the width) of two and one, respectively. The capacity of the cell for confining pressure is 100 MPa, the axial piston can apply a force of 500 kN and the horizontal piston a force of 700 kN, which correspond to a differential stress with respect to the confining pressure of 670 MPa and 530 MPa, respectively, for a specimen with a slenderness ratio of two, and half that for a 50 mm width specimen.

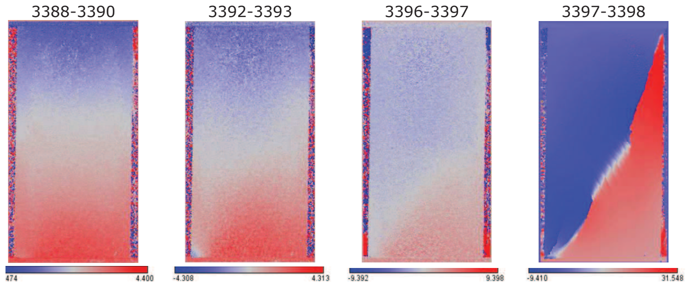

**Fig. 3** Fields of axial displacement increments close to the stress peak. Couples of numbers on the top of each picture correspond to the photographs numbers used for the DIC. The color scales are expressed in term of pixel size (about 10 $\mu$m)

## 3 Selected results

We present here a test that has been performed on a clay rock specimen, the Callovo-Oxfordian argillite, from the underground research laboratory (URL) at Bure (Eastern France) at approximately 500 m below the ground surface. It is a sedimentary rock composed of particles of calcite and quartz in a clay matrix [9]. The specimen has been prepared with a diamond wire saw and then polished with a fine sandpaper. The surface of the specimen in contact with the window of the triaxial apparatus has been painted with a thin layer of white ink and then a speckle of black ink, using an airbrush. The size of pixels in the photographs correspond to about 10 $\mu$m on the sample surface. The test has been performed with an initial isotropic loading to 2 MPa and then an axial loading in plane strain conditions with a displacement rate of 1.25 $\mu$m.s$^{-1}$, *i.e.*, a strain rate of 2.5 $10^{-5}$ s$^{-1}$.

Figure 2 shows the evolution of the differential stress (major stress minus minor stress) with respect to the axial strain (specimen shortening divided by its initial height). A zoom of the full curve (left) is presented (right) for the period when the analyzed photographs were taken. The beginning of the curve at left is quite linear, followed by a small curvature and a first stress peak at 0.02 axial strain, followed by a strong stress drop. Then a slow stress increase is observed, followed by a second stress drop at 0.42 axial strain. After, the stress is quite constant. The two stress drops are associated with major failure by faulting in the specimen. The crack that appeared during the second drop is conjugate to the first crack set, which appeared at the first drop. We focus later on the strain localization at first stress peak.

Figure 3 presents the fields of a few axial displacement increments before and after the stress peak. The specimen deformation during increment 3388 - 3390 seems quite homogeneous, and the displacements are primarily vertical[1]. The increment 3392 - 3393 shows a loss of the homogeneity with a gradient of displacement ori-

---

[1] the top displacement is approximately the same but opposite to the bottom displacement, due to the conception of the apparatus. The middle of the specimen does not move in the axial direction.

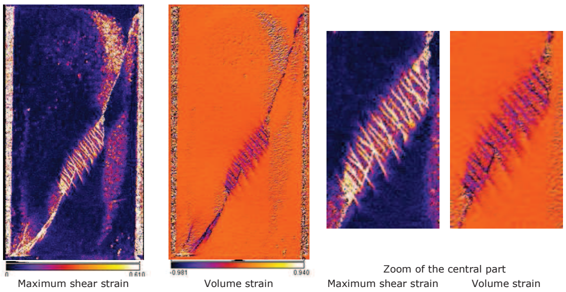

**Fig. 4** Fields of shear and volume strain during increment 3397-3398.

ented along an inclined line from the bottom left to the top right of the specimen. This corresponds to an incipient strain localization arriving at the stress peak. A shear band is observed in further increments up to photograph 3397. During increment 3397 - 3398, a strong discontinuity is observed in the displacement field, which corresponds to a crack initiation in the place of the previous shear band. The strain field of this increment is shown in figure 4, where the maximum shear strain and volume strain are plotted. A major crack crosses the specimen from the bottom left to the top right. In the central zone of the specimen, there is a set of small conjugate cracks, showing two, quite close, preferential orientations. These small cracks are arranged inside an elongated zone parallel to the major crack. In most of cases, the major and small crack initiation is associated with a compaction combined with shear sliding. The sub-vertical zone of concentration of the shear strain on the right of the specimen is in fact an artefact of the measure due to a change of luminosity of the surface of the specimen in contact with the window (probably a consequence of an initial small default of planarity of the specimen).

A post-mortem analysis of the specimen using our X-ray CT apparatus shows the 3D network of cracks. The major cracks cross the specimen roughly parallel to the direction of intermediate stress, confirming a 2D mechanism of deformation in the specimen. The central zone of conjugate small cracks extends about half of the way into the specimen in the intermediate stress direction, which confirms that the conjugated cracks are not a surface effect but bulk mechanism of deformation.

## 4 Conclusions

The ability to characterize localized failure in rocks and, in particular, to follow the strain field evolution inside rock specimens during loading using a new true-triaxial apparatus has been demonstrated. Displacement and strain fields results, using DIC, from a plane-strain loading test on a clay rock have been presented, which reveal a complex pattern of localization at failure. Furthermore the evolution of the deformation has been followed from an initially homogeneous deformation through the development of a shear band and subsequent initiation of a set cracks resulting in major faults and small conjugate cracks arranged inside a band parallel to the major fault. Further experiments will focus on the effect of confinement on the processes of failure and localization and also on reproducibility in similar conditions.

**Acknowledgements** The authors thank the French radioactive waste management agency (ANDRA) who provides the clay rock from its URL at Bure. The development of the true triaxial apparatus has been supported by the 'ACI jeunes chercheurs JC8029' from the French government, by the national research group 'GDR FORPRO' from CNRS and by ANDRA.

## References

1. Atkinson RH, Ko H-Y (1973) A fluid cushion, multiaxial cell for testing rock specimens. Int J Rock Mech Mining Sci Geomech Abstr 10:351–361
2. Bésuelle P, Desrues J, Raynaud S (2000) Experimental characterisation of the localisation phenomenon inside a Vosges sandstone in a triaxial cell. Int J Rock Mech Mining Sci 37:1223–1237
3. Desrues J, Viggiani G (2004) Strain localization in sand: an overview of the experimental results obtained in Grenoble using stereophotogrammetry. Int J Num Anal Meth Geomech 28:279–321
4. Haimson B, Chang C (2000) A new true triaxial cell for testing mechanical properties of rock, and its use to determine rock strength and deformability of Westerly granite. Int J Rock Mech Mining Sci 37:285–296
5. Hall SA, Bornert M, Desrues J, Pannier Y, Lenoir N, Viggiani G, Bésuelle P (2010) Discrete and Continuum analysis of localised deformation in sand using X-ray micro CT and Volumetric Digital Image Correlation. Géotechnique 60:315–322
6. Hall SA, Muir Wood D, Ibraim E, Viggiani G (2000) Localised deformation patterning in 2D granular materials revealed by digital image correlation. Granular Matter, DOI: 10.1007/s10035-009-0155-1
7. King MS (2002) Elastic wave propagation in and permeability for rocks with multiple parallel fracture. Int J Rock Mech Mining Sci 39:1033–1043
8. Labuz JF, Dai S-T, Papamichos E (1996) Plane-strain compression of rock-like materials. Int J Rock Mech Mining Sci Geomech Abstr 33:573–578
9. Lenoir N, Bornert M, Desrues J, Bésuelle P, Viggiani G (2007) Volumetric Digital Image Correlation Applied to X-ray Microtomography Images from Triaxial Compression Tests on Argillaceous Rock. Strain 43:193–205
10. Michelis P (1985) A true triaxial cell for low and high pressure experiments. Int J Rock Mech Mining Sci Geomech abstr 22:193–188
11. Mogi K (1967) Effect of the intermediate principal stress on rock failure. J Geophys Res 72:5117–5131
12. Naumann M, Hunsche U, Schulze O (2007) Experimental investigations on anisotropy in dilatancy, failure and creep of Opalinus Clay. Phys Chemistry Earth 32:889–895
13. Ord A, Vardoulakis I, Kajewski R (1991) Shear band formation in Gosford sandstone. Int J Rock Mech Mining Sci Geomech Abstr 28:397–409
14. Popp T, Salzer K (2007) Anisotropy of seismic and mechanical properties of Opalinus clay during triaxial deformation in a multi-anvil apparatus. Phys Chemistry Earth 32:879–888
15. Takemura T, Oda M, Takahashi M (2004) Microstructure observation in deformed geomaterials using microfocus X-ray computed tomography. In: Otani J, Obara Y (eds) X-ray CT for Geomaterials, GeoX2004. Balkema
16. Wawersik WR, Carlson LW, Holcomb DJ, Williams RJ (1997) New method for true-triaxial rock testing. Int J Rock Mech Mining Sci 34:330

# Sélection de publications :
# Travaux de Modélisation

JOURNAL OF GEOPHYSICAL RESEARCH, VOL. 106, NO. B7, PAGES 13,435–13,442, JULY 10, 2001

# Compacting and dilating shear bands in porous rock: Theoretical and experimental conditions

Pierre Bésuelle
Laboratoire de Géologie, Ecole Normale Supérieure, Paris, France

**Abstract.** The failure of rocks in the brittle regime is generally associated with the appearance of strain localization bands. For very porous rocks, three types of strain localization can be distinguished: extension bands, shear bands, and compaction bands. The first is associated with an extensional normal strain concentration inside the band; the second, with a shear strain concentration; and the third, with a compressive normal strain concentration. This paper shows the continuous transition between pure extension bands and pure compaction bands, via shear bands that evolve from dilating shear bands to compacting shear bands. By an extension to the analysis of *Rudnicki and Rice* [1975] (RR) on strain localization in pressure sensitive rocks, the prediction of the strain type inside bands at the onset of localization shows that inside shear bands, the shear strain can be associated with a volumetric dilatancy or compaction depending on the constitutive parameters of the material. The theoretical determination of the strain type is in accordance with recent observations of dilating and compacting shear bands in laboratory tests on porous sandstone specimens. A limit for the existence of a localized reduction of porosity within the band is expressed. A physical limit to the RR model is also proposed to insure continuity of the strain mechanism of localization with respect to the constitutive parameters.

## 1. Introduction

The phenomenon of porosity reduction inside strain localization bands has been observed in naturally deformed porous sandstone [*Antonellini et al.,* 1994; *Mollema and Antonellini,* 1996]. The deformation bands are thin and linear and often preferentially oriented with respect to the stress fields. These field observations show that strain localization bands are not necessarily associated with a dilatational strain but sometimes with a reduction of porosity. They suggest that such structures can locally reduce the permeability inside thin bands, which can have implications for petroleum reservoirs by changing the global permeability. Compacting shear bands have also been observed under laboratory conditions in a porous Vosges sandstone [*Bésuelle et al.,* 2000] and porous clays [*Tillard-Ngan et al.*, 1993; *Hicher and Wahyudi,* 1994]. *Olsson* [1999] has also discussed experimental observations of compaction bands. All of these results show that localized shear strain is often associated with a volumetric strain, which is dilating or compacting depending on the boundary conditions. Moreover, there is a continuous transition from dilating shear bands to compacting shear bands.

*Rudnicki and Rice* [1975] (hereinafter referred to as RR) proposed a model and a bifurcation analysis to predict the conditions for the onset of localized deformation in dilatant material. This work was extended by *Perrin and Leblond* [1993], who determined the limits for the possible existence of shear bands. *Olsson* [1999] and *Issen and Rudnicki* [2000] reinterpreted this result to analyze the existence of pure compaction bands in porous rocks. Pure compaction bands are bands that exhibit a normal compacting strain and a zero shear strain. Such bands have recently been recognized in the field [*Mollema and Antonellini,* 1996]. They can be explained in porous sandstone by the existence of a yield cap at high pressure. This yield cap is a compactive yield envelope with a negative pressure dependence [*Wong et al.,* 1997].

The aim of this paper is to extend the initial analysis of RR, by studying not only the conditions for the onset of localized bands that were already described, but also the predicted strain type inside the band at the onset of localization. This work shows the continuous evolution of the strain type with respect to the constitutive parameters between the pure extension bands and the pure compaction bands. It enables determination of the conditions for a compacting strain mechanism inside shear bands. These new theoretical results are well in accordance with experimental observations in laboratory tests.

Paper number 2001JB900011.
0148-0227/01/2001JB900011$09.00

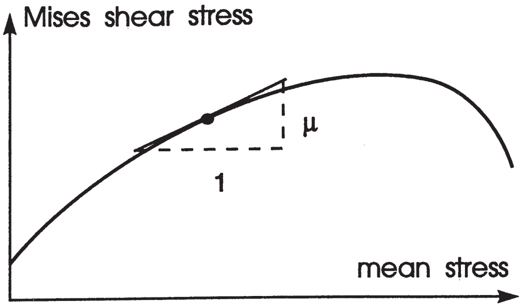

**Figure 1.** Schematic yield surface in the Mises shear stress versus mean stress plane. The slope of the curve ($\mu$) decreases when mean stress increases.

## 2. Theoretical Conditions

### 2.1. Review of the Rudnicki and Rice Analysis

*Rudnicki and Rice* [1975] considered an elastoplastic constitutive law with a Drücker-Prager yield surface and a nonassociated flow rule to describe the response of brittle rocks. The yield surface delimits regions in stress space of elastic unloading and plastic loading. Such a yield surface is shown in Figure 1 in a plot of shear stress versus mean stress. The slope $\mu$ depends on the mean stress and is generally called a friction coefficient, except when it takes negative values. Figure 2a shows the relationship between the plastic volumetric strain and the plastic differential strain for a typical axisymmetric compression test where the slope of the curve is defined by using a dilatancy factor. Figure 2b shows axial stress as a function of plastic axial strain where the slope is defined by using a hardening modulus. The relation between the strain rate and the stress rate (compressive stress and strain are assumed to be negative) can be written as [*Rudnicki,* 1984]

$$D_{ij} = \frac{1}{2G}\left(\overset{\triangledown}{\sigma}_{ij} - \frac{\nu}{1+\nu}\,\dot{\sigma}_{kk}\,\delta_{ij}\right) + \frac{1}{h}\,P_{ij}\,Q_{kl}\,\overset{\triangledown}{\sigma}_{kl}\,, \quad (1)$$

where $D_{ij} = 1/2(v_{i,j} + v_{j,i})$ is the symmetric part of the velocity gradient tensor and $\overset{\triangledown}{\sigma}$ and $\dot{\sigma}$ are the corotational Jaumann stress rate and the material derivative of stress, respectively. The first term is the elastic contribution with shear modulus $G$ and Poisson coefficient $\nu$; $\delta_{ij}$ is the Kronecker delta. The second term is the plastic contribution with the hardening modulus $h$, and the direction of the plastic strain rate is given by

$$P_{ij} = \sigma'_{ij}/2\bar{\tau} + (1/3)\,\beta\,\delta_{ij}\;; \quad (2)$$

where $\beta$ is the dilatancy factor and the normal to the yield surface is given by

$$Q_{kl} = \sigma'_{kl}/2\bar{\tau} + (1/3)\,\mu\,\delta_{kl}\,, \quad (3)$$

and the Mises equivalent stress is

$$\bar{\tau} = \sqrt{\frac{1}{2}\,\sigma'_{ij}\sigma'_{ij}}\,, \quad (4)$$

where $\sigma'$ is the deviatoric stress ($\sigma'_{ij} = \sigma_{ij} - 1/3\,\sigma_{kk}\delta_{ij}$). The constitutive relation can also be written as $\overset{\triangledown}{\sigma}_{ij} = \mathcal{L}_{ijkl}\,D_{kl}$, with

$$\begin{aligned}\mathcal{L}_{ijkl} \;=\;& G(\delta_{ik}\delta_{jl} + \delta_{il}\delta_{jk}) + \left(K - \frac{2}{3}G\right)\delta_{ij}\delta_{kl} \\ & - \frac{(G\sigma'_{ij}/\bar{\tau} + K\beta\delta_{ij})\,(G\sigma'_{kl}/\bar{\tau} + K\mu\delta_{kl})}{h + G + \mu\beta K}\,, \quad (5)\end{aligned}$$

where $K$ is the elastic bulk modulus.

RR studied the bifurcation conditions from a homogeneous stress and strain state to a band-localized strain state. They assumed a band normal to the $x_2$ coordinate axis and wrote the kinematic condition of the discontinuity of the strain rate as

$$\Delta D_{ij} = 1/2\,(g_i\delta_{j2} + g_j\delta_{i2})\,, \quad (6)$$

where $\Delta D_{ij}$ is an additional velocity gradient tensor inside the band with respect to the tensor outside the band and $g_i$ is an arbitrary vector which varies only with position across the band. The equilibrium on the interfaces of the band is

$$\Delta\dot{\sigma}_{2j} = 0,\; j = 1, 2, 3\,, \quad (7)$$

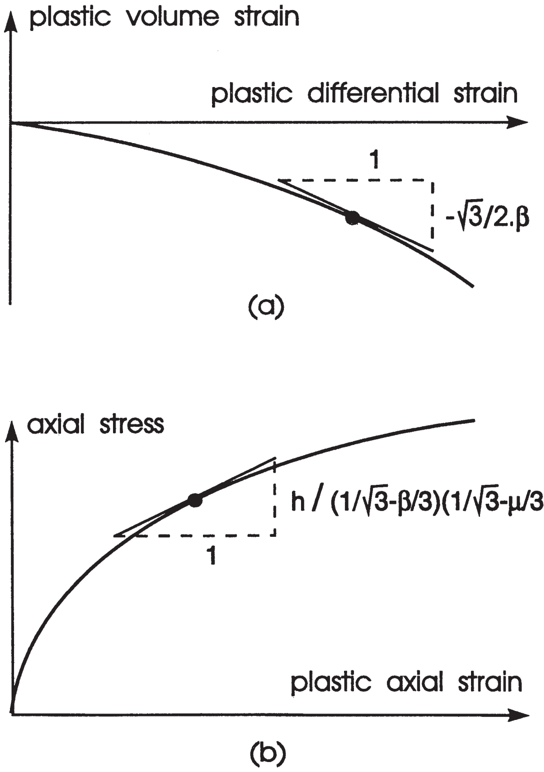

**Figure 2.** Schematic of a typical specimen response in an axisymmetric compression test. (a) Slope of the plastic volume strain versus the plastic differential strain using a dilatancy factor $\beta$. (b) Evolution of the axial stress with respect to the plastic axial strain using a hardening modulus $h$.

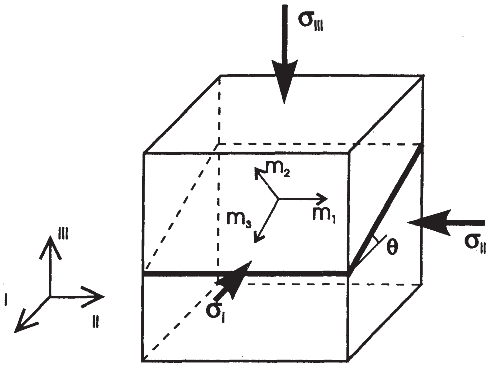

**Figure 3.** Definition of the local Cartesian system $m_1m_2m_3$, with respect to the principal stress directions $(\sigma_{\mathrm{I}}, \sigma_{\mathrm{II}}, \sigma_{\mathrm{III}})$; $\theta$ is the angle between the band (the thicker line) and the $\sigma_{\mathrm{I}}$ direction.

where $\Delta\dot{\sigma}_{ij}$ is the difference of the stress rate tensor inside and outside the band. By considering (5)-(7), and approximating the Jaumann stress rate tensor to the material derivative of the stress tensor, the condition for the possible existence of a planar localization (i.e., the existence of a solution with g $\neq 0$) is

$$\det(\mathcal{L}_{2jk2}) = 0\,; \tag{8}$$

from expression (5), the bifurcation condition (8) leads to the hardening modulus

$$\begin{aligned}\frac{h}{G} \;=\; & \frac{(\sigma'_{22} + \beta K/G\bar{\tau})(\sigma'_{22} + \mu K/G\bar{\tau})}{(4/3 + K/G)\bar{\tau}^2} + \frac{{\sigma'_{21}}^2 + {\sigma'_{23}}^2}{\bar{\tau}^2} \\ & -1 - \mu\beta K/G\,. \end{aligned} \tag{9}$$

*Rudnicki and Rice* [1975] considered that the critical onset of bifurcation corresponds to the case of a maximum modulus $h$ and searched the conditions on the Cartesian system orientation, where stress state was initially expressed, in comparison with the principal stress directions. The principal stresses are defined as $\sigma_{\mathrm{I}} > \sigma_{\mathrm{II}} > \sigma_{\mathrm{III}}$ and the normalized deviatoric stresses are expressed by

$$\begin{aligned} N &= \sigma'_{\mathrm{II}}/\bar{\tau} \\ N_{\mathrm{I}} &= \sigma'_{\mathrm{I}}/\bar{\tau} = -\tfrac{1}{2}N + \tfrac{1}{2}\sqrt{4-3N^2} \\ N_{\mathrm{III}} &= \sigma'_{\mathrm{III}}/\bar{\tau} = -\tfrac{1}{2}N - \tfrac{1}{2}\sqrt{4-3N^2}\,. \end{aligned} \tag{10}$$

The axisymmetric compression stress state $\sigma_{\mathrm{I}} = \sigma_{\mathrm{II}} > \sigma_{\mathrm{III}}$ is defined by $N = N_{\mathrm{I}} = 1/\sqrt{3}$, and the axisymmetric extension stress state $\sigma_{\mathrm{I}} > \sigma_{\mathrm{II}} = \sigma_{\mathrm{III}}$ is defined by $N = N_{\mathrm{III}} = -1/\sqrt{3}$; $n_{\mathrm{I}}, n_{\mathrm{II}}, n_{\mathrm{III}}$ are the projections of the unit normal to the band (the $x_2$ coordinate axis) on the three principal stress directions.

*Perrin and Leblond* [1993] showed in an elegant analysis that $n_{\mathrm{II}} = 0$, $n_{\mathrm{I}} \neq 0$, and $n_{\mathrm{III}} \neq 0$ (i.e., the band is parallel to the intermediate principal stress direction) only in the following range of $(\beta + \mu)$:

$$\begin{aligned} (1-2\nu)N - \sqrt{4-3N^2} &\leq \tfrac{2}{3}(1+\nu)(\beta+\mu) \\ &\leq (1-2\nu)N + \sqrt{4-3N^2}\,. \end{aligned} \tag{11}$$

It follows that one can write $n_{\mathrm{I}} = \sin(\theta), n_{\mathrm{III}} = \cos(\theta)$, where $\theta$ is the angle between the normal to the band and the $\sigma_{\mathrm{III}}$ direction. Expression (9) is maximized when

$$\tan^2(\theta) = (\xi - N_{\mathrm{III}})/(N_{\mathrm{I}} - \xi)\,, \tag{12}$$

where $\xi = (1+\nu)(\beta+\mu)/3 - N(1-\nu)$, which gives the critical hardening modulus

$$\frac{h_c}{G} = \frac{1+\nu}{9(1-\nu)}(\beta-\mu)^2 - \frac{1+\nu}{2}\left(N + \frac{\beta+\mu}{3}\right)^2 \;; \tag{13}$$

otherwise, outside the range of equation (11) [*Issen and Rudnicki,* 2000],

$$\begin{aligned}\frac{h_c}{G} \;=\; & \frac{1+\nu}{9(1-\nu)}(\beta-\mu)^2 - \frac{1+\nu}{1-\nu}\left(\frac{1}{2}N_\zeta - \frac{\beta+\mu}{3}\right)^2 \\ & - \left(1 - \frac{3}{4}N_\zeta^2\right), \end{aligned} \tag{14}$$

with $\zeta = \mathrm{I}$ if the upper inequality of (11) is violated and $\zeta = \mathrm{III}$ if the lower inequality is violated.

The condition where $\zeta = \mathrm{III}$ corresponds to $n_{\mathrm{I}} = n_{\mathrm{II}} = 0$ and is possible if $(\beta + \mu)$ can be negative, which is realistic for porous rock due to a yield cap [*Olsson,* 1999; *Issen and Rudnicki,* 2000; *Wong et al.*, 1997] (see also the discussion in appendix I of RR's paper). This case corresponds to a band perpendicular to the axis of compression in an axisymmetric compression test and is discussed by *Olsson* [1999] and *Issen and Rudnicki* [2000] which they termed compaction bands. Extension bands are predicted for the case where $\zeta = \mathrm{I}$ and correspond to $n_{\mathrm{II}} = n_{\mathrm{III}} = 0$, i.e., a band parallel to the most compressive stress.

All these previous studies concentrated on the condition for localization by predicting the onset of localization (giving the critical hardening modulus $h_c$) and the orientation of the band with respect to the principal stress directions (the angle $\theta$). The following section proposes an analysis of the strain inside the incipient localization band to determine the ratio between the volumic strain and the shear strain. My goal is to specify the type of strain that exists inside the band, which can be dilating, isovolumetrically shearing, or compacting.

### 2.2. Shear Strain and Volumetric Strain at the Onset of Localization

I examine the mechanism of localization, i.e., the expression for the discontinuity of the strain rate at the onset of localization. From the principal stress directions, the orientation of the band is defined by the angle $\theta$. In any reference frame $Om_1m_2m_3$, where the second direction $Om_2$ is perpendicular to the band, the bifurcation condition (8) is met. For simplification, one can choose to take the first coordinate axis $Om_1$ to be equal to the second principal stress $\sigma_{\mathrm{II}}$ direction (Figure 3), which has no influence on the final result. The unit vectors of $Om_1m_2m_3$ are expressed in the principal stress

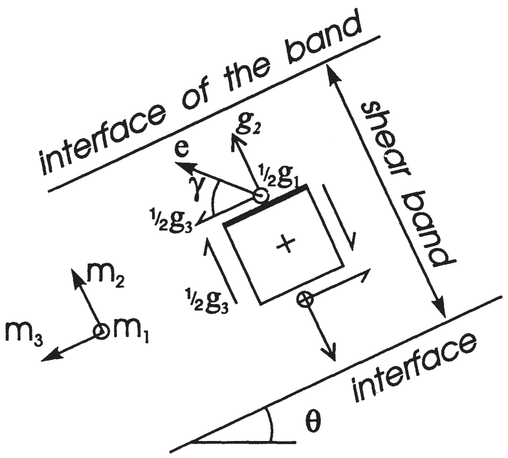

**Figure 4.** Strain rate inside the band expressed by the condition of discontinuity superimposed over the homogeneous strain rate. Vector **e** is the additional strain vector on a surface parallel to the interface of the band; $\gamma$ is a band dilatancy angle.

directions reference system by $m_1 = (0,1,0)$; $m_2 = (\sin(\theta), 0, \cos(\theta))$; $m_3 = (\cos(\theta), 0, -\sin(\theta))$. In the $Om_1m_2m_3$ reference frame, the discontinuity of the strain rate (Figure 4) is expressed by

$$\Delta D_{ij} = \begin{pmatrix} 0 & \frac{1}{2}g_1 & 0 \\ \frac{1}{2}g_1 & g_2 & \frac{1}{2}g_3 \\ 0 & \frac{1}{2}g_3 & 0 \end{pmatrix} . \tag{15}$$

The terms $g_1$ and $g_3$ account for the shear strain inside the band, whereas $g_2$ accounts for the volumetric strain ($g_2$ is positive for dilatancy and negative for compaction). The nonsymmetric constitutive tensor $\mathcal{N}_{ij} = \mathcal{L}_{2ij2}$ is expressed by

$$\begin{aligned} \mathcal{N}_{ij} \quad = \quad & G(\delta_{i2}\delta_{j2} + \delta_{ij}) + (K - \tfrac{2}{3}G)\,\delta_{i2}\delta_{j2} \\ & - \frac{(G\sigma'_{i2}/\bar{\tau} + K\beta\delta_{i2})\,(G\sigma'_{j2}/\bar{\tau} + K\mu\delta_{j2})}{h + G + K\mu\beta} . \end{aligned} \tag{16}$$

The deviatoric stress in the $Om_1m_2m_3$ reference system is expressed from the principal deviatoric stresses by

$$\begin{aligned} \sigma'_{22} = {} & \tfrac{1}{2}(\sigma'_{\mathrm{I}} + \sigma'_{\mathrm{III}}) - \tfrac{1}{2}(\sigma'_{\mathrm{I}} - \sigma'_{\mathrm{III}})\cos(2\theta) \\ \sigma'_{12} = {} & 0 \\ \sigma'_{32} = {} & \tfrac{1}{2}(\sigma'_{\mathrm{I}} - \sigma'_{\mathrm{III}})\sin(2\theta) . \end{aligned} \tag{17}$$

By combining (16) and (17), the tensor $\mathcal{N}$ is reduced to the expression

$$\mathcal{N}_{ij} = \begin{bmatrix} G & 0 & 0 \\ 0 & \mathcal{N}_{22} & \mathcal{N}_{23} \\ 0 & \mathcal{N}_{32} & \mathcal{N}_{33} \end{bmatrix} , \tag{18}$$

where

$$\begin{aligned} \mathcal{N}_{22} = {} & 2G\tfrac{1-\nu}{1-2\nu} - \tfrac{G^2}{4(h_c+G+\mu\beta K)} \\ & \cdot \left[N_{\mathrm{I}} + N_{\mathrm{III}} - (N_{\mathrm{I}} - N_{\mathrm{III}})\cos(2\theta) + \tfrac{4}{3}\beta\tfrac{1+\nu}{1-2\nu}\right] \\ & \cdot \left[N_{\mathrm{I}} + N_{\mathrm{III}} - (N_{\mathrm{I}} - N_{\mathrm{III}})\cos(2\theta) + \tfrac{4}{3}\mu\tfrac{1+\nu}{1-2\nu}\right] \end{aligned} \tag{19a}$$

$$\begin{aligned} \mathcal{N}_{23} = {} & -\tfrac{G^2}{4(h_c+G+\mu\beta K)}(N_{\mathrm{I}} - N_{\mathrm{III}})\sin(2\theta) \\ & \cdot \left[N_{\mathrm{I}} + N_{\mathrm{III}} - (N_{\mathrm{I}} - N_{\mathrm{III}})\cos(2\theta) + \tfrac{4}{3}\beta\tfrac{1+\nu}{1-2\nu}\right] \end{aligned} \tag{19b}$$

$$\begin{aligned} \mathcal{N}_{32} = {} & -\tfrac{G^2}{4(h_c+G+\mu\beta K)}(N_{\mathrm{I}} - N_{\mathrm{III}})\sin(2\theta) \\ & \cdot \left[N_{\mathrm{I}} + N_{\mathrm{III}} - (N_{\mathrm{I}} - N_{\mathrm{III}})\cos(2\theta) + \tfrac{4}{3}\mu\tfrac{1+\nu}{1-2\nu}\right] \end{aligned} \tag{19c}$$

$$\mathcal{N}_{33} = G - \tfrac{G^2}{4(h_c+G+\mu\beta K)}(N_{\mathrm{I}} - N_{\mathrm{III}})^2\sin^2(2\theta) . \tag{19d}$$

The equilibrium equation (7) at the interface of the band is expressed by

$$\mathcal{N}_{ij}\,g_j = 0, \; i = 1,2,3 . \tag{20}$$

The first relation of (20) leads to $g_1 = 0$, which shows that the discontinuity of the strain state is a plane strain state in the plane determined by the major and minor principal stress directions. This means, if one considers an axisymmetric test, for example, that the strain becomes nonaxisymmetric at the onset of localization.

The second and third equations of (20) are equivalent since det $(\mathcal{N}) = 0$. Consider now that **e** is the additional strain vector on a surface inside the band parallel to the interface of the band, i.e., $e_i = \Delta D_{i2}$ (Figure 4), and $\gamma$ is the angle between the $m_3$ direction and **e**. The angle $\gamma$ is defined by

$$\tan(\gamma) = -2\mathcal{N}_{23}/\mathcal{N}_{22} = -2\mathcal{N}_{33}/\mathcal{N}_{32} . \tag{21}$$

The component $g_3$ is chosen to be positive. If $\pi/2 > \gamma > 0$, then the shear strain is associated with a volumetric dilatancy, and if $-\pi/2 < \gamma < 0$, a volumetric compaction. The angle $\gamma = 0$ corresponds to a pure shear case with no dilation or compression; $\gamma$ can be called the band dilatancy angle.

For low values of $\mu$ and $\beta$, the condition $\tan(\gamma) = \pi/2$ corresponds to the upper limit of (11) (i.e., $\theta = \pi/2$), while $\tan(\gamma) = -\pi/2$ corresponds to the lower limit (i.e., $\theta = 0$). The shear component of the strain discontinuity inside the band is zero when the band is parallel to the major or minor principal stress direction. This means that there is a continuous variation of the nature of the strain inside the band of localization, between the so-called shear bands and the pure extension or compaction bands. The condition $\tan(\gamma) = 0$ corresponds physically to a pure shear band, without volumetric strain. This condition is expressed by

$$3(1-2\nu)(1-\nu)N = (1+\nu)\left[(1-2\nu)(\beta+\mu) + 2\beta\right] . \tag{22}$$

The variation of $\gamma$ is continuous with respect to $\mu$ and $\beta$ (Figure 5a) for low values of $\mu$ and $\beta$. One can distinguish two zones in the plane $(\mu, \beta)$ which are called compacting shear bands and dilating shear bands, delimited by (22). Figure 5b shows the continuous evolution of the band orientation angle $\theta$ with respect to $\mu$ and $\beta$. The different domains (pure compaction bands, compacting shear bands, dilating shear bands, and pure extension bands) are also represented in Figure 6. The limit between the pure compaction band and the shear band and the limit between the pure extension band

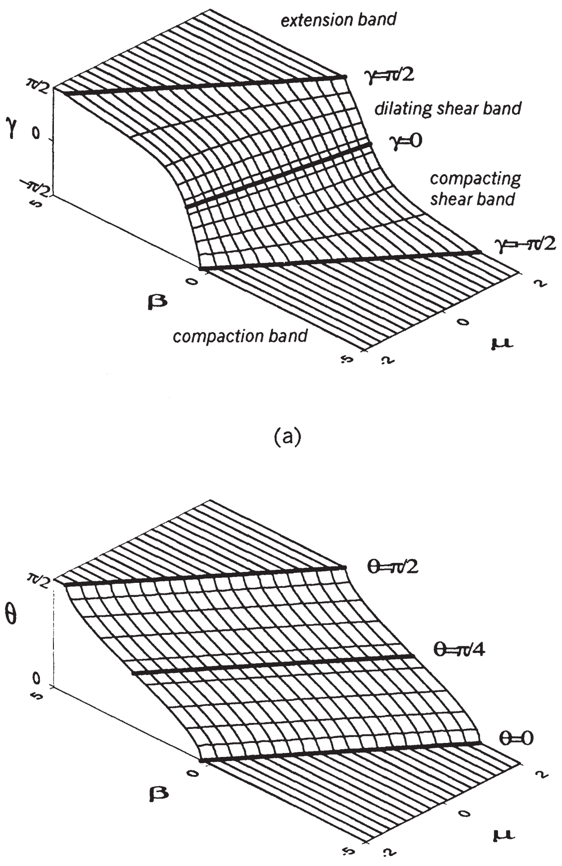

(a)

(b)

**Figure 5.** Evolution of (a) the band dilatancy angle $\gamma$ and (b) the band orientation angle $\theta$ with respect to $\beta$ and $\mu$, for an axisymmetric compression stress state (i.e., $N = 1/\sqrt{3}$) and $\nu = 0.2$.

and the shear band are parallel and correspond to the values of $\theta = 0, \pi/2$ and $\gamma = -\pi/2, \pi/2$. Inside the area of shear band, the isovalue curves of $\theta$ are not parallel to the isocurves of $\gamma$, and one can have a pure shear band with an orientation $\theta$ lower or higher than $\pi/4$. For an associated plastic model (i.e., $\beta = \mu$), the conditions $\gamma = 0$ and $\theta = \pi/4$ are equivalent and can be written

$$\mu = \frac{3(1-2\nu)}{4(1+\nu)} N \ . \tag{23}$$

Nevertheless, for nonassociated models, the condition $\tan(\gamma) = 0$ can correspond to the limits of (11), for higher positive values or lower negative values of $\mu$. In this condition, the vector $\mathbf{g}$ is undetermined. These limit values of $\mu$ and $\beta$ are expressed by

$$\begin{aligned} \tfrac{4}{3}(1+\nu)\mu &= (1-2\nu)N \pm (3-2\nu)\sqrt{4-3N^2} \\ \tfrac{4}{3}(1+\nu)\beta &= (1-2\nu)N \mp (1-2\nu)\sqrt{4-3N^2} \ . \end{aligned} \tag{24}$$

Outside these values of $\mu$, there is a discontinuity of the angle $\gamma$ with respect to $\beta$ at the limits of (11). This theoretical discontinuity of the strain mechanism is physically improbable and is considered to be a limitation of the RR formulation. However, for the range of different stress states (i.e., $-1/\sqrt{3} < N < 1/\sqrt{3}$) and $\nu = 0.2$, $\mu$ must be between $-2.598$ and $2.598$ to assure continuity of $\gamma$. These values for $\mu$ are well within the estimated experimental range.

## 3. Comparison With Experimental Results

Experimental evidence of compacting shear bands in a porous Vosges sandstone (porosity of about 22%) has been obtained in an axisymmetric triaxial cell [*Bésuelle et al.,* 2000; *Bésuelle,* 1999]. The sandstone is a pink quartz sandstone (quartz, 93%) with a few percent of feldspar and white mica. The mean grain size is about 0.3 mm, and the diameter and the height of the specimens are 40 and 80 mm, respectively. Several axisymmetric compression tests (the compressive axial stress is higher than the compressive lateral stress) and axisymmetric extension tests (the compressive lateral stress is higher than the axial stress which can be compressive or extensive) have been performed from 0 to 60 MPa confining pressure with an axial strain rate equal to $10^{-5} s^{-1}$. Observations by X ray computerized tomography (CT) and scanning electron microscope (surface porosity) of specimens tested in compression showed a dilating shear band at 30 MPa and compacting shear band at 50 MPa confining pressure. The spatial resolution of the X ray apparatus is 0.7 mm for the lateral directions of the specimen and 2 mm for the axial direction. In the X ray reconstructions (Figure 7), an initial heterogeneity of the rock is illustrated by a density difference in the upper and lower half of the specimens. In the more porous half of the specimens (the darker half), the dilating shear band initiated during the test

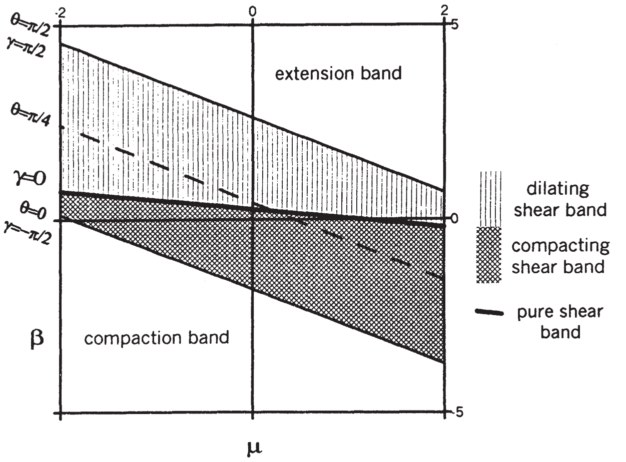

**Figure 6.** Distinction in the plane $(\mu, \beta)$ of the areas corresponding to the dilating and compacting shear bands and the extension and compaction bands, for an axisymmetric compression stress state ($N = 1/\sqrt{3}$) and $\nu = 0.2$.

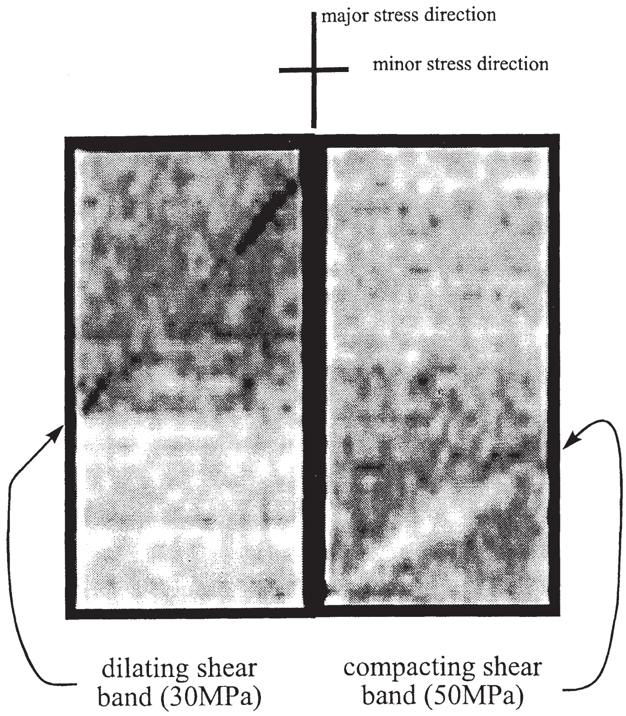

**Figure 7.** X ray CT reconstruction of specimens tested at 30 MPa (left, inclined dark band, dilating shear band) and 50 MPa (right, inclined light band, compacting shear band) confining pressure in triaxial compression test. Heterogeneity of the specimens (one half part is denser than the other part) already existed before the test.

is darker and the compacting shear band is lighter than outside the band.

Compressive stress and strain are assumed to be positive in this section. The elastic Poisson coefficient $\nu$ and the Young modulus are determined at the beginning of the axial loading when the stress-strain curves are quasi-linear. The friction coefficient $\mu$ is the slope of the theoretical yield surface in the Mises equivalent stress versus mean stress plane. Near the ultimate loading (i.e., near the onset of localization) this yield surface is assumed to be closed to the failure envelope determined from tests at several confining pressures [*Olsson*, 1999]. The Mohr envelope at failure (stress peak) in the shear stress versus normal stress plane (Figure 8) shows a strong nonlinearity, with a positive slope at low confining pressure and a negative slope at high confining pressure, and $\mu$ is approximated here as the local slope of the Mohr envelope multiplied by $2/\sqrt{3}$. For extension tests, the choice of $\mu$ is problematic and is arbitrarily taken to be the same as the value of $\mu$ determined from the uniaxial compression tests. Note that when the slope of the yield surface $\mu$ is negative, $\mu$ should not have the meaning of an internal friction coefficient. In this case, the negative value of $\mu$ occurs due to a decrease of shear strength as a result of grain crushing, which itself is due to high mean pressure.

During the experiments, the three axial and four lateral transducers enable detection of the loss of homogeneity of the strain field inside the specimen, which is associated with strain localization. Details of the strain measurements are given in *Bésuelle and Desrues* [2001]. The onset of localization was systematically observed before the stress peak. From these results, the parameter $\beta$ associated with the plastic part of the RR formulation is determined at the onset of localization by the relation $\beta = -\sqrt{3}/2(\dot{\varepsilon}_a^p + 2\dot{\varepsilon}_l^p)/(\dot{\varepsilon}_a^p - \dot{\varepsilon}_l^p) \times \operatorname{sign}(\sigma_a - \sigma_l)$, where $\dot{\varepsilon}_a^p$ and $\dot{\varepsilon}_l^p$ are the plastic axial and lateral strain rate and $\sigma_a$ and $\sigma_l$ are the axial and lateral stress (plastic strain is computed as the total strain minus the elastic strain determined from the elastic parameters). The hardening modulus $h$ at the onset of localization is computed from the slope of the axial stress versus axial strain curves (see Figure 2b). The experimental parameters $\mu, \beta, \nu, h$, and $\theta$, and the state of strain within the deformation bands are summarized in Table 1 for compression and extension tests conducted at confining pressures of 0 to 60 MPa.

The predicted values of $\theta_c, \gamma$, and $h_c$ are computed from the experimental data $\mu, \beta$, and $\nu$ with (12), (21), and (13)-(14). The failure modes observed experimentally were differentiated by direct observation and CT imaging and compared with theoretical predictions: axial splitting (AS) is associated with a theoretical pure extension band (PE), the compacting shear bands (CB) predicted theoretically are associated with compacting shear bands observed inside the specimen, and theoretical dilating shear bands (DB) correspond to the experimental dilating shear bands. The volumetric strain inside the band of localization in extension tests has not been studied in specimens. At a confining pressure of 30-40 MPa the bands are parallel to the maximum principal stress direction. This observation suggests that the bands are dilating with nominally zero shear strain. The theoretical model predicts dilating shear bands for extension tests if the absolute magnitude of $\mu$ is assumed to be the same as the observed in uniaxial compression tests. However, at 30 MPa confining pressure, a small increase of $\mu$ up to 1.15 predicts a pure extension band, perpendicular to the least compressive stress direction as observed on the specimen. The angles between the band and the greatest compressive principal stress predicted for compression tests are

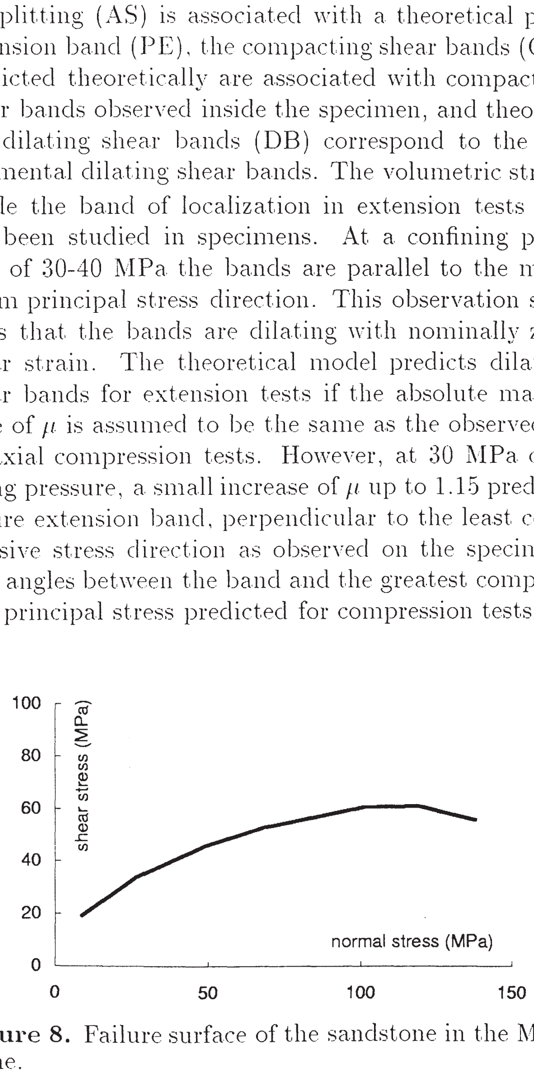

**Figure 8.** Failure surface of the sandstone in the Mohr plane.

**Table 1.** Experimental and Predicted Results in Axisymmetric Compression (C) and Extension (E) Tests for Several Confining Pressures from 0 to 60 MPa

| | Experimental | | | | | | Predicted | | |
|---|---|---|---|---|---|---|---|---|---|
| Test | $\mu$ | $\theta$, deg | $\beta$ | $\nu$ | $h/G$ | Mechanism[a] | Mechanism[a] ($\gamma$) | $\theta_c$, deg | $h_c/G$ |
| C: 0.5 MPa | 0.97 | 90 | 1.55 | 0.4 | $\sim 0.76$ | AS | PE ($90^\circ$) | 90 | -1.37 |
| C: 10 MPa | 0.78 | 54 | 0.94 | 0.29 | $\sim 0.03$ | DB | DB ($66^\circ$) | 67 | -0.85 |
| C: 20 MPa | 0.56 | 50 | 0.73 | 0.21 | $\sim -0.01$ | DB | DB ($45^\circ$) | 57 | -0.61 |
| C: 30 MPa | 0.38 | 48 | 0.47 | 0.26 | $\sim 0.04$ | DB | DB ($27^\circ$) | 52 | -0.46 |
| C: 40 MPa | 0.20 | 47 | 0.26 | 0.26 | $\sim 0.31$ | DB | DB ($6^\circ$) | 47 | -0.33 |
| C: 50 MPa | 0.2 to | 40 | 0.1 | 0.21 | $\sim 0.78$ | CB | CB ($-10^\circ$) | 43 | -0.27 |
| | -0.1 | ... | ... | ... | ... | ... | CB ($-16^\circ$) | 39 | -0.19 |
| C: 60 MPa | -0.38 | 37 | 0 | 0.25 | $\sim 1.47$ | CB | CB ($-28^\circ$) | 35 | -0.10 |
| E: 30 MPa | 0.97 | 90 | 0.59 | 0.34 | $\sim 0$ | PE | DB ($75^\circ$) | 78 | 0.03 |
| | 1.15 | ... | ... | ... | ... | ... | PE ($90^\circ$) | 90 | 0.07 |
| E: 40 MPa | 0.97 | 90[b] | 0.4 | 0.33 | $\sim 0$ | PE | DB ($65^\circ$) | 72 | 0.06 |
| | 1.15 | ... | ... | ... | ... | ... | DB ($70^\circ$) | 77 | 0.12 |
| E: 50 MPa | 0.97 | 71 | 0.43 | 0.37 | $\sim 0$ | DB | DB ($65^\circ$) | 73 | 0.06 |
| E: 60 MPa | 0.97 | 69 | 0.37 | 0.4 | $\sim 0$ | DB | DB ($62^\circ$) | 71 | 0.08 |

[a] Mechanisms of localization are: AS, axial splitting; PE pure extension band; DB, dilating shear band; CB, compacting shear band.

[b] Surfaces of failure in extension tests at low confining pressure (<40 MPa) were particularly influenced by a special shape of the specimen and are suspected to not be perfectly representative [*Bésuelle et al.*, 2000].

well in accordance with the measured angles. A maximum difference of $10^\circ$ is observed at 10 MPa confining pressure, and values smaller than $45^\circ$ are observed at high confining pressure. Similar results were reported by *Olsson* [1999]. The comparison of the experimental results (band angles and volumetric behavior inside the bands) and theoretical results suggests that the constitutive parameters associated with the homogeneous behavior before localization can be used to predict nature and orientation, and conditions necessary for the initiation of deformation bands.

## 4. Discussion

The above analysis for the strain mechanism of shear band formation predicts conditions for a reduction of the porosity inside a band. Small positive values of the dilatancy coefficient $\beta$ and negative or small positive values of the friction coefficient $\mu$ are sufficient to explain such a behavior. Experimental results show that these conditions can be met when the mean pressure increases because both friction and dilatancy coefficients become small or negative. Such results enable a better understanding of the transition between localized deformation and cataclastic flow [*Bésuelle*, 2001]. This could be important during deformation of porous rocks in the crust.

From a micromechanical point of view, dilation within bands would occur when deformation is dominated by intergranular and intragranular microcracks. By contrast, compacting bands would arise when processes such as grain boundary sliding, grain rotation or grain crushing dominate.

The conditions for compacting shear bands are easier to reproduce in laboratory tests than conditions for pure compaction bands (pure normal strain), which require very low or negative values of the dilatancy coefficient and very high confining pressures. This latter strain type can be viewed as an endmember case of the compacting shear band, where the shear strain component becomes infinitesimal. These theoretical results enable interpretation of geological observations of bands with a low porosity in comparison with the porosity outside the band. Such analyses can be used to estimate the field stress conditions at the onset of localization by estimating the ratio between the shear and volumic strain inside the band. However, field observation of bands should be carefully considered because bands have generally sustained a large postlocalization history. *Antonellini et al.* [1994] have observed compacting shear bands in a porous sandstone. *Mollema and Antonellini* [1996] have observed bands with a reduction of porosity but no shear displacement, which may correspond to pure compaction bands.

The results presented here suggest that compacting shear bands can also exist in axisymmetric extension tests, as suggested from experimental considerations [*Bésuelle et al.*, 2000; *Zhu et al.*, 1997]. In this case, shear bands are oriented approximately parallel to the least principal stress direction. A high confining pressure should be necessary to produce them. By contrast, axial splitting characterized by cracks opening parallel to the compressive stress in uniaxial tests could be considered as extension bands.

The analysis of strain inside the band at the onset of localization shows values of $\mu$ ranging from about

$-2.5$ to $2.5$, outside of which the continuity of the strain mechanism with respect to $\mu$ and $\beta$ is not ensured. One could have a complete change of strain type inside the band for a small change in the constitutive parameter. This is a limit to the formulation of Rudnicki and Rice which has to be considered to model the mechanical behavior of rocks, although these theoretical restrictions on $\mu$ seem physically improbable.

The hardening modulus $h$ is predicted to be negative in axisymmetric compression tests for the range of $\mu$ and $\beta$ used, which means that localization should theoretically occur during strain softening. However, experimental data showed that localization occurs during strain hardening. This problem was discussed by RR, who considered as suspect the predicted onset of localization for the axisymmetric compression. A resolution of this problem depends on the mathematical formulation of the constitutive relations. Other laws predict localization in the hardening regime for axisymmetric stress condition [e.g., *Desrues and Chambon,* 1989].

## 5. Conclusions

Porous rocks have a specific behavior in that their yield surface is strongly nonlinear (i.e., the yield surface has a positive pressure dependence for low mean stress and a negative pressure dependence for high mean stress). This behavior is associated with the existence of dilating shear bands at low mean stress or even pure extension bands at very low stress (axial splitting), compacting shear bands at higher mean stress, and pure compaction bands at very high stress. This evolution from pure extension bands to pure compaction bands is continuous via shear bands. The latter are dilating at low stress and gradually become compacting with increasing mean stress, until they are purely compacting bands at high mean stress. The more compacting a band is, the higher the angle is between the band (the heavy line) and the major compressive stress direction, varying from 0 for pure extension band to $\pi/2$ for pure compaction band.

The angle between the shear bands and the principal stress directions depends on: the friction coefficient $\mu$, the dilatancy factor $\beta$, Poisson's coefficient $\nu$, and the stress state (i.e., $N$). For associated models ($\beta = \mu$), shear bands that have an angle with respect to the greatest principal stress direction that is lower than $\pi/4$ are dilating, while they are compacting if the angle is greater than $\pi/4$. For rocks that have a nonassociated behavior ($\beta \neq \mu$), the transition between dilating and compacting shear bands corresponds approximately to $\pi/4$.

The phenomenon of localized porosity reduction has important consequences for field applications, notably for transport of fluids. As was suggested for a pure compaction band [*Issen and Rudnicki,* 2000], compacting shear band can locally reduce the permeability and act as permeability barriers with preferential orientations, which may reduce (inducing a strong anisotropy) the global permeability of a geological structure.

**Acknowledgments.** I would like to thank Y. Guéguen and G. Simpson for their helpful discussions.

## References

Antonellini, M. A., A. Aydin, and D. D. Pollard, Microstructure of deformation bands in porous sandstones at Arches National Park, Utah, *J. Struct. Geol., 16,* 941-959, 1994.

Bésuelle, P., Déformation et rupture dans les roches tendres et les sols indurés : Comportement homogène et localisation, Ph.D. thesis, 370 pp., Univ. of Grenoble, Grenoble, France, 1999.

Bésuelle, P., Evolution of strain localisation with stress in a sandstone: Brittle and semi-brittle regimes, *Phys. Chem. Earth, 26,* 101-106, 2001.

Bésuelle, P., and J. Desrues, An internal instrumentation for axial and radial strain measurements in triaxial tests, *Geotech. Test. J., 24,* 193-199, 2001.

Bésuelle, P., J. Desrues, and S. Raynaud, Experimental characterisation of the localisation phenomenon inside a Vosges sandstone in a triaxial cell, *Int. J. Rock Mech. Min. Sci., 37,* 1223-1237, 2000.

Desrues, J., and R. Chambon, Shear band analysis for granular materials: The question of incremental non-linearity, *Ing. Arch., 59,* 187-196, 1989.

Hicher, P.Y., and H. Wahyudi, Microstructural analysis of strain localisation in clay, *Comput. Geotech., 16,* 205-222, 1994.

Issen, K. A., and J. W. Rudnicki, Conditions for compaction bands in porous rock, *J. Geophys. Res., 105,* 21,529-21,536, 2000.

Mollema, P. N., and M. A. Antonellini, Compaction bands: A structural analog for anti-mode I cracks in aeolian sandstone, *Tectonophysics, 267,* 209-228, 1996.

Olsson, W. A., Theoretical and experimental investigation of compaction bands in porous rock, *J. Geophys. Res., 104,* 7219-7228, 1999.

Perrin, G., and J. B. Leblond, Rudnicki and Rice's analysis of strain localization revisited, *J. Appl. Mech., 4,* 842-846, 1993.

Rudnicki, J. W., A class of elastic-plastic constitutive laws for brittle rock, *J. Rheol., 28,* 759-778, 1984.

Rudnicki, J. W., and J. R. Rice, Conditions for the localization of deformation in pressure-sensitive dilatant materials, *J. Mech. Phys. Solids, 23,* 371- 394, 1975.

Tillard-Ngan, D., J. Desrues, and S. Raynaud, Strain localisation in beaucaire marl, in *Proceedings of Geotechnical Engineering of Hard Soils-Soft Rocks,* pp. 1679-1686, A.A. Balkema, Brookfield, Vt., 1993.

Wong, T.-F., C. David, and W. Zhu, The transition from brittle faulting to cataclastic flow in porous sandstone: Mechanical deformation, *J. Geophys. Res., 102,* 3009-3025, 1997.

Zhu, W., L. G. J. Montesi, and T.-F. Wong, Shear-enhanced compaction and permeability reduction: Triaxial extension tests on porous sandstone, *Mech. Mater., 25,* 199-214, 1997.

---

P. Bésuelle, Laboratoire de Géologie, Ecole Normale Supérieure, 24 rue Lhomond, 75231 Paris Cedex 05, France. (besuelle@geologie.ens.fr)

(Received March 31, 2000; revised November 21, 2000; accepted December 21, 2000.)

JOURNAL OF MECHANICS OF MATERIALS AND STRUCTURES
Vol. 1, No. 7, 2006

# SWITCHING DEFORMATION MODES IN POST-LOCALIZATION SOLUTIONS WITH A QUASIBRITTLE MATERIAL

PIERRE BÉSUELLE, RENÉ CHAMBON AND FRÉDÉRIC COLLIN

Localization in a quasibrittle material is studied using a local second-gradient model. Since localization takes place in a medium assumed to be initially homogeneous, nonuniqueness of the solutions of an initial boundary value problem is then also studied. Using enhanced models generalizes the classical localization analysis. In particular, it is necessary to study solutions more continuous (that is, continuous up to the degree one) than the ones used in analysis involving classical constitutive equations. Within the assumptions done, it appears that localization is possible in the second-gradient model if it is possible in the underlying classical model. Then the study of nonuniqueness is conducted for the numerical problem, using different first guesses in the full Newton–Raphson procedure solving the incremental nonlinear equations. Thanks to this method, we are able to simulate qualitatively the nonreproducibility of usual experiment in the postpeak regime.

## 1. Introduction

Modeling the degradation of materials is a very challenging task. If the degradation is sufficiently high — if the material exhibits some softening (here in a vague sense) — it is now well known that some unpleasant features appear both in experiments and in computations.

From the experimental point of view, as soon as the softening is reached, it seems that the behavior is poorly reproducible or nonreproducible. The first reason is that in main cases strain localization occurs which means that contrary to current assumptions, laboratory samples are not strained homogeneously up to the failure. Moreover localization patterns themselves are not easily reproduced. Let us first quote Desrues and Viggiani [2004], who performed some biaxial tests twice:

> [E]very test is somewhat unique as for the patterns of strain localization (location of the shear band, appearance of nonpersistent and/or multiple bands).

Quite clearly such behavior is related to the loss of uniqueness of the problem (that is, in the reported case the biaxial test) which allows shear bands to emerge. But, what is clear in [Desrues and Viggiani 2004] is that there is a large variability in the observed patterns. This means that there is not only one alternative solution involving a unique localized band. If it is quite clear that if orientation and width of the bands are easily reproduced, on the contrary the number of bands and their position as well as their persistence cannot be predicted in advance. This has some consequences for the load versus displacement curves which can exhibit very different results in their postpeak parts (that is, when some localization can be

---

*Keywords:* continuum with microstructure, second gradient, finite element, bifurcation, strain localization, mode switching, reproducibility.

P.B. gratefully acknowledges financial support for a two-month stay for at the University of Liège through a Research Fellowship of the Fonds National de la Recherche Scientifique (FNRS) of Belgium.

expected). This is clearly illustrated in [Desrues and Hammad 1985] or in [Desrues 1984] where the two curves of duplicate tests are in many cases rather different as soon as the peak value is attained. Other similar observations about tests performed twice can be found in [Viggiani et al. 2001]. These results are often interpreted as the consequence of some (unfortunately unknown) initial imperfection in the studied samples, and based on the deterministic principle, it is argued that if the initial state is completely known the problem should disappear.

Following the previous ideas, numerical modeling of such postpeak phenomena is usually achieved by introducing some (deterministic) initial imperfection into the computation, and it is believed that uniqueness of the solution is restored. Consequently changing the imperfection can change the final solution of the computation since it is assumed that there is a correspondence between a given imperfection and the resulting solution. Unfortunately we demonstrated recently that this way of thinking may be erroneous; see [Chambon and Moullet 2004]. For the same imperfection several (properly converged) solutions can be found provided an appropriate searching algorithm is used. Recently, introducing an initial fluctuation of the mechanical properties has been used to deal with this problem, for instance in [Nübel and Huang 2004]. In the quoted paper the introduction of this initial fluctuation is achieved by initializing randomly the density for a model sensitive with respect to this parameter. The computations performed seem very similar to what is usually observed. However, even in this case, it seems that the author assumes implicitly that uniqueness is restored. Alternative solutions should be searched in order to clarify this point.

Another way is followed in the numerical experiments detailed in the present paper. We choose to solve the “perfect” (which means without any intentional imperfection) problem, and we try to exhibit several solutions for this problem. Usually the method used to find alternative solutions is related to a spectral analysis of the linearized velocity problem. Numerically this is achieved by searching when the least eigenvalue of the tangent stiffness matrix related to the velocity discretized problem goes to zero; see for instance [de Borst 1986] or [Ikeda and Murota 2002]. This method is based on a linearization of the problem which is completely sound if the nonlinear problem is incrementally linear. Since we use an elastoplastic model, elastic up to a given threshold and exhibiting a sudden softening as soon as this threshold is reached, there are many possible linearizations depending on the choice of the unloading area within the computed domain. Then the drawback of such a method is that the mode corresponding to the null eigenvalue which allows theoretically to follow the bifurcated solution can correspond for some point of the studied structure to a constitutive branch (loading or unloading) different to the one used to compute the linearized stiffness matrix. In this paper we prefer to follow the ideas initially applied in [Chambon et al. 2001b] where the solution for a time step is searched with a Newton–Raphson method with different first estimations which can (if the problem has more than one solution) yield different properly converged solutions.

On the other hand, it is now well known that localizations cannot be properly modeled with classical media since this implies rupture without energy consumption as proved by Pijaudier-Cabot and Bažant [1987]. Enhanced models are necessary. However, contrary to what is often believed, the use of an enhanced model does not guarantee uniqueness of the solution of the corresponding boundary value problems; this has been demonstrated in [Chambon et al. 1998; Chambon and Moullet 2004], the latter employing the same model used in this paper. But it seems that the result is more general. Challamel and Hijaj [2005] also found solutions for the same problem, but using a nonlocal, enhanced model.

In this paper a second-gradient theory is used in conjunction with the method to search alternative solutions recalled above. The first section of this paper is devoted to a brief recall of the model used and of the principle of its numerical implementation.

In order to be able to perform easily different computations, the element has been first implemented in the general purpose finite element code Lagamine developed at University of Liège [Charlier 1987], and we checked the accuracy of this implementation using extended tests. This is described in the second section of this paper.

Then a localization analysis is performed in the third section of the paper. Such an analysis is necessarily different from the original ones of [Rudnicki and Rice 1975] since the type of discontinuity assumed in the aforementioned reference cannot be used due to the second-order terms.

After briefly recalling the method, the fourth section deals with the numerical experiments of non-uniqueness and describes computations exhibiting switching modes. Such mode switching has already been studied by Ikeda et al. [1997] in a different context. It has been made mainly for the incrementally linear comparison solid, which on the one hand allows a sound mathematic treatment, but on the other discards modes involving a change in the loading branches of the constitutive equations. Here, as explained above, no assumption is done concerning the behavior but only a numerical treatment of the problem is made.

As for our notations, a component of a tensor (or vector) is denoted by the name of the tensor (or vector) accompanied by the indices. All tensorial indices are in lower position, since there is no need to distinguish between covariant and contravariant components. Upper indices have specific meanings defined in the text. The summation convention with respect to repeated tensorial indices is used.

## 2. Local second-gradient models

**2.1. *A microstructured continuum with kinematic constrains.*** Models with microstructure descend from the pioneer works of the Cosserat brothers [Cosserat and Cosserat 1909], via [Toupin 1962], [Mindlin 1964] and [Germain 1973]. They use an enriched kinematic description of the continuum, with respect to classical continua, recalled hereafter. In addition to the displacement field, $u_i$, a second-order tensor, the microkinematic gradient $v_{ij}$, is introduced. Particular subclasses of enriched models introduce a constraint on the microkinematic field. For example, Cosserat models can be viewed as a microstructured model for which the microstrain is vanishing, that is, the symmetric part of the tensor $v_{ij}$ is zero. In the same spirit, (local) second-gradient models assume that the microkinetic gradient is equal to the displacement gradient $v_{ij} = \partial u_i / \partial x_j$, where $x_j$ is the spatial coordinate. Recently, such models have been developed for geomaterials [Chambon et al. 2001a; Matsushima et al. 2002; Chambon and Moullet 2004] and for metals [Fleck and Hutchinson 1997].

For local second-gradient models, the virtual work principle can be summarized as follows. For every kinematically admissible virtual displacement fields $u_i^\star$,

$$\int_\Omega \left( \sigma_{ij} \varepsilon_{ij}^\star + \Sigma_{ijk} \frac{\partial^2 u_i^\star}{\partial x_j \, \partial x_k} \right) dv = \int_\Omega G_i u_i^\star \, dv + \int_{\partial\Omega} \left( t_i u_i^\star + T_{ij} \frac{\partial u_i^\star}{\partial x_j} \right) ds, \tag{1}$$

where $\sigma_{ij}$ is the Cauchy stress, $\varepsilon_{ij}^\star$ is the virtual macrostrain, $\Sigma_{ijk}$ is the dual static variable associated to the second gradient of the virtual displacement, the so-called *double stress*; see [Germain 1973]. Further,

$G_i$ is the body force per unit volume, $t_i$ is the traction force per unit surface and $T_{ij}$ is the double force per unit surface. However $t_i$ and $T_{ij}$ cannot be taken independently, since $u_i^\star$ and $\partial u_i^\star/\partial x_j$ are not independent. More conveniently, the virtual work of external forces can be rewritten using the normal derivative $Du_i = n_k\, \partial u_i/\partial x_k$ on the boundary. Here and in the following $n_k$ is the normal to the boundary (assumed to be regular).

$$\int_\Omega \left( \sigma_{ij}\varepsilon_{ij}^\star + \Sigma_{ijk} \frac{\partial^2 u_i^\star}{\partial x_j\, \partial x_k} \right) dv = \int_\Omega G_i u_i^\star\, dv + \int_{\partial\Omega} \left( p_i u_i^\star + P_i D u_i^\star \right) ds, \tag{2}$$

where $p_i$ and $P_i$ are two independent variables which can be prescribed on the boundary.

For such a class of models, the balance equations and boundary conditions yield

$$\frac{\partial \sigma_{ij}}{\partial x_j} - \frac{\partial^2 \Sigma_{ijk}}{\partial x_j\, \partial x_k} + G_i = 0, \tag{3}$$

$$\sigma_{ij} n_j - n_k n_j D\Sigma_{ijk} - \frac{D\Sigma_{ijk}}{Dx_k} n_j - \frac{D\Sigma_{ijk}}{Dx_j} n_k + \frac{Dn_l}{Dx_l} \Sigma_{ijk} n_j n_k - \frac{Dn_j}{Dx_k} \Sigma_{ijk} = p_i, \tag{4}$$

$$\Sigma_{ijk} n_j n_k = P_i, \tag{5}$$

where $Dq/Dx_j$ denotes the tangential derivatives of any quantity $q$:

$$\frac{Dq}{Dx_j} = \frac{\partial q}{\partial x_j} - n_j Dq. \tag{6}$$

**2.2.** ***Numerical implementation in a finite element code.*** A direct application of virtual work principle (2) to solve equations of a boundary value problem needs to use $C^1$ elements. To avoid this constraint, a weak form of equation (2) can be introduced with help of a Lagrange multipliers field $\lambda_{ij}$, which yields, for any time $t$ and any kinematically admissible virtual fields $u_i^\star$ and $v_{ij}^\star$,

$$\int_{\Omega^t} \left( \sigma_{ij}^t \frac{\partial u_i^\star}{\partial x_j^t} + \Sigma_{ijk}^t \frac{\partial v_{ij}^\star}{\partial x_k^t} + \lambda_{ij}^t \left( \frac{\partial u_i^\star}{\partial x_j^t} - v_{ij}^\star \right) \right) dv = \int_{\Omega^t} G_i^t u_i^\star dv + \int_{\partial\Omega^t} \left( p_i^t u_i^\star + P_i D u_i^\star \right) ds, \tag{7}$$

and for any virtual field $\lambda_{ij}^\star$,

$$\int_{\Omega^t} \lambda_{ij}^\star \left( \frac{\partial u_i^t}{\partial x_i^t} - v_{ij}^t \right) dv = 0. \tag{8}$$

A complete description of the numerical treatment can be found in [Chambon and Moullet 2004]. The problem is discretized in time and for each finite step a full Newton–Raphson is applied to solve the resulting nonlinear problem. In order to get the equations suitable for Newton–Raphson technique, the unbalanced quantities are computed after the $n$-th iteration of the current time step. The same equations are applied for the $n+1$-th iteration, assuming these equations are well balanced. Then, by differentiation, one gets a proper linearization of the set of equations for the Newton–Raphson method. Equations are written in the actual configuration and the small strain assumption is not made, which introduces some geometrical terms in the linearized equations.

The finite element is organized with 8 nodes for the displacement field $u_i$, 4 nodes for the displacement gradient field $v_{ij}$, and a single node for the Lagrange multipliers field $\lambda_{ij}$. The element was introduced

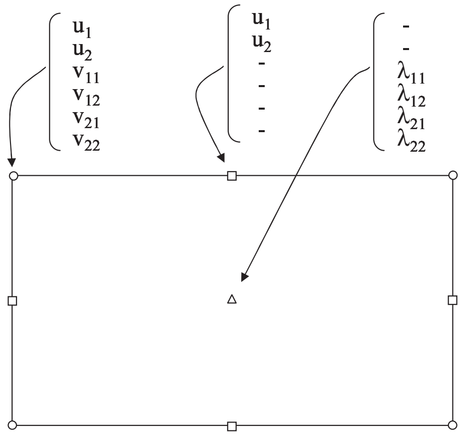

**Figure 1.** Nodal variables used in the finite element introduced in Lagamine.

in the finite element code Lagamine, initially developed at Liège University in Belgium [Charlier 1987]. The element used in Lagamine to implement our second-gradient model contains in fact 9 nodes each with 6 possible degrees of freedom. For the present application, some of these are not used (see Figure 1): only 36 degrees of freedom are activated by element [Bésuelle 2005].

The following algorithm is adopted for computing one time step from $t-\Delta t$ to $t$.

(1) Initial configuration: stress $\sigma^{t-\Delta t}$, double stress $\Sigma^{t-\Delta t}$, coordinates $x^{t-\Delta t}$.

(2) Assumption on the final configuration for the first iteration $n = 1$:
   - initialization of the increment of nodal values $[\Delta U^{t,n}_{\text{node}}]$,
   - update coordinates: $x^{t,n}$.

(3) Beginning of the iteration $n$.

(4) For each element:
   - for each integration point:
     - compute the strain rate, the rotation rate and the second-gradient rate,
     - compute $\Delta\sigma^{t,n}$ and $\Delta\Sigma^{t,n}$ using the constitutive equations,
     - update the stress and the double stress $\sigma^{t,n} = \sigma^{t-\Delta t} + \Delta\sigma^{t,n}$, $\Sigma^{t,n} = \Sigma^{t-\Delta t} + \Delta\Sigma^{t,n}$,
     - compute the consistent tangent stiffness matrices of constitutive laws.
   - compute the element stiffness matrix.
   - compute the element out of balance forces.

(5) Compute the global stiffness matrix.

(6) Compute the global out of balance forces.

(7) Compute the corrections $[\delta U^{t,n}_{\text{node}}]$ of the increment of nodal values by solving the Newton–Raphson linearized system.

(8) Check the accuracy of the computed solution:
   - if convergence: go to 9,

- if no convergence: update the new assumed final configuration, $n = n + 1$ and go to 3.

(9) End of the step.

## 3. Validation

**3.1. *Constitutive model: a quasibrittle material.*** The constitutive model used in this paper is the same as in [Matsushima et al. 2002] and [Chambon and Moullet 2004], and it can be decoupled into two independent relations. The first is classical, and links the stress to the displacement gradient; it is a Von Mises elastoplastic law based on the Prandt–Reuss model, with a strain softening regime. The second relation gives the double stress as a function of the gradient of the field $v_{ij}$ (that is, the second gradient of the displacement); it is a linear elastic law. Concerning the constitutive equation used here, we emphasize that the classical part of the model involves no hardening but only sudden softening as soon as a threshold is attained. Moreover this part is not a hyperelastoplastic model, contrary to the ones used for bifurcation analyses in [Steinmann et al. 1997; Borja 2002; Ikeda et al. 2003]. From a thermodynamical point of view it would presumably be better to use the hyperelastoplastic model, but in the second-gradient context it is then necessary to build up a new theory. This has already been done in [Tamagnini et al. 2001b] and [Chambon et al. 2004], but the implementation of such a model in a finite element code has not yet been made.

The classical relation is

$$\dot{\sigma} = 3\, K\, \dot{e},$$

$$\overset{\triangledown}{s}_{ij} = \begin{cases} 2\, G_1\, \dot{\varepsilon}_{ij} & \text{for } \|\varepsilon\| \le e_{\text{lim}}, \\ 2\, G_1 \left( \dot{\varepsilon}_{ij} - \dfrac{G_1 - G_2}{G_1} \dfrac{s_{kl}\dot{\varepsilon}_{kl}}{\|s\|^2} s_{ij} \right) & \text{for } \|\varepsilon\| > e_{\text{lim}}, \end{cases} \tag{9}$$

where $\overset{\triangledown}{s}_{ij}$ is the Jaumann rate of the deviatoric Cauchy stress tensor, $\dot{\varepsilon}_{ij}$ is the deviatoric strain rates, $\dot{\sigma}$ is the mean stress rate and $\dot{e}$ is the mean strain rate. $K$, $G_1$ and $G_2$ are the bulk modulus, the shear moduli before peak and after peak, respectively. $\|\varepsilon\|$ is the second invariant of the Green–Lagrange deformation tensor, $e_{\text{lim}}$ is a deformation parameter of the model which corresponds to the deviatoric stress peak.

The bulk modulus $K$ is assumed to be constant. The elastic shear modulus available for unloading is assumed to be constant, while an exponential function is assumed as follows for the shear modulus after the yield point so that the material could reach its residual state smoothly:

$$G_2 = \bar{G}_2 \exp\left( \frac{\bar{G}_2}{G_1 e_{\text{lim}} - \sigma_{\text{res}}} (\|\varepsilon\| - e_{\text{lim}}) \right), \tag{10}$$

where $\bar{G}_2$ is the value of the shear modulus just after yielding and $\sigma_{\text{res}}$ is the residual deviatoric stress.

The second-gradient law has been chosen as simple as possible. It is a particular case of the more general isotropic linear relation derived in [Mindlin 1964], involving six parameters corresponding to five independent coefficients. The following relation is slightly different from the one in [Matsushima

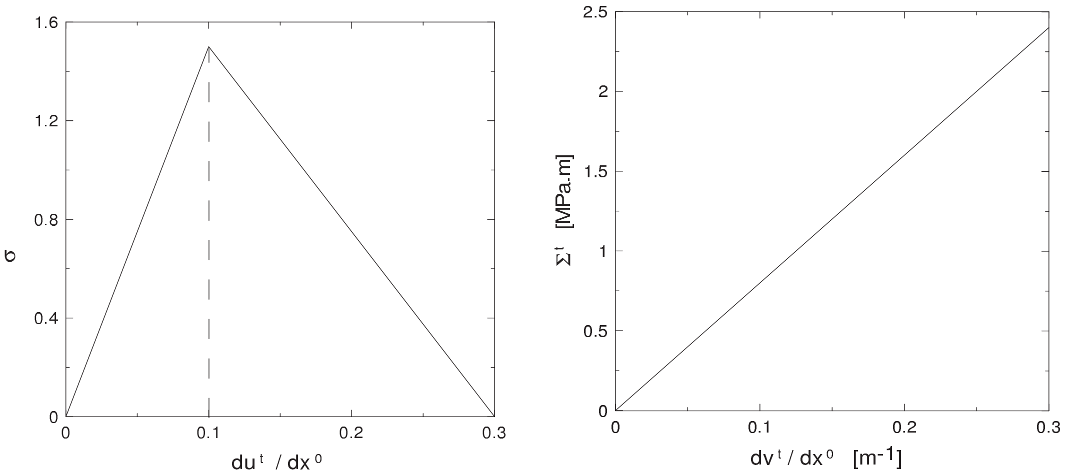

**Figure 2.** Constitutive relations in the one-dimensional case: (left) first grade term; (right) second grade term.

et al. 2002] and [Chambon and Moullet 2004], in that some inaccuracies have been corrected:

$$\begin{bmatrix} \overset{\triangledown}{\Sigma}_{111} \\ \overset{\triangledown}{\Sigma}_{112} \\ \overset{\triangledown}{\Sigma}_{121} \\ \overset{\triangledown}{\Sigma}_{122} \\ \overset{\triangledown}{\Sigma}_{211} \\ \overset{\triangledown}{\Sigma}_{212} \\ \overset{\triangledown}{\Sigma}_{221} \\ \overset{\triangledown}{\Sigma}_{222} \end{bmatrix} = \begin{bmatrix} D & 0 & 0 & 0 & 0 & D/2 & D/2 & 0 \\ 0 & D/2 & D/2 & 0 & -D/2 & 0 & 0 & D/2 \\ 0 & D/2 & D/2 & 0 & -D/2 & 0 & 0 & D/2 \\ 0 & 0 & 0 & D & 0 & -D/2 & -D/2 & 0 \\ 0 & -D/2 & -D/2 & 0 & D & 0 & 0 & 0 \\ D/2 & 0 & 0 & -D/2 & 0 & D/2 & D/2 & 0 \\ D/2 & 0 & 0 & -D/2 & 0 & D/2 & D/2 & 0 \\ 0 & D/2 & D/2 & 0 & 0 & 0 & 0 & D \end{bmatrix} \begin{bmatrix} \partial \dot{v}_{11}/\partial x_1 \\ \partial \dot{v}_{11}/\partial x_2 \\ \partial \dot{v}_{12}/\partial x_1 \\ \partial \dot{v}_{12}/\partial x_2 \\ \partial \dot{v}_{21}/\partial x_1 \\ \partial \dot{v}_{21}/\partial x_2 \\ \partial \dot{v}_{22}/\partial x_1 \\ \partial \dot{v}_{22}/\partial x_2 \end{bmatrix}, \tag{11}$$

where $\dot{v}_{ij}$ is the material time derivative of $v_{ij}$, and $\overset{\triangledown}{\Sigma}_{ijk}$ is the Jaumann double stress derivative, defined by $\overset{\triangledown}{\Sigma}_{ijk} = \dot{\Sigma}_{ijk} + \Sigma_{ljk}\omega_{li} + \Sigma_{imk}\omega_{mj} + \Sigma_{ijp}\omega_{pk}$, where $\omega_{li}$ is the spin tensor.

**3.2.** ***One-dimensional simulation.*** In order to validate the implementation of the element in Lagamine, first a one-dimensional compression is computed. This problem has analytic solutions under the assumption of small strain; see [Chambon et al. 1998]. The bar is 1 meter long. The degrees of freedom $u_1$, $v_{11}$, $v_{12}$ and $v_{21}$ are blocked at each node, the direction 2 being the direction of compression. In order to study the symmetrical localized solution composed of a central patch in the softening loading part and two end patches in the elastic unloading part, two elements at the middle of the bar have a $e_{\text{lim}}$-value reduced by 2%. The constitutive parameters are the same as those used in [Matsushima et al. 2002]:

$$\begin{gathered} G_1 = 16.875\,\text{MPa}, \quad \bar{G}_2 = 0\,\text{MPa}, \quad e_{\text{lim}} = 0.082, \\ K = -7.5\,\text{MPa}, \quad D = 0.08\,\text{MN}. \end{gathered} \tag{12}$$

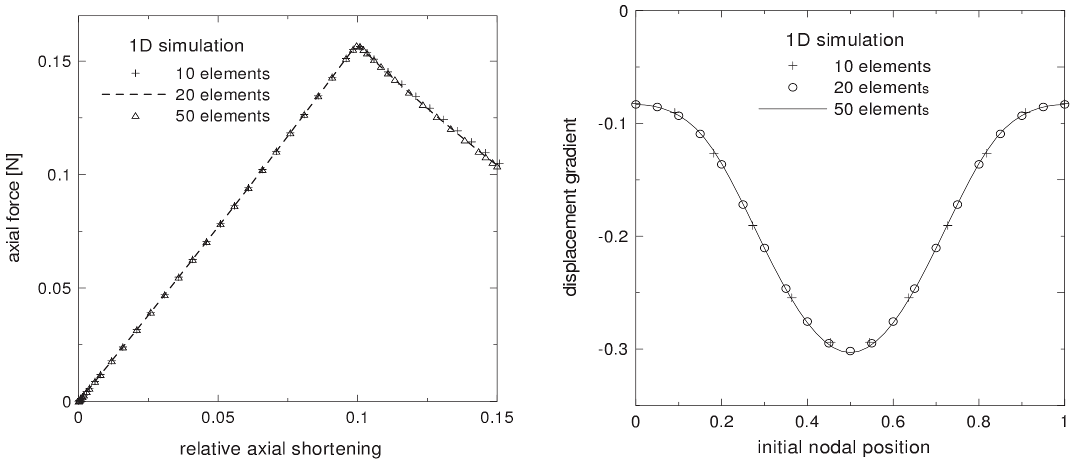

**Figure 3.** Comparison of three mesh refinements in one-dimensional simulations: (left) evolution of the resulting force versus the axial shortening, and (right) displacement gradient along the bar.

The two constitutive relations are plotted in Figure 2. To observe the influence of the mesh on the numerical solutions, three mesh refinements are used, with 11, 20 and 50 elements, respectively. The three solutions are very close (Figure 3), in terms of force versus bar shortening and deformation profile.

**3.3.** ***Two-dimensional simulation.*** A biaxial test is computed in this section as an example of a two-dimensional problem. Figure 4 shows the initial configuration of the specimen. It is 0.5 m wide and 1 m high (and 1 m thick). The (classical) surface tractions per unit area at both sides of the specimen are set equal to zero. The external additional double forces per unit area $P_i$ are assumed to be zero all along the boundaries. At the top there is a smooth rigid plate remaining horizontal. Through this plate

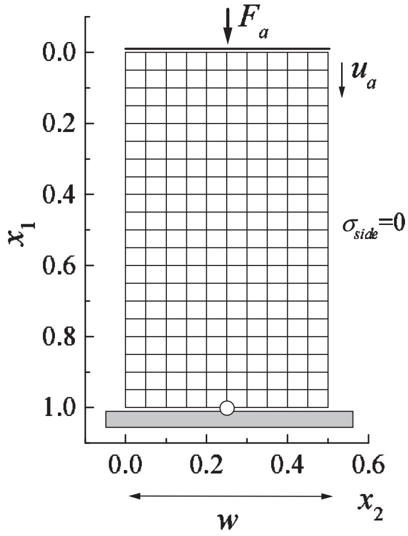

**Figure 4.** Initial configuration and boundary condition for biaxial test.

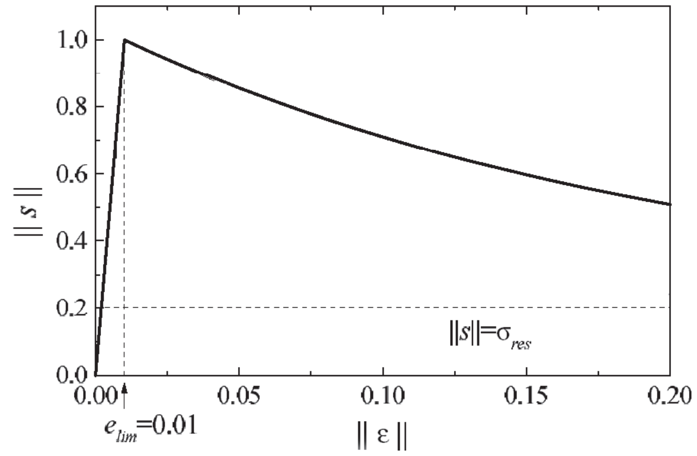

**Figure 5.** Classical part of the constitutive relation.

a compressive force $F_a$ is applied. The vertical displacement of this top plate is denoted by $u_a$. At the bottom, there is another rigid and smooth plate, which remains horizontal too. The central point of the bottom plate is fixed to avoid rigid body displacement. The classical part of the constitutive relation is plotted in Figure 5. The parameters are chosen as follows:

$$\begin{aligned} G_1 &= 50\,\text{MPa}, \quad \bar{G}_2 = -2\,\text{MPa}, \quad e_{\text{lim}} = 0.01, \\ K &= 97.3856\,\text{MPa}, \quad \sigma_{\text{res}} = 0.2\,\text{MPa}, \quad D = 0.2\,\text{kN}. \end{aligned} \tag{13}$$

Several meshes are compared: structured meshes with 10 × 20, 15 × 30, 20 × 40 and 40 × 80 elements, and an unstructured mesh with 300 elements. The left bottom element of the mesh has a $e_{\text{lim}}$-value reduced of 10% in order to force a localization band in this area. Here, we try to find similar solutions; that is, we don't try to find more than one alternative solution contrary to what is done in the following sections.

The implementation of our element in a general purpose code allows us to go further in the validation procedure. For example, we can work with unstructured meshes, an impossibility until now. Moreover, the use of a general code makes it possible to compare more precisely the similarities (and likely the differences) between different computations. It is often especially difficult to compare solutions of the same problem obtained with different meshes. In the following computations, in order to determine the width of the shear band, instead of comparing contours of some variable (often obtained by some interpolation procedure), we have chosen to look directly at the part of the computed body which loads plastically (inside the localized band). For this purpose, we have marked by a small open square the (plastically) loading Gauss points. In the area where there are no such marks the material unloads elastically.

The localization patterns of solutions (Figure 6) are very close, and the band thickness depends very little on the mesh size. We want here to emphasize a new result: an unstructured mesh changes neither the orientation nor the width of the band even if its position seems to be a little shifted. However, we have to keep in mind that, since we use an imperfection related to an element, the problems solved in

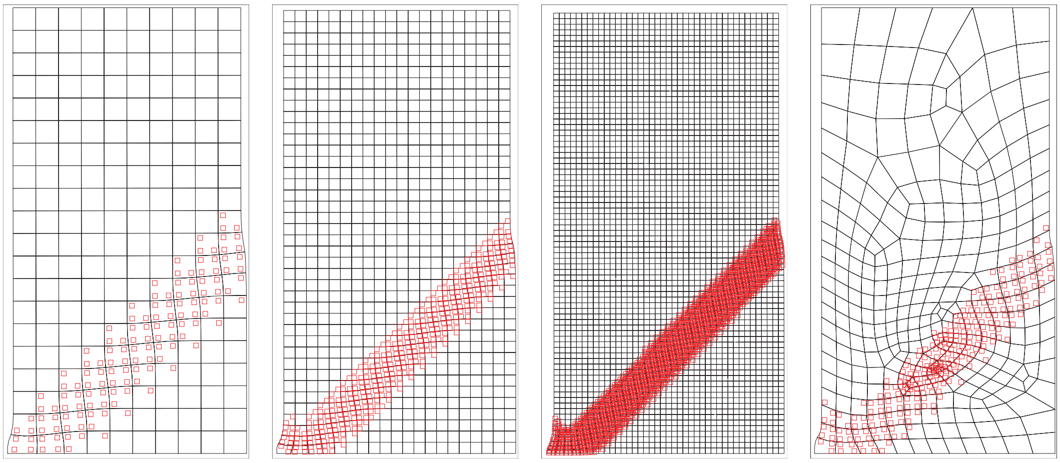

**Figure 6.** Comparison of the localization patterns for the four meshes 10 × 20, 20 × 40, 40 × 80 and an unstructured mesh with 300 elements, respectively. The imperfection is located in the left bottom element. The squares correspond to the integration points which are in the softening loading part; the other integration points are in the elastic regime.

the four cases are not exactly the same. The curves of the loading force versus the specimen shortening (Figure 7) are also very close. The step of band propagation from the imperfection concerns the force peak zone, and as soon as the band is completely propagated through the specimen, the force decreases. When the number of elements is sufficiently high (about 300 elements), or, more objectively, when there are at least about three elements in the band thickness, the curves are perfectly superimposed.

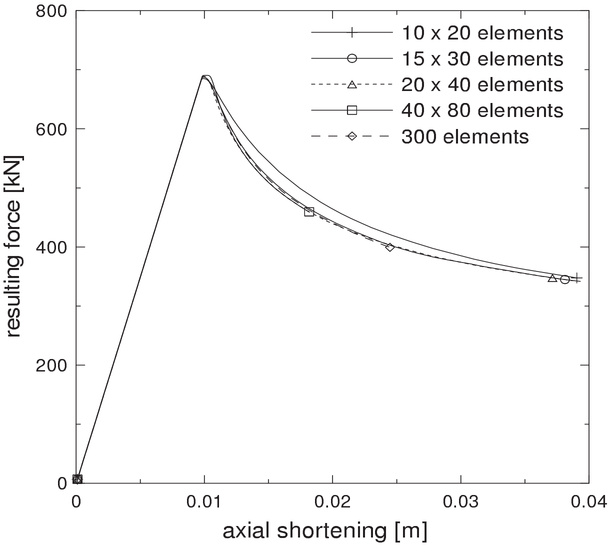

**Figure 7.** Comparison of the resulting force versus axial shortening curves for the same meshes.

## 4. Nonuniqueness of solutions

The aim of this section is to show that as soon as strain localization is possible, there can exist several solutions to a boundary value problem, despite of the use of a second-gradient model. Moreover, consistent with experimental observations, it is possible that the computed solutions switch from one pattern to another.

Generalizing Hill's uniqueness theorem [Hill 1958], Chambon and Moullet [2004] demonstrated that, under certain assumptions on the model, local second-gradient models (in the small strain framework) enjoy a uniqueness property. These results, applied to the biaxial problem, allow us to prove that uniqueness of solution is preserved in the elastic regime. In the biaxial problem described above, this unique solution is the homogeneous elastic response for which the response of the second-gradient model is similar to the response of a classical law. When the state of stress reaches the peak of the law, the uniqueness theorem cannot be applied, and, consistent with the numerical results in [Chambon et al. 1998] and in [Chambon and Moullet 2004], more than one solution is possible. It is then interesting to try to generalize the shear band analysis in the spirit of [Rudnicki and Rice 1975].

We present here a bifurcation analysis to search the condition for existence of a localized band. Applied to the second-gradient model used here, such an analysis is a generalization of the pioneering work of Rice [1976] and Rudnicki and Rice [1975]. We will show that for second-gradient models, at least when classical and second-gradient parts are decoupled, the bifurcation analysis is reduced to a bifurcation analysis on the classical part of the constitutive relation. However, the result is weaker in the sense that as soon as the criterion is met, localized solutions are possible, but not in all cases. Let us emphasize this point. This means that the second-gradient model and the underlying classical model have the same prebifurcation curve since second-gradient effects are only active for inhomogeneous fields. But the bifurcation point of the second-gradient model is located beyond the bifurcation point of the classical model, with the difference depending on the size of the modeled sample. It is likely that from the limit case of an infinite sample, both models have the same bifurcation point. Clearly the postbifurcation behavior is different for the two models.

The classical part of the rate law is assumed to be bilinear, and the second gradient law linear. We restrict this analysis by assuming that the so-called small strain assumption holds. So we use the ordinary material stress rates instead of some objective ones like the Jaumann stress rates:

$$\dot{\sigma}_{ij} = K^{e}_{ijkl}\,\frac{\partial \dot{u}_k}{\partial x_l} \quad \text{or} \quad \dot{\sigma}_{ij} = K^{ep}_{ijkl}\,\frac{\partial \dot{u}_k}{\partial x_l} \quad \text{depending on} \quad \frac{\partial \dot{u}_k}{\partial x_l},$$

$$\dot{\Sigma}_{ijk} = A_{ijklmn}\,\frac{\partial^2 \dot{u}_l}{\partial x_m\,\partial x_n}.$$

The nonhomogeneous solution is assumed to have the form of a planar band with unit normal $n_i$. Inside and outside the band, the velocity gradient depends only on the position across the band. The velocity gradient inside and outside the band must have the form

$$\frac{\partial \dot{u}^{\zeta}_i}{\partial x_j} = \frac{\partial \dot{U}_i}{\partial x_j} + g^{\zeta}_i\, n_j,$$

where $\zeta = 1$ inside the band, and $\zeta = 0$ outside. The displacement gradient $\partial \dot{U}_i / \partial x_j$ is assumed homogeneous, and $g_i^\zeta = g_i^\zeta(\alpha)$ are arbitrary vectors depending on the position $\alpha = x_k\, n_k$ across the band. $g_i^1$ characterizes the strain field inside the band and $g_i^0$ corresponds to the near field on each side of the band. To insure the strain continuity, we assume that

$$g_i^1 = g_i^0 \tag{14}$$

at the boundaries of the band. This point deserves a discussion. This is a salient difference with the localization analysis for classical materials. To some extent, we use a second-gradient theory in order to have more regular solutions. From the theoretical point of view, solutions have to be $C^1$ continuous. Moreover, contrary to what happens for a classical model, a discontinuity of the strain rate could imply that some forces are infinite. Consequently a classical shear band analysis cannot apply a priori to the models used here.

The $C^1$ continuity requirement is not imposed in the localization analysis developed in [Huang et al. 2005; Iordache and Willam 1998]. In this case, a discontinuity of the Cosserat rotation rate is assumed, which should imply an infinite curvature. However, these studies used *pure* Cosserat models, which means that there is no link between microrotation and macrorotation (see for instance [Chambon et al. 2001a] for a study of the difference between the pure Cosserat model and second-gradient Cosserat model). An analysis allowing discontinuities might be interesting, but an analysis with $C^1$ continuous fields should be made as well, as we suggested in [Chambon et al. 2001a]. Our opinion is corroborated by the results of Iordache and Willam [1998]. These authors found that the analysis with discontinuities gives results corresponding to compaction or extension bands—for the case for which Cosserat effects are vanishing, which means finally for a classical model.

For simplicity's sake, we assume that the direction of $g_i^\zeta$ over the band is constant and then

$$g_i^\zeta(\alpha) = g^\zeta(\alpha)\, m_i^\zeta,$$

where $g^\zeta(\alpha)$ are scalar functions and $m_i^\zeta$ are constant unit vectors. To simplify the notation, we consider that the solutions on each side of the band are the same (symmetry with respect to the band) and we do not make any difference between the solution on one side and that on the other.

In each point of the body, the stress and double stress fields satisfy conditions of equilibrium in (3). Because the prebifurcation field is presumed uniform, the stress rate and double stress rate at the onset of localization satisfy

$$\frac{\partial \dot{\sigma}_{ij}^\zeta}{\partial x_j} - \frac{\partial^2 \dot{\Sigma}_{ijk}^\zeta}{\partial x_j\, \partial x_k} = 0. \tag{15}$$

Moreover, at the boundaries of the band, conditions (4) and (5) must be satisfied (the tangential derivative on the boundaries of the band are zero because the displacement gradient depends only on $\alpha$):

$$\dot{\sigma}_{ij}^0 n_j - \frac{\partial \dot{\Sigma}_{ijk}^0}{\partial x_p} n_p n_j n_k = \dot{\sigma}_{ij}^1 n_j - \frac{\partial \dot{\Sigma}_{ijk}^1}{\partial x_p} n_p n_j n_k, \tag{16}$$

$$\dot{\Sigma}_{ijk}^0 n_j n_k = \dot{\Sigma}_{ijk}^1 n_j n_k, \tag{17}$$

where $(\cdot)^0$ and $(\cdot)^1$ denote quantities outside and inside the band, respectively.

The equilibrium condition inside and outside the band can be written

$$K^{\zeta}_{ijkl}\, n_j n_l\, (g^{\zeta}_k)' - A_{ijklmn}\, n_j n_k n_m n_n\, (g^{\zeta}_l)''' = 0, \tag{18}$$

where $(g^{\zeta}_k)'$ is the derivative of $g^{\zeta}_k(\alpha)$ in the direction orthogonal to the band. It seems reasonable to assume that $K^{1}_{ijkl} = K^{ep}_{ijkl}$ and $K^{0}_{ijkl} = K^{e}_{ijkl}$.

The limit conditions at the two boundaries of the band depend on the constitutive relation which is considered on each side of the interface. For classical constitutive laws, it can be shown that the softer response (that is, the one corresponding to the tensor $\mathbf{K}^{ep}$) can be considered on each side of the interface to track the first bifurcation condition (see [Bésuelle and Rudnicki 2004] for a review).

Here, Equation (17) becomes:

$$A_{ijklmn}\, n_j n_k n_m n_n\, \big((g^{0}_l)' - (g^{1}_l)'\big) = 0. \tag{19}$$

Since function $g_i(\alpha)$ is continuous at the boundaries of the band (see Equation (14)) and since the material is loading inside the band and unloading outside, this means that it undergoes a neutral loading:

$$K^{ep}_{ijkl}\, \frac{\partial \dot{u}^{0}_k}{\partial x_l}\bigg|_{\alpha=\alpha_a \text{ or } \alpha_b} = K^{e}_{ijkl}\, \frac{\partial \dot{u}^{0}_k}{\partial x_l}\bigg|_{\alpha=\alpha_a \text{ or } \alpha_b}. \tag{20}$$

Then the limit condition (16) can be written

$$K^{ep}_{ijkl}\, n_j n_l\, \big(g^{0}_k - g^{1}_k\big) - A_{ijklmn}\, n_j n_k n_m n_n\, \big((g^{0}_l)'' - (g^{1}_l)''\big) = 0. \tag{21}$$

Finally the problem can be summarized as follows:

- outside the band, the following condition, which comes from Equation (15), must be satisfied:

$$\mathcal{K}^{e}_{ij}\, (g^{0}_j)' - \mathcal{A}_{ij}\, (g^{0}_j)''' = 0; \tag{22}$$

- inside the band, once more coming from Equation (15), we observe that

$$\mathcal{K}^{ep}_{ij}\, (g^{1}_j)' - \mathcal{A}_{ij}\, (g^{1}_j)''' = 0; \tag{23}$$

- there must exist two values $\alpha^a$ and $\alpha^b$ for which the following conditions are satisfied:

$$\mathcal{A}_{ij}\, \big((g^{0}_j)' - (g^{1}_j)'\big) = 0, \tag{24}$$

  which comes from Equation (19), and

$$\mathcal{A}_{ij}\, \big((g^{0}_j)'' - (g^{1}_j)''\big) = 0, \tag{25}$$

  which comes from Equation (21),

where $\mathcal{K}^{ep}_{ik} = K^{ep}_{ijkl}\, n_j n_l$, $\mathcal{K}^{e}_{ik} = K^{e}_{ijkl}\, n_j n_l$ and $\mathcal{A}_{il} = A_{ijklmn}\, n_j n_k n_m n_n$. Note that $|\alpha^a - \alpha^b|$ corresponds to the band thickness.

Since Equations (22)–(23) are ordinary linear differential equations, one can search solutions of the form $g^{\zeta}_i(\alpha) = \gamma_\zeta\, \exp(\lambda_\zeta \alpha)\, m^{\zeta}_i$, where $\gamma_\zeta$ are nonzero constants (if $\gamma_\zeta = 0$, there is no localization) and $\lambda_\zeta$ are the two unknowns of the problem. Then one has to solve

$$(\mathcal{K}^{ep}_{ij} - (\lambda_1)^2 \mathcal{A}_{ij})\, m^{1}_j = 0 \tag{26}$$

and

$$(\mathcal{K}^{e}_{ij} - (\lambda_0)^2 \mathcal{A}_{ij})\, m^0_j = 0. \tag{27}$$

There is then a solution corresponding to a nonuniform field if

$$\det(\mathcal{K}^{ep}_{ij} - \Lambda_1\, \mathcal{A}_{ij}) = 0, \tag{28}$$

and

$$\det(\mathcal{K}^{e}_{ij} - \Lambda_0\, \mathcal{A}_{ij}) = 0, \tag{29}$$

where $\Lambda_\zeta = (\lambda_\zeta)^2$.

A localized solution corresponds to a strain field involving an extremum. Then this implies $\Lambda_1 < 0$ for an harmonic form for $g^1(\alpha)$ inside the band (while one expects $\Lambda_0 > 0$ outside the band for a hyperbolic form). In fact, we are also guided in this reasoning by the one dimensional analytical solutions obtained by Chambon et al. [1998] and by El Hassan [1997], who demonstrated that the hyperbolic form corresponds to a kind of boundary layer.

Equation (28) is an algebraic equation of degree 3. The third-order term reads $\det(\mathcal{A})$ whereas the zero-order terms reads $\det(\mathcal{K}^{ep})$. If $\Lambda_a$, $\Lambda_b$, $\Lambda_c$ are the solutions of this equation, then consequently

$$\det(\mathcal{A})\Lambda_a\ \Lambda_b\ \Lambda_c = \det(\mathcal{K}^{ep}). \tag{30}$$

As a consequence of the choice of an isotropic tensor for the second-order part of the model, we have $\mathcal{A} = D\,\mathbf{I}$, where $\mathbf{I}$ is the identity tensor. This can be easily checked for the particular value of $A_{ijklmn}$ detailed in Equation (11). So, $\det(\mathcal{A}) = D^3$.

Before the onset of localization, the roots are expected to be positive (no localized solutions). So without any additional assumption, the bifurcation condition as in classical (bilinear) constitutive equation [Chambon et al. 2000] is

$$\det(\mathcal{K}^{\mathbf{ep}}) \le 0. \tag{31}$$

If we assumed the incremental continuity of the classical part of the law, then a necessary and sufficient condition for the sign of one root to change (that is, to have a vanishing root) is

$$\det(\mathcal{K}^{\mathbf{ep}}) = 0, \tag{32}$$

which corresponds to the classical bifurcation condition for a classical bilinear law. In this case the result can be found directly by inspecting the annulment of the zero-order term of Equation (28). Moreover, $\det(\mathcal{K}^{\mathbf{e}}) > 0$, and so the solution $g^0_i$ outside the band is hyperbolic.

As far as the band thickness is concerned, it is given by finding $\alpha_a$ and $\alpha_b$ that satisfy the double condition (24)–(25), which can be reduced here to

$$\big((g^1)' - (g^0)'\big)\big|_{\alpha=\alpha_a \text{ or } \alpha_b} = 0 \quad \text{and} \quad \big((g^1)'' - (g^0)''\big)\big|_{\alpha=\alpha_a \text{ or } \alpha_b} = 0.$$

Note that we assume in the particular form (11) that the parameter $D$ is constant and positive. With other models such as the ones detailed in [Chambon et al. 2001a], plasticity can also occur in the second-gradient part of the model and in this case, $D$ can evolves during the loading. Since the order of magnitude of the thickness of the band is given by the inverse of $\lambda_\zeta$, the evolution of the thickness of the band is related to the variations of $D$ and of $\det(\mathcal{K}^{\mathbf{ep}})$ according to Equation (30).

Coming back to the model defined by Equation (11), where $D$ is assumed to be constant, the thickness of the emerging band corresponding to condition (32) is infinite and decreases when $\det(\mathcal{H}^{\mathbf{ep}})$ decreases. Since an infinite thickness for a finite size boundary value problem is not realistic, the onset of localization can be somewhat delayed when second-gradient models are used. Consequently this criterion is not completely similar to the one of classical media. It is a necessary condition of localization, however since second-gradient models implicitly include an internal length, it is possible that this criterion could be met but without loss of uniqueness for some ”small” (with respect to the internal length) problems.

For the particular law adopted in Equations (9)–(11), the bifurcation criterion is satisfied after the deviatoric stress peak.

## 5. Switching mode of deformation

**5.1.** ***Algorithm for nonuniqueness search.*** When several solutions for a given boundary value problem exist, it can be difficult to know that they exist and to find the other (or some of the other) solutions, especially when the boundary value problem is nonlinear.

As we recall from Section 1, it is not satisfactory to search the null space of one eigenvalue of the tangent stiffness matrix related to the linearized discretized velocity problem. This way is useful for incrementally linear problems such as the ones induced by using a large strain elastic theory, but is only a guess for incrementally nonlinear problems arising when a constitutive equation incorporates some unloading branches.

For numerical computations involving classical constitutive equations, we have developed an algorithm to search several (eventual) solutions to a problem. It takes advantage of the fact that at the beginning of a time step, for the first iteration, the nodal quantities denoted $[\Delta U^{t_n}_{\text{node}}]$ in the algorithm presented in Section 2.2 can be freely chosen. The standard choice is to use nodal values related to the ones obtained at the end of the previous time step. Such a choice applied to an initially homogeneous problem generally (though not in all cases) leads to the homogeneous solution. If a random initialization is adopted for $[\Delta U^{t_n}_{\text{node}}]$, then it is possible to find nonhomogeneous solutions. In fact, for classical continua, our experience (see [Chambon et al. 2001b]) is that as soon as uniqueness is lost, the duplication of numerical experiments can yield different solutions, changing only some numerical parameters such as the time step size or the first guess of a given time step. Since all of them are properly converged, this means that they are all different solutions of the same initial boundary value problem defined by the same history of boundary conditions.

Recently, this algorithm has been adapted to second-gradient models [Chambon and Moullet 2004]. It has also been implemented in Lagamine, leading to the following numerical results.

**5.2.** ***Numerical loss of uniqueness.*** We present in Figure 8 several localized solutions (well converged) found after a few random initializations. The random initialization algorithm has been activated after a specimen shortening of 0.012 m while the stress peak corresponds to a shortening of 0.01 m. In order to clearly visualize the localized zones, the (plastically) loading Gauss points are marked with small open squares. As in experiments, the width of the bands is completely reproducible. On the contrary, the position, the number, and, more generally, the patterning between several bands are quite different from one numerical experiment to another.

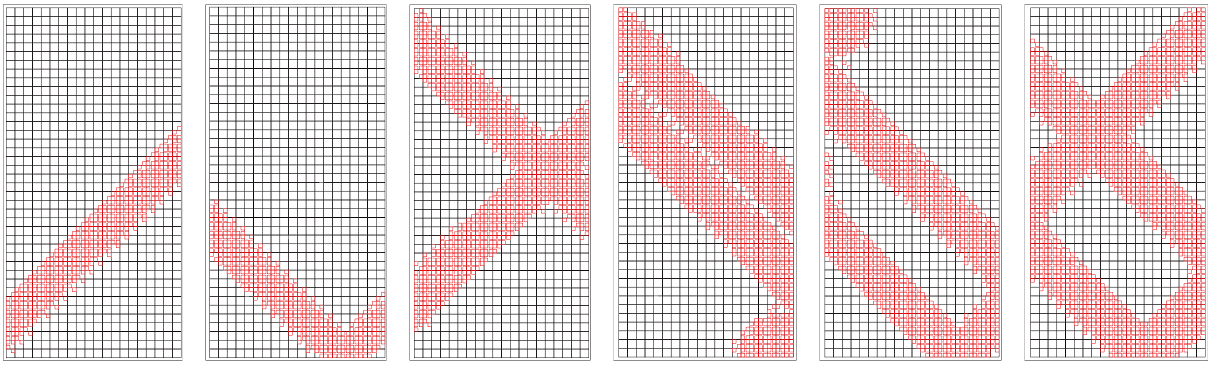

**Figure 8.** Example of localized solutions obtained after a random initialization, showing solutions with 1, 2 or 3 bands. The squares correspond to the integration points which are in the softening loading part; the other integration points are in the elastic part.

Figure 9 presents the global curves of the resulting force versus the axial shortening; they are clearly organized in several packages, each package being characterized by the number of deformation bands. This observation is similar to what has been seen in the one-dimensional case in [Chambon et al. 1998]. It is clear that the more numerous the bands are, the larger are the areas where plastic loading takes place, and, consequently, the closer the global curves are to the homogeneous case. We can observe that there is no difference between the case with bands crossing the specimen directly from a lateral surface to the opposite one and with band reflection, either on the top or on the bottom rigid plate.

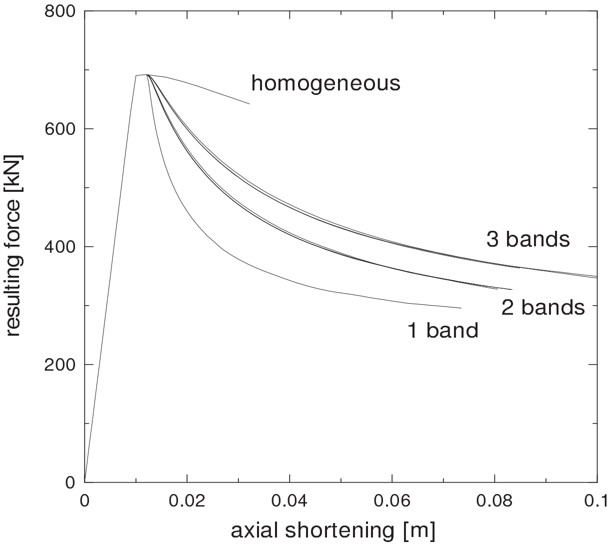

**Figure 9.** Comparison of the force versus axial shortening evolution of 10 simulations after a random initialization at a shortening of 0.012 m. Curves show that the responses depend on the number of bands. The higher the number of bands, the closer to the homogeneous response the curve is.

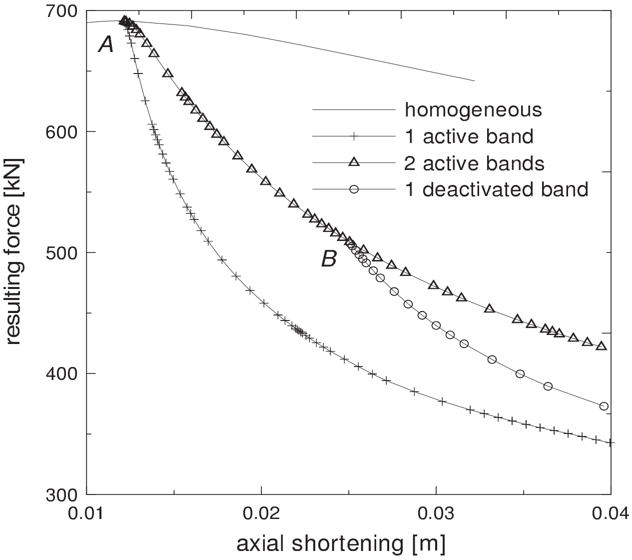

**Figure 10.** Comparison of the force versus axial shortening evolution in the postpeak regime of (converged) solutions with 1 active band, 2 active bands; and solution after the deactivation of one band. Step A corresponds to the random initialization, and step B corresponds to an *ad hoc* initialization in order to deactivate one band.

So, clearly these results show the nonuniqueness of solutions after the stress peak. The position and the number of bands are not prescribed by this boundary value problem, and we retrieve a variability of the responses similar to what is observed in experiments.

**5.3.** ***Numerical mode switching.*** From the initial homogeneous problem, after the onset of localization, several patterns of localization are possible for the numerical problem. The question addressed in this section is: is a given pattern stable, once activated? In fact, we will show that the pattern can evolve during the loading. If a solution has several bands which are active during the loading process, a solution for the next increment of loading is to keep all the bands active, but other solutions with fewer active bands are also possible. Since the areas outside the bands unload elastically, new bands cannot in fact appear, but it is possible that at a given time, some existing bands start to unload and become inactive.

To check this possibility, we use a method similar to the random initialization algorithm. The first guess used to start the Newton–Raphson iterative procedure is an *ad hoc* set of nodal values $[\Delta U^{t_n}_{\text{node}}]$ corresponding to a deactivation of some bands. An example of such a computation is shown for a two-band solution in Figure 10. A random initialization has been made for a specimen shortening of 0.012 m (step A), giving a two band solution, and the *ad hoc* initialization (step B) has been performed at a shortening of 0.025 m, to deactivate one of the bands. Then, the curve evolves from the two active band solutions to the one active band solution. The deformed meshes and the loading zones are shown in Figure 11 for an axial specimen shortening of 0.04 m. Figure 11, left, shows the result corresponding to a pattern of two active bands. The right hand side of the figure corresponds to a pattern where a band (the upper one) has been deactivated at step B. This figure shows clearly that the area corresponding to the deactivated band is still plastically deformed although it exhibits elastic unloading.

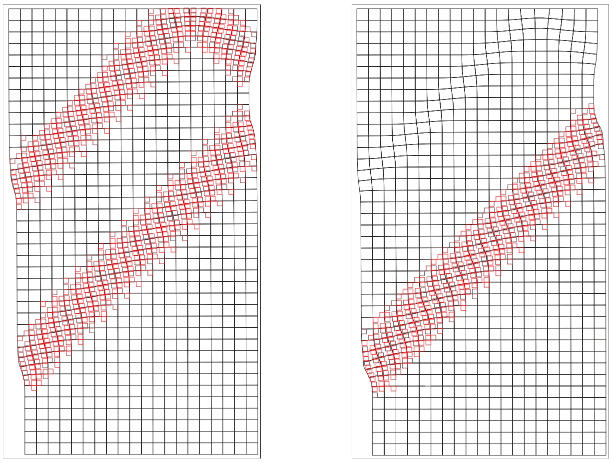

**Figure 11.** Pattern of active localization bands after the random initialization and (left) without deactivation of band, (right) after deactivation of the upper band. Deformed meshes correspond to the true deformation after a specimen shortening of 0.04 m, without displacement amplification.

## 6. Conclusion

To properly model localization patterns, the validation of the local second gradient theory has been extended. Localization analysis for this kind of model has been established. This theory is now mature and can be used in computation with some confidence. Similarly, the way of (partially) solving the bifurcation problem by means of different initializations of the Newton–Raphson iteration for a given time step has been extended to multiple bifurcations.

From a qualitative point of view, we are able to retrieve numerically the main features of observations made on experimental data. Especially, the great variability of the postpeak behavior of a sample is modeled realistically. These results have some consequences. First, the postpeak part of the curve cannot be interpreted as the result of a homogeneous response. Consequently, modeling the degradations of material needs enhanced models; moreover, the postpeak part of the curve can be used to get some material parameters only if the complete velocity field is known.

Clearly the results presented here have to be developed. Geomaterials are mainly polyphasic media, which implies the extension of the present model and methods to poromechanics. This has already been done; see [Collin et al. 2006] for details. Similarly, it is interesting to apply the methods presented to a classical constitutive equation less simple (elastic and sudden softening) than the one used here. This is work in progress [Bésuelle and Chambon 2006].

Finally a question arises. Is the loss of uniqueness observed and modeled for laboratory tests significant only for those tests for which homogeneity is required? In other words, can we find similar nonuniqueness problems for engineering situations? Answering such questions is not so easy, but some preliminary results [Al Holo 2005; Chambon and Al Holo 2006] indicate that for some problems, such as the borehole stability problem, the loss of uniqueness is important and may indicate poor reproducibility.

## 7. Acknowledgments

The authors thank R. Charlier (Liège) and D. Caillerie (Grenoble) for their helpful contributions.

## References

[Al Holo 2005] S. Al Holo, *Etude numérique de la localisation à l'aide d'un modèle de second gradient : perte d'unicité et évolution de la zone localisée*, Ph.D. thesis, University of Grenoble, France, 2005.

[Bésuelle 2005] P. Bésuelle, "Implémentation d'un nouveau type d'élément fini dans le code Lagamine pour une classe de lois à longueur interne", Internal report, FNRS, Belgique, 2005. 1–17.

[Bésuelle and Chambon 2006] P. Bésuelle and R. Chambon, "Modelling the post-localization regime with local second gradient models: non uniqueness of solutions and non persistent shear bands", pp. 209–221 in *Modern trends in geomechanics*, edited by W. Wu and H. S. Yu, Springer, Berlin, 2006.

[Bésuelle and Rudnicki 2004] P. Bésuelle and J. W. Rudnicki, "Localization: shear bands and compaction bands", pp. 219–321 in *Mechanics of fluid-saturated rocks*, edited by Y. Guéguen and M. Boutéca, International geophysics series **89**, Elsevier, 2004.

[Borja 2002] R. I. Borja, "Bifurcation of elastoplastic solids to shear band mode at finite strain", *Mech. Engng.* **191** (2002), 5287–5314.

[de Borst 1986] R. de Borst, *Non linear analysis of frictional materials*, Ph.D. thesis, University of Delft, Netherlands, 1986.

[Challamel and Hijaj 2005] N. Challamel and M. Hijaj, "Non local behavior of plastic softening beams", *Acta Mechanica* **178** (2005), 125–146.

[Chambon and Al Holo 2006] R. Chambon and S. Al Holo, "The borehole stability problem revisited", 2006. in preparation.

[Chambon and Moullet 2004] R. Chambon and J. C. Moullet, "Uniqueness studies in boundary value problems involving some second gradient models", *Comput. Meth. Appl. Mech. Engng.* **193** (2004), 2771–2796.

[Chambon et al. 1998] R. Chambon, D. Caillerie, and N. El Hassan, "One dimensional localisation studied with a second grade model", *Eur. J. Mech. A/Solids* **17** (1998), 637–656.

[Chambon et al. 2000] R. Chambon, S. Crochepeyre, and J. Desrues, "Localization criteria for non-linear constitutive equations of geomaterials", *Mech. Cohesive-Frictional Mater.* **5** (2000), 61–82.

[Chambon et al. 2001a] R. Chambon, D. Caillerie, and T. Matsushima, "Plastic continuum with microstructure, local second gradient theories for geomaterials: localization studies", *Int. J. Solids Struct.* **38**:46-47 (2001a), 8503–8527.

[Chambon et al. 2001b] R. Chambon, S. Crochepeyre, and R. Charlier, "An algorithm and a method to search bifurcation point in non linear problems", *Int. J. Numer. Meth. Engng.* **51** (2001b), 315–332.

[Chambon et al. 2004] R. Chambon, D. Caillerie, and C. Tamagnini, "A finite deformation second gradient theory of plasticity", *Comput. Meth. Appl. Mech. Engng.* **193** (2004), 2797–2826.

[Charlier 1987] R. Charlier, *Approche unifiée de quelques problèmes non linéaires de mécanique des milieux continus par la méthode des éléments finis*, Ph.D. thesis, University of Liège, Belgium, 1987.

[Collin et al. 2006] F. Collin, R. Chambon, and R. Charlier, "A finite element method for poro mechanical modelling of geotechnical problems using local second gradient models", *Int. J. Numer. Meth. Engng.* **193** (2006), 2771–2796.

[Cosserat and Cosserat 1909] E. Cosserat and F. Cosserat, *Théorie des corps déformables*, Hermann, Paris, 1909.

[Desrues 1984] J. Desrues, *La localisation de la déformation dans les matériaux granulaires*, Ph.D. thesis, University of Grenoble, France, 1984.

[Desrues and Hammad 1985] J. Desrues and W. Hammad, "Shear banding dependency on mean stress level in sand", pp. 57–68 in *Proc. 2nd Int. Workshop on Localisation and Bifurcation*, edited by E. Dembicki et al., Techn. Univ. Gdansk, Gdansk, 1985.

[Desrues and Viggiani 2004] J. Desrues and G. Viggiani, "Strain localization in sand: an overview of the experimental results obtained in Grenoble using stereophotogrammetry", *Int. J. Numer. Anal. Meth. Geomech.* **28** (2004), 279–321.

[El Hassan 1997] N. El Hassan, *Modélisation théorique et numérique de la localisation de la déformation dans les géomatériaux*, Ph.D. thesis, University of Grenoble, France, 1997.

[Fleck and Hutchinson 1997] N. A. Fleck and J. W. Hutchinson, "Strain gradient plasticity", *Advances Appl. Mech., Academic Press* **33** (1997), 295–361.

[Germain 1973] P. Germain, "La méthode des puissances virtuelles en mécanique des milieux continus, première partie : théorie du second gradient", *J. Méc.* **12**:2 (1973), 235–274.

[Hill 1958] R. Hill, "A general theory of uniqueness and stability in elastic-plastic solids", *J. Mech. Phys. Solids* **6** (1958), 236–249.

[Huang et al. 2005] W. Huang, M. Hijaj, and S. C. Sloan, "Bifurcation analysis for shear localization in non-polar and micro-polar hypoplastic continua", *J. Engng. Math.* **52** (2005), 167–184.

[Ikeda and Murota 2002] K. Ikeda and K. Murota, *Imperfect bifurcation in structures and materials*, Springer, Berlin, 2002.

[Ikeda et al. 1997] K. Ikeda, K. Murota, Y. Yamakawa, and E. Yanagisawa, "Modes switching and recursive bifurcation in granular materials", *J. Mech. Phys. Solids* **45** (1997), 1929–1953.

[Ikeda et al. 2003] K. Ikeda, Y. Yamakawa, and S. Tsutumi, "Simulation and interpretation of diffuse mode bifurcation of elastoplastic solids", *J. Mech. Phys. Solids* **51** (2003), 1649–1673.

[Iordache and Willam 1998] M. M. Iordache and K. Willam, "Localized failure analysis in elastoplastic Cosserat continua", *Comput. Meth. Appl. Mech. Engng.* **193** (1998), 559–586.

[Matsushima et al. 2002] T. Matsushima, R. Chambon, and D. Caillerie, "Large strain finite element analysis of a local second gradient model: application to localization", *J. Numer. Meth. Engng.* **54** (2002), 499–521.

[Mindlin 1964] R. D. Mindlin, "Micro-structure in linear elasticity", *Arch. Rat. Mech. Anal.* **4** (1964), 50–78.

[Nübel and Huang 2004] K. Nübel and W. Huang, "A study of localized deformation pattern in granular media", *Comput. Meth. Appl. Mech. Engng.* **193** (2004), 2719–2743.

[Pijaudier-Cabot and Bažant 1987] G. Pijaudier-Cabot and Z. Bažant, "Nonlocal damage theory", *J. Engng. Mech.* **113** (1987), 1512–1533.

[Rice 1976] J. R. Rice, "The localization of plastic deformation", pp. 207–220 in *14th Int. Cong. Theor. Appl. Mech.*, edited by W. T. Koiter, Theoretical and Applied Mechanics (North-Holland Pub. Comp., Delft, 1976.

[Rudnicki and Rice 1975] J. W. Rudnicki and J. R. Rice, "Conditions for the localization of deformation in pressure-sensitive dilatant materials", *J. Mech. Phys. Solids* **23** (1975), 371–394.

[Steinmann et al. 1997] P. Steinmann, R. Larsson, and K. Runesson, "On the localization properties of multiplicative hyper-elasto-plastic continua with strong discontinuities", *Int. J. Solids Struct.* **34** (1997), 969–990.

[Tamagnini et al. 2001b] C. Tamagnini, R. Chambon, and D. Caillerie, "A second gradient elastoplastic cohesive frictional model for geomaterials", *C.R.A.S-Série II b.* **329** (2001b), 735–739.

[Toupin 1962] R. A. Toupin, "Elastic materials with couple-stresses", *Arch. Rat. Mech. Anal.* **11** (1962), 385–414.

[Viggiani et al. 2001] G. Viggiani, M. Küntz, and J. Desrues, *Continuous and discontinuous modelling of cohesive-frictional materials*, Chapter An experimental investigation of the relationships between grain size distribution and shear banding in sand, pp. 111–127, Springer, Berlin, 2001.

Received December 11, 2005.

PIERRE BÉSUELLE: `Pierre.Besuelle@hmg.inpg.fr`
*Laboratoire 3S, Grenoble, Université Joseph Fourier, Institut National Polytechnique, C.N.R.S. U.M.R. 5521, B.P. 53X, 38041 Grenoble Cedex 9, France*

RENÉ CHAMBON: `Rene.Chambon@hmg.inpg.fr`
*Laboratoire 3S, Grenoble, Université Joseph Fourier, Institut National Polytechnique, C.N.R.S. U.M.R. 5521, B.P. 53X, 38041 Grenoble Cedex 9, France*

FRÉDÉRIC COLLIN: `F.Collin@ulg.ac.be`
*Geomac, FNRS-ULG, Liège, Belgium*

# Modeling the Post-localization Regime with Local Second Gradient Models: Non-uniqueness of Solutions and Non-persistent Shear Bands

P. Bésuelle* and R. Chambon†

*Laboratoire 3S (Sols, Solides, Structures), UJF/INPG/CNRS, Grenoble, France
pierre.besuelle@hmg.inpg.fr
†Laboratoire 3S, Grenoble, France
Rene.Chambon@hmg.inpg.fr

## 1 Introduction

The strain localization is a classical mode of failure of geomaterials. Numerical simulations of this phenomena need a specific approach to overcome the practical problem of mesh size dependence. Several technics have been developed recently, among others, models with internal length like nonlocal models ( e.g., [17]) or second gradient models (e.g., [16, 20]). Then, one restores an objectivity of computations and it becomes significant to study the postlocalization regime.

A preliminary question is the representability of such computations. What is the validity which can be given to a simulation or, in other terms, is a solution of a limit conditions problem unique, and if not, is it possible to quantify the variation between solutions? The aim of this paper is to explore this question. We use the framework of local second gradient models [6, 14]. The constitutive law (the classical part) is an elasto-plastic model initially developed for a rock [13]. We will study some key points as the onset of localization, pattern and orientation of deformation bands.

Afterward, we will explore by a simple constitutive parametric study, the kind of postlocalization responses which can be obtained, depending on the characteristics of the model used: strain hardening or strain softening. We will compare these preliminary results with some experimental observations of geomaterial behavior, and more precisely make a parallel with the brittle regime and brittle–ductile regime of failure that is observed when the mean stress level change.[1]

---

[1] In the following, the usual sign convention of mechanics (compression negative) is adopted throughout.

## 2 Local Second Gradient Model

Local second gradient models belong to a particular subclasses of models with microstructure which descend from pioneer works of [8, 12, 15, 19]. They use an enriched kinematic description of the continuum, with respect to classical continua. In addition to the displacement field $u_i$, a second-order tensor, the so-called microkinematic gradient $v_{ij}$, is introduced. Particular subclasses of enriched models introduce a constrain on the microkinematic field. For example, Cosserat models can be viewed as a microstructured model for which the microstrain is vanishing, i.e., the symmetric part of the tensor $v_{ij}$ is zero. In the same spirit, (local) second gradient models assume that the microkinetic gradient is equal to the displacement gradient

$$v_{ij} = \partial u_i / \partial x_j, \tag{1}$$

where $x_j$ is the spatial coordinate. Such models have been developed recently for geomaterials [5, 6, 14] and metals [10].

For local second gradient models, the virtual work principle can be summarized as follow, [12]: for every virtual displacement field $u_i^*$ kinematically admissible

$$\int_{\Omega} \left( \sigma_{ij} \varepsilon_{ij}^* + \Sigma_{ijk} \frac{\partial^2 u_i^*}{\partial x_j \, \partial x_k} \right) \mathrm{d}v = \int_{\Omega} G_i u_i^* \, \mathrm{d}v + \int_{\partial\Omega} \left( t_i u_i^* + T_{ij} \frac{\partial u_i^*}{\partial x_j} \right) \mathrm{d}s, \tag{2}$$

where $\sigma_{ij}$ is the Cauchy stress, $\varepsilon_{ij}^*$ is the virtual macro strain, $\Sigma_{ijk}$ is the dual static variable associated to the second gradient of the virtual displacement, so called *double stress*. $G_i$ is the body force by unit volume, $t_i$ is the traction force by unit surface and $T_{ij}$ is the double force by unit surface. More conveniently, the virtual work of external forces can be rewritten using the normal derivative $\mathrm{D}u_i = n_k \partial u_i / \partial x_k$ on the boundary (here, assumed to be regular)

$$\int_{\Omega} \left( \sigma_{ij} \varepsilon_{ij}^* + \Sigma_{ijk} \frac{\partial^2 u_i^*}{\partial x_j \partial x_k} \right) \mathrm{d}v = \int_{\Omega} G_i u_i^* \, \mathrm{d}v + \int_{\partial\Omega} (p_i u_i^* + P_i \mathrm{D}u_i^*) \, \mathrm{d}s, \tag{3}$$

where $p_i$ and $P_i$ are two independent variables which can be prescribed on the boundary.

For such a class of models, the balance equations and boundaries conditions yield:

$$\frac{\partial \sigma_{ij}}{\partial x_j} - \frac{\partial^2 \Sigma_{ijk}}{\partial x_j \, \partial x_k} + G_i = 0, \tag{4}$$

$$\sigma_{ij} n_j - n_k n_j \mathrm{D}\Sigma_{ijk} - \frac{\mathrm{D}\Sigma_{ijk}}{\mathrm{D}x_k} n_j - \frac{\mathrm{D}\Sigma_{ijk}}{\mathrm{D}x_j} n_k + \frac{\mathrm{D}n_l}{\mathrm{D}x_l} \Sigma_{ijk} n_j n_k - \frac{\mathrm{D}n_j}{\mathrm{D}x_k} \Sigma_{ijk} = p_i, \tag{5}$$

$$\Sigma_{ijk} n_j n_k = P_i, \tag{6}$$

where $\mathrm{D}q/\mathrm{D}x_j$ denotes the tangential derivatives of any quantity $q$:

$$\frac{\mathrm{D}q}{\mathrm{D}x_j} = \frac{\partial q}{\partial x_j} - n_j \mathrm{D}q. \tag{7}$$

More details on the theoretical aspects can be found in [6]. The numerical treatments and the development of a finite element for this kind of model is detailed in [14]. The element has been implemented in the F.E.M. code *Lagamine*, initially developed in Liège, Belgium. It has been chosen to write the constitutive relation in two independent parts. A classical part links the strain rate to the rate of deformation, it is decoupled from the second gradient part which links the double stress rate to the rate of second gradient of displacement. The classical relation is detailed in Sect. 3. The second gradient part has been chosen as simple as possible, i.e., a linear elastic isotropic relation with only one parameter:

$$\begin{bmatrix} \overset{\triangledown}{\Sigma}_{111} \\ \overset{\triangledown}{\Sigma}_{112} \\ \overset{\triangledown}{\Sigma}_{121} \\ \overset{\triangledown}{\Sigma}_{122} \\ \overset{\triangledown}{\Sigma}_{211} \\ \overset{\triangledown}{\Sigma}_{212} \\ \overset{\triangledown}{\Sigma}_{221} \\ \overset{\triangledown}{\Sigma}_{222} \end{bmatrix} = \begin{bmatrix} D & 0 & 0 & 0 & 0 & D/2 & D/2 & 0 \\ 0 & D/2 & D/2 & 0 & -D/2 & 0 & 0 & D/2 \\ 0 & D/2 & D/2 & 0 & -D/2 & 0 & 0 & D/2 \\ 0 & 0 & 0 & D & 0 & -D/2 & -D/2 & 0 \\ 0 & -D/2 & -D/2 & 0 & D & 0 & 0 & 0 \\ D/2 & 0 & 0 & -D/2 & 0 & D/2 & D/2 & 0 \\ D/2 & 0 & 0 & -D/2 & 0 & D/2 & D/2 & 0 \\ 0 & D/2 & D/2 & 0 & 0 & 0 & 0 & D \end{bmatrix} \begin{bmatrix} \frac{\partial \dot{v}_{11}}{\partial x_1} \\ \frac{\partial \dot{v}_{11}}{\partial x_2} \\ \frac{\partial \dot{v}_{12}}{\partial x_1} \\ \frac{\partial \dot{v}_{12}}{\partial x_2} \\ \frac{\partial \dot{v}_{21}}{\partial x_1} \\ \frac{\partial \dot{v}_{21}}{\partial x_2} \\ \frac{\partial \dot{v}_{22}}{\partial x_1} \\ \frac{\partial \dot{v}_{22}}{\partial x_2} \end{bmatrix}, \tag{8}$$

where $\dot{v}_{ij}$ is the material time derivative of $v_{ij}$ and $\overset{\triangledown}{\Sigma}_{ijk}$ is the Jaumann double stress rate.

## 3 Constitutive Law

The classical part of the law used in this work is an elasto-plastic law inspired from the model published by Holcomb and Rudnicki [13] for a rock (Tennessee marble), itself issues from the constitutive framework of Rudnicki and Rice [18]. The law has been simplified a little bit in order to reduce the number of parameters, in particular, we assume a vanishing cohesion because we believe that it has not a qualitative influence for the aim of this study.

It is a nonassociated model where the yield surface and the plastic potential are smooth, depending on the first and second stress invariants, and linear with respect the first one (Drucker-Prager type surfaces). The surfaces can evolve with the accumulated plastic shear strain.

We define, from the Cauchy stress $\sigma_{ij}$, the equivalent shear stress $\overline{\tau}$ as:

$$\overline{\tau} = \sqrt{(1/2) s_{ij}\, s_{ij}}, \tag{9}$$

where the repeated subscript implies the summation and where $s_{ij} = \sigma_{ij} - \sigma\, \delta_{ij}$ is the deviatoric stress, $\delta_{ij}$ being the Kronecker delta, and $\sigma = 1/3\ \mathrm{tr}(\sigma_{ij})$ the mean stress. The accumulated plastic shear strain is defined as:

$$\overline{\gamma}^p = \int \sqrt{2 \mathrm{d}e^{\mathrm{p}}_{ij} \mathrm{d}e^{\mathrm{p}}_{ij}}, \tag{10}$$

where $\mathrm{d}e^{\mathrm{p}}_{ij} = \mathrm{d}\varepsilon^{\mathrm{p}}_{ij} - 1/3\ \mathrm{d}e^{\mathrm{p}} \delta_{ij}$ is the deviatoric part of the plastic strain increment and $\mathrm{d}e^{\mathrm{p}} = \mathrm{tr}(\mathrm{d}\varepsilon_{ij})$ is the plastic volumic strain increment.

The yield surface is defined by

$$F = \overline{\tau} + \sigma \mu(\overline{\gamma}^{\mathrm{p}}), \tag{11}$$

$\mu$ is a friction coefficient function of the accumulated plastic shear strain.

The consistency condition implies that

$$\mathrm{d}F = \mathrm{d}\overline{\tau} + \mu \mathrm{d}\sigma - H \mathrm{d}\overline{\gamma}^{\mathrm{p}} = 0, \tag{12}$$

where $H = -\sigma . \partial\mu / \partial\overline{\gamma}^{\mathrm{p}}$ is a hardening parameter, positive for a strain hardening and negative for a strain softening. This relation can also be wrote as:

$$\mathrm{d}\overline{\gamma}^{\mathrm{p}} = \frac{1}{H} \left( \frac{s_{ij}}{2\overline{\tau}} + \frac{1}{3} \mu\ \delta_{ij} \right) \mathrm{d}\sigma_{ij}. \tag{13}$$

The plastic potential is defined as:

$$G = \overline{\tau} + \sigma \beta(\overline{\gamma}^{\mathrm{p}}), \tag{14}$$

$\beta$ is a dilatancy coefficient function of the accumulated plastic shear strain. The flow rule can be expressed as:

$$\mathrm{d}\varepsilon^{\mathrm{p}}_{ij} = \mathrm{d}\lambda \frac{\partial G}{\partial \sigma_{ij}}, \tag{15}$$

where $\mathrm{d}\lambda$ is a positive term, which in fact, due to the expression of $\overline{\gamma}^{\mathrm{p}}$ in (10) is equal to $\mathrm{d}\overline{\gamma}^{\mathrm{p}}$. So, the plastic strain can be expressed as:

$$\mathrm{d}\varepsilon^{\mathrm{p}}_{ij} = \frac{1}{H} \left( \frac{s_{ij}}{2\overline{\tau}} + \frac{1}{3} \beta \delta_{ij} \right) \left( \frac{s_{kl}}{2\overline{\tau}} + \frac{1}{3} \mu \delta_{kl} \right) \mathrm{d}\sigma_{kl} \tag{16}$$

and also decomposed in two parts:

$$\begin{cases} \mathrm{d}e^{\mathrm{p}}_{ij} = \frac{1}{2}\ \frac{s_{ij}}{\overline{\tau}} \mathrm{d}\overline{\gamma}^{\mathrm{p}} \\ \mathrm{d}e^{\mathrm{p}} = \beta \mathrm{d}\overline{\gamma}^{\mathrm{p}}. \end{cases} \tag{17}$$

The functions $\mu$ and $\beta$ are defined by:

$$\mu(\overline{\gamma}^{\mathrm{p}}) = (h_0 - h_\infty)\gamma_0 \ \mathrm{atan}\,(\overline{\gamma}^{\mathrm{p}}/\gamma_0) + h_\infty\,\overline{\gamma}^{\mathrm{p}}, \tag{18}$$

$$\beta(\overline{\gamma}^{\mathrm{p}}) = \beta_\infty - \frac{\beta_\infty - \beta_0}{1 + (\overline{\gamma}^{\mathrm{p}}/c_0)^2}, \tag{19}$$

such that $H(\overline{\gamma}^{\mathrm{p}} = 0) = -h_0\sigma$, $H(\overline{\gamma}^{\mathrm{p}} = \infty) = -h_\infty\sigma$, $\beta(\overline{\gamma}^{\mathrm{p}} = 0) = \beta_0$ and $\beta(\overline{\gamma}^{\mathrm{p}} = \infty) = \beta_\infty$. $\gamma_0$ and $c_0$ are constitutive parameters. $h_0$ is (generally) positive in order to have a strain hardening at the beginning of the loading, but $h_\infty$ can be either positive to have a law which is always hardening, or negative to have a softening regime. Illustration of the constitutive relation is given in Fig. 1.

The elastic part of the law is assumed to be linear and isotropic and can be written as:

$$\mathrm{d}\sigma_{ij} = [G(\delta_{ik}\delta_{jl} + \delta_{il}\delta_{jk}) + (K - 2/3G)\delta_{ij}\delta_{kl}]\ \mathrm{d}\varepsilon^{\mathrm{e}}_{kl}, \tag{20}$$

where superscript "e" denotes the elastic part of the strain and $K$ and $G$ are the bulk modulus and the shear modulus, respectively. That can be decomposed in two parts:

$$\begin{cases} \mathrm{d}s_{ij} = 2G\mathrm{d}e^{\mathrm{e}}_{ij} \\ \mathrm{d}\sigma \ \ = K\mathrm{d}e^{\mathrm{e}} \end{cases} \tag{21}$$

And finally, we have assumed as usual that the total strain is the sum of the plastic strain and the elastic strain: $\mathrm{d}\varepsilon_{ij} = \mathrm{d}\varepsilon^{\mathrm{p}}_{ij} + \mathrm{d}\varepsilon^{\mathrm{e}}_{ij}$.

The law has been implemented in the finite element code *Lagamine* by an implicit backward Euler method and subtime increments. We used the Jaumann rate of the Cauchy stress tensor to compute the stress increment during a time step.

For the following computations, we have adopted the parameters given in Table 1. They do not correspond to a specific material but seem reasonable.

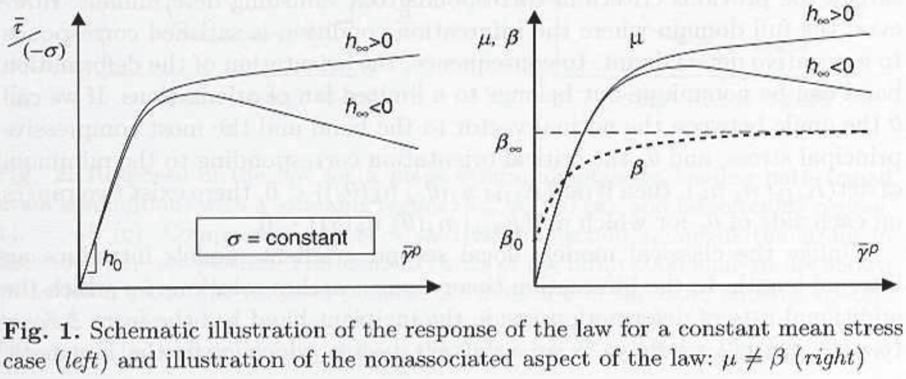

**Fig. 1.** Schematic illustration of the response of the law for a constant mean stress case (*left*) and illustration of the nonassociated aspect of the law: $\mu \neq \beta$ (*right*)

**Table 1.** Values of the constitutive parameters of the classical part of the law

| parameter | value | unit |
|---|---|---|
| $G$ | 23.1 | GPa |
| $K$ | 50 | GPa |
| $h_0$ | 1,000 | |
| $h_\infty$ | $-30$ or $+5$ | |
| $\gamma_0$ | $5 \times 10^{-4}$ | |
| $\beta_0$ | 0.01 | |
| $\beta_\infty$ | 0.4 | |
| $c_0$ | $5 \times 10^{-4}$ | |

## 4 Nonunicity of Solutions

### 4.1 Theoretical Analysis

We focus here on the loss of uniqueness of solutions by emergence of solutions with strain localization, i.e., deformation bands. The bifurcation theory which consists to exhibit conditions for existence of a deformation band (e.g., [2,18]) can be extended to local second gradient models. It appears that bifurcation condition for such models, at least when classical law and second gradient law are decoupled, is the same than for classical models but it introduces in addition a size effect [4].

The classical law used here is a bilinear rate law, and, assuming a small strain hypothesis, the bifurcation condition can be expressed as [5]:

$$\det(K_{ijkl}\ n_j\ n_k) \leq 0, \tag{22}$$

where $K_{ijkl}$ is the constitutive tensor which links the stress rate to the rate of deformation (for simplicity, we neglect the additional terms introduced by the Jaumann rate), and $n_i$ is a unit normal vector to the incipient deformation band.

As there is a continuous evolution of the stiffness modulus during the accumulation of plastic strain in the model used here, the first possibility to satisfy the previous criterium corresponds to a vanishing determinant. However, the full domain where the bifurcation condition is satisfied corresponds to a negative determinant. In consequence, the orientation of the deformation band can be nonunique but belongs to a limited fan of orientations. If we call $\theta$ the angle between the normal vector to the band and the most compressive principal stress, and $\theta_c$ the critical orientation corresponding to the minimum of $\det(K_{ijkl}\ n_j\ n_k)$, then if $\det(K_{ijkl}\ n_j(\theta_c)\ n_k(\theta_c)) < 0$, there exist two ranges on each side of $\theta_c$ for which $\det(K_{ijkl}\ n_j(\theta)\ n_k(\theta)) \leq 0$.

Unlike the classical models, local second gradient models introduce an internal length. In the bifurcation theory, one searches solutions for which the additional rate of deformation inside the incipient band has the form $\Delta\dot{\varepsilon}_{ij} = (g_i n_j + g_j n_i)/2$ where $g_i$ is an arbitrary vector which gives the kinematic inside the band. Due to the second gradient law, this vector has an harmonic form $g_i(\alpha) = g_i^0 \sin(\alpha/\xi)$, where $\alpha$ is the position across the band and $\xi$ is a specific length [4]. The latter depends on the modulus of the constitutive law and can be viewed as an indicator of the band thickness. It appears that when $\det(K_{ijkl}\ n_j(\theta)\ n_k(\theta)) = 0$, the band has an infinite thickness, and a finite thickness if the determinant is strictly negative. In consequence, theoretically, the bifurcation onset for local second gradient models is not different from one for the underlying classical models. However, there is a size effect which delays the onset of localization.

We illustrate these results on a plane strain compression path in Fig. 2. In direction 3, a stress of $10^6$ Pa is imposed, the direction 2 corresponds to the plane strain direction and direction 1 to the direction of compression. Two cases are illustrated, on the left, the case $h_\infty = -30$ which means a softening regime after an initial hardening regime, and on the right, the case $h_\infty = +5$ which means a law exhibiting always strain hardening. Due to the nonassociated aspect of the law, the first onset where the bifurcation condition (22) is satisfied, is in the hardening regime (indicated by a star in Fig. 2a, c).

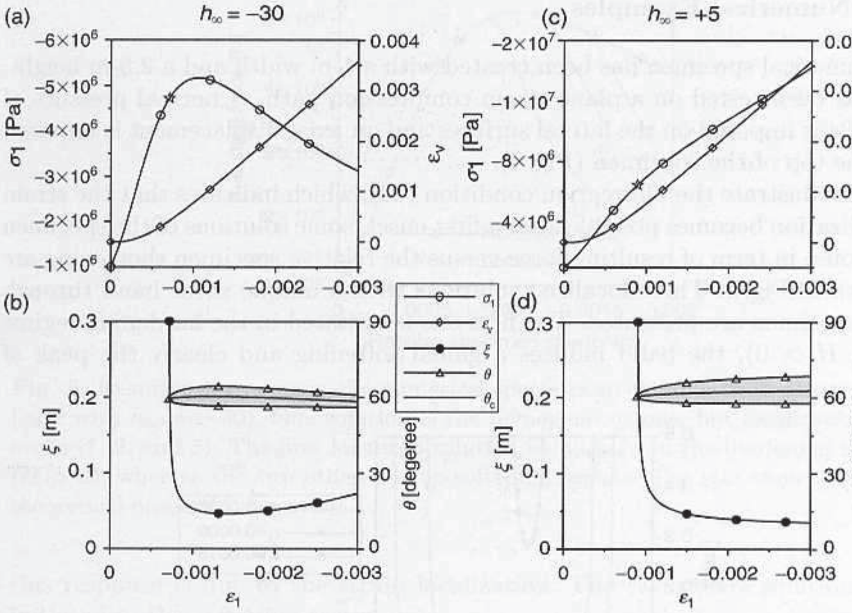

**Fig. 2.** Response of the law for a plane strain compression loading path (small strain assumption) with a softening regime, $h_\infty = -30$ (**a**), and no softening regime, $h_\infty = +5$ (**c**). Compression stress $\sigma_1$ and volumic strain $\varepsilon_v$ versus the strain in direction 1, $\varepsilon_1$, are plotted. The characteristics of the bifurcation analysis are shown in the lower part. The range of possible orientation $\theta$ of the band and the specific length $\xi$ corresponding to the critical angle $\theta_c$ (**b**) and (**d**) are plotted versus $\varepsilon_1$. The star in (**a**) and (**c**) corresponds to the first onset of possible localization

At this onset, the specific length, which should be considered as an indicator of the incipient band thickness, is infinite. This length decreases quickly during the subsequent loading and becomes more or less constant (Fig. 2b, d). This limit value is depending, among others, on the second gradient law modulus which has been choose here at $D = 5 \times 10^5$ Pa m$^2$, and more precisely is proportional to the square root of $D$. It can be adjusted, so, length values are essentially qualitative in this present work. As far as the band orientation is concerned, at the first possible onset of bifurcation, the orientation is unique, but a range of orientation is possible in the subsequent loading. The critical orientation $\theta_c$ corresponds to the middle of this range.

The specific length $\xi$ is itself dependent on the band orientation angle $\theta$. The specific length plotted in Fig. 2b, d corresponds to the critical angle $\theta_c$, and is the minimum of $\xi$ on the range of possible orientations. The evolution of $\xi$ with respect to the band orientation angle $\theta$ is shown in Fig. 3 for three steps of loading on the previous plane strain path. On the limits of the orientation range, the length tends toward infinity. There is also here a size effect which tends to limit the range of possible orientations.

## 4.2 Numerical Examples

A numerical specimen has been created with a 1-m width and a 2.5-m height. It has been tested on a plane strain compression path. A normal pressure of $10^6$ Pa is imposed on the lateral surfaces and an axial displacement is imposed at the top of the specimen (Fig. 4).

To illustrate the bifurcation condition (22), which indicates that the strain localization becomes possible after a first onset, some solutions of the specimen response in term of resulting force versus the relative specimen shortening are shown in Fig. 5. Three localized solutions with a unique shear band through the specimen are presented. The first one is initiated in the hardening regime (i.e., $H > 0$), the band induces a global softening and clearly the peak of

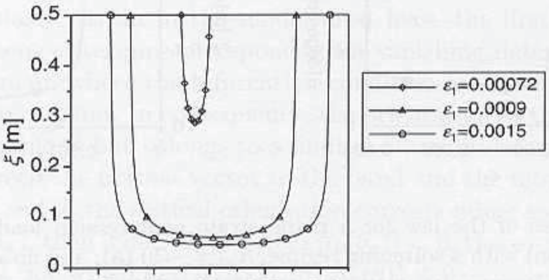

**Fig. 3.** Evolution of the specific length $\xi$ with respect to the band orientation angle $\theta$ for three steps of the plane strain path (case with $h_\infty = -30$)

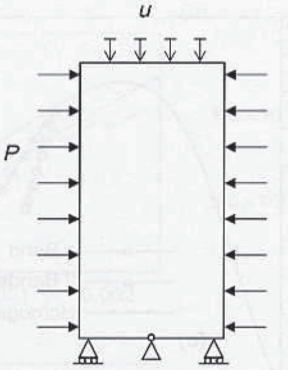

**Fig. 4.** Limit conditions of the plane strain compression. $P$ is a constant normal pressure and $u$ is a vertical imposed displacement

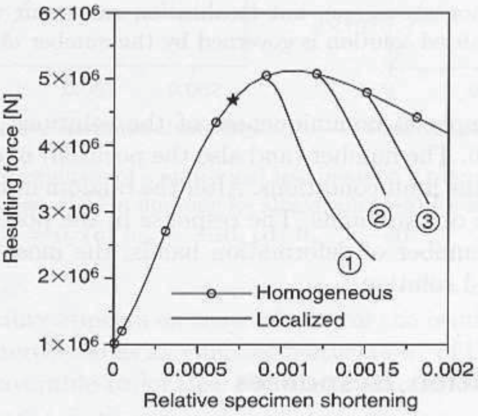

**Fig. 5.** Example of responses of a numerical specimen in a plane strain compression (case with $h_\infty = -30$). One solution is the homogeneous one, but localization can occur (1, 2, and 3). The first localized solution is initiated in the hardening regime ($H > 0$), whereas the two others in the softening regime. The star shows the first theoretical onset of bifurcation

this response is due to the strain localization. The two others solutions are initiated in the softening regime.

The localized solutions have been found using a so-called directional research algorithm. It consists, when in a time step of the computation, a full Newton–Raphson method is used to solve the linearized problem, to initiate the method with a random nodal values field. The algorithm has been used initially for classical models [7] and then for second gradient models [4, 5]. More details can be found in these references.

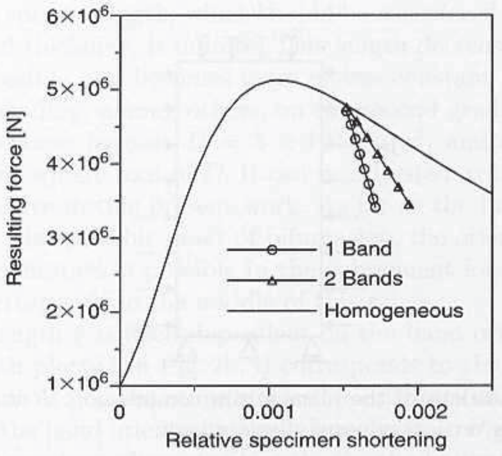

**Fig. 6.** Example of responses of a numerical specimen in a plane strain compression (case with $h_\infty = -30$, $D = 3 \times 10^5$ Pa m$^2$, and a specimen height of 3 m). One solution is the homogeneous one, but localization can occur with one or several bands. The postlocalized solution is governed by the number of bands

An other example of nonuniqueness of the solutions of the problem is illustrated in Fig. 6. The number (and also the position) of deformation bands is not imposed by the limit conditions. After the random initiation, one obtains solutions with one or two bands. The response in the postlocalized regime is governed by the number of deformation bands, the most softening solution being the one band solution.

## 5 Postlocalisation Responses

It seems interesting to explore the effect of the constitutive model on the postlocalization response, what kind of response we are able to obtain? We have studied here only the effect of the parameter $h_\infty$. If this one is positive, then the law is always a strain hardening one and if it is negative, there is a softening regime after an initial strain hardening one. We did not change the other parameters of the model, in particular, we keep the parameters related to the plastic volume variation. Homogeneous and a localized solutions are shown in Fig. 7 for four values of $h_\infty : +5, 0, -10, -30$. For the four localized solutions, one observes a global decrease of the axial force at the onset of localization, even if sometimes this drop is very small. Then, for $h_\infty = +5$ and 0, one observe a global force increase in the localized solutions, and for $h_\infty = -10$ and $-30$, a global force decrease of the response. For these two last cases, the zone of strain localization remains the same during the loading history, but for the two first cases, one observes a nonpersistence of the zone of localization, this zones change abruptly and several times during the specimen

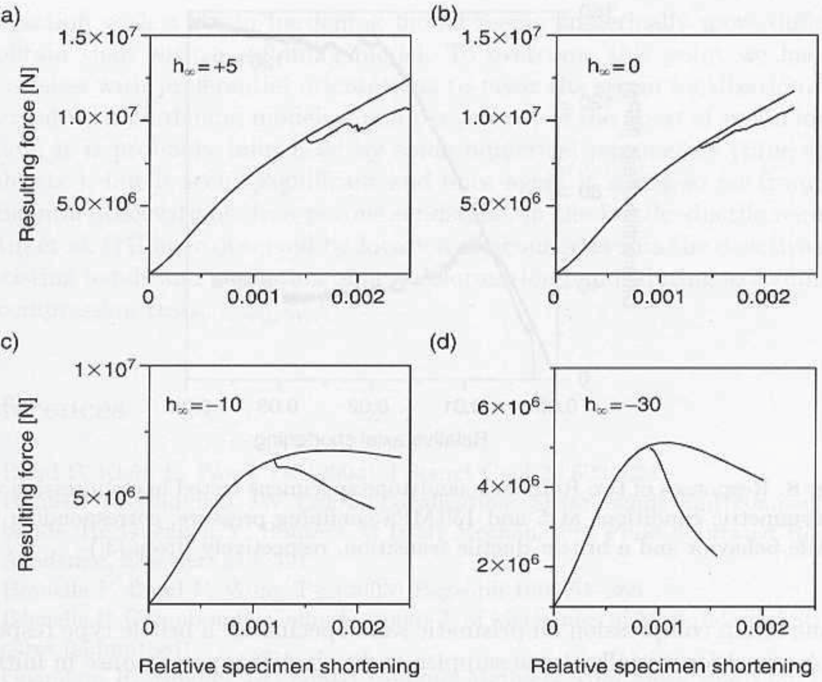

**Fig. 7.** Examples of responses of a numerical specimen on a plane strain compression path (the homogeneous solution and one localized solution) for several values of $h_\infty$: (a) $h_\infty = +5$, (b) $h_\infty = 0$, (c) $h_\infty = -10$, (d) $h_\infty = -30$

loading. This volatility appears on the evolution of the resulting force as small peaks. It can be interpreted as an effect of "saturation" of the shear band and it becomes more favorable to localize elsewhere than to continue to activate the current band.

These results have a strong similitude with the experimental observations on soft porous rocks or sands. For example, in experimental axisymmetric triaxial compression tests controlled by the rate of axial shortening, which are classical tests in rock mechanics, it is well known that the porous rock behavior changes with the level of confining pressure (e.g., [1,3]). For the low confining pressure, the behavior is generally called brittle and the failure is characterized by a strong decrease of the axial force and the presence of a few deformation bands. For high confining pressure, in the brittle–ductile transitional regime, it can be observed, after the strain localization, an increase of the axial force and a large number of deformation bands. Moreover, the evolution of the axial force presents also several small peaks which are generally associated with a high level of acoustic emission events and explained by an apparition of some new deformation bands. An illustration of such a behavior is given in Fig. 8, at two levels of confining pressure on a porous sandstone. More or less similar loading force evolutions can be observed in sand specimens. For example in

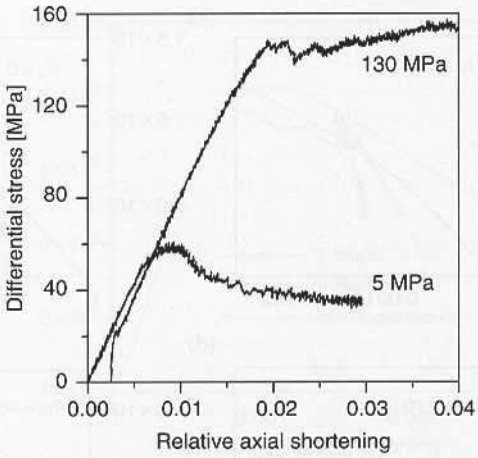

**Fig. 8.** Responses of two Rothbach sandstone specimens tested in compression with axisymmetric conditions at 5 and 130 MPa confining pressure, corresponding to a brittle behavior and a brittle–ductile transition, respectively (from [3])

plane strain compression on prismatic sand specimens, a brittle type response is observed for initially dense samples and a ductile type response in initially loose samples (e.g., [9]).

## 6 Conclusion

If models with an internal length like local second gradient models resolve the problem of mesh size dependence, the uniqueness of solution is not necessarily restored. In fact, there is no reason to restore the uniqueness. If one considers this question from the experimental point of view, it is known that the post localization regime is rarely reproducible, even with the best care as possible for preparing a specimen and performing a test. This nonrepeatability is probably induced by a large part to some microstructural details in the material which make that for a given specimen, localization will occur earlier or latter, in this zone and not elsewhere, with one shear band or several, etc. These details cannot be captured with constitutive models and it is our opinion that we have to make the comparison between the numerical nonuniqueness and the experimental nonrepeatability.

Therefore, we showed that postlocalized behaviors observed experimentally like the brittle regime or the brittle–ductile transition can be simulated. For example, the resulting axial force applied during a plane strain compression of a numerical specimen can, after localization, decrease but also increase, depending on the constitutive parameters. We showed also, and this confirms the theoretical predictions, that the localization can occur with a strain hardening model and that the softening is not necessarily for that. However, the localization with a strain hardening model seems numerically more difficult to obtain than with a softening model. To overcome this point we had to use meshes with preferential orientations to favor the strain localization. We observed with hardening models a non persistence of the areas of strain localization, it is probably influenced by some numerical parameters (time step, mesh, etc.), but it seems significant and once again it is not so far from experimental observations. In a porous sandstone, in the brittle–ductile regime, Fortin et al. [11] have observed by location of acoustic events the deactivation of existing bands and activation of new deformation bands during axisymmetric compression tests.

## References

1. Baud P, Klein E, Wong T-f (2004) J Struct Geol 26:603–624
2. Bésuelle P, Rudnicki JW (2004) Localization: Shear bands and compaction bands. In: Guéguen Y, Boutéca M (eds) Mechanics of Fluid-Saturated Rocks. Academic, Elsevier, 219–321.
3. Bésuelle P, Baud P, Wong T-f (2003) Pageoph 160:851–868
4. Bésuelle P, Chambon R, Collin F (2006) J. of Mechanics of Materials and Structures (submitted)
5. Chambon R, Moullet J-C (2004) Comput Methods Appl Mech Eng 193:2771–2796
6. Chambon R, Caillerie D, Matsushima T (2001) Int J Solids Struct 38:8503–8527
7. Chambon R, Crochepeyre S, Charlier R (2001) Int J Numer Methods Eng 51:315–332
8. Cosserat E, Cosserat F (1909), Théorie des Corps Déformables. Hermann, Paris
9. Desrues J, Viggiani G (2004) Int J Numer Anal Methods Geomech 28:279–321
10. Fleck NA, Hutchinson JW (1997) Adv Appl Mech 33:295–361
11. Fortin J, Stanchits S, Dresen G, Guéguen Y (2005) J Geophys Res, *submitted*
12. Germain P (1973) J Méc 12:235–274
13. Holcomb DJ, Rudnicki JW (2001) Int J Numer Anal Methods Geomech 25:109–129
14. Matsushima T, Chambon R, Caillerie D (2002) Int J Numer Methods Eng 54:499–521
15. Mindlin RD (1964) Arch Ratlonal Mech Anal 4:50–78
16. Mühlhaus H, Aifantis E (1991) Int J Solids Struct 28:845–857
17. Pijaudier-Cabot G, Bažant ZP (1987) J Eng Mech 113:1512–1533
18. Rudnicki JW, Rice JR (1975) J Mech Phys Solids 23:371–394
19. Toupin RA (1962) Arch Ratlonal Mech Anal 11:385–414
20. Vardoulakis I, Aifantis E (1991) Acta Mech. 87:197–217